INVESTIGATION OF SOIL-FLEXIBLE FOUNDATION-STRUCTURE INTERACTION FOR INCIDENT PLANE SH WAVES

by

Vlado Gicev

A Dissertation Presented to the
FACULTY OF THE GRADUATE SCHOOL
UNIVERSITY OF SOUTHERN CALIFORNIA
In Partial Fulfillment of the
Requirements for the Degree
DOCTOR OF PHILOSOPHY
(CIVIL ENGINEERING)

May 2005

ACKNOWLEDGEMENTS

I would like to express my sincerest thanks to Professor Mihailo Trifunac for his masterful guidance and help throughout the research, without which this thesis would not exist. He has been not only a great scientific advisor but also a friend whose company made my life in the U.S. easier. Equally, I would like to thank Professor Marija Todorovska, who brought me to USC, and financially supported my research from her grants, and whose advice was very useful in my studies.

I am grateful to Professors V.W. Lee and W. Proskurowski for their superb teaching of the classes related to my research and for their enthusiasm in giving advice whenever I asked them.

I would like to thank Professor F.J. Sanchez Sesma from Universidad National Autonoma de Mexico for advice regarding numerical treatment of artificial boundaries.

The teaching experience I had as a teaching assistant in the Civil Engineering Department at USC was very valuable for my career, and I want to express my gratitude to the Department of Civil Engineering for giving me this opportunity.

Finally, I want to thank my beloved daughter Sofija and my wife Maja for their endless patience. I dedicate this dissertation to them.

TABLE OF CONTENTS

LIST OF TABLES

LIST OF FIGURES

ABSTRACT

A numerical scheme is used for simulation of SH wave propagation through three different media: soil, a semi-circular flexible foundation, and a structure. The response is studied for two types of input: monochromatic steady-state wave and half-sine pulse.

The steady-state solution is presented for the example of the Hollywood Storage Building for two angles of incidence and for two different foundation stiffness. The displacement and strain amplitudes for the flexible foundation are generally larger than the amplitudes for the rigid foundation, except in the frequency range close to the natural frequencies of the building on a fixed base.

The transient response to a half-sine wave is analyzed with emphasis on three aspects of the problem:

1. Energy distribution
2. Response at the contacts
3. Response when the soil is nonlinear.

It is shown that the distribution of the maximum energy in the building and the scattered energy from the foundation are invariant with the duration of the pulse. Also, the input energy reaching the foundation is independent of the angle of incidence. The results of the energy distribution are illustrated for the Hollywood Storage building and the Holiday Inn hotel in Van Nuys, both in the Los Angeles metropolitan area.

The response at the contacts (soil-foundation and foundation-building) is studied for the Holiday Inn hotel for four angles of incidence and three foundation stiffness. The results are presented as normalized average displacements and as functions of dimensionless frequencies.

The constitutive law of nonlinear soil is assumed to be ideally elasto-plastic. Three levels of nonlinearity are considered, and the energy distribution and the distribution of the permanent strain are shown graphically for the above-mentioned two buildings.

Through analysis of the response at the contacts, it is shown that the response in the presence of small and intermediate nonlinearity generally does not differ appreciably from the linear response. There are significant differences between the response experiencing large nonlinearity and the linear response.

CHAPTER I

INTRODUCTION

1.1 Numerical methods

In the era of fast computers, obtaining solutions to many previously unsolvable problems became a reality, especially for problems involving partial differential equations (PDE), in which the analytical solutions exist only for the simplest conditions. By utilizing numerical methods, one can solve a problem from initial time to some desired time at all spatial points. The most popular numerical methods for solving PDEs are the finite element method (FEM) and the finite difference method (FD). Usually, FEM uses implicit schemes in which the unknown quantities at all spatial points are obtained simultaneously for each time step by solving a system of linear algebraic equations. Most finite difference schemes are explicit, wherein the solution is obtained from the solution of the previous time step and the equations are uncoupled. Solving a full linear system of N^{th} order requires $O(N^2)$ operations, while for the uncoupled system the order of complexity is O(N). Thus, the explicit schemes are preferable in the numerical analyses, especially for large-scale problems (where N is big). The systems occurring in the implicit schemes are usually banded and symmetric, and so the order of complexity is much smaller than $O(N^2)$ but still bigger than the one for explicit schemes. Also, the implicit schemes are unconditionally stable, which is not the case with the explicit schemes. Further, the finite elements as a numerical tool are more suitable than finite

differences for modeling complicated and irregular geometries. On the other hand, for large-scale problems, as inseismological practice, for example, the explicit schemes are preferable because they are cheaper and easier to implement in numerical algorithms.

Our goal in this work is to utilize a numerical scheme for simulation of wave propagation through bounded and unbounded media and to study the phenomena accompanying this wave passage.

The idea of the numerical methods for PDEs is to replace the derivatives with small but finite differences at discrete space and time increments. Using an iterative procedure, the solution advances in time and, for the wave equation, in space as well. This iteration can go on forever, and it is up to the particular application when the algorithm should be ended. From many numerical schemes for hyperbolic PDE described in the literature (e.g., Smith,1985; Sod, 1985; Katsaounis & Levy,1999; Levy et al., 2000), the Lax-Wendroff (Lax & Wendroff,1964) scheme is chosen. This is an explicit scheme, with second-order accuracy, both in time and in space $O(\Delta t^2, \Delta x^2)$.

The problems we wish to study, can be classified into three groups:

- Heterogeneities and discontinuities of the medium
- Modeling of the free surfaces
- Artificial boundaries.

According to Moczo (1989) and Zahradnik et al. (1993), the computational finite difference schemes that are used in applications of wave propagation, can be divided as follows:

- Homogeneous schemes in which the boundary conditions of continuity of the displacements and the stresses are applied explicitly at the contact points,
- Heterogeneous schemes in which all of the points in the inner computational domain, including the contact points, are computed with the same formula.

In the earlier works, the wave-propagation problems were formulated with the second-order wave equation in terms of the displacement. Alterman and Karal (1968) used the homogeneous formulation to solve elastic wave propagation in layered media. At the contact points, using the continuity of the stresses and displacements, they consider additional rows of fictitious points, which they use for computing the displacements at the contact. After obtaining the displacements at the contact, the motion in the next medium can be computed using the displacement at the boundary points from the previous medium.

Boore (1972) proposed the heterogeneous scheme. At an interface point m, he approximated the derivative by

$$\frac{\partial}{\partial x}\left(\mu\frac{\partial u}{\partial x}\right)=\frac{\mu_{m+1/2}\left(u_{m+1}-u_m\right)-\mu_{m-1/2}\left(u_m-u_{m-1}\right)}{\Delta x^2}. \qquad (1.1)$$

When this derivative is used in the second-order wave equation directly, the displacement at the boundary point m is obtained without explicitly considering the stress-continuity boundary condition $\left(\mu\frac{\partial w}{\partial x}\right)_1=\left(\mu\frac{\partial w}{\partial x}\right)_2$, where x is the normal of the contact at the considered point and the subscripts represent the two media. Boore treated the free surface as a special interface with $\mu_2 = 0$ and the boundary condition at the free surface, $\frac{\partial w}{\partial n}=0$, where

n is normal of the free surface. This approximation of the free surface, known as vacuum formalism, was used by Zahradnik and Urban (1984) in studying variation of the ground motion due to the presence of a mountain. Other schemes, as in Vidale and Clayton (1986), Levander (1988), and Hayashi et al. (2001), use special formulae for computing the needed functions at the points of the free surface.

Kummer et al. (1987) approximated the mixed derivatives that appear in the equations of P (pressure) and SV (shear, in plane of propagation) wave motion by expanding the first derivative in a specific direction in terms of a Taylor series. For example

$$\frac{\partial f(x,y)}{\partial y} = \frac{\partial f(x_i,y_j)}{\partial y} + \Delta x \frac{\partial^2 f(x_i,y_j)}{\partial x \partial y} + \frac{\Delta x^2}{2} \frac{\partial^3 f(x_i,y_j)}{\partial x^2 \partial y} \qquad (1.2)$$

Zahradnik et al. (1993) tested the above scheme and three other schemes for their behavior at discontinuities. Moczo (1989) used a heterogeneous scheme with variable grid spacing in the vertical direction and the Reynolds artificial boundary (Reynolds, 1978) for solving a sedimentary basin. Virieux (1984) introduced the first-order finite difference scheme for SH (shear, normal to the plane of propagation) waves by replacing the displacement field with the particle velocity and the shear stress field. With this new scheme, he solved a quarter plane, a sedimentary basin, and a salt dome problem for impulsive and plane wave excitation. Levander (1988) proposed $O(k^2,h^4)$, a staggered grid. Lin (1996) proposed Zwas's scheme (Eilon et al.,1972), used in gas dynamics, for solving crack problems.

At present, authors are mostly concerned with developing multigrid and 3-D schemes, as in Hayashi et al. (2001), Ohminato and Chouet (1997), Wang and Schuster (2001), Graves (1996) that provide high-order accuracy in space $O(k^2,h^4)$. Accurate higher-order schemes, especially in space, can be tailored by using more neighboring points in the stencil, as shown by Dablain (1986).

1.2 Soil-Structure Interaction

The particular problem studied in this work is the soil-structure interaction with flexible foundation. By its nature, this is a 3-D problem because both the superstructure and the foundation are 3-D media. For simplicity, in this work only a two-dimensional representation of the problem will be studied by taking one dimension (the length) of the structure and the foundation as being infinite. For this 2-D model, we will study only the anti-plane response caused by the propagation of SH waves.

Wong and Trifunac (1975) studied the wall-soil-wall interaction with the presence of two or more shear walls, and Abdel-Ghaffar and Trifunac (1977) studied the soil-bridge interaction both with a semi-cylindrical rigid foundation and for an input plane SH wave. Other studies were conducted to analyze the dependence of the interaction on the shape of the rigid foundation. Wong and Trifunac (1974) solved the interaction of the shear wall erected on the elliptical rigid foundation for shallow and deep embedment. Westermo and Wong (1977) studied three different boundary models for soil-structure interaction of an embedded semi-

circular rigid foundation and showed the differences in their dynamic behavior. They concluded that without a transmitting boundary all of the models develop resonant behavior and that the introduced damping in the soil cannot adequately model the radiation damping. Luco and Wong (1977) studied a rectangular foundation welded to an elastic half space and excited by a horizontally propagating Rayleigh wave. V.W. Lee (1979) solved a 3-D interaction problem consisting of a single mass supported by an embedded hemispherical, rigid foundation for incident plane P, SV, and SH waves, in spherical coordinates.

While considerable research has been carried out on the phenomena of interaction with a rigid foundation, only several recent publications deal with a flexible foundation. Todorovska et al. (2001) solved an interaction of a dike on a flexible embedded foundation, and Hayir et al. (2001) described the same dike but in the absence of a foundation. Todorovska (2001) gave the estimate that for the ratio of the stiffness of the foundation and the soil $\frac{\mu_f}{\mu_s} > 20$, and for $\rho_f = \rho_s$ the model with an absolutely rigid foundation is approximately valid for many analyses. Aviles et al. (2002) analyzed in-plane motion of a 4 degrees of freedom model with 3 DOF (horizontal, vertical, and rocking) at the flexible foundation and 1 DOF (horizontal) in the superstructure. They described the dependence of the system properties (the effective period and damping) with the change of the geometry of the model.

1.3 Organization

This work is organized in two parts. The first part presents the theory, while the second part illustrates applications and results.

The theoretical part consists of Chapters II and III.

1. The second chapter in the thesis describes the model and the parameters of the numerical scheme. First, a short review of the grid parameters is given, after which the derivation of the numerical scheme is presented. Appendix I in which the finite difference equations are presented for characteristic points in the model, belongs to this chapter.

2. The third chapter starts with a review of the artificial boundaries. In the second section of this chapter, the artificial boundary algorithm is derived, and in the third section it is illustrated using two numerical examples.

The applications part consists of four chapters, which deal with particular applications of the method.

3. The fourth chapter deals with steady-state aspects of the soil-structure interaction, with a flexible foundation. In the first section, some aspects of the soil-structure interaction for a rigid circular foundation are reviewed. In the second section, the input and the grid parameters for this application are introduced, and after that the results and the observations are presented.

4. The fifth chapter deals with the distribution of energy in the system. First, it provides some insight about the interaction system for pulse-like input with a simple 1-D model. In the second section, the input and the grid parameters are explained. Then, in the third section, the

distribution of the energy for two different buildings is studied, and the limitations of the accuracy of the model are discussed. In the last section, conclusions about the energy distribution are presented.

5. In the sixth chapter, input parameters for energy-based engineering design of earthquake-resistant structures are given in the form of averaged amplitudes of the response (displacement and velocity) at the contacts soil-foundation and building-foundation, and as functions of the dimensionless frequency of the ground motion. Also, the displacements at two bottom corners of the building are given as functions of dimensionless frequency. These results are presented for four different incident angles and for three different foundation stiffnesses.

6. Chapter VII illustrates some aspects of the response when the soil is nonlinear. In the first section, assumptions on the constitutive law $\sigma = \sigma(\varepsilon)$, with internal definition of three kinds of nonlinearity, are presented. The next section deals with the balance and distribution of energy in the nonlinear system, and the last section shows the average displacements at the contacts, as functions of dimensionless frequency, and compares the results with those of the linear case.

Finally, general conclusions and a plan for future work are presented.

CHAPTER II

COMPUTATIONAL MODEL

2.1 Numerical schemes and grid parameters: Introduction

The problem under consideration is the soil-foundation-structure interaction of a 2-D rectangular structure with a semicircular foundation embedded in linear or nonlinear soil. The geometric and material properties are given in Fig. 2.1. The physical domain of the problem is infinite in the soil, and for computational purposes, with an imposed artificial boundary (efgh in Fig. 2.2), the problem is defined in the finite domain $\Omega = \Omega_s \mathbf{U} \Omega_f \mathbf{U} \Omega_b$, which consists of three sub-domains. The foundation is flexible, with finite density ρ_f and shear wave velocity β_f. Moreover, without loss of generality, the foundation density is taken to be equal to the soil density $\rho_f = \rho_s$ for simplification of the numerical scheme.

When a continuous problem of wave propagation is approximated with an explicit discrete scheme, the grid spacings and the time step must be chosen in such a way as to properly represent the waveform. First, the grid must satisfy the stability criterion, which requires that the eigenvalues of the system matrix are not greater than 1. For a second-order scheme in two dimensions for the SH case, it is known (Mitchell, 1969) that the stability condition is given by the Courant number :

$$\chi = \beta_{\max} \Delta t \sqrt{\frac{1}{\Delta x^2} + \frac{1}{\Delta y^2}} \leq 1. \qquad (2.1)$$

Fig. 2.1 SOIL-FOUNDATION-STRUCTURE SYSTEM

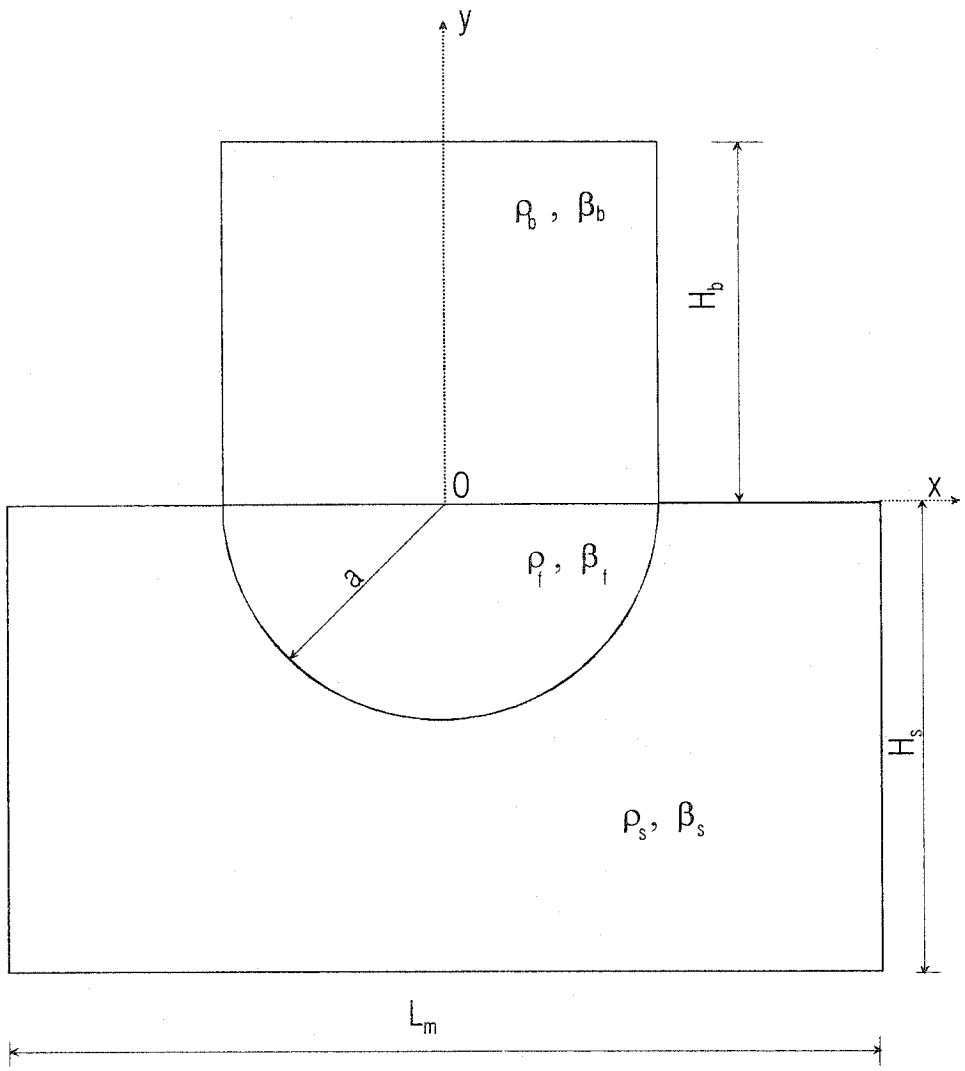

Fig.2.2 THE MODEL WITH THE ARTIFICIAL BOUNDARY

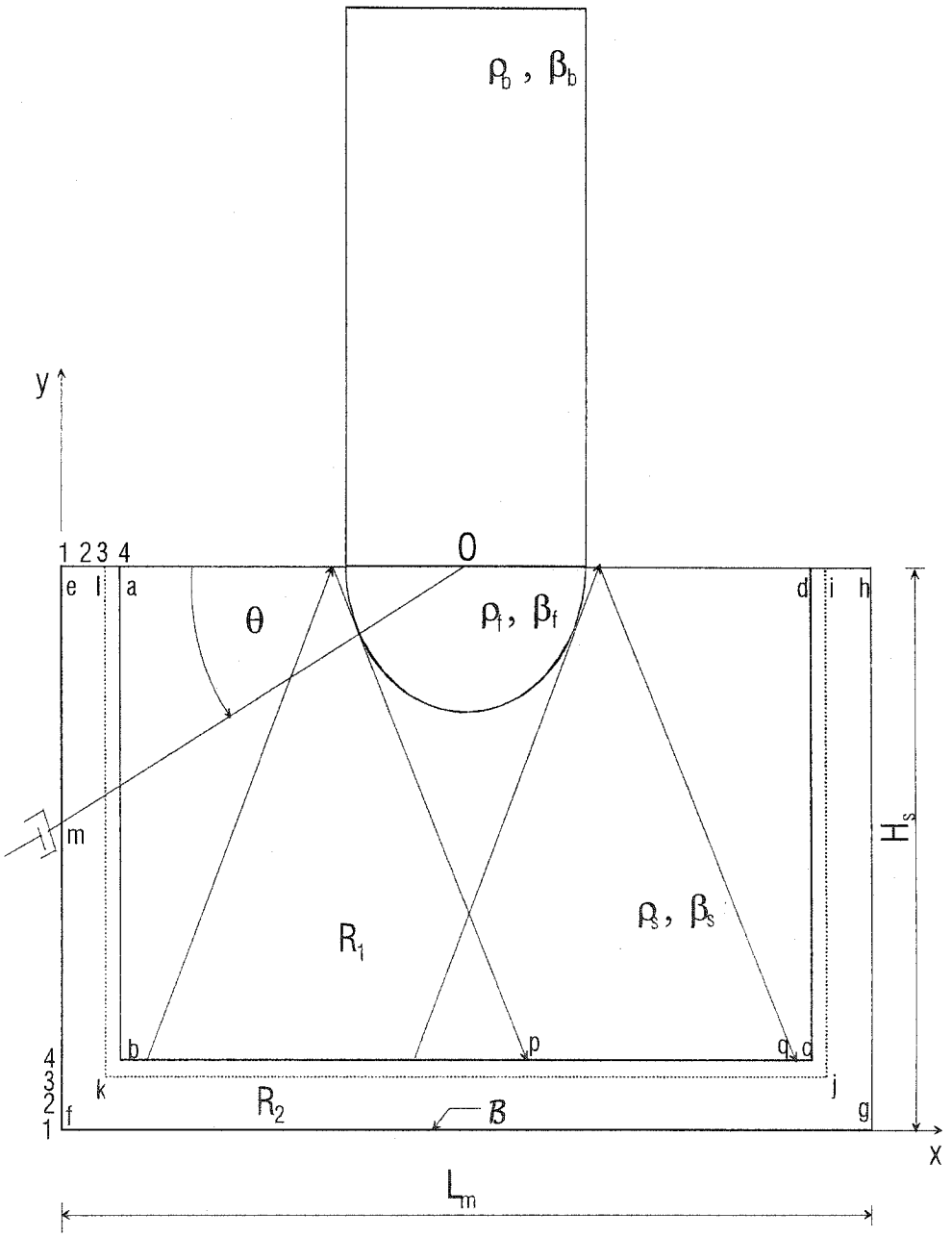

For a homogeneous grid, $\Delta x = \Delta y$, the stability condition becomes

$$\frac{\beta_{\max}\Delta t}{\Delta x} \le \frac{1}{\sqrt{2}}, \tag{2.2}$$

where $\beta_{\max} = \max(\beta_f, \beta_s, \beta_b)$.

An approximation of the continuous-wave propagation problem by a discrete grid leads to errors in the solution. The most important one is the grid dispersion, because it causes the velocity of the wave propagation to be a function of the grid spacing. Alford et al. (1974), Dablain (1986), and Fah (1992) studied the effect of different parameters on the grid dispersion. A measure of accuracy is the ratio between the numerical and the physical velocity of propagation $r = \frac{c}{\beta}$, which ideally should be 1. The parameters that influence this error are:

- The density of the grid $m = \lambda / \Delta x$ (m - number of points per wavelength),
- The Courant number χ
- The angle of the wave incidence θ.

It was shown (Alford et al.,1974; Dablain,1986; Fah,1992) that the error increases when m decreases, χ decreases, and θ is close to 0 or $\pi/2$.

To increase the accuracy of the numerical schemes, usually researchers use higher-order approximations of the space derivatives. In this way, for smaller m the same accuracy is achieved as for bigger m with a lower-order approximation. For example, for the L^{th} order derivative in x:

$$\frac{\partial f}{\partial x} = \sum_{l=1}^{L/2} d_{2l-1} \cdot \frac{f\left[x + (2l-1)\frac{\Delta x}{2}\right] - f\left[x - (2l-1)\frac{\Delta x}{2}\right]}{\Delta x}, \qquad (2.3)$$

where (L = 2,4,6,...) and the coefficients d_{2l-1} can be obtained from the Taylor series.

For second-order approximation, Moczo (1989) recommended m = 12. Alford et al. (1974) have shown that with m = 11 points for a half-power wavelength for second-order approximation and with m = 5.5 points for a half-power wavelength for fourth-order approximation, the results for diffraction around a corner are very similar. Fah (1992) concluded that for $m \geq 10$ the error due to the grid dispersion is less than 1%. Levander (1988) was the first to use a fourth-order scheme. Dablain (1986) compared $O(\Delta t^2, \Delta x^2)$, $O(\Delta t^2, \Delta x^4)$, and a very high $O(\Delta t^4, \Delta x^{10})$ scheme and showed that for the same achieved accuracy the ratios between these densities are $m_{2,2} : m_{2,4} : m_{4,10} = 8 : 4 : 3$.

Holberg (1987) analyzed the error in the group velocity $\frac{\partial \omega}{\partial k}$ involved with the spatial sampling and showed how to maximize the spatial frequency so that the error is smaller than the initially adopted admissible error. Also the relations between the order of the spatial operator and the required grid points per wavelength (m) for five admissible errors in the group velocity E_{gr} = 0.0003; 0.001; 0.003; 0.01; 0.03 were plotted. Holberg showed that for the standard operator (two samples, second-order approximation), and admissible error $E_{gr} = 0.01$, the required number of points, per wavelength, that will keep the error within this bound is m = 16. For $E_{gr} = 0.03$ and for the same operator the required m = 9. This shows that the

recommendations from the previous authors involve error in the group velocity smaller than 3%. For higher accuracy, m grows rapidly, so for $E_{gr} = 0.0003$, m $\approx$ 100 points/wavelength. Also, it was noted that the errors at the interfaces are controlled by the direction of the transmitted and the reflected wave.

2.2 Numerical scheme

For our problem, the system of three partial differential equations (for u, v, and w) describing the dynamic equilibrium of an elastic body is reduced to the third equation only (because $u = v = \frac{\partial}{\partial z} = 0$). Neglecting the body forces in the z direction ($F_z = 0$), this equation is:

$$\rho \frac{\partial^2 w}{\partial t^2} = \left(\frac{\partial \tau_{xz}}{\partial x} + \frac{\partial \tau_{yz}}{\partial y} \right). \qquad (2.4)$$

Introducing the new variables $v = \frac{\partial w}{\partial t}$, $\varepsilon_{xz} = \frac{\partial w}{\partial x}$, and $\varepsilon_{yz} = \frac{\partial w}{\partial y}$, and dividing (2.4) with ρ, the order (of 2.4) is reduced to the system of three first-order PDE:

$$\underline{U}_{,t} = \underline{F}_{,x} + \underline{G}_{,y}, \qquad (2.5)$$

where :

$$\underline{U} = \begin{Bmatrix} v \\ \varepsilon_{xz} \\ \varepsilon_{yz} \end{Bmatrix} \qquad \underline{F} = \underline{F}(\underline{U}) = \begin{Bmatrix} \frac{1}{\rho}\tau_{xz} \\ v \\ 0 \end{Bmatrix} \qquad \underline{G} = \underline{G}(\underline{U}) = \begin{Bmatrix} \frac{1}{\rho}\tau_{yz} \\ 0 \\ v \end{Bmatrix}. \qquad (2.6)$$

The first equation in (2.5) represents the dynamic equilibrium of forces in the z direction with neglected body force F_z, while the second and the third equations give the relations between the strains and the velocity. The abbreviations $\varepsilon_x = \varepsilon_{xz}$, $\sigma_x = \tau_{xz}$, $\varepsilon_y = \varepsilon_{yz}$, and $\sigma_y = \tau_{yz}$ are used later in the text. Instead of using velocity-stress formulation as in most previous studies, we use a velocity-strain-stress formulation, because in the nonlinear analysis it is more convenient to update $\tau = \tau(\varepsilon)$ than $\varepsilon = \varepsilon(\tau)$. The equation (2.5) can be seen as a conservation law, by which the time rate of change of the quantity $\underline{U}$ on a differential area $dA = dx \cdot dy$ is equal to the sum of the differences of the fluxes $\underline{F}$ (in the x direction) and $\underline{G}$ (in the y direction) on the boundaries of that area. Moreover, the equation (2.5) is the most general mathematical representation of our physical problem, in which we only assume that the strains are small so that we have geometric linearity $\frac{\partial w}{\partial x_i} = \tan\varepsilon_{i3} \approx \varepsilon_{i3}$ (i = 1,2). With this formulation, we can study the nonlinear response of the structure due to material nonlinearities $\frac{d\tau_{i3}}{d\varepsilon_{i3}} = \mu_{i3} \neq const$ (i = 1,2).

A review of the artificial boundaries will show that the exact artificial boundaries are usually defined with a circular shape for 2-D problems or a spherical shape for 3-D problems.

Naturally, the coordinate systems that best describe these shapes are polar for 2-D problems or spherical for 3-D ones. Because of the rectangular shape of the structures, it is obvious that the polar coordinate formulation for the considered problem is not suitable, and thus the Cartesian formulation is used.

For defining the grid spacing, in our problem we have an additional requirement for modeling the semicircular foundation. The soil and the foundation subdomains, Ω_s and Ω_f, are discretized with square grids, while for the structure, Ω_b, we will use the rectangular grid.

Because of the Cartesian formulation, the semicircle is approximated with a symmetric hexagon with an axis of symmetry at x = 0. This requires an even number of grid intervals in the x direction. For different grid densities $m_f = L/\Delta x$, this approximation is shown in Fig. 2.3, where L = 2a is the width of the structure. The vertical grid spacing in the structure is obtained from the formula $\Delta y_b = \frac{\beta_b}{\beta_s}\Delta y_s$, which prevents the dispersion relation in the vertical direction at the contact foundation-structure. The horizontal spacing Δx is constant along the whole grid. The time step Δt, as was mentioned above and in Lin (1996), should be as big as possible to provide that χ in (2.1) can be as close as possible to 1. In the numerical examples, Δt is computed from $\chi = 0.95$.

The Taylor series expansion of the field $\underline{U}(t)$ at the point (x,y) gives:

$$\underline{U}(t+\Delta t) = \underline{U}(t) + \left(\frac{\partial \underline{U}}{\partial t}\right)_t \Delta t + \frac{1}{2}\left(\frac{\partial^2 \underline{U}}{\partial t^2}\right)\Delta t^2 + O\left(\Delta t^3\right). \qquad (2.7)$$

Fig. 2.3. APPROXIMATION OF THE FOUNDATION

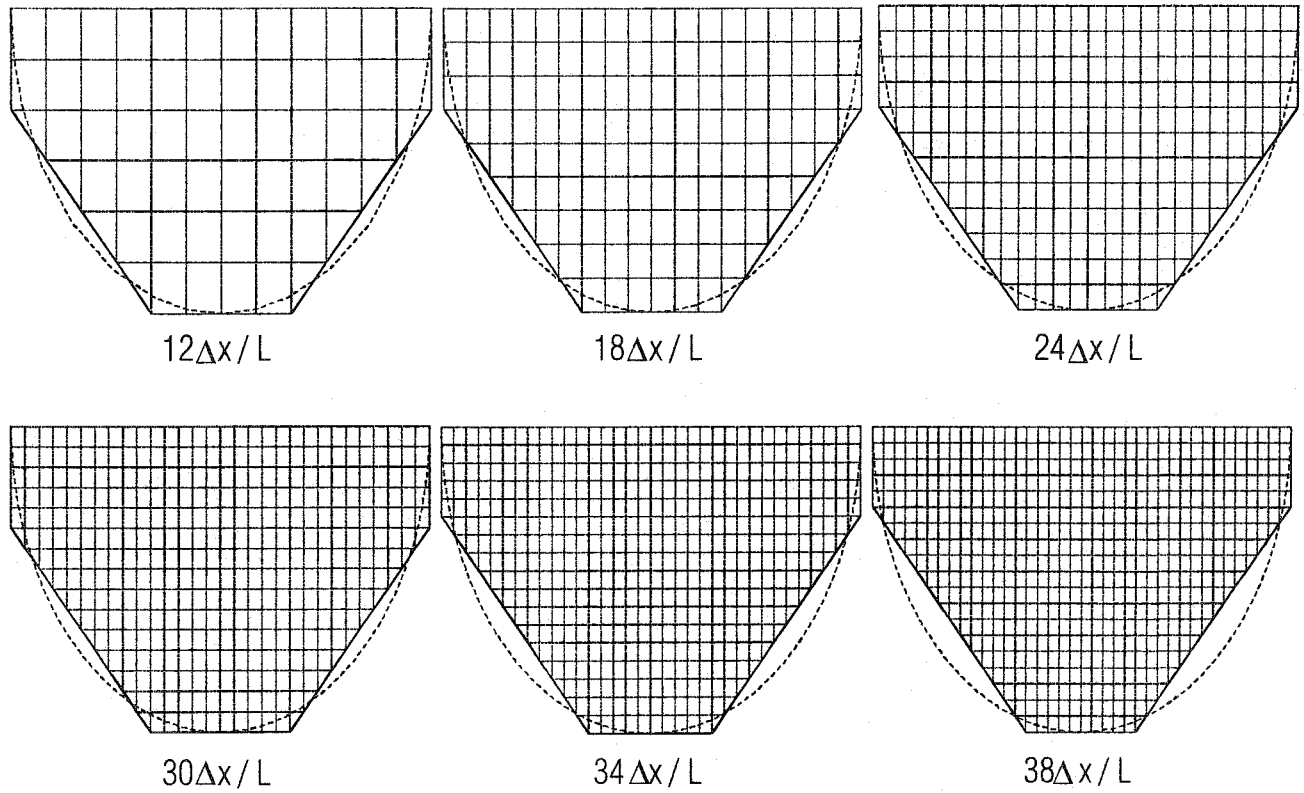

Fig. 2.4 CHARACTERISTIC GRID POINTS

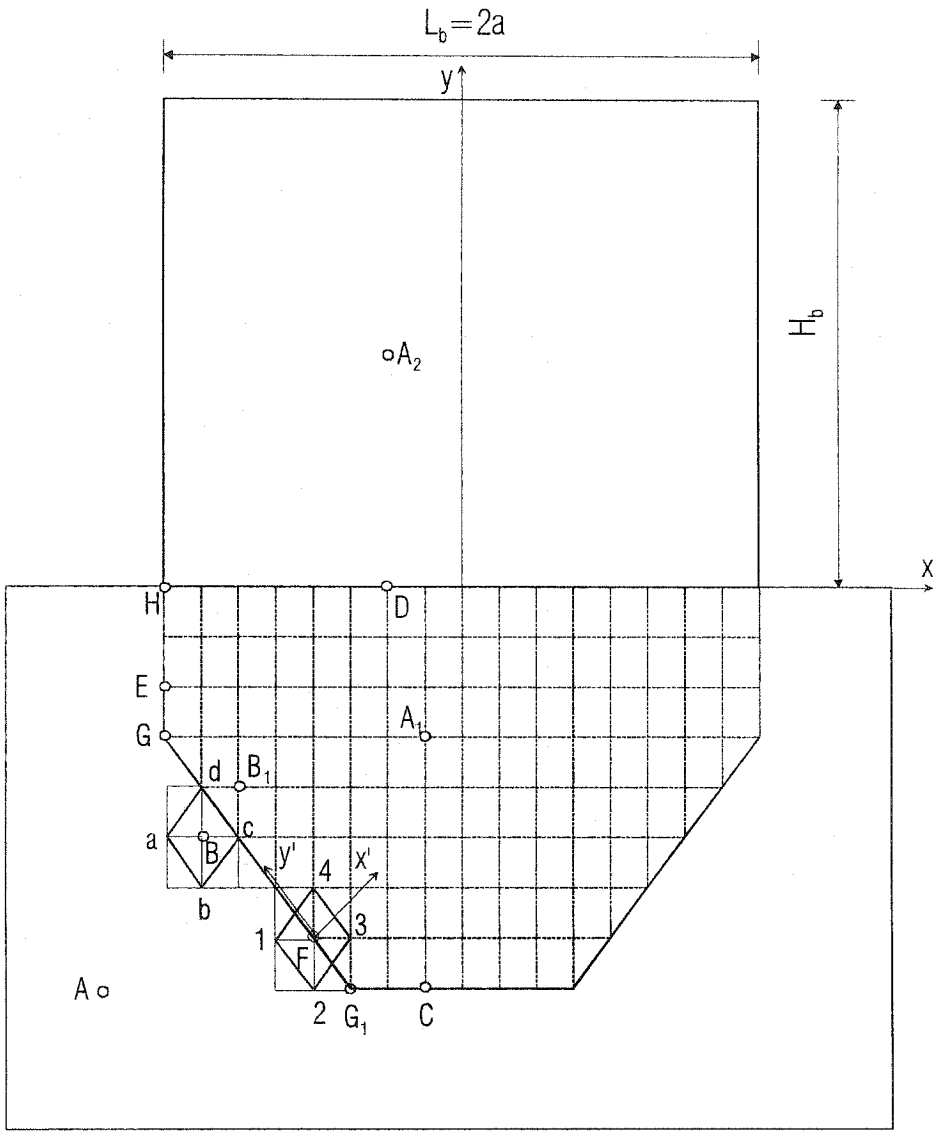

Using the relation (2.5), the time derivatives of $\underline{U}$ are substituted with the space derivatives of the fluxes, and (2.7) becomes:

$$\underline{U}(t+\Delta t)=\underline{U}(t)+\left(\frac{\partial F}{\partial x}+\frac{\partial G}{\partial y}\right)_{(x,y)}\Delta t+ \frac{\Delta t^2}{2}\left\{\frac{\partial}{\partial x}\left[A\left(\frac{\partial F}{\partial x}+\frac{\partial G}{\partial y}\right)\right]+\frac{\partial}{\partial y}\left[B\left(\frac{\partial F}{\partial x}+\frac{\partial G}{\partial y}\right)\right]\right\}+O\left(\Delta t^3\right), \tag{2.8}$$

where :

$$A=\frac{\partial \underline{F}}{\partial \underline{U}}=\begin{bmatrix}0 & \dfrac{\partial \sigma_x}{\rho \partial \varepsilon_x} & 0\\ 1 & 0 & 0\\ 0 & 0 & 0\end{bmatrix} \text{ and } B=\frac{\partial \underline{G}}{\partial \underline{U}}=\begin{bmatrix}0 & 0 & \dfrac{\partial \sigma_y}{\rho \partial \varepsilon_y}\\ 0 & 0 & 0\\ 1 & 0 & 0\end{bmatrix}. \tag{2.9}$$

For the problem at hand, from numerical tests it seems that the Zwas' numerical scheme proposed by Lin (1996) becomes unstable when the upgoing field from the soil and the foundation and the downgoing one from the structure meet at the point H (Fig. 2.4).

The problem is solved numerically for steady-state and transient half-sine excitation using the finite difference Lax-Wendroff method (Lax & Wendroff,1964) for approximating the system of three first-order partial differential equations (2.5). The typical cell (i,j) for central-difference approximation is shown in Fig. 2.5. The points denoted by numbers are not grid points; the quantities at the points 1 to 4 are obtained as mean values of the quantities in the two neighboring grid points (denoted by circles), while the quantities for points 5 to 8 are obtained as mean values of quantities in the neighboring four grid points. The finite-difference equations for characteristic points in the model (Fig. 2.4), are given in Appendix I.

Fig. 2.5 TYPICAL COMPUTATIONAL CELL

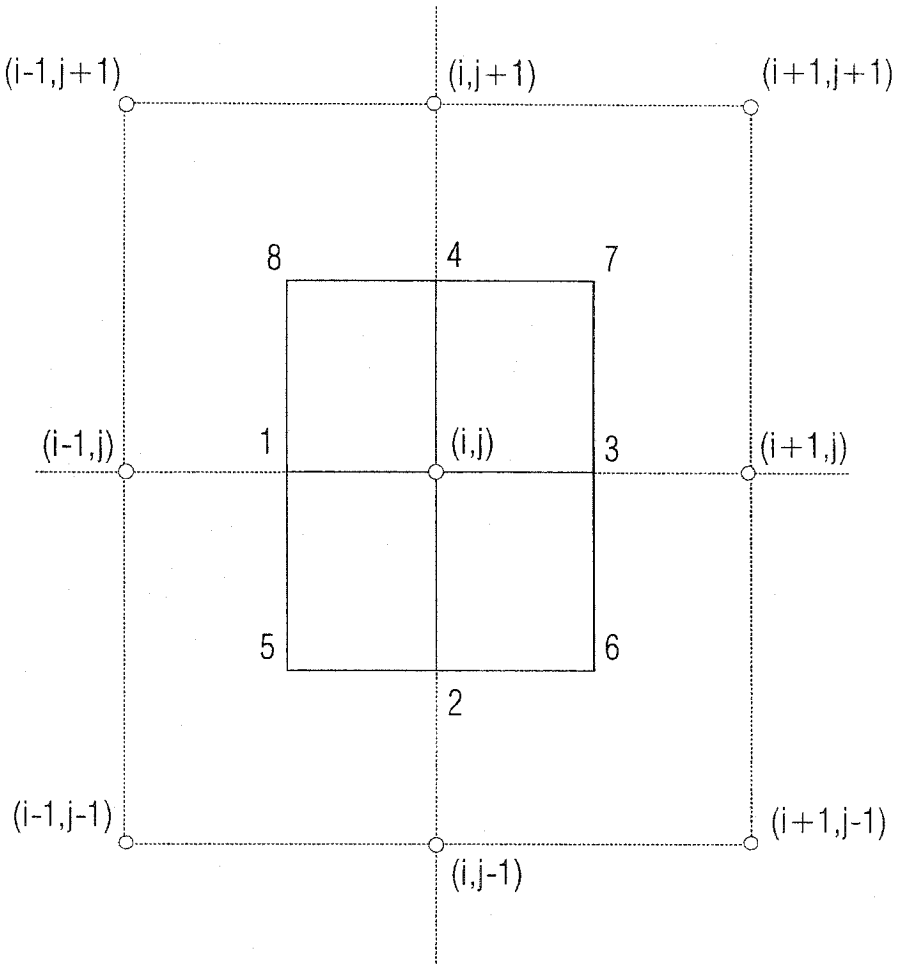

At the points of the physical boundaries, $B_1 = \{M(x,y) \mid \mathrm{y} = 0, |x| > a$ and $B_2 = \{N(x,y) \mid \mathrm{y} = \mathrm{H_b}, |x| \le a$, the boundary condition $\sigma_y = 0$ is prescribed. To customize these points to the numerical scheme given with the equations I.1A-I.3A in Appendix I and to calculate for the velocities and the strains (stresses) in the x direction, we introduce a row of fictitious points at the distance Δy_s above B_1 and another one at the distance Δy_b above B_2. To satisfy the boundary condition $\sigma_y = 0$ for the boundary point (i,j), we use the vacuum formalism to update the quantities of the fictitious points so that for the fictitious point (i,j+1)

$v_{i,j+1} = v_{i,j-1}$; $\sigma_{yi-1,j+1} = -\sigma_{yi-1,j-1}$; $\sigma_{yi,j+1} = -\sigma_{yi,j-1}$; $\sigma_{yi+1,j+1} = -\sigma_{yi+1,j-1}$; $\mu_{i,j+1/2} = 0$

in every time instant. In a similar way, we proceed along the physical boundaries $G_1 = \{P(x,y) \mid \mathrm{x} = \text{-a}, \mathrm{y} > 0$ and $G_2 = \{Q(x,y) \mid \mathrm{x} = \mathrm{a}, \mathrm{y} > 0\}$, where $\sigma_x = 0$ is prescribed. For example, for G_1 we introduce a column of fictitious points $x = -a - \Delta x; y > 0$ with prescribed values as follows :

$v_{i-1,j} = v_{i+1,j}$; $\sigma_{xi-1,j-1} = -\sigma_{xi+1,j-1}$; $\sigma_{xi-1,j} = -\sigma_{xi+1,j}$; $\sigma_{xi-1,j+1} = -\sigma_{xi+1,j+1}$; $\mu_{i-1/2,j} = 0$.

The values of the velocities and the strains (stresses) in the y direction can be computed from the equations I.1A - I.3A. For G_2, the x indices take opposite signs relative to the previous numerical boundary conditions.

The artificial boundaries are a constitutive part of the model, but because of their complexity and the considerable research done in this field the next chapter is dedicated to the subject of artificial boundaries only.

CHAPTER III

ARTIFICIAL BOUNDARY

3.1 Artificial boundaries: A Review

For dynamic analysis of a problem defined in an infinite domain in terms of discrete methods, there is need for a boundary called an "absorbing," "artificial," or "nonreflecting" transparent boundary. For practical reasons, the computational domain has to be finite, and the role of these artificial boundaries is to replace the effect of the truncated domain. It is obvious that this task can be accomplished only if we can solve for the unknown quantities at the absorbing boundaries.

Kausel and Tassoulas (1981) classified the boundaries that occur in wave propagation problems into three groups :

1. elementary (nontransmitting) boundaries,
2. consistent (global) boundaries, and
3. imperfect (local) boundaries

In essence, there is no sharp separation between the global and local boundaries because many of the local boundaries are obtained just by truncation of the infinite series obtained at some global boundaries. Nevertheless, the classification here is done with the ideas the authors use in developing the boundary.

3.1.1 Elementary boundaries

At the points on an elementary boundary, either the displacements or the stresses are prescribed. In the first case, we have a Dirichlet, and in the second a Neumann boundary condition. These two conditions occur at the existing physical boundaries, where either the boundary is stress-free so that the prescribed stresses (spatial derivatives of the displacement) are zero or the boundary is fixed so that the prescribed displacements are zero for all time.

At the artificial boundaries, the Dirichlet and Neumann nonzero conditions can be applied only for the simplest problems in which an analytical solution exists at the boundary. This is a case for a pure half-space problem in which the solution can be obtained from the ray theory in any point of the domain, or for 1-D wave propagation problem (Fujino & Hakuno, 1978) in which at the artificial-boundary point the solution can be uniquely defined from the solution of the neighboring point, with shifting in time. These two examples are trivial, but they can be used as test examples for accuracy of the actual numerical schemes that describe an artificial boundary.

If, at the boundary, zero displacement (fixed boundary) or zero stress (free boundary) are prescribed, the boundary behaves as a perfect reflector: that is, the energy reflected back into the inner domain is equal to the incident energy on the boundary. The fixed boundary reflects the incident field out of phase, and the free boundary reflects it in phase.

Smith (1974) used the above properties of the fixed and free boundary and constructed an absorbing boundary by solving at the boundary twice, first implying the fixed, then the

stress-free boundary condition, and then taking the average as a solution. As pointed out by Kausel (1988) this boundary is a perfect absorber if only one boundary interface exists in the model. In the case of more than one boundary in the model, this boundary fails because the waves are reflected more than once.

3.1.2 Consistent (global) boundaries

During the past decade, due to the need for highly accurate solutions to the problems involving infinite domains, the use of consistent boundaries became attractive. These boundaries are perfect absorbers, but they cannot be readily applied in 'marching in time' procedures because of their nonlocality, both in time and space. This nonlocality comes from the terms that appear in the boundary equations in the transformed (Laplace or Fourier) space. The inverse transform of these terms back into the physical space does not yield regular, local differential operators, but rather some pseudo differential operators (Tsynkov, 1998). The result is that the solution at a boundary point depends upon the time history of the solutions in all of the boundary points.

It should be pointed out that this is not so for 1-D problems, in which the boundary condition can be obtained readily in the physical space. Furthermore, for Courant number $\frac{\beta \Delta t}{\Delta x} = 1$ there is even no truncation error from the numerical scheme (Dablain,1986), as can be tested for the case of linear and nonlinear shear beam sitting on a 1-D linear half space.

Tsynkov (1998) provided a detailed review of the existing global and local artificial boundaries and showed how to use the difference potential method for solving problems in aerodynamics.

One of the first global boundaries is that developed by Engquist and Majda (1979). The key point of this boundary is to eliminate the incoming (reflected) field on the boundary. The solution of the linear wave equation :

$$\frac{\partial^2 u}{\partial t^2} = \beta^2 \left(\frac{\partial^2 u}{\partial x^2} + \frac{\partial^2 u}{\partial y^2} \right) \tag{3.1}$$

for the plane wave can be written as $u = u(\omega t + k_x x + k_y y)$, and the dispersion relation of the solution is $\frac{\omega^2}{\beta^2} = k_x^2 + k_y^2$. The constant-phase surfaces are planes given with the equation $\omega t + k_x x + k_y y = C$. These planes travel in the space in direction $\left(-k_x, -k_y\right)$. Now, if the computational domain is x ≥ 0 and the artificial boundary is at x = 0, then solving the dispersion relation for k_x we have

$$k_x = \pm \sqrt{\frac{\omega^2}{\beta^2} - k_y^2} \,. \tag{3.2}$$

For the given setup above and for the positive radical, the incoming (reflected) waves from the boundary travel in the positive x direction and should have $k_x < 0$. This corresponds to the minus sign in the expression for k_x and the opposite for the outgoing waves. The Fourier transform of (3.1) in t and y gives the relation: $-\left(\frac{\omega^2}{\beta^2} - k_y^2 \right) \hat{u} = \frac{d^2 \hat{u}}{dx^2}$,

where $\hat{u}(\omega, x, k_y) = \iint_{t,y} u(t, x, y) e^{-i(\omega t + k_y y)} dt dy$,

or from (3.2)

$$\frac{d^2\hat{u}}{dx^2} + k_x^2 \hat{u} = 0, \tag{3.3}$$

with solution

$$\hat{u} = C_1 e^{-i|k_x|x} + C_2 e^{i|k_x|x} = C_1 \hat{u}^{(1)} + C_2 \hat{u}^{(2)}. \tag{3.4}$$

As mentioned above, the mode with negative exponent is incoming (reflected from the boundary) and should be eliminated from the solution at the boundary. This means that the solution at the boundary should be parallel (equal up to the constant) with the outgoing mode $e^{i|k_x|x}$ (the mode traveling in direction –x). This linear dependence between the solution and the outgoing mode at the artificial boundary at x = 0, for the second-order ordinary differential equation (ODE) (3.3) is given with the zero-valued Wronskian of second order as follows:

$$W = \begin{vmatrix} \hat{u} & \hat{u}^{(2)} \\ \dfrac{d\hat{u}}{dx} & \dfrac{d\hat{u}^{(2)}}{dx} \end{vmatrix}_{x=0} = 0.$$

Replacing $\hat{u}^{(2)} = e^{i|k_x|x}$ and using (3.2), the boundary condition at x = 0 in the transformed space becomes

$$\frac{d\hat{u}}{dx} - i\sqrt{\frac{\omega^2}{\beta^2} - k_y^2} \cdot \hat{u} = 0. \tag{3.5}$$

The boundary condition (3.5) can be obtained also by factorization of the operator (3.3):

$$\left(\frac{d^2}{dx^2} + k_x^2\right)\hat{u} = \left(\frac{d}{dx} + ik_x\right)\left(\frac{d}{dx} - ik_x\right)\hat{u}.$$

Note that the square root in (3.5) appears as an irrational term for which the inverse Fourier transform back to the physical space does not have a derivative of u. In utilizing this boundary for numerical computation, the square root is rationalized by using a series of Pade' approximants (Clayton & Engquist,1977).

A considerable amount of research was done on constructing artificial boundaries using so-called Dirichlet to Neumann (DtN) mapping on the artificial boundary (Givoli & Keller, 1990; Grote & Keller, 1996; Givoli, 2001). The idea of this approach is to express the normal derivative of the solution in terms of the solution itself at the boundary.

Givoli and Keller (1990) used DtN for solving problems in 2-D elastodynamics using circular artificial boundary r = R. Starting with the Helmholtz decomposition of the displacement vector field and using the Sommerfeld radiation condition for the irrotational and rotational potentials

$$\lim_{r\to\infty} r^{1/2}(\Phi_{,r} - ik_L\Phi) = 0 \qquad \lim_{r\to\infty} r^{1/2}(\Psi_{,r} - ik_L\Psi) = 0. \tag{3.6a}$$

The solution for the displacement in polar coordinates is found as a series of Hankel functions of first kind. Next, the radial and transverse components of the displacement at the boundary r = R are expanded in a single Fourier series along a circular coordinate. Matching the similar terms of these two sets of series, the coefficients of the series involving Hankel functions are found, and with that the displacement field at the boundary r = R. Using this solution and the relations between the tractions and the displacements, the traction in polar coordinates at r = R is obtained. The final step is to go back to Cartesian coordinates with the well-known orthogonal transformation. In this way, the computational domain becomes annulus with the artificial

boundary as the outer boundary and the inner boundary with arbitrary shape, where the displacements and/or tractions are prescribed. This boundary was implemented in FE (finite element) formulation (Givoli and Keller,1990). The effect of the boundary condition on the standard FE scheme is the adding of additional matrix K^b, the entries of which are an infinite series along the circular coordinates in the standard stiffness matrix.

Kallivokas and Lee (2004) developed an artificial boundary with elliptic shape. They analyzed the scattering problem in an infinite fluid domain from a scatterer with arbitrary shape with a prescribed Neumann condition at its boundary. The computational domain was enclosed with an elliptic artificial boundary. The main concern was to satisfy the Sommerfeld radiation condition (3.6a), which in terms of the pressure p (the shear potential for fluid is zero) in physical space is given by

$$\lim_{r\to\infty} r^{1/2}\left(p_{,r} + \frac{\dot{p}}{c}\right) = 0. \qquad (3.6b)$$

First, the governing wave equation of the problem is Laplace-transformed in time in the inner domain Ω. Next, the authors consider the auxiliary problem in the outer domain Ω^+ :

$$s^2\hat{P}(\mathbf{x},s;t) = c^2\Delta\hat{P}(\mathbf{x},s;t),\ \ \mathbf{x}\in\Omega^+\ \ ;\quad \hat{P}(\mathbf{x},s;t) = p(\mathbf{x},t),\ \ \mathbf{x}\in\Gamma_a, \qquad (3.7)$$

where Γ_a is the characteristic equation of the artificial boundary (ellipse) and $\hat{P}(\mathbf{x},s;t)$ is an auxiliary field.

It was shown by using the Duhamel's principle that the Laplace-transform of the solution in the outer domain is the Laplace transform of the solution of the auxiliary problem (3.7)

$$\hat{p}(\mathbf{x},s)=\int_0^{\infty} e^{-st}\hat{P}(\mathbf{x},s;t)dt\,,\quad \mathbf{x}\in\Omega^{+} \tag{3.8}$$

and also on the boundary

$$\hat{p}_{\nu}(\mathbf{x},s)=\int_0^{\infty} e^{-st}\hat{P}_{\nu}(\mathbf{x},s;t)dt\,,\quad \mathbf{x}\in\Gamma_a\,. \tag{3.8a}$$

For the auxiliary field, the asymptotic expansion from geometrical optics is chosen as follows:

$$\hat{P}(\mathbf{x},s;t)\cong e^{-\frac{s}{c}\chi(x)}\sum_{k=0}^{\infty}\left[\frac{c}{(s+\gamma(\mathbf{x}))a}\right]^{k}A^{(k)}(\mathbf{x},t)\,,\quad \mathbf{x}\in\Omega^{+}\,. \tag{3.9}$$

(3.9) will satisfy the second equation in (3.7) if and only if for $\mathbf{x}\in\Gamma_a$:

$$\chi(\mathbf{x})=0$$
$$A^{(0)}(\mathbf{x},t)=p(\mathbf{x},t)$$
$$A^{(k)}(\mathbf{x},t)=0,\quad k\geq 1.$$

Taking the normal derivative of (3.9) and using (3.8a) we get

$$\hat{p}_{\nu}(\mathbf{x},s)=-\frac{s}{c}\chi_{\nu}\hat{A}_0(\mathbf{x},s)+\sum_{k=0}^{\infty}\hat{A}_{\nu}^{(k)}(\mathbf{x},s)\left[\frac{c}{(s+\gamma(\mathbf{x}))a}\right]^{k}\,,\quad \mathbf{x}\in\Gamma_a\,. \tag{3.10}$$

The nonnegative parameter $\gamma(\mathbf{x})$ acts as damping and is used to provide stability for the higher-order absorbing boundary conditions. By introducing (3.9) into (3.7) and matching the terms with the same powers of $(s+\gamma)$, the equations for the unknown functions $\chi(\mathbf{x})$ and $A^{(k)}(\mathbf{x},t)$ are obtained. Using the Fermi-type coordinate system, the normal derivatives of these functions can be expressed in terms of the curvature and the arc coordinate. The m-th order of the boundary $(m=0,1,2,3,\ldots)$ is set by keeping m terms in the equation (3.10) and

truncating terms $k \geq m+1$. The authors present the first four orders of the boundary (m = 0,1,2,3).

Lee and Kallivokas (2004), using a second-order boundary of the previously mentioned boundary and image theory, show how to solve a scattering problem in a half space with an absorbing boundary of elliptical shape. The above two boundaries are classified as being of the global type because they are derived through truncation of the infinite series (3.10).

All global methods involve high-order derivatives in time and in tangential direction on the artificial boundary. For implementation of these boundaries in finite element formulation, one needs to develop special finite elements that have high-order regularity in tangential direction at the artificial boundary. An alternative approach, which reduces the order of the boundary condition, so called arbitrary high-order condition (AHOC), was proposed by several authors. The trade-off in this approach involves new unknowns on the boundary. In this approach, the originally developed high-order boundary is replaced by an equivalent low-order one.

Givoli (2001) used AHOC for steady state (Helmholtz equation) and time-dependent (wave equation) problems. The Helmholtz equation is elliptic PDE in which only the spatial derivatives exist. He considered a k-th order artificial boundary in the form

$$-\frac{\partial u}{\partial r} = L_K u \,. \tag{3.11}$$

If the artificial boundary involves only the tangential derivatives of higher order, then (3.11) has the form

$$-\frac{\partial u}{\partial r} = \sum_{j=0}^{k} \alpha_j \partial_\theta^j u \,. \tag{3.12}$$

The order of (3.12) is reduced from k to 1 by involving k new unknowns:

$$\begin{aligned} v_0 &= u \\ v_j &= \frac{\partial}{\partial \theta} v_{j-1} = v'_{j-1}. \end{aligned} \tag{3.13}$$

If only even tangential derivatives occur in the original artificial high-order boundary, the order of the boundary can be reduced to 2. The matrix form of the modified boundary, for both odd and even tangential derivatives appearing on the artificial boundary is

$$-\frac{\partial u}{\partial r}\mathbf{e}_1 = \mathbf{YU} + \mathbf{ZU}', \tag{3.14}$$

and for artificial boundaries involving only even derivatives

$$-\frac{\partial u}{\partial r}\mathbf{e}_1 = \mathbf{YU} + \mathbf{ZU}''. \tag{3.15}$$

For some local boundaries where a high order of radial derivatives occurs, as in the boundary of Bayliss and Turkel (1980), the modified reduced-order boundary has the form

$$-\frac{\partial u}{\partial r}\mathbf{e}_1 = \mathbf{YU} + \mathbf{Z}\frac{\partial}{\partial r}\mathbf{U}. \tag{3.16}$$

The matrices Y and Z are symmetric, $U = (u\ v_1 v_2 \ldots v_k)^T$ is the unknown vector and $\mathbf{e}_1 = (1\ 0\ 0\ \ldots .0)^T$ is a k-order vector.

The approach for constructing AHOC for a time-dependent case (wave equation) is similar to the steady-state case, with the difference that (3.12) involves a double series because the time derivatives should be reduced also. The number of the additional unknowns becomes

(k*m), where k is the highest derivative in the tangential direction and m is the highest derivative in time.

Because of their non-rectangular shape, most of the global boundaries cannot be utilized in standard finite difference formulations.

Grote and Keller (1996) proposed an artificial boundary and a finite difference algorithm for treating a spherical artificial boundary with a spherical grid. Their artificial boundary has the form

$$\left(\frac{\partial}{\partial t}+\frac{\partial}{\partial r}\right)(ru)=-\sum_{n=1}^{\infty}\sum_{m=-n}^{n}\mathbf{c}_n\mathbf{z}_{nm}Y_{nm}, \tag{3.17}$$

where $\mathbf{z}_{nm}=\mathbf{z}_{nm}(t)$ is the solution of the ordinary differential equation :

$$\frac{d}{dt}\mathbf{z}_{nm}(t)=\mathbf{A}_n\mathbf{z}_{nm}(t)+\mathbf{u}_{nm}(t)\quad \mathbf{z}_{nm}(0)=\mathbf{0}. \tag{3.18}$$

The n nxm matrices $\mathbf{A}_n=[\mathbf{A}_n^{ij}]$ are defined as follows :

$$A_n^{ij}=\begin{cases} -n(n+1)/(2a)^j & if \quad i=1 \\ (n+i)(n+1-i)/(2i) & if \quad i=j+1, \\ 0 & otherwise \end{cases} \tag{3.19}$$

and

$$Y_{nm}(\theta,\varphi)=\left[(2n+1)(n-|m|)!/4\pi(n+|m|)!\right]^{1/2}e^{im\varphi}P_n^{|m|}(\cos\theta) \tag{3.20}$$

is the nm-th spherical harmonic normalized over a unit sphere,

and

$$u_{nm}=\left\{\left(Y_{nm},u|_{r=a}\right)\ 0\ 0.....0\right\}^T \tag{3.21}$$

is a vector function having as the only nonzero entry the inner product

$$\left(Y_{nm}, u\big|_{r=a}\right) = \int_0^{2\pi}\int_0^{\pi} \bar{Y}_{nm}(\theta,\varphi)u(a,\theta,\varphi,t)\sin\theta d\theta d\varphi \,. \qquad (3.22)$$

The authors used the leap-frog FD (finite difference) scheme with the artificial boundary r = a and the algorithm as follows:

0. Initialize U^k at t = 0 and t = Δt. Set $\mathbf{z}_{nm}^0 = \mathbf{0}$ and $\mathbf{z}_{nm}^1 = \mathbf{0}$
1. Compute U^{k+1} at all inner points using the FD scheme
2. Using the adopted FD scheme and FD approximation of the artificial boundary (3.17), compute $U_{a+\Delta r}^k$ and U_a^{k+1}.
3. Compute $\mathbf{z}_{nm}^{k+1}$ (the authors used trapezoidal rule of Runge-Kutta 2-step method) and go to 1.

Using the above FD algorithm, the authors solved three problems,

a) Time harmonic source in full space
b) Scattering of low frequency plane wave vertically impinging upon a spherical obstacle
c) Radiation from a circular piston on a sphere.

Then they compared results with the local Bayliss-Turkel (1980) boundary (BT). In all of the problems, the obstacle has the radius $r_0 = 0.5$ with artificial boundary at r = 1. For all of the problems, the proposed algorithm gives accurate results. The BT gives accurate result for the second problem and fails for the first and the third ones. This is expected because the scattered field from a sphere for small wave numbers is almost spherical and BT is derived to annihilate such waves.

Hagstrom et al. (2003) developed a high-order boundary based on the multi-pole expansion of the outgoing field for solving the convective wave equation. The starting point is the Bayliss-Turkel boundary. Gachter and Grote (2003) derived and implemented in FE formulation an exact spherical boundary for 3-D elastic waves. Premrov and Spacapan (2004) presented an interesting idea for improving local asymptotic low-order DtN mapping, for problems involving higher modes.

Tsynkov (1998) described the construction of exact boundary conditions using the difference potential method on the 3-D problem of transonic fluid flow near a wing. The artificial boundary in this method can have arbitrary shape.

3.1.3 Imperfect (local) boundaries

The main advantage of the local artificial boundaries is that they are local in space and time - that is, the solution at a boundary point depends only upon the solutions in several neighboring points in several time steps backwards. The other advantage for the time step procedures is that they are defined in the time domain and are not frequency dependent. Even though they are not perfect absorbers, because of the above properties the local boundaries are widely used in practical applications.

The local absorbing boundaries can be subdivided in several classes depending upon the idea used in their development. We distinguish:

- Paraxial boundaries
- Viscous boundaries
- Multidirectional boundaries
- Boundaries based on expansion of the outgoing field
- Extrapolation boundaries.

3.1.3.1 Paraxial boundaries

One of the most widely used artificial boundaries is the paraxial boundary developed by Clayton and Engquist (1977) which is based on the global boundary of Engquist and Majda.

The two-dimensional scalar wave equation is

$$P_{xx} + P_{yy} = \frac{1}{\beta^2} P_{tt}, \tag{3.23}$$

where the scalar field has form

$$P(x, z, t) = Ae^{i(\omega t \pm k_x x \pm k_y y)}. \tag{3.24}$$

For wave propagating in the positive direction of an axis, the minus sign should be used in the corresponding term. Here, A is the amplitude of the scalar and is a constant. Plugging (3.24) into (3.23) and performing the differentiation, we obtain the dispersion relation

$$\omega = \beta\sqrt{k_x^2 + k_y^2}. \tag{3.25}$$

If we want to "cut" the field in the y direction, say by imposing artificial boundary y = const. we should express the wave number k_y

$$\frac{\beta k_y}{\omega} = \pm\sqrt{1-\frac{\beta^2 k_x^2}{\omega^2}}. \tag{3.26}$$

By using the Pade' rational approximation of the square root (Clayton & Engquist, 1977), we can obtain the first three paraxial boundary conditions in the frequency domain. For a positive sign in (3.24), those are

$$\text{A1}: \quad \frac{\beta k_y}{\omega} = 1 + O\left(\left|\frac{\beta k_x}{\omega}\right|^2\right), \tag{3.27}$$

$$\text{A2}: \quad \frac{\beta k_y}{\omega} = 1 - \frac{1}{2}\left(\frac{\beta k_x}{\omega}\right)^2 + O\left(\left|\frac{\beta k_y}{\omega}\right|^4\right), \text{ and} \tag{3.28}$$

$$\text{A3}: \quad \frac{\beta k_y}{\omega} = \frac{1-\frac{3}{4}\left(\frac{\beta k_x}{\omega}\right)^2}{1-\frac{1}{4}\left(\frac{\beta k_x}{\omega}\right)^2} + O\left(\left|\frac{\beta k_x}{\omega}\right|^6\right). \tag{3.29}$$

A graphical representation of the dispersion relations A1, A2, and A3, together with the dispersion relation of the wave equation $k_z^2 + k_x^2 = k^2 = \left(\frac{\omega}{\beta}\right)^2$, is given in Fig. 3.1. From the figure and from the relations (3.27), (3.28), and (3.29), it is obvious that the error is smaller as k_x becomes smaller or as the angle θ between the ray and the normal of the boundary becomes smaller (because $k_x = k\sin\theta$). In the ultimate case in which θ = 0, the wave is perfectly absorbed in all three approximations.

Fig. 3.1 DISPERSION RELATIONS FOR THE PARAXIAL BOUNDARIES

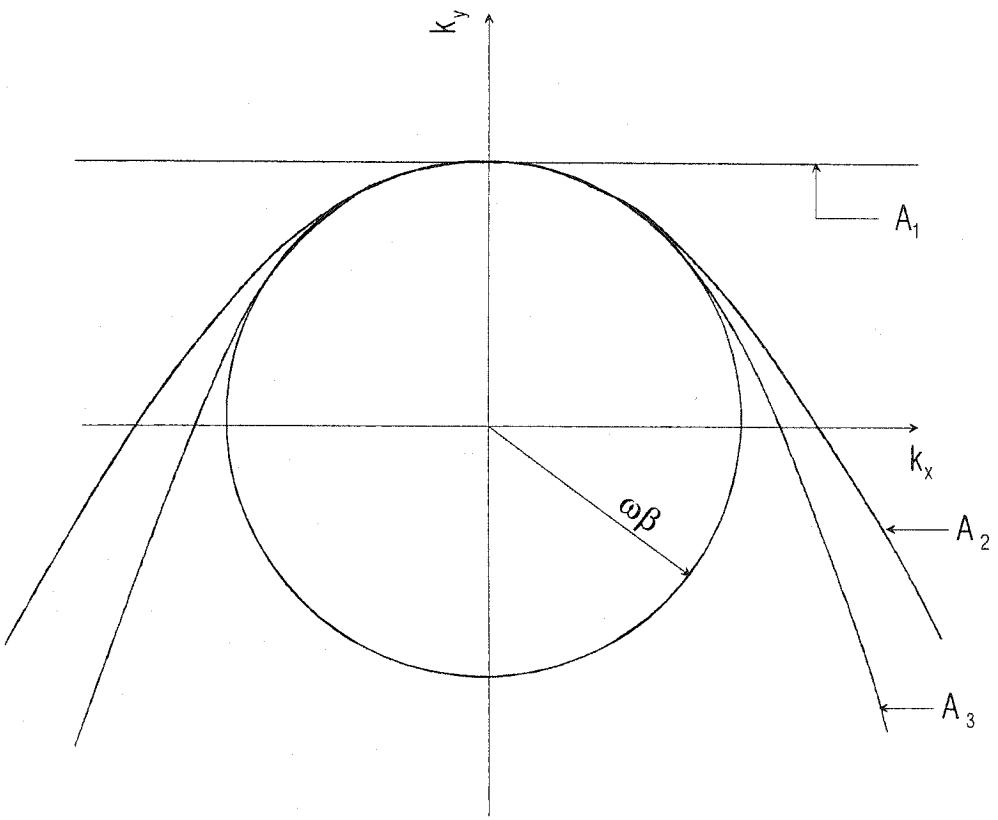

Fig. 3.2 WAVE PROPAGATING TOWARD ARTIFICIAL BOUNDARY $y = C$

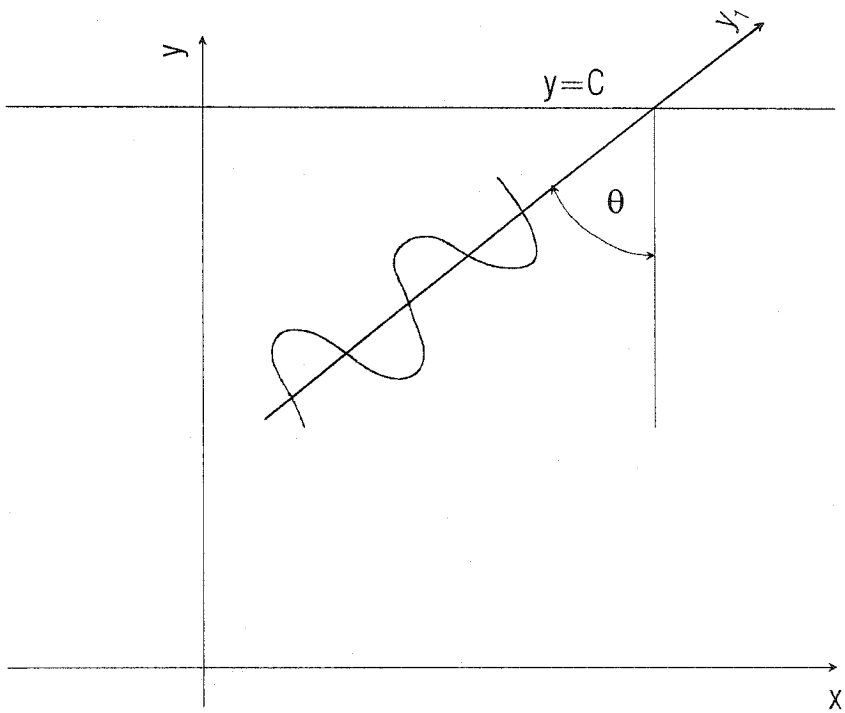

The equations (3.27), (3.28), and (3.29) are not applicable in finite difference schemes, but they can be transformed to the time domain. For example, if we want to use the A2 approximation for the boundary y = const, and if the propagation is in a positive x and y direction (Fig.3.2), the scalar field can be represented as

$$P = C \cdot e^{-i(\omega t - k_x \cdot x - k_y \cdot y)}. \tag{3.30}$$

We want to match (3.28) with a proper relation of the partial derivatives of P. The desired derivatives are

$$P_{tt} = -\omega^2 P \qquad P_{yt} = k_y \omega P \qquad P_{xx} = -k_x^2 P.$$

The equation (3.28) in time domain becomes

$$-\frac{\beta P_{yt}}{P_{tt}} = 1 - \frac{\beta^2}{2} \cdot \frac{P_{xx}}{P_{tt}}. \tag{3.31}$$

In a similar way, we can represent the A1 and A3 boundaries, so that the three boundaries in the time domain are

$$\text{A1}: \quad P_y + \frac{1}{\beta} \cdot P_t = 0 \tag{3.32}$$

$$\text{A2}: \quad P_{yt} + \frac{1}{\beta} \cdot P_{tt} - \frac{\beta}{2} \cdot P_{xx} = 0 \tag{3.33}$$

$$\text{A3}: \quad P_{ytt} - \frac{\beta^2}{4} \cdot P_{yxx} + \frac{1}{\beta} P_{ttt} - \frac{3\beta}{4} \cdot P_{txx} = 0, \tag{3.34}$$

as given by Clayton and Engquist (1977). The reflection coefficients for paraxial boundaries are

$$r = -\left(\frac{1-\cos\theta}{1+\cos\theta}\right)^j, \tag{3.35}$$

where j is the order of the boundary. It is obvious that for $\theta \to \pi/2$, $r \to 1$, which corresponds to total reflection, but, as was pointed out by the authors, in practical problems these components of the field will be absorbed by the next, perpendicular boundary before interaction with the inner field. Nevertheless, one should expect some amount of reflection.

Using factorization of the differential operators in the 2-D wave equation, Reynolds (1978) has derived a similar boundary, which for absorbing boundary x = const is given as

$$\frac{1}{\beta}\frac{\partial^2 u}{\partial x \partial t} + \frac{\partial^2 u}{\partial x^2} + \frac{p}{1+p}\cdot\frac{\partial^2 u}{\partial y^2} = 0, \tag{3.36}$$

where $p = \beta \cdot \Delta t / \Delta x$. The reflection coefficient is

$$R = \frac{\cos\theta - \cos^2\theta - \dfrac{p}{1+p}\cdot\sin^2\theta}{\cos\theta + \cos^2\theta + \dfrac{p}{1+p}\cdot\sin^2\theta}. \tag{3.37}$$

It can be seen that for p = 1 the reflection coefficient R is the same as r in (3.35) for a paraxial boundary of order 2. For different parameters p and different angles θ, Reynolds tabulated and graphed the reflection coefficient R given in (3.37). From the table, for $\theta = \pi/6$, the least reflection gives p = 1. For $\theta = \pi/4$ the equation (3.36) is a perfect absorber for $p = 1/\sqrt{2}$, and for $\theta = \pi/3$ it is a perfect absorber for $p = 1/2$.

3.1.3.2 Viscous boundaries

This type of local artificial boundaries, based on Lysmer and Kuhlemeyer (1969), is often used in practical computations because of its simplicity. For a SH wave, the principal strain (in the direction of propagation) is given by $\varepsilon = -\frac{\dot{u}}{\beta}$, and the strain in the direction perpendicular to the boundary (Fig.3.2) is

$$\varepsilon_y = -\frac{\dot{u}}{\beta} \cdot \cos\theta . \tag{3.38}$$

Multiplying (3.38) by $G = \rho \cdot \beta^2$, we obtain the viscous boundary in the form

$$\tau_{xy} + \rho\beta \cos\theta \cdot \frac{\partial u}{\partial t} = 0 . \tag{3.39}$$

This expresses the dynamic equilibrium at the boundary y = C.

The wave numbers in (3.30) can be expressed in terms of the direction of propagation of the wave (the angle θ in Fig. 3.2), as follows:

$$k_x = k\sin\theta = \frac{\omega}{\beta}\sin\theta \qquad k_y = \frac{\omega}{\beta}\cos\theta .$$

The equation (3.30) in a more general form can be written as

$$P = f(t - k_x x - k_y y) = f\left(t - \frac{x\sin\theta + y\cos\theta}{\beta}\right), \tag{3.40}$$

and the scalar field P must satisfy the wave equation

$$P_{tt} = \beta^2\left(P_{xx} + P_{yy}\right) \Rightarrow P_{yy} = \frac{P_{tt}}{\beta^2} - P_{xx} . \tag{3.41}$$

If we take symbolically the square root of the differential operators, we can write :

$$P_y = \pm\sqrt{\frac{P_{tt}}{\beta^2} - P_{xx}}\,. \tag{3.42}$$

Recalling that $x = \dfrac{\beta t}{\sin\theta} \Rightarrow t = \dfrac{x\sin\theta}{\beta}$,

we can write $P_{xx} = P_{tt}\dfrac{\partial^2 t}{\partial x^2} = \dfrac{\sin^2\theta}{\beta^2}P_{tt}$.

Performing the required differentiation in (3.42), we obtain for a wave propagating in positive y (positive sign in 3.42) :

$$\left(\frac{\partial}{\partial y} + \frac{\cos\theta}{\beta}\frac{\partial}{\partial t}\right)P = 0\,. \tag{3.43}$$

Taking the scalar field P in (3.43) as the displacement field u and multiplying (3.43) by $G = \rho\beta^2$ we obtain the viscous boundary (3.39). The viscous boundary is a perfect absorber for the waves with normal incidence, in which case the viscous boundary is identical with the paraxial boundary of order 1 (3.32).

3.1.3.3 Multi-directional boundaries

An approach to multi-directional boundaries can start from the concept of viscous boundaries. If a SH wave propagates in direction y_1 (see Fig.3.2), the relation between the particle velocity and the strain is given by

$$\frac{\partial u}{\partial t} = -\beta \frac{\partial u}{\partial y_1}, \tag{3.44}$$

which is obtained from the 1-D wave equation written in the y_1 direction. Because we want the derivative with respect to y, the RHS (right-hand side) of (3.44) should be modified. Using the relation $y = \frac{y_1}{\cos\theta}$, the derivative on the RHS of (3.44) becomes $\frac{\partial u}{\partial y_1} = \frac{\partial u}{\partial y}\cdot\frac{\partial y}{\partial y_1} = \frac{1}{\cos\theta}\cdot\frac{\partial u}{\partial y}$. Replacing this in (3.44), we again obtain the equation (3.43), where the scalar field is u. From this comes the idea of the multi-directional boundary. Since in the general case the incidence of the waves onto the boundary is from different angles, Higdon (1986; 1991) approximated this continuous incidence with a finite set of m angles of incidence. The absorbing boundary then can be written in form:

$$\left\{\prod_{j=1}^{m}\left[\left(\cos\alpha_j\right)\frac{\partial}{\partial t} + \beta\frac{\partial}{\partial y}\right]\right\}u = 0, \tag{3.45}$$

where α_j are presumed angles of incidence. Thus, the components of the wave that impinge upon the boundary with angles of incidence equal to α_j will be perfectly absorbed. Theoretically, as $m \to \infty$, this boundary is a perfect absorber for any scalar wave field. Also, it is seen that in a special case, $\alpha_j = 0 \quad \forall\, 1 \le j \le m$, this boundary becomes identical with the A1 paraxial boundary (3. 32).

A question arises as to how many angles, m, should be included in (3.45) and what their values should be for a successful absorption. From numerical tests, Higdon (1991) concluded that m = 2 is a practical choice but that the values of α_j are problem dependent.

For example, if the waves near normal incidence are expected, all α_j in (3.45) should be taken equal to 0. But from numerical tests, Higdon concluded that the amount of reflection is not very sensitive to the values of these angles. Apparently, the range of these values must be $|\alpha_j| < \frac{\pi}{2}$, which follows from the geometry (Fig. 3.2) and the assumed direction of propagation. The reflection coefficient for this boundary is

$R_m = \prod_{j=1}^{m} \left| \frac{\cos\alpha_j - \cos\theta}{\cos\alpha_j + \cos\theta} \right|$, which is a big improvement compared with the viscous and A1 boundaries, because all of the multipliers in the product are smaller than 1 and the product is smaller than any multiplier.

The advantages of this boundary are

- It is simple (it is composed of derivatives of the first order and can easily be implemented).
- There is no need for corner conditions as in paraxial boundaries.
- The difference approximation uses values at the existing grid points compared with the extrapolation boundary where "monitoring" (non-existing grid points) should be introduced.

The main drawback is the problem dependence of the number m and the values of α_j.

3.1.3.4 Expansion boundaries

Bayliss and Turkel (1980) derived artificial boundary conditions based on the expansion of the outgoing pressure for 2-D flow as follows:

$$p(t,r,\theta,\phi)=\sum_{j=1}^{\infty}\frac{f_j(t-r,\theta,\phi)}{r^j}. \tag{3.46}$$

Multiplying (3.46) by r^m and applying operator $L^m=\left(\frac{\partial}{\partial t}+\frac{\partial}{\partial r}\right)^m$ we obtain

$$L^m\left(r^m p\right)=O\left(r^{-m-1}\right).$$

To have the operator operating only on p, the authors involved new operators :

$$B_m p=\prod_{l=1}^{m}\left(L+\frac{2l-1}{r}\right) \tag{3.47}$$

with leading term of the error being $O\left(r^{-2m-1}\right)$.

3.1.3.5 Extrapolation boundaries

Again, the idea of 1-D wave propagation is used for this type of boundaries. The total wave field can be represented as a sum of components propagating in different directions ξ_i (Liao & Wong, 1984):

$$U(x,y,z,t)=\sum_i u_i\left(\xi_i-\beta t\right). \tag{3.48}$$

The displacement of a point P in time t + Δt, due to the wave component propagating in direction ξ, can be predicted as (Fig. 3.3):

$$u\left(\xi_p - c(t+\Delta t)\right) = u\left(\left(\xi_p - c\Delta t\right) - ct\right) = u\left(\left(\xi_p - 2c\Delta t\right) - c(t-\Delta t)\right) = \ldots \quad (3.49)$$

Therefore, the displacement of P in time t + Δt is expressed as the displacement in points E on a distance kcΔt (k = 1,2,...) from P backward along the direction of propagation, in times t, t - Δt , t - 2Δt ,... .

It can be seen that (3.49) cannot be applied in practical computations because there are infinitely many directions of propagation and the components of the field cannot be separated into the points E, even if we suppose that a grid can be chosen with these points. We can pick the points on a normal erected from P and introduce monitoring points. These points play the role of points that lie on the same wave front as the points E, at distances kc'Δt (k = 1,2,...) from the point P in direction of the normal. However, because the direction of propagation is not known, these points cannot be located on the same wavefront as the points E. What can be done is to locate these monitoring points at equal distances d so that the error from their exact location is $k\varepsilon_0$ (k=1,2,...). Then, using the backward differences, the Newton-Gregory extrapolation formula can be used to obtain the displacement in P in time t + Δt as

$$u = u_0 + \Delta u_0 + \Delta^2 u_0 + .. + \Delta^N u_0 + O\left(\varepsilon_0^{N+1}\right), \quad (3.50)$$

where Δ are backward differences in space (in the direction of the normal-x) and time

$$\Delta u_0 = u_0 - u_{-1} \quad \Delta^2 u_0 = u_0 - 2u_{-1} + u_{-2} = \Delta u_0 - \Delta u_{-1} \quad \ldots. \quad \Delta^m u_0 = \Delta^{m-1} u_0 - \Delta^{m-1} u_{-1}.$$

The displacements are then evaluated as

Fig. 3.3 EXTRAPOLATION BOUNDARY

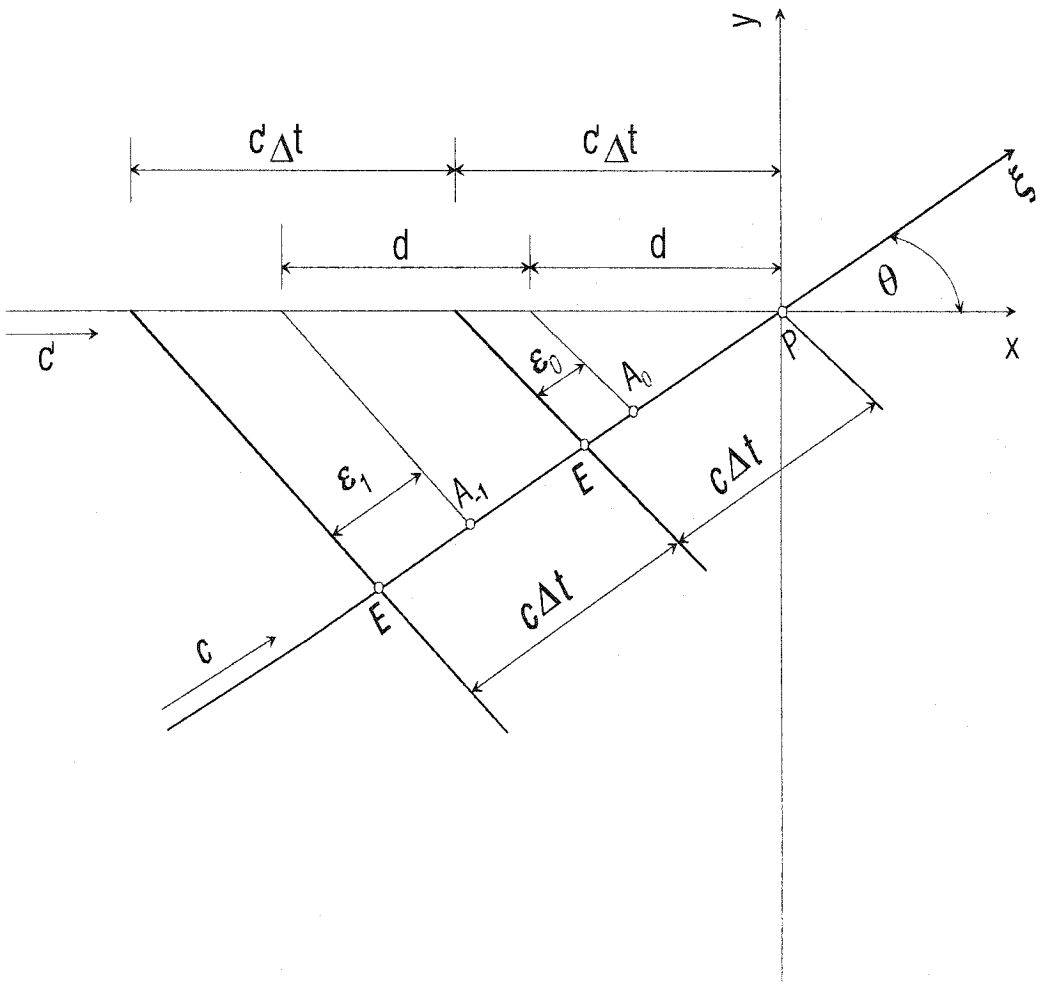

$$u_{-k} = u\left[x_p - (k+1)d, y_p, t - k\Delta t\right]. \tag{3.51}$$

Because in general the monitoring points A_{-k} are not the grid points, performing the extrapolation (3.50) requires that the values of the displacements (3.51) should be interpolated at all of the monitoring points from the neighboring grid points. This is the main drawback of this boundary. A similar idea for an extrapolation boundary was used by Liao et al. (1978) in solving a circular rigid disc welded to the surface of a homogeneous isotropic halfspace.

Many other authors have proposed local artificial boundaries that can be viewed as modifications of the above five. Kausel (1988) presented a review of the local artificial boundaries and concluded that all of them can be expressed with similar equations at least in the continuous domain, as we saw above for paraxial, viscous, and multi-directional boundaries. He suggested that for finite difference applications the paraxial type boundaries seem to be the most convenient and that for finite element applications extrapolation boundaries are most suitable.

3.1.4. Conclusion

In practical computation of wave propagation problems in an infinite or semi-infinite domain there is need to use artificial boundaries. They are a set of points that bound the computational domain but physically are just points of the full space. These artifacts can be classified into two main groups:

- Exact (perfect) boundaries that are perfect absorbers but are global both in time and space and for practical implementation should be truncated. These are more suitable for FE formulation because of their non-rectangular shape. The FE formulations are more flexible for modeling nonrectangular geometries than the FD schemes.
- Local boundaries that are mostly derived for rectangular shapes. Their time and space derivatives are of low order and so are easily implemented in numerical algorithms.

The first group uses mostly DtN maps to replace the Sommerfeld radiation condition at the artificial boundary. Because in their original formulation they involve high-order derivatives in time and in the tangential direction, for practical computation the exact infinite series are truncated, which means that some error is introduced. Some boundaries deal with reducing the order of the derivatives by involving additional unknowns. Most of these boundaries are derived for full space. Finally, the behavior of the boundary cannot be predicted in a case in which the incoming plane wave and the outgoing cylindrical wave meet at the boundary.

The local boundaries are not exact, and the error (reflection from the boundary) depends upon the distance from the scatterer. The further away the boundary is imposed, the smaller the error will be. Nevertheless, local boundaries are popular in FD applications, which involve rectangular domains and complicated outgoing fields with wide frequency ranges.

3.2 Rotated viscous artificial boundary

The artificial boundary $\mathcal{B}$ in the model is a viscous type of boundary rotated to absorb the wave field coming under angle θ in the point $m \in \mathcal{B}$ (Fig. 2.2). The idea for this boundary comes from the consideration of spherical (3-D) or circular (2-D) propagation of the scattered wave field. It is also related to the case of the Higdon multi-directional boundary with $m = 1$ in (3.45) and with different α_1 at different boundary points. Based on many numerical tests with different boundaries, this one appears to give the best results. For example, the second-order Clayton-Engquist boundary and the two-directional Higdon boundary lead to instability at the corner points for some combinations of angles of incidence and durations of the pulse in our transient analysis. This is a local boundary, and some small residual reflected field is expected, but it is stable for all incident angles and frequencies considered in this work. The residual field is larger for higher frequencies when the diffraction is more pronounced and when the ray theory involves larger errors. Nevertheless, this artificially reflected field is negligible compared with the solution, and the model gives satisfactory results that can be seen in the next section and in Chapter V.

To implement this artificial boundary, the soil island $R = \Omega_s \cup \Omega_f$ (where Ω_s is the region occupied by soil and Ω_f is the region occupied by the foundation) is divided into two regions: $R_1 = \{M(x,y) \mid x_a \le x \le x_d, y_b \le y \le y_a\}$ with boundaries $\Gamma_1 = \overline{ab} \cup \overline{bc} \cup \overline{cd}$, and, $R_2 = R \setminus R_1$ with inner boundary $\Gamma_2 = \overline{lk} \cup \overline{kj} \cup \overline{ji}$ and an outer boundary that is the artificial boundary $\mathcal{B} = \overline{ef} \cup \overline{fg} \cup \overline{gh}$ (Fig. 2.2). At the top, these two regions are bounded by the half space. We want the finite difference solution in region R_1 to be the solution for the total field and in region R_2 to be the solution for the scattered field only. The two rows (2,3) next to the bottom artificial boundary $\overline{fg}$, the two columns (2,3) next to the left artificial boundary $\overline{ef}$, and the two columns next to the right artificial boundary $\overline{gh}$ are inserted in the model (Fig. 3.4) for practical purposes. As will be shown later, the analytical (half-space) solution is evaluated on the boundaries Γ_1 and Γ_2. The role of the inserted rows and columns is to decrease the error arising from the difference between the solution in the discrete domain (FD solution for the total field) and the solution in the continuous domain (half space, analytical solution).

To solve in R_1, we first should solve on Γ_1 for the total field. This can be accomplished if we know the total field in all neighboring points of the boundary Γ_1 including the points on Γ_2. For that purpose, in the finite difference (scattered) solution on $\Gamma_2 \in R_2$ the analytical (half-space) solution should be added. The procedure for solving in R_2 is similar. First, we subtract the analytical (half-space) solution from the finite difference (total) solution on $\Gamma_1 \in R_1$ to obtain the scattered field on Γ_1, and then, using finite differences, the solution for the scattered

field is obtained on Γ_2. In this way, the problem under consideration is replaced by two auxiliary problems (Fig.3.4).

Assuming that the upgoing displacement field w_u (t) at a point f and the angle of incidence γ are known, we proceed for each time step (refer to Fig.3.4) as follows

1. Update the analytical solution for the half space at the points on the lines:

   - ab - the fourth column of the model
   - bc - the fourth row of the model
   - cd - the third to the last column

in two consecutive time steps t - $\Delta t = (k-1)\Delta t$ and $t = k\Delta t$ $k = 1,2,3,\ldots,T/\Delta t$,

where T is the time at the end of the analysis and Δt is the time step.

For example, on the line ab (the fourth column) the solution for the displacements is

$$w_{4,j}(t) = w_u(t-t_0)H(t-t_0) + w_u(t-t_1)H(t-t_1),$$

where w_u is the prescribed displacement of the upgoing field at the point f(0,0) (Fig.2.2),

$t_0 = \frac{(j-1)\Delta y}{c_y} + \frac{(4-1)\Delta x}{c_x}$, and $t_1 = \frac{H_s - (j-1)\Delta y + H_s}{c_y} + \frac{(4-1)\Delta x}{c_x}$ are arrival times at the point (4,j) of the incident and reflected waves, respectively; $c_x = \frac{\beta}{\sin\gamma}$ and $c_y = \frac{\beta}{\cos\gamma}$ are the phase velocities in x and y, respectively; $\Delta x = \Delta y$ are spatial steps for the soil; H_s is the height of the soil island in the model; and H() is the Heaviside function.

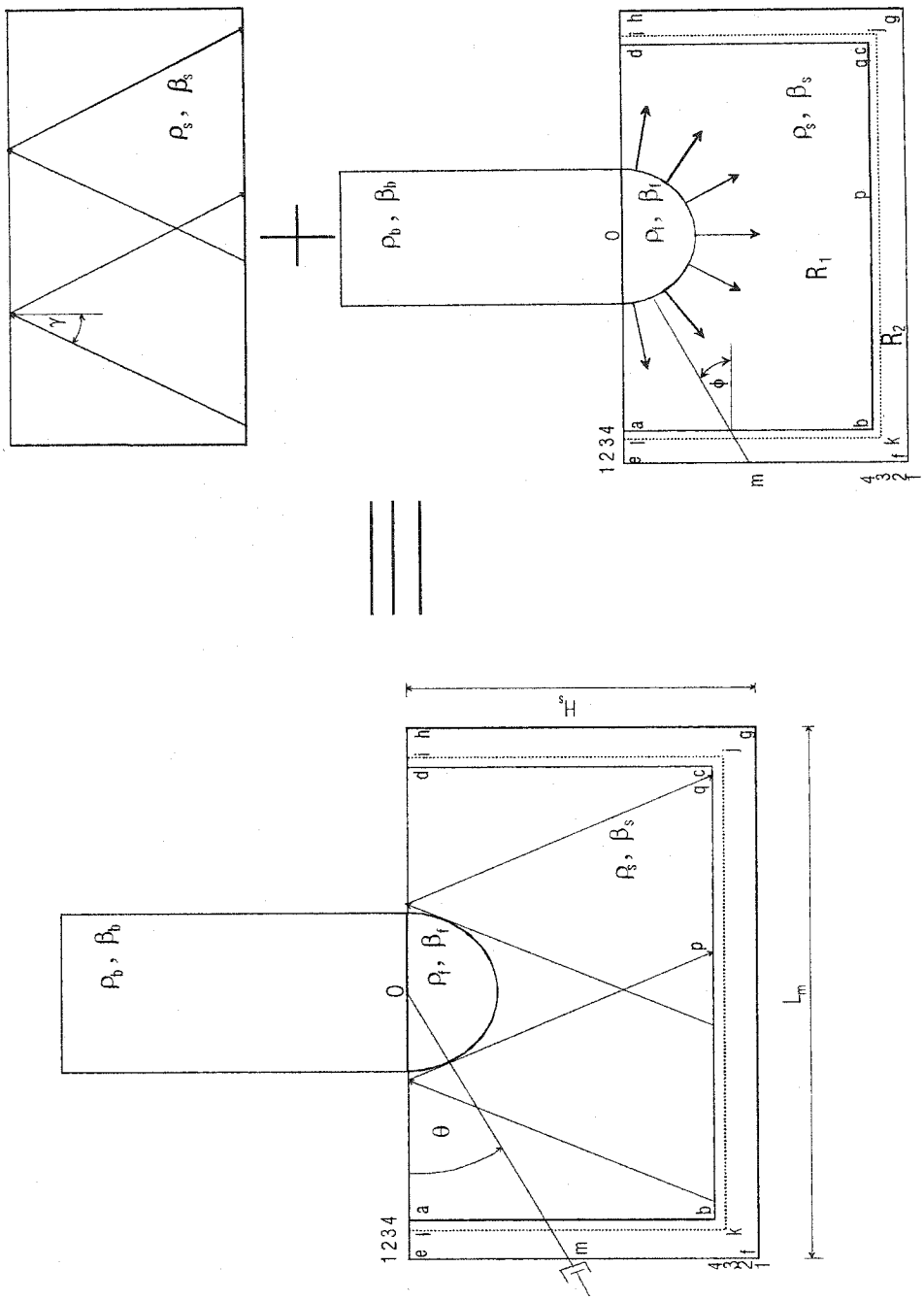

Fig. 3.4 DECOMPOSITION OF THE PROBLEM

We now perform the above for the fifth column, the fifth row, and the second-to-last column at time t = kΔt. The velocities and the stresses for the half-space solution at the boundary Γ_1 (lines ab, bc, and cd) are:

$$v_{i,j}^k = \frac{w_{i,j}^k - w_{i,j}^{k-1}}{\Delta t} \quad , \sigma_{xi,j}^k = \mu_s \frac{w_{i+1,j}^k - w_{i,j}^k}{\Delta x}, \sigma_{yi,j}^k = \mu_s \frac{w_{i,j+1}^k - w_{i,j}^k}{\Delta y} \qquad \forall (x_i, y_j) \in \Gamma_1,$$

where μ_s is the shear modulus of the soil,

$i = \frac{x_i}{\Delta x}$ and $j = \frac{y_j}{\Delta y}$ are discrete spatial coordinates in the x and y directions, respectively,

$k = \frac{t}{\Delta t}$ is the discrete time coordinate,

$v_{i,j}^k$ is the velocity at the point (x_i, y_j) in time $t = k \cdot \Delta t$, and

$\sigma_{xi,j}^k, \sigma_{yi,j}^k$ are the shear stresses τ_{xz} and τ_{yz} at the point (x_i, y_j) in time $t = k \cdot \Delta t$.

The above notation for the velocities and the stresses with the discrete spatial coordinates as subscripts and the discrete time coordinate as a superscript will be used in the following text.

2. From the finite difference solution on the lines ab, bc, and cd (obtained by solving region R_1), subtract the above half-space solution. This difference gives us the scattered field on Γ_1 (the boundary condition for region R_2).

3. Solve the second and the third rows and columns, as well as the next-to-last and the second-to-last columns using FD scheme. This solution is the scattered field in R_2.

4. Solve for the points at the absorbing boundary $B = \overline{ef} \cup \overline{fg} \cup \overline{gh}$. The absorbing boundary is a local, viscous type of boundary, consisting of rotated dashpots as shown on

Fig.3.4 for the point m. For example, the velocities at ef (the wave travels in the direction of negative x) are computed from the scalar equation

$$\frac{\partial v}{\partial t} = \beta \frac{\partial v}{\partial s} = \beta \frac{\partial v}{\partial x}\frac{dx}{ds} = \beta \frac{\partial v}{\cos\phi \cdot \partial x}, \qquad (3.2.1)$$

where s is the spatial coordinate in the direction of propagation of the wave,

$\theta = \tan^{-1}\left(\dfrac{H_s - (m-1)dy}{\frac{L_m}{2}}\right)$ is the polar coordinate, (3.2.2)

and $\phi = \theta$ is the incident angle of the outgoing field (the angle between the normal to the boundary at m and the polar ray Om) (Fig.3.4). The outgoing components of the stress σ_x and σ_y are computed when the velocity in the equation (3.2.1) is replaced with the desired stress. With similar equations, the velocities and the stresses are computed at all of the points of the absorbing boundary $\mathcal{B}$.

The finite difference approximations of (3.2.1) with a coordinate system as in Fig.2.2 are as follows.

On the left boundary: $\left(D_+^t - \dfrac{\beta}{\cos\phi} D_+^x\right) S_{i,j}^k = 0, \qquad \phi = \theta$ (3.2.3a)

On the bottom boundary: $\left(D_+^t - \dfrac{\beta}{\cos\phi} D_+^y\right) S_{i,j}^k = 0, \qquad \phi = \dfrac{\pi}{2} - \theta$ (3.2.3b)

On the right boundary: $\left(D_+^t + \dfrac{\beta}{\cos\phi} D_-^x\right) S_{i,j}^k = 0, \qquad \phi = \pi - \theta$ (3.2.3c)

$S_{i,j}^k$ in the equations (3.2.3) stands for v, σ_x and σ_y.

The three points at the left $\{(0,0);(0,\Delta y_s);(\Delta x,0)$ and the three points at the right bottom corners $\{(L_m,0);(L_m,\Delta y_s);(L_m-\Delta x,0)\}$ are treated as in Clayton and Engquist (1977). For example, for the left bottom corner (Fig. 3.5 where h stands for Δx) it is assumed that the outgoing scalar field impinges upon the boundary under angle $\phi=\frac{\pi}{4}$ in the points P, Q, and R and has the form

$$S=S_0e^{i(\omega t+k_x x+k_y y)}. \tag{3.2.4}$$

Considering simultaneous 1-D wave propagations in the x and y directions, we proceed as follows:

$$\frac{\partial S}{\partial t}=c_x\frac{\partial S}{\partial x}=\sqrt{2}\beta\frac{\partial S}{\partial x} \tag{3.2.5}$$

$$\frac{\partial S}{\partial t}=c_y\frac{\partial S}{\partial y}=\sqrt{2}\beta\frac{\partial S}{\partial y}, \tag{3.2.6}$$

where c_x and c_y are the phase velocities of the outgoing wave impinging upon the corner under angle $\phi=\frac{\pi}{4}$.

Summing equations (3.2.5) and (3.2.6) we obtain

$$\frac{\sqrt{2}}{\beta}\frac{\partial S}{\partial t}=\left(\frac{\partial S}{\partial x}+\frac{\partial S}{\partial y}\right). \tag{3.2.7}$$

It is seen from Fig.3.5 that the spatial derivatives cannot be approximated with central difference and that to get the explicit scheme the temporal derivative must be approximated by backward

Fig. 3.5 THE LEFT BOTTOM CORNER OF THE MODEL

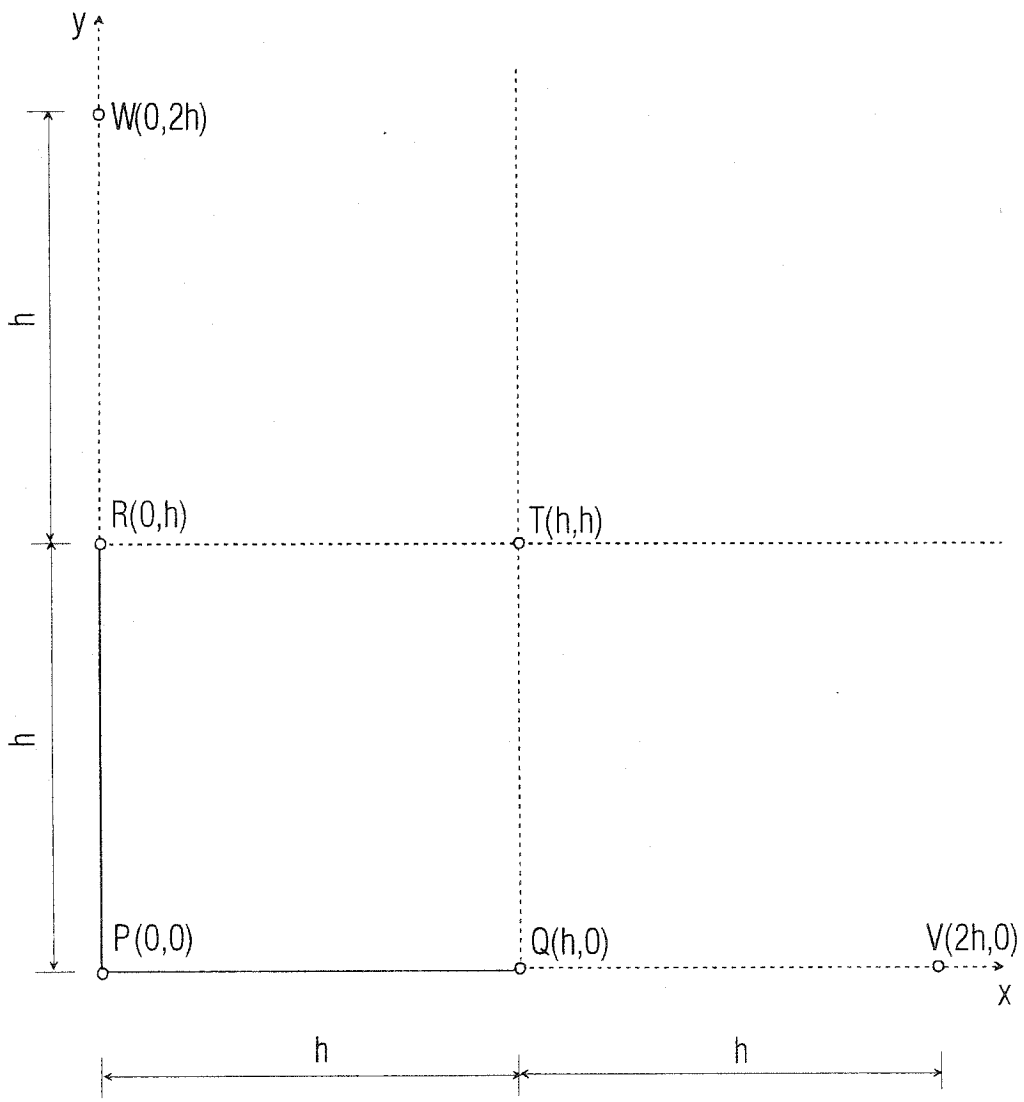

difference. For the coordinate system in Fig.3.5 (in Clayton & Engquist,1977, y is directed downward), the finite difference approximation of (3.2.7) is

$$\left(\frac{\sqrt{2}}{\beta}D_{-}^{t}-D_{+}^{x}-D_{+}^{y}\right)S_{A}^{k}=0\,, \tag{3.2.8}$$

where k is the discrete temporal coordinate, β is the shear wave velocity in the soil, and the subscript A stands for the point P, Q, or R. First, the points Q and R are solved. For example, for the point R, keeping in mind that $\Delta y_s = \Delta x$ and referring to Fig.3.5, from (3.2.8) we have

$$S_{R}^{k}=\frac{1}{\frac{\sqrt{2}}{\beta}+2\frac{\Delta t}{\Delta x}}\left[\frac{\sqrt{2}}{\beta}S_{R}^{k-1}+\frac{\Delta t}{\Delta x}\left(S_{T}^{k}+S_{W}^{k}\right)\right]. \tag{3.2.9}$$

The scalar at the point Q is computed in a similar way. Having S_R^k and S_Q^k, the scalar in P is computed as

$$S_{P}^{k}=\frac{1}{\frac{\sqrt{2}}{\beta}+2\frac{\Delta t}{\Delta x}}\left[\frac{\sqrt{2}}{\beta}S_{P}^{k-1}+\frac{\Delta t}{\Delta x}\left(S_{Q}^{k}+S_{R}^{k}\right)\right]. \tag{3.2.10}$$

S in the above equations stands for v, σ_x and σ_y of the scattered field, and all of these dynamic quantities must be resolved with the described procedure at the six corner points to obtain a stable solution. It is important to note that the three corner points give the necessary transition between the boundary conditions on the vertical and horizontal boundaries (and vice versa), which makes the boundary stable. Also it should be pointed out that the quantities S in the six corner points are always computed in one time step of retarded time. They are computed

in the beginning of the algorithm, but because these points belong to the boundary B, the procedure is presented here.

5. Update the analytical solution for the half space in the points on the lines :

- kl - the third column of the model
- kj - the third row of the model
- ji - the second to last column

in two consecutive time steps $t - \Delta t = (k-1)\Delta t$ and $t = k\Delta t$ $\quad k=1,2,3,\ldots,T/\Delta t$

For example on the line kl (the third column) the solution for the displacements is :

$$w_{3,j}(t) = w_u(t-t_0)H(t-t_0) + w_u(t-t_1)H(t-t_1)$$

where $t_0 = \frac{(j-1)\Delta y}{c_y} + \frac{(3-1)\Delta x}{c_x}$ and $t_1 = \frac{H_s - (j-1)\Delta y + H_s}{c_y} + \frac{(3-1)\Delta x}{c_x}$ are arrival times at the point (3,j) for the incident and reflected waves, respectively, with $c_x = \frac{\beta}{\sin\gamma}$, $c_y = \frac{\beta}{\cos\gamma}$, and H() is the Heaviside function.

We now perform the above for the fourth column, the fourth row, and the next-to-last column at time $t = k\Delta t$. The velocities and stresses for the half-space solution at the lines ab, bc, and cd are

$$v_{i,j}^k = \frac{w_{i,j}^k - w_{i,j}^{k-1}}{dt} \quad , \quad \sigma_{xi,j}^k = \mu_s \frac{w_{i+1,j}^k - w_{i,j}^k}{dx} \quad , \quad \sigma_{yi,j}^k = \mu_s \frac{w_{i,j+1}^k - w_{i,j}^k}{dy}.$$

6. Add the finite difference solution for the points on the lines kl, kj, and ji (obtained from solving in region R_2) to the above solution for the half space. This sum is the total field on Γ_2 (the boundary condition for region R_1).

7. Solve for the points $\{M(x,y) \mid M \in R_1\}$.

8. If k <= T/dt return to step 1.

9. End.

3.3 Numerical tests

To test the model, and in particular the artificial boundary, the structure (Fig.3.6) is loaded at the top $(|x'| \le a, y' = H_b)$ with excitation in the form of a half-sine displacement pulse with duration $t_d = 0.1s$ and amplitude $A = 0.5m$:

$$u_0 = A \sin \frac{\pi t}{t_d}. \qquad (3.3.1)$$

This pulse is Fourier transformed into the frequency space, and only the components with Fourier amplitudes larger than 3% of the Fourier amplitude of the zero-th component (k = 0) are kept.

For the last kept component (the largest wave number), the corresponding frequency is found from $\omega_{\max} = \omega_c = \beta_b \cdot k_{\max}$. This is the cut-off frequency with which the pulse (3.3.1) is low-pass filtered using an Ormsby filter (Trifunac, 1971). All of the top points of the structure,

Fig. 3.6 TEST MODEL - BUILDING LOADED ON THE TOP

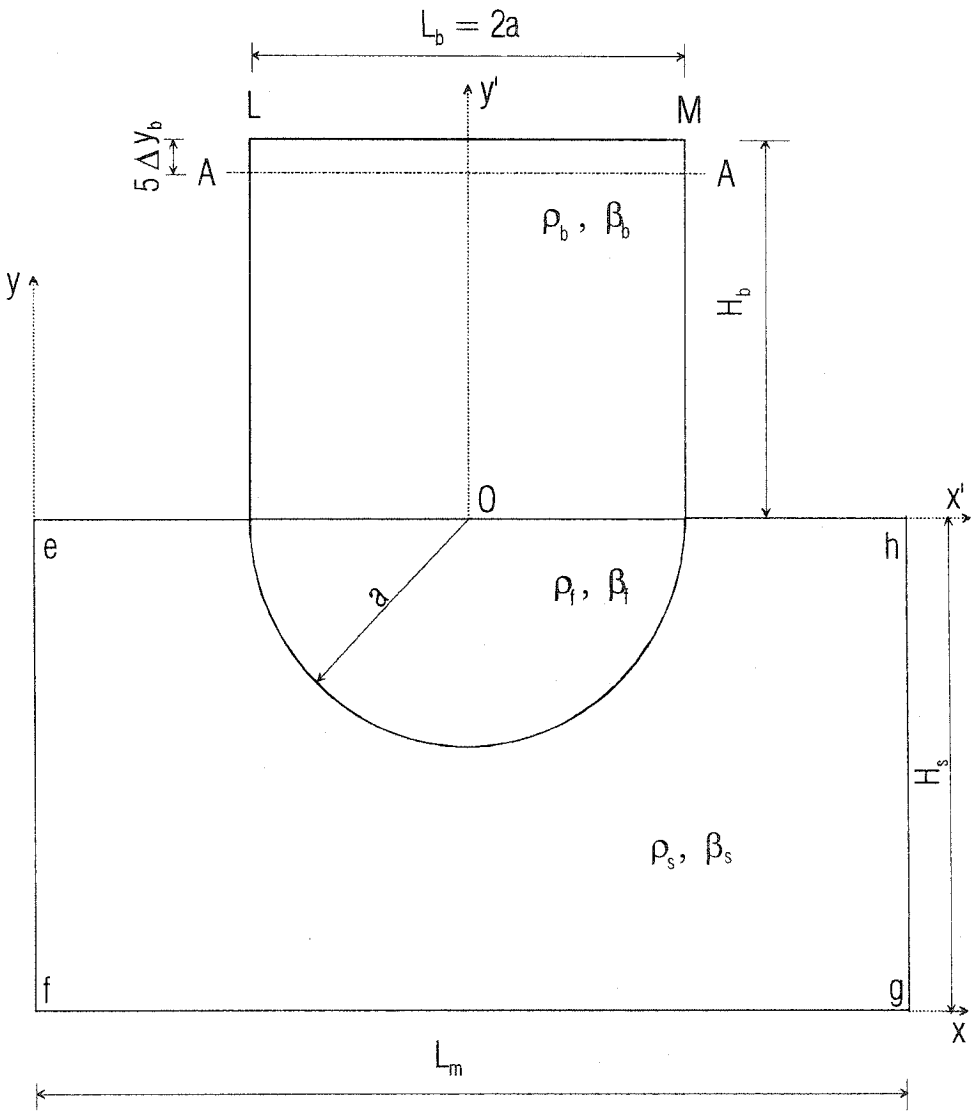

at $y' = H_b$ are loaded with the same excitation. As a measurement of the error, we take the difference between the input and the sum of radiated energy and the energy in the building, divided by the input energy

$$\varepsilon = \frac{\left|E_{inp} - \left(E_{rad} + E_b\right)\right|}{E_{inp}}, \tag{3.3.2}$$

where the input energy is computed using the formula for continuous space (Aki & Richards,1980):

$$E_{inp} = \rho_b \beta_b A \int_0^{T_d + t_a} v^2 dt, \tag{3.3.3}$$

where ρ_b is the density of the building, β_b is the shear wave velocity of the building, $A = 2a \cdot 1$ is the area normal to the direction of the wave propagation, v is the velocity at the points of the section A-A, T_d is duration of the filtered pulse, and $t_a = \frac{5\Delta y_b}{\beta_b}$ is the travel time of the wave from the top of the building to section A-A.

To avoid the singularity at the line of the application of the load, the input energy is computed at section A-A (Fig. 3.6). The duration of the pulse is chosen to satisfy the relation:

$$t_d + \left(2 \cdot n_f + 1\right) \cdot \Delta t < \frac{2\left(H_b - 5\Delta y_b\right)}{\beta_b}, \tag{3.3.4}$$

where t_d is the duration of the unfiltered pulse, the left-hand side is the total duration of the filtered pulse T_d, and the right-hand side of is the travel time at section A-A of the pulse to and from the building-foundation contact. After the pulse is completely applied at the top section

$y' = H_b$, this section behaves like a free boundary. The equation (3.3.3) in discrete space is

$$E_{inp} = \rho_b \beta_b \Delta x \Delta t \sum_{k=1}^{(T_d+t_a)/\Delta t} \left(\frac{v_{L,k}^2 + v_{M,k}^2}{2} + \sum_{i=L+1}^{M-1} v_{i,k}^2 \right), \tag{3.3.5}$$

where k is the discrete time coordinate, and i is the discrete spatial coordinate in the x direction. The sets of points $x = (L-1)\Delta x, y > H_s$ and $x = (M-1)\Delta x, y > H_s$ are the left and right free boundaries of the building (Fig.3.6). The radiated energy is computed as

$$E_{rad} = \rho_s \beta_s \Delta x \sum_{k=1}^{T/dt} \left(\sum_{i,j} \cos\phi_{i,j} v_{i,j,k}^2 \Delta t \right), \tag{3.3.6}$$

where $(i, j) \in \mathcal{B}$, T is the time at the end of the analysis, $\phi_{i,j}$ is the angle of incidence of the outgoing ray at the point (i,j) described in step 4 in section 3.2 and $v_{i,j,k}$ is the velocity at the point (x_i, y_j) in time $t = k \cdot \Delta t$.

In the first test example, the properties of the Hollywood Storage building described in Duke et al. (1970) are used. According to their model, the properties of the building, the soil, and the foundation (Fig. 3.6) for east-west (longitudinal) response are

- Radius of the foundation: $a = 7.8\,m$
- Height of the building: $H_b = 45.6\,m$
- Fundamental frequency: $f_0 = 1.85\,Hz$
- Ratios of the masses: $\frac{M_b}{M_s} = 1.4$ $\frac{M_0}{M_s} = 1.0$,

where M_b and M_0 are the masses of the building and the foundation per unit length, and M_s is the mass of the soil occupying the volume of the foundation, also per unit length. With the fundamental frequency and the height of the building known, the shear wave velocity of the building is $\beta_b = 4 \cdot H_b \cdot f_0 = 337.44\, m/s$.

From the depth profile of the shear wave velocities, close to the surface (in the first 100 - 150 feet of soil) the shear wave velocity varies from 500 to 1,200 ft/s. In our test example, we adopted $\beta_s = 250\, m/s$, which is approximately the mean value for the above measured velocity. The density of the soil is taken as $\rho_s = 2000\, kg/m^3$.

The distribution of the energy is shown in Fig. 3.7. E_{inp} is the cumulative input energy, E_{rad} is the cumulative radiated energy measured at the points of the artificial boundary $B = \overline{ef} \cup \overline{fg} \cup \overline{gh}$ (Fig.3.6), and E_b is the instantaneous energy in the building computed as

$$E_b = \sum_{i,j} \left(\frac{\mu_b \varepsilon_{i,j}^2}{2} + \frac{\rho v_{i,j}^2}{2} \right) \Delta x_i \Delta y_{bj} , \qquad (3.3.7)$$

where $\varepsilon_{i,j}^2 = \varepsilon_{xi,j}^2 + \varepsilon_{yi,j}^2$ is square of the resultant strain at the point $\left\{ (i,j) \mid L \le i \le M, j > \frac{H_s}{\Delta y_s} + 1 \right\}$

$$\Delta x_i = \begin{cases} \frac{\Delta x}{2} & \text{for x} = \text{L, M} \\ \Delta x & \text{otherwise} \end{cases} \qquad \Delta y_{bj} = \begin{cases} \frac{\Delta y_b}{2} & \text{for j} = \frac{\text{H}_s}{\Delta \text{y}_s} + \frac{H_b}{\Delta y_b} + 1 \\ \Delta y_b & \text{otherwise} \end{cases}$$

and $\mu_b = \rho_b \beta_b^2$ is the shear stiffness of the building.

The energy was measured for two different model sizes (Fig.3.6):

1. $H_s = \frac{L_m}{2} = 4a$

2. $H_s = \frac{L_m}{2} = 5a$.

At the end of the analysis (T = 4s) the values of the energy and the computed error (3.3.2) are:

For model size 1: $E_{inp} = 5102413J,\ E_{rad} = 5092446J,\ E_b = 4544J \qquad \varepsilon = 0.16\%$

For model size 2: $E_{inp} = 5102413J,\ E_{rad} = 5078163J,\ E_b = 4731J \qquad \varepsilon = 0.38\%$.

For our second test example, the properties of the Holiday Inn hotel described in Blume and Assoc. (1973) are used. The dimensions and the properties of the building, the soil, and the foundation (Fig. 3.6) in the transversal direction of the building are:

- Radius of the foundation: $a = 9.55\,m$
- Height of the building: $H_b = 20.0\,m$
- Shear wave velocity of the building: $\beta_b = 100\,m/s$
- Shear wave velocity of the soil: $\beta_s = 250\,m/s$
- Shear wave velocity of the foundation: $\beta_f = 300\,m/s$
- Density of the building: $\rho_b = 270\,kg/m^3$
- Density of the soil and the foundation: $\rho_s = \rho_f = 2000\,kg/m^3$.

Again the energy was measured for two different model sizes

1. $H_s = \frac{L_m}{2} = 4a$

2. $H_s = \frac{L_m}{2} = 5a$.

The distribution of the energy versus time is shown in Fig. 3.8.

At the end of the analysis (T = 14.59s), the values of the energy and the computed error (3.3.2) were:

For model size 1: $E_{inp} = 1244629J,\ E_{rad} = 1224142J,\ E_b = 8208J \qquad \varepsilon = 0.99\%$

For model size 2: $E_{inp} = 1244629J,\ E_{rad} = 1221035J,\ E_b = 8459J \qquad \varepsilon = 1.22\%$.

With these test examples, it can be seen that the model gives satisfactory results when the artificial boundary is located far enough from the foundation. With this setting, we assume that the artificial boundary "sees" the foundation as a point source generating cylindrical outgoing waves, which then allows us to make an approximation of the incident angle of the waves, ϕ, relative to the normal on the boundary $\mathcal{B}$.

As can be seen from figures 3.7 and 3.8, the building radiates the energy partially when the pulse reaches the building-foundation contact. Then, one part of the pulse is transmitted into the foundation and one part is reflected back in the building. In the figures, this interval of time corresponds first to the sharp decrease of the instantaneous energy in the building, and second, after travel time t_t from the building-foundation contact to $\mathcal{B}$, to the sharp increase of the radiated energy. After the pulse has passed the contact (its reflected part is completely in the building), there is a state of "constant energy" in the building and, after time t_t, a constant

cumulative energy, which has passed through $\mathcal{B}$. This state is represented by flat parts of the curves $E_b = E_b(t)$ and $E_{rad} = E_{rad}(t)$. From Fig. 3.7 for the Hollywood Storage building (HSB), the decrease of energy in the building can be represented with the ratio of the amplitudes (measured directly from the plot) of the flat parts as follows:

$$\frac{E_{b1}}{E_{b2}} = \frac{6.3}{3} = 2.1;\ \frac{E_{b2}}{E_{b3}} = \frac{3}{1.4} = 2.14;\ \frac{E_{b3}}{E_{b4}} = \frac{1.4}{0.69} = 2.03;\ \frac{E_{b4}}{E_{b5}} = \frac{0.69}{0.33} = 2.09 \ldots\ldots$$

or generally

$$\frac{E_{bi}}{E_{bi+1}} \approx 2.1. \qquad (3.3.8a)$$

Recalling that the energy in some instant of time is proportional to the square of the velocity, when we take the square root of (3.3.8a) we have

$$\frac{v_i}{v_{i+1}} \approx 1.45. \qquad (3.3.9a)$$

We can construct an equivalent single-degree-of-freedom (SDOF) oscillator with a natural frequency equal to the fundamental natural frequency of the building with the damping ratio

$$\zeta \approx \frac{\delta}{2\pi}, \qquad (3.3.10)$$

where $\delta = \ln\frac{u_i}{u_{i+1}} = \ln\frac{v_i}{v_{i+1}}$ is the logarithmic decrement, u_i is the i^{th} positive (negative) peak displacement, and u_{i+1} is $(i+1)^{st}$ positive (negative) peak displacement. The damping ratio of the equivalent SDOF oscillator for HSB computed from (3.3.10) is

$$\zeta_{HSB} = 0.059. \qquad (3.3.11a)$$

In a similar way, from Fig.3.8, for the Holiday Inn hotel (HIH) we obtain

$$\frac{E_{bi}}{E_{bi+1}} \approx 1.17 \qquad (3.3.8b)$$

$$\frac{v_i}{v_{i+1}} \approx 1.08 \qquad (3.3.9b)$$

$$\zeta_{HSB} = 0.012\,. \qquad (3.3.11b)$$

The fundamental natural frequencies of the above buildings can be obtained from the solution of the wave equation for a building on a fixed base as $\omega = \frac{\pi\beta_b}{2H_b}$, where β_b is the shear wave velocity in the building and H_b is the height of the building. We then have

$$\omega_{HSB} = 3.7\pi \qquad (\zeta \cdot \omega)_{HSB} = 0.68$$

$$\omega_{HIH} = 2.5\pi \qquad (\zeta \cdot \omega)_{HIH} = 0.094\,.$$

For example, if both SDOF oscillators have initial displacement $u_0 = 1$ we can compute the time in which the amplitude will decrease to 1/a (a > 1). From $e^{-\zeta\omega t} = \frac{1}{a} \Rightarrow t = \frac{\ln a}{\zeta\omega}$.

For example, the time in which the amplitude will decrease to 1/4 of the initial displacement (a = 4) for the Hollywood Storage building is

$$t_{HSB} = \frac{\ln 4}{0.68} = 2.04\,s \qquad (3.3.12a)$$

and for the Holiday Inn hotel it is

$$t_{HIH} = \frac{\ln 4}{0.094} = 14.75\,s\,. \qquad (3.3.12b)$$

For these examples, where $\rho_f \beta_f$ is close to $\rho_s \beta_s$, the damping ratio can be evaluated by the use of the reflection and transmission coefficients at the contacts. From the boundary conditions of continuity of the stress and displacement at the contact between building and foundation, the reflection coefficient from building to building is (Fig.3.6)

$$k_{ref} = \frac{1 - \dfrac{\rho_f \beta_f}{\rho_b \beta_b}}{1 + \dfrac{\rho_f \beta_f}{\rho_b \beta_b}}, \tag{3.3.13}$$

and the transmission coefficient from building to foundation is

$$k_{tr} = \frac{2}{1 + \dfrac{\rho_f \beta_f}{\rho_b \beta_b}}. \tag{3.3.14}$$

The energy remaining in the building after the wave has passed the contact is

$$E_b^{new} = k_{ref}^2 E_b^{old}. \tag{3.3.15}$$

From (3.3.15),

$$\frac{E_b^{old}}{E_b^{new}} = \frac{E_{bi}}{E_{bi+1}} = \frac{1}{k_{ref}^2}. \tag{3.3.16}$$

For HSB $k_{ref} = -0.651$, for HIH $k_{ref} = -0.914$, and from (3.3.16),

$$\left(\frac{E_{bi}}{E_{bi+1}} \right)_{HSB} = 2.358 \tag{3.3.17a}$$

$$\left(\frac{E_{bi}}{E_{bi+1}} \right)_{HIH} = 1.197. \tag{3.3.17b}$$

Fig. 3.7 TEST EXAMPLE: HOLLYWOOD STORAGE BUILDING

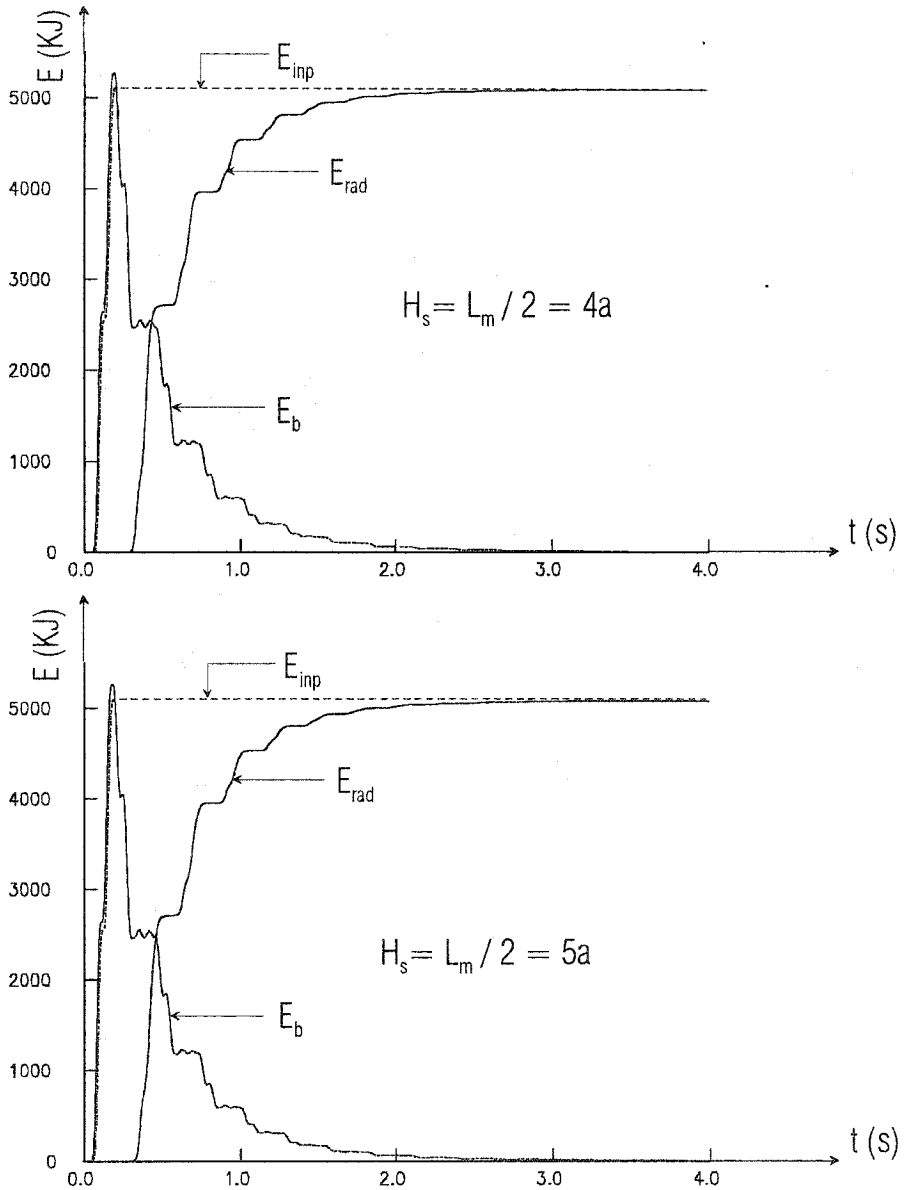

Fig. 3.8 TEST EXAMPLE: HOLIDAY INN HOTEL

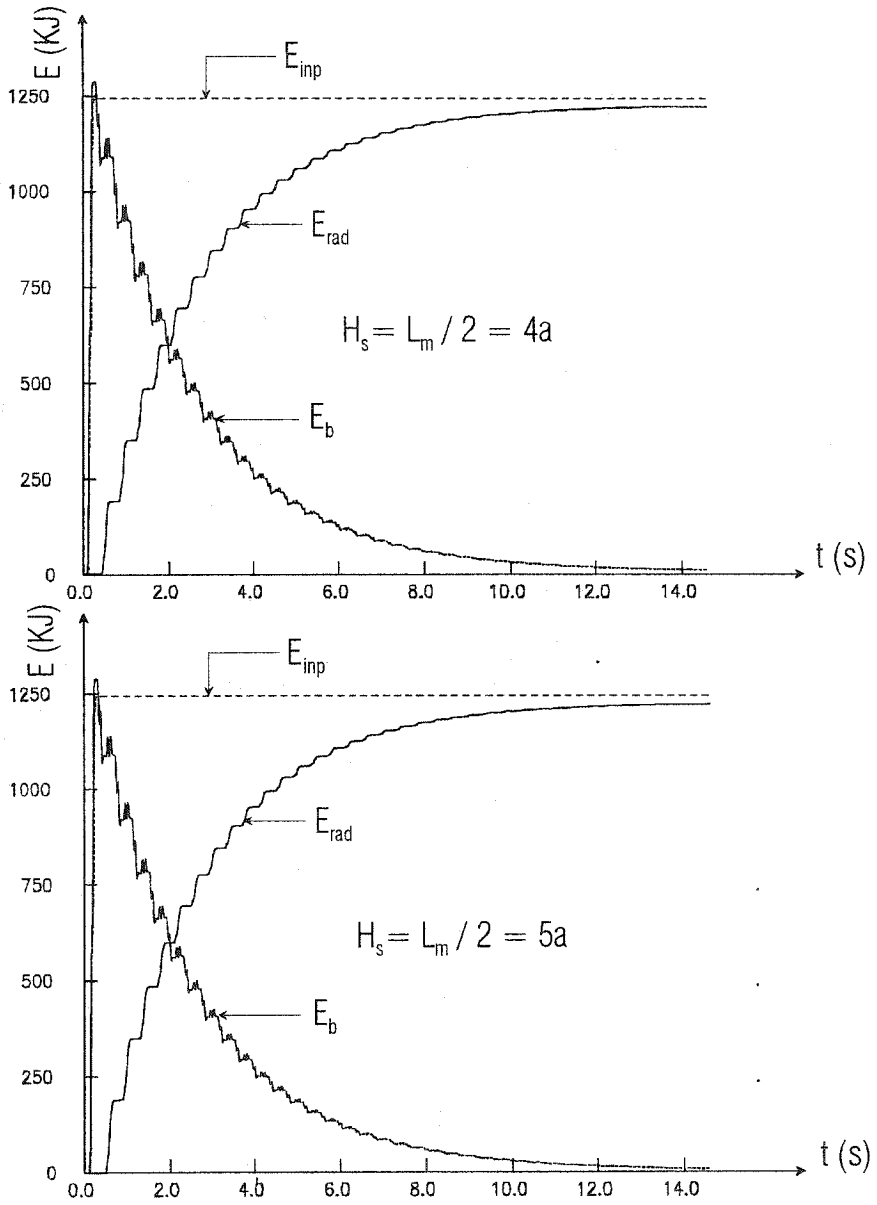

Comparing (3.3.8a,b) and (3.3.17a,b), we can see that these ratios of energies are close. The equations (3.3.17a,b) involve errors because they do not account for the reflection of the wave from foundation to foundation at the foundation-soil contact and later transmission of that reflected wave from the foundation to the building. The equation (3.3.16) will be accurate if the foundation properties are the same as the soil properties.

The curve $E_{rad} = E_{rad}(t)$ represents the cumulative energy passing through the artificial boundary $\mathcal{B}$. The increases along the curve are equal to the dissipated energy from the building during each passing of the wave through the building-foundation contact.

CHAPTER IV

SOIL-STRUCTURE INTERACTION WITH A FLEXIBLE FOUNDATION: STEADY-STATE ANALYSIS

4.1 Introduction

Trifunac (1972) presented an analytical solution of the interaction of an infinitely long shear wall supported by a rigid semi-circular foundation embedded in linear homogeneous half space and excited by plane SH waves with arbitrary incidence. The amplitude of the foundation motion Δ was found in terms of Bessel and Hankel functions, and several important conclusions were drawn:

1. The amplitude of the foundation motion does not depend upon the angle of incidence.
2. When the excitation frequency is equal to any natural frequency of a structure with a fixed base, Δ becomes zero.
3. The relative displacement of the structure $|_R u_z| = |w_r| = |w_{0'} - w_0|$ (Fig.4.1) with zero structural damping at resonant frequencies is finite, unlike the same structure with neglected interaction, where the relative displacement goes to infinity with the time. This difference is caused by radiation of wave energy into the half space. As shown in Trifunac (1972), the relative displacement of the structure (wall) is:

$$|_R u_z| = \left| \Delta \left(\frac{1}{\cos(k_n H_b)} - 1 \right) \right| . \qquad (4.1)$$

If $\cos(k_n H_b) = \cos\frac{(2n+1)\pi}{2} = 0$ (n = 0,1,2,...), then $k_n = \frac{\omega_n}{\beta_b}$ is the wave number of the n-th natural frequency of the structure. From (4.1), with neglected interaction, $\Delta = 1$ and $|_R u_z| \to \infty$. But if the interaction is considered, then because $\Delta = 0$ at k_n, the first term in (4.1) becomes undefined (0/0), and the finite limit at 0 exists.

The steady-state solutions for the foundation motion and the relative motion for different combinations of ratios $\frac{M_b}{M_s}$, $\frac{M_0}{M_s}$ (explained in Section 3.3) and $\varepsilon = \frac{\beta_s H_b}{\beta_b a}$ are given. M_b and M_0 are the masses of the building and the foundation per unit length, and M_s is the mass of the soil occupying the volume of the foundation, also per unit length. β_s and β_b are the shear wave velocities of propagation in the soil and in the building, respectively, H_b is the height of the building, and a is the radius of the semicircular foundation. ε is a dimensionless parameter.

4.2 Numerical example

4.2.1 Input and grid parameters

Using the model described in Chapters II and III, the steady-state response for the Hollywood Storage building (Duke et al.,1970) is obtained. The model with the geometry and the material properties of the constitutive parts is shown in Fig.4.1.

Fig. 4.1 MODEL: HOLLYWOOD STORAGE BUILDING

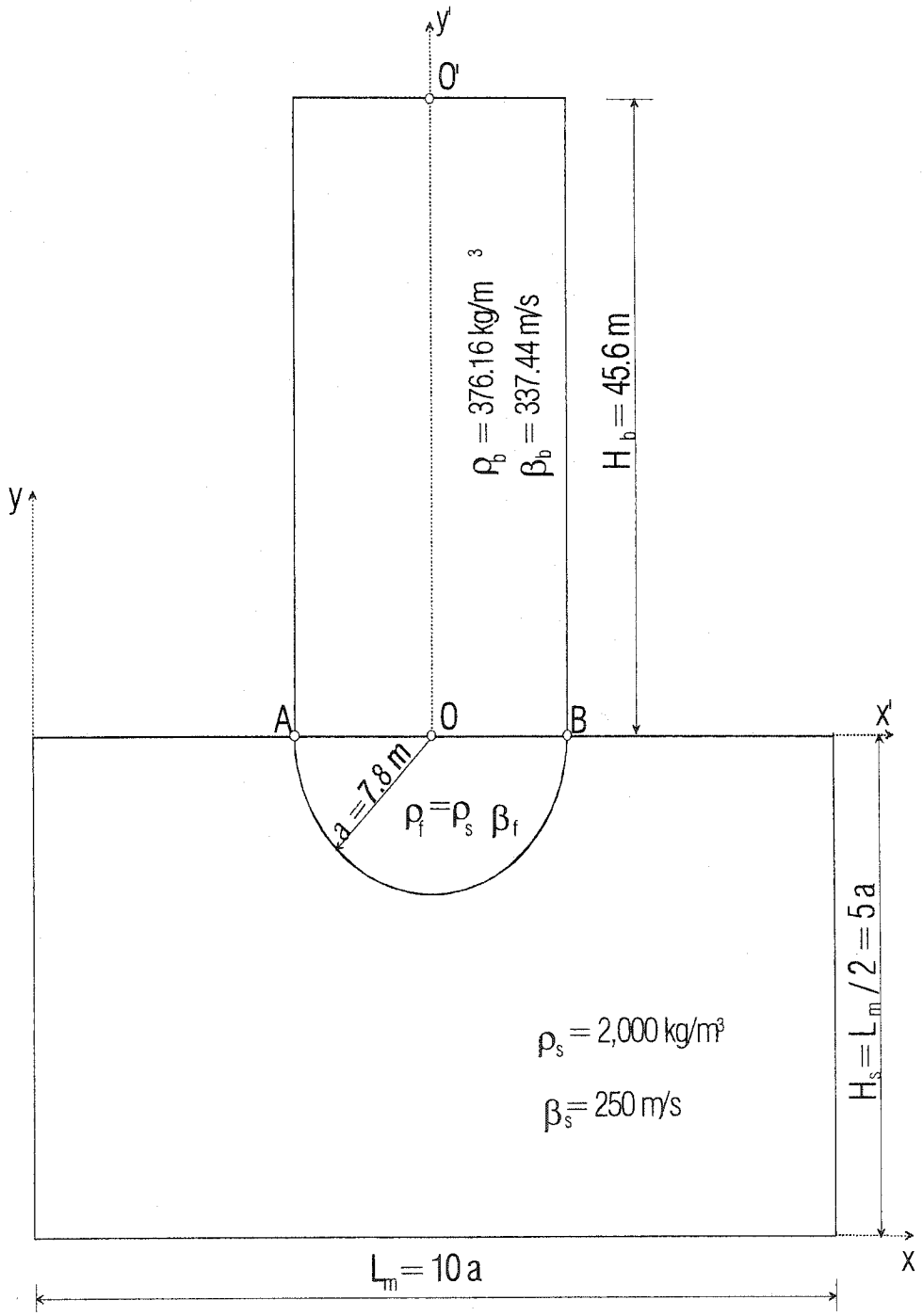

Recalling the algorithm presented in Chapter III, the half-space analytical solution must be computed for every time step on the curves $\Gamma_1 = \overline{ab} \cup \overline{bc} \cup \overline{cd}$ and $\Gamma_2 = \overline{lk} \cup \overline{kj} \cup ji$ (Fig.2.2, Fig.3.4). The excitation is a monochromatic sinusoidal plane wave of the form:

$$u(x_i, y_j, t) = A[\sin(\Omega(t - t_1))H(t - t_1) + \sin(\Omega(t - t_2))H(t - t_2)] \quad \forall(x_i, y_j) \in \Gamma_1, \forall(x_i, y_j) \in \Gamma_2, \tag{4.2}$$

where:

$A = 0.5m$ is amplitude of the wave,

$t_1 = \frac{x_i \sin\gamma}{\beta} + \frac{y_j \cos\gamma}{\beta}$ is travel time of the wave from the origin (point f in Fig.2.2) to the considered point,

$t_2 = \frac{x_i \sin\gamma}{\beta} + \frac{(H_s + y_j)\cos\gamma}{\beta}$ is travel time of the wave from the origin to the free surface and from the free surface to the considered point,

γ is the angle of incidence, and

H() is the Heaviside function.

The natural frequencies of the fixed-base building for the elastic modes in the y direction are:

$$f_n = \frac{(2n-1)\beta}{4H_b} \ (\text{Hz}) \quad \text{n} = 1,2,3,\ldots \ . \tag{4.3}$$

The first three natural frequencies in the y direction are $f_{0,1} = 1.85\,Hz$, $f_{0,2} = 5.55\,Hz$, and $f_{0,3} = 9.25\,Hz$.

The modes in the x direction represent the torsional response of the structure. From the solution of the linear wave equation and the boundary condition in the x direction, the

characteristic numbers in the x direction are $k_{xm} = \frac{m\pi}{L_b}$ (m = 0,1,2,...) with corresponding angular natural frequencies $\omega_m = k_{xm}\beta_b$. The lowest elastic mode m = 1 (m = 0 corresponds to rigid mode) has natural frequency $\omega_{1,0} = 21.63 \cdot \pi$. The first subscript in the natural frequencies denotes the number of the mode (including the rigid-body mode 0) in the x direction, and the second one, the number of the mode in the y direction.

The analysis is performed for the frequency range of the input motion $0.5\,Hz \le \Omega \le 6.0\,Hz$, the amplitude A = 0.5 m, and for incident angles $\gamma = 30^0$ and $\gamma = 60^0$. The minimum wavelength is $\lambda_{\min} = \lambda_{\Omega=6Hz} = \frac{2\pi\beta_s}{12\pi} \approx 42\,m > L_b = 2a = 15.6\,m$, and so Δx is chosen from the criterion for proper modeling of the foundation (Fig.2.3):

$$\left(m_f\right)_{\min} = 12 = \frac{L_b}{\Delta x_{\max}} \Rightarrow \Delta x_{\max} = \frac{L_b}{12}.$$

The vertical spacing for the finite difference grid in the building is obtained as $\Delta y_b = \frac{\beta_b}{\beta_s} \cdot \Delta x$. The effective horizontal and vertical spacing for the cells B (Fig.2.4) is $\Delta x^B = \Delta y^B = \frac{\Delta x}{\sqrt{2}}$. The time step is then obtained from (2.1) as

$$\Delta t = \left(\frac{\chi}{\left(\beta_{i,j} \sqrt{\frac{1}{\Delta x_i^2} + \frac{1}{\Delta y_j^2}} \right)_{\forall(i,j)}} \right)_{\min} \qquad (4.4)$$

and for the given properties the point B' (Fig. 2.4) has the biggest denominator and the smallest Δt. The artificial boundary is located at $H_s = \frac{L_m}{2} = 5a$.

With the above parameters our model is completely defined.

4.2.2 Results

We generate motion in the system by using $u(x_i, y_j, t)$ as given by the equation (4.2). A point is in rest until the wave arrives, and then experiences a sudden change in velocity from 0 to $A\Omega$. The situation is similar at all of the points in the model. The transition of the regime from rest to harmonic steady state is present in the first phase of the analysis (Fig.4.1a) until the transients go out of the system. For our numerical example, the steady-state regime for any frequency is established after 7 - 8 s from the beginning of the analysis, when the amplitudes of the motion become constant. In Fig. 4.1a, the time histories of the displacement at point O are shown for several input frequencies for the stiffer foundation $\beta_f = 500\, m/s$ and for the angle of incidence $\gamma = 30^0$.

In Figures 4.2 to 4.5, the dynamic amplification factor versus input frequency is shown for three points on the foundation-structure contact (Fig. 4.1) for angles of incidence $\gamma = 30^0$ and $\gamma = 60^0$, and for foundation stiffnesses $\beta_f = 300\, m/s$ and $\beta_f = 500\, m/s$. For comparison, amplitude Δ plots for the rigid foundation are also shown.

Fig. 4.1a TIME HISTORY OF THE DISPLACEMENT AT POINT O FOR SOME FREQUENCIES $\beta_f = 500$ m/s, $\gamma = 30^o$

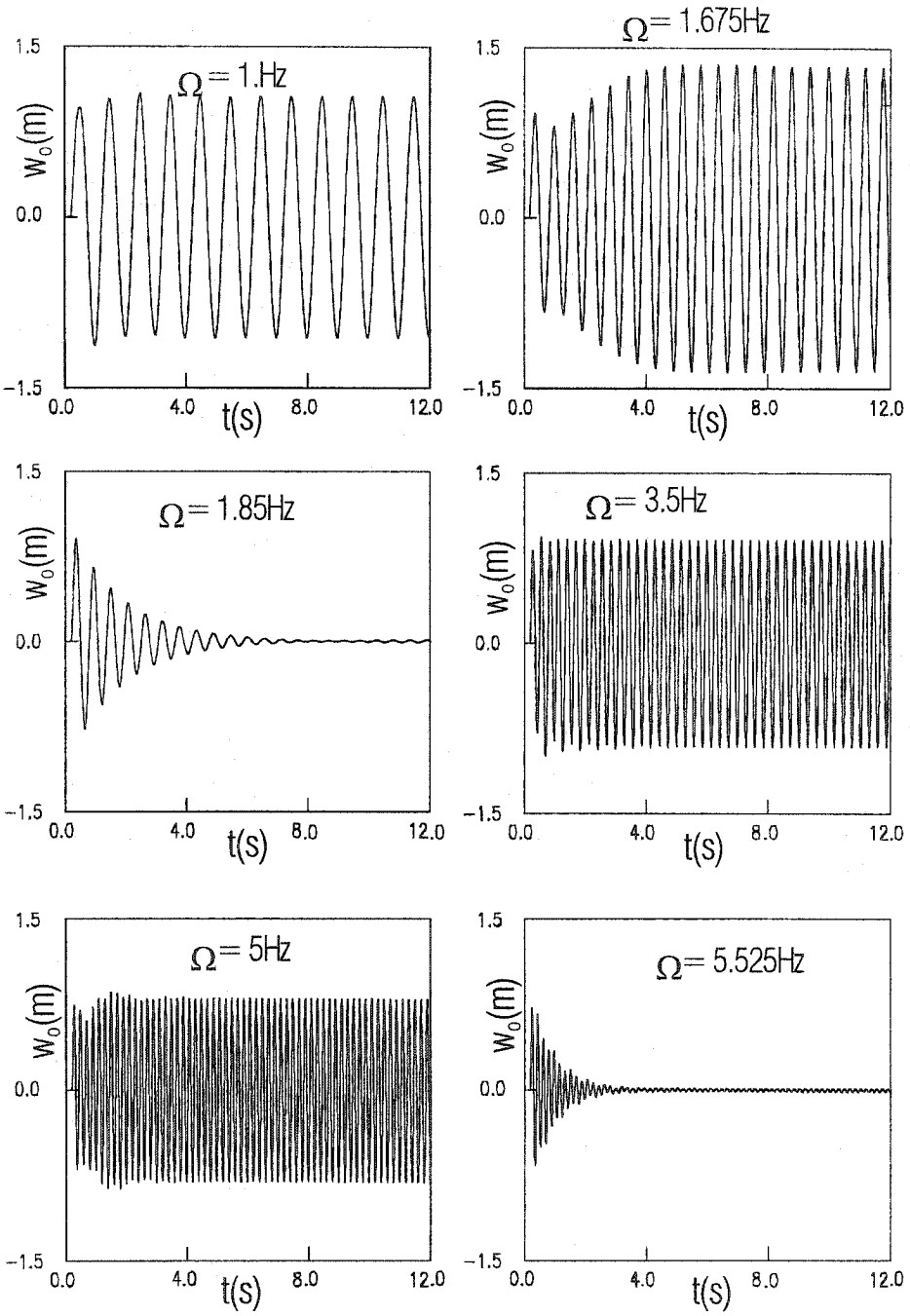

Fig. 4.2 RESPONSE AT THE BUILDING - FOUNDATION CONTACT NORMALIZED BY FREE SURFACE RESPONSE

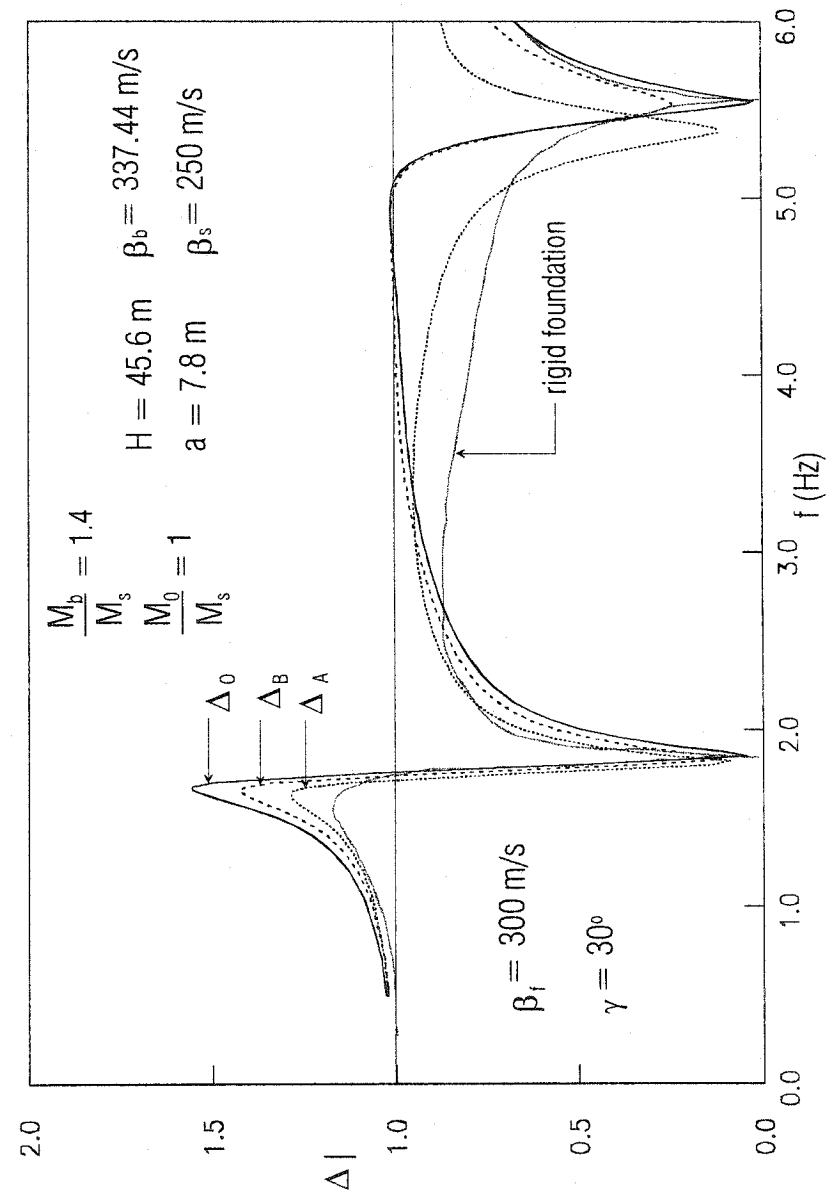

Fig. 4.3 RESPONSE AT THE BUILDING - FOUNDATION CONTACT NORMALIZED BY FREE SURFACE RESPONSE

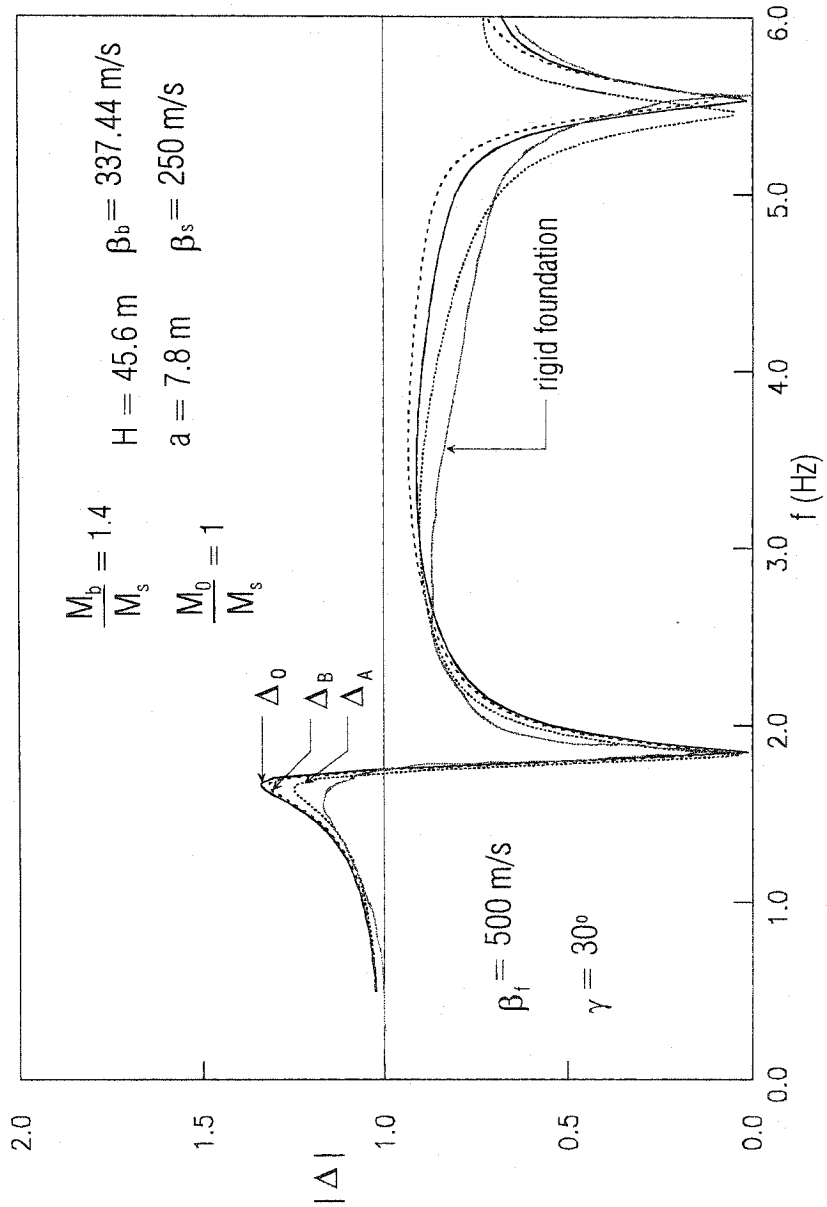

Fig. 4.4 RESPONSE AT THE BUILDING - FOUNDATION CONTACT
NORMALIZED BY FREE SURFACE RESPONSE

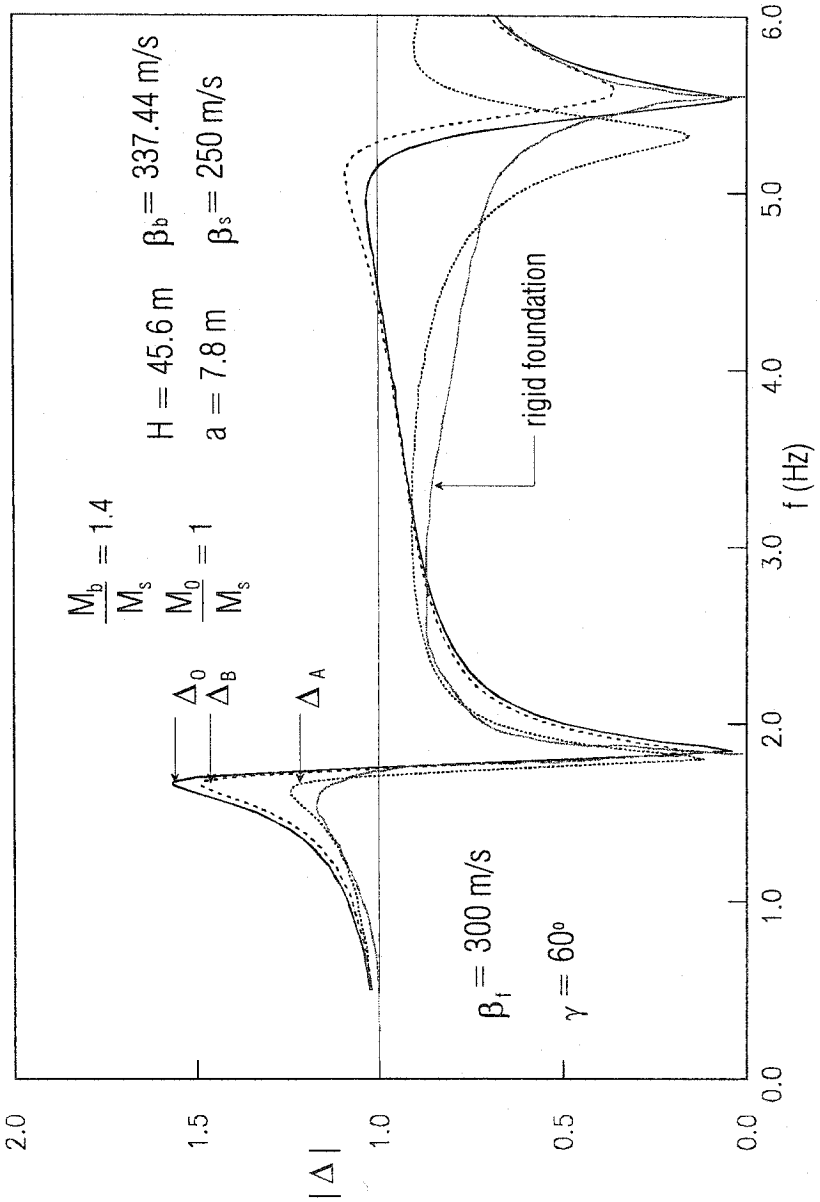

Fig. 4.5 RESPONSE AT THE BUILDING - FOUNDATION CONTACT
NORMALIZED BY FREE SURFACE RESPONSE

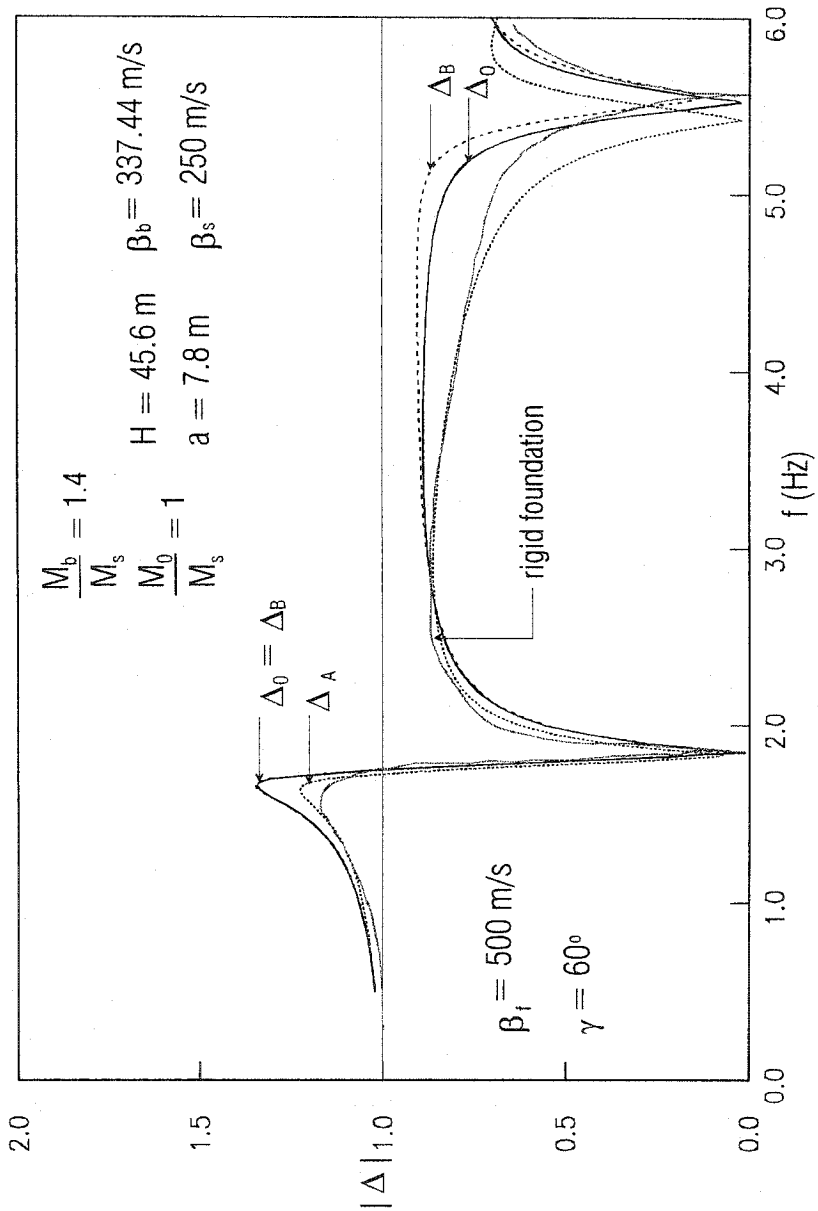

For all cases, at small frequencies, the amplitudes of all three points (A, O, B) are the same and approach 1 as f approaches 0. This can be explained by the fact that for an input wave much longer than the foundation dimension and of such small frequency that the inertial forces become negligible the whole system just rides on the wave and the effect of the interaction is negligible. Relative displacements are negligible in this frequency interval (Fig.4.6).

As the input wavelength becomes smaller, and as the input frequency approaches the natural frequency of the building, the amplitudes at the three different contact points begin to differ. This difference is partially caused by the horizontal wave passage through the foundation (differential motion as discussed in Trifunac & Todorovska, 1997), which causes a torsional response by the foundation, and partially by the soil-structure interaction. The smaller the incident angle, the larger is the relative contribution of the soil-structure interaction to the response, and the larger the incident angle, the larger is the relative contribution of the wave passage. In extreme cases, when the incident angle $\gamma = 0$ there is no effect of the differential motion, and when the incident angle $\gamma = \frac{\pi}{2}$ the effect of wave passage is most prominent.

Fig. 4.6 RELATIVE RESPONSE

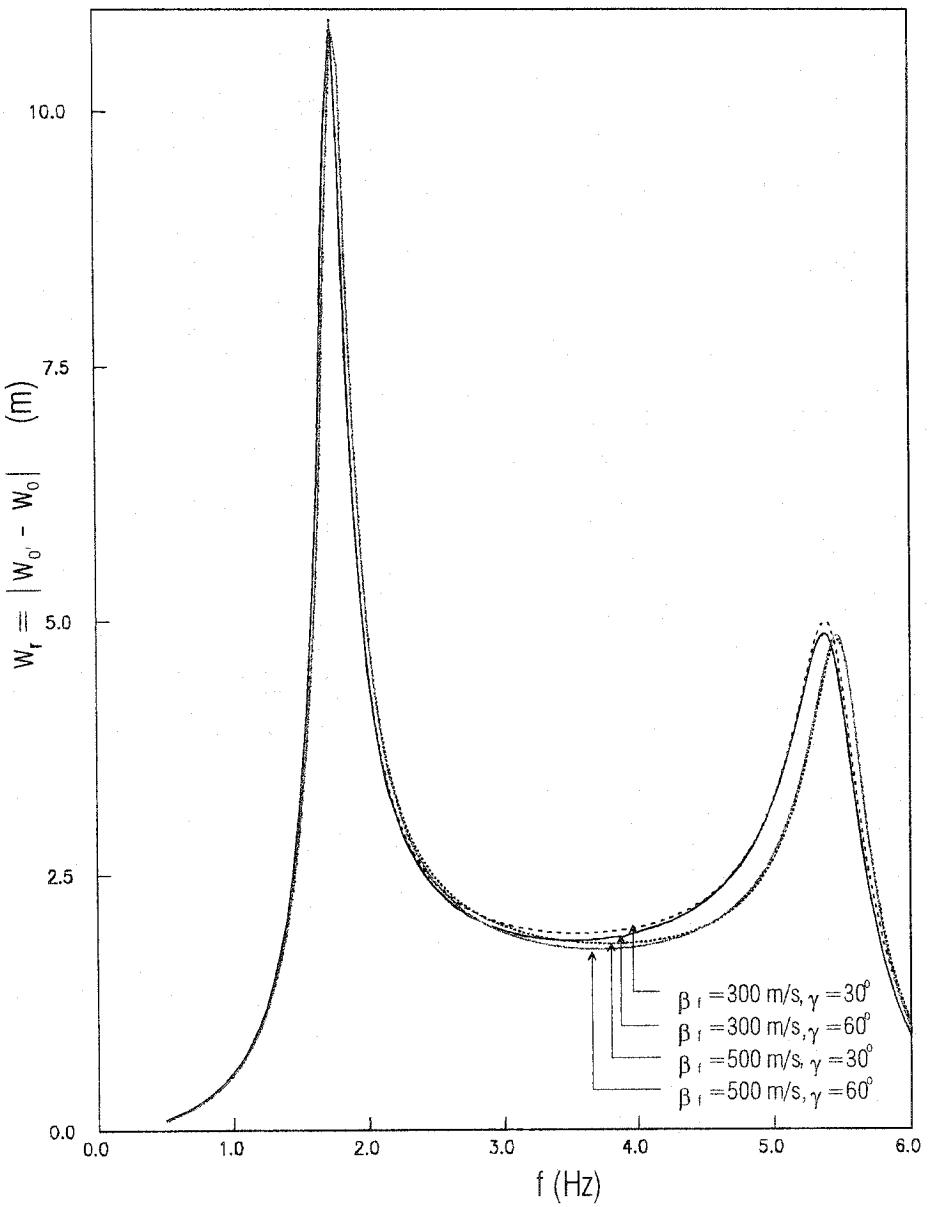

From the plots in Fig. 4.2 to 4.5 it can be seen that for the same angle of incidence, and for the softer foundation, there is bigger difference between the motions of the left and right ends of the building. Also, for the same foundation stiffness, the difference between the motions at A and B is larger for the larger angle of incidence. The first observation results from the fact that as the foundation is stiffer it resists the incident wave deformations more, and the solution is closer to the solution for the rigid foundation. The second observation comes from the fact that the phase wavelength in the horizontal direction $\lambda_x = c_x T = \frac{\beta_s}{\sin\gamma} T$ is smaller for the larger incidence angle γ and for smaller wavelengths the differential motions are more pronounced.

In this frequency range, where the frequencies of the input motion are smaller than the smallest natural frequency of the building, the response of the model can be seen as a response of the half space, with the building as an added mass. If the building and foundation did not exist, the soil could be considered as an equivalent single-degree-of-freedom oscillator (SDOF) with mass m_s and stiffness k_s, which under the steady-state excitation oscillates with an amplitude equal to one. The forces resisting the motion of undamped SDOF are the inertial (d'Alambert force), F_{sI}, and the elastic, F_{sE}, forces, which at any time have the same direction. The total force resisting the motion for this "oscillator" can be written as $F_s = F_I + F_e$.

Fig. 4.7a THE EFFECT OF THE BUILDING AS ADDED MASS TO THE HALF SPACE

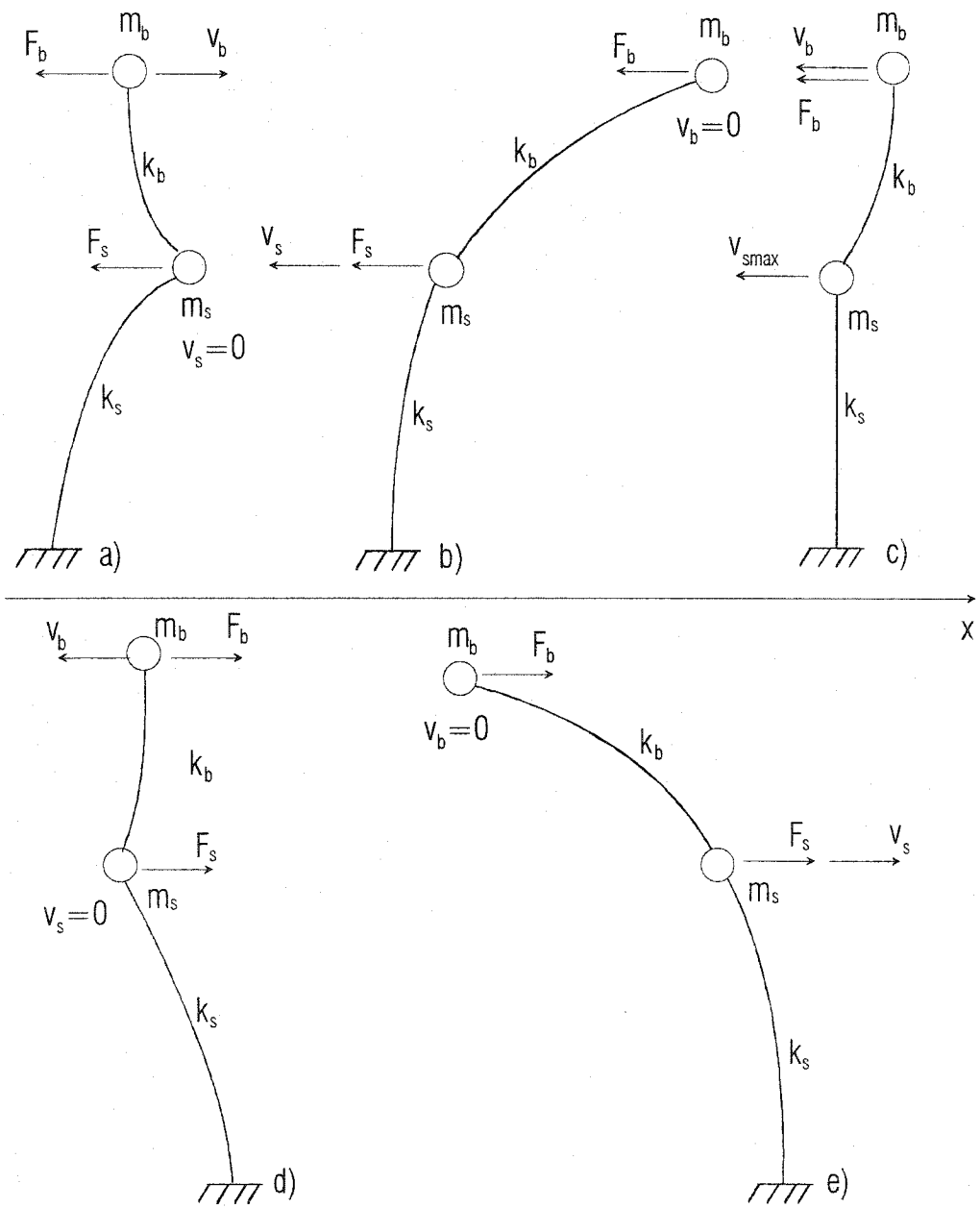

Fig. 4.7b TIME HISTORIES OF DISPLACEMENTS, VELOCITIES, AND ACCELERATIONS AT THE TOP AND BOTTOM OF THE BUILDING

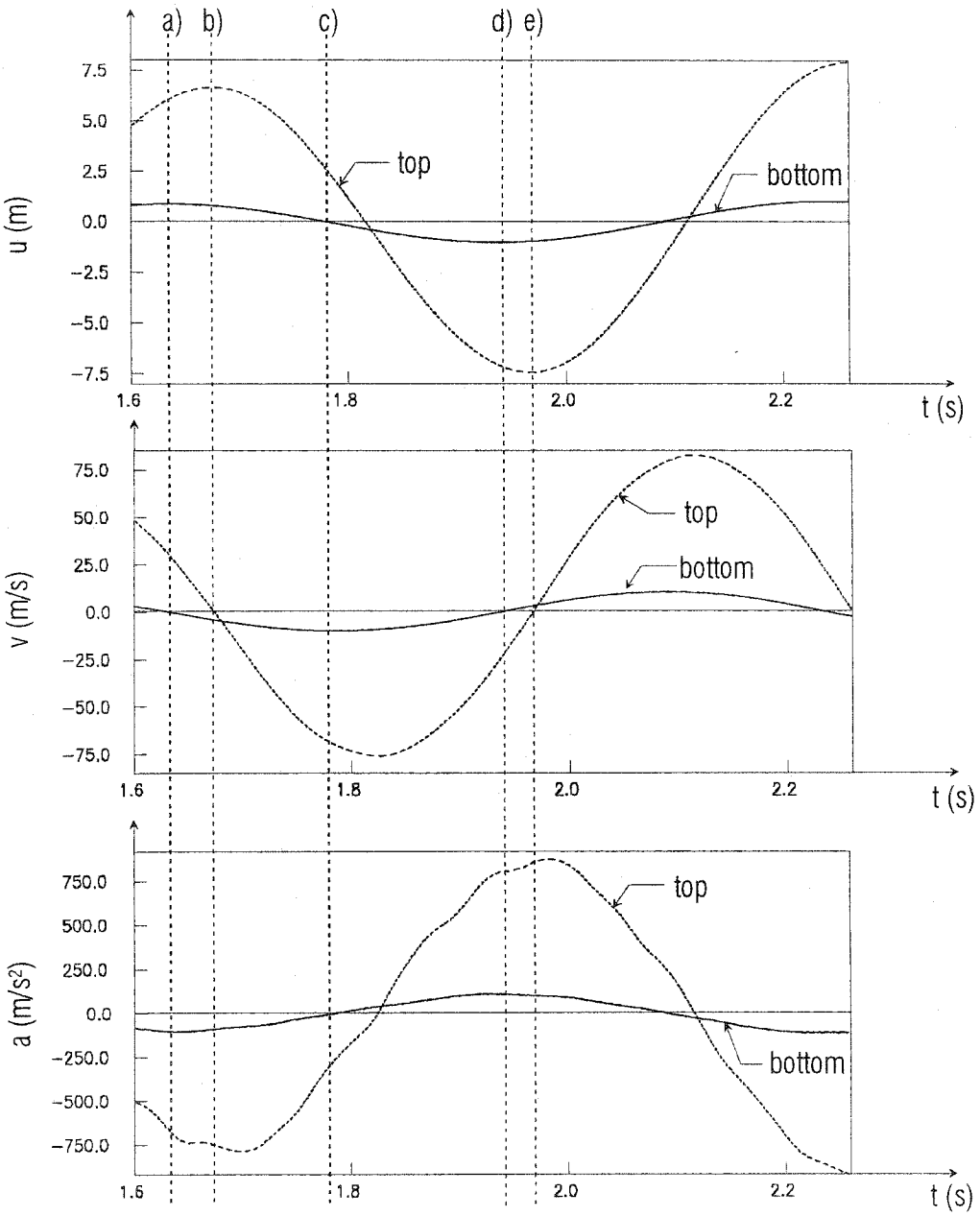

If we consider the system with a building placed on the soil, the equivalent system becomes a two-degree-of-freedom oscillator (TDOF), as shown in Fig. 4.7a, with the building represented by the top oscillator with mass m_b and stiffness k_b, and corresponding forces $F_b = F_{bI} + F_{bE}$, where F_{bI} is the inertial force and F_{bE} is the elastic force in the building. Because the frequency of the input motion is lower than the fundamental frequency of the building, the deformation in the building is small and so is the elastic force F_{bE} with respect to the inertial force F_{bI} and the elastic force of the half space F_{sE}. In Fig.4.7a, five early stages of the system excited by harmonic motion for $t \geq 0$ are shown, when the steady-state regime is still not established. The Fig.4.7a is supplemented by Fig.4.7b, where the time histories of the displacements, velocities, and accelerations in the points O (at the building-foundation contact) and O'(at the top of the building) (see Fig.4.1) are shown between the third and fourth positive peaks when the steady-state regime is still not established.

If the soil is rigid, there is no interaction, and the system frequency is equal to the frequency of the building. Because of the finite stiffness of the soil, the system frequency is always smaller than the fundamental frequency of the building. In our example, the system natural frequency is $\Omega_{sys} \approx 1.675\ Hz$. The amplitudes for all cases and for all three points are the largest for this frequency.

In Fig. 4.6, this frequency range is characterized with rapid growth of the relative displacement. The displacements for $\gamma = 30^0$ and for the peak frequency $\Omega_{sys} \approx 1.675\ Hz$ are shown in the second plots in Fig. 4.8a,b for $\beta_f = 300\ m/s$ and $\beta_f = 500\ m/s$

Fig. 4.8a DISPLACEMENT FOR SOME CHARACTERISTIC FREQUENCIES $\beta_i = 300$ m/s, $\gamma = 30^{\circ}$

Fig. 4.8b DISPLACEMENT FOR SOME CHARACTERISTIC FREQUENCIES $\beta_t = 500$ m/s, $\gamma = 30°$

Fig. 4.8c DISPLACEMENT FOR SOME CHARACTERISTIC FREQUENCIES $\beta_f = 300$ m/s, $\gamma = 60^\circ$

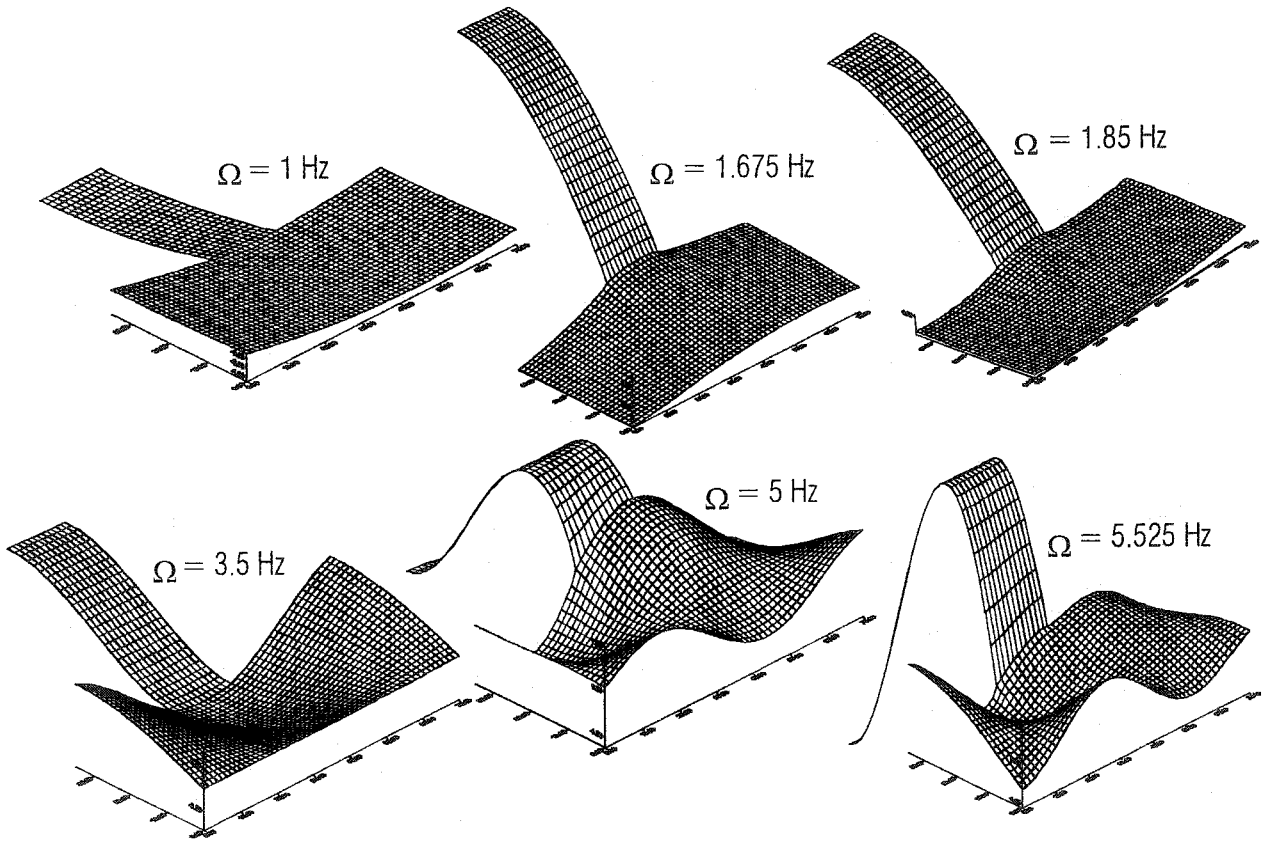

Fig. 4.8d DISPLACEMENT FOR SOME CHARACTERISTIC FREQUENCIES $\beta_t = 500$ m/s, $\gamma = 60°$

respectively. The displacements for the same frequency and $\gamma = 60^0$ are shown in the second plots in Fig. 4.8c,d for $\beta_f = 300\,m/s$ and $\beta_f = 500\,m/s$ respectively.

After reaching the maximum values near 1.68 Hz, all three curves decrease. At the fundamental frequency of a building on a fixed base, the amplitude at the middle point O approaches zero for a rigid foundation, while the ends have small, nonzero values larger and more separated for a softer foundation and for angle $\gamma = 60^0$. The relative response of the building (Fig. 4.6, Table 1) is the largest for frequencies between the frequency at which the maximum foundation motion occurs and the fundamental frequency of the building on its fixed base, for all cases.

Immediately after the natural frequency of the building, and approximately until the curve for the rigid foundation reaches its second maximum, it seems that for all cases the flexibility of the foundation acts like a damper and that the amplitude of the rigid foundation is larger than the amplitude at the middle point of flexible foundations. Also, in this frequency range only the amplitude of the left end is larger than the amplitudes in the center and at the right end. This is more pronounced for a flexible foundation and for the larger γ. For all other frequency ranges, the amplitude at the point O of the flexible foundation is larger than the corresponding amplitude of the rigid foundation.

The frequency range between the two natural frequencies of the building $(2.5\,Hz \le f \le 5\,Hz)$ for $\beta_f = 500\,m/s$, is characterized by fairly flat displacements for the points O and B, while the curve for point A follows more closely the curve for the rigid

foundation. This is especially pronounced for $\gamma = 60^0$, which suggests that the center of torsion is closer to point A. For the softer foundation, the amplitudes of displacements of points O and B increase, while for point A they are approximately flat (i.e., they do not depend upon frequency). In this frequency range, the wavelength range is $100\,m \geq \lambda \geq 50\,m$. The quarter of the wavelength λ_x as an indicator of the differential motion at the surface is in range $\frac{25\,m}{\sin\gamma} \geq \frac{\lambda_x}{4} \geq \frac{12.5\,m}{\sin\gamma}$. The length of the building $L_b = 2a = 15.6\,m$ is either smaller than or close to this range for $\gamma < \sin^{-1}\frac{12.5}{15.6} \approx 53^0$, or it is in the range for $\gamma \geq \sin^{-1}\frac{12.5}{15.6} \approx 53^0$. The foundation experiences substantial differential motion and strong torsional excitation, while the effect of interaction is smaller because the natural periods of the building and of the system are outside this range (Fig.4.6). This explains why the right end of the building (point B) has large amplitudes and why the difference in the displacements for the right and left ends is the largest in this interval. Such trends are more pronounced for larger γ when the wavelength of incident motion λ_x is smaller.

The effect of the differential motion, if the foundation has the same properties as the soil, is the largest when $\frac{\lambda_x}{4} = L_b = 15.6\,m$ or

$$\lambda_x = c_x^s \cdot T = \frac{\beta_s}{\sin\gamma} \cdot \frac{1}{f} = 62.4\,m \qquad (4.5)$$

(c_x^s is the phase velocity in the soil, and T is the period of the input motion), which

corresponds to the frequency of the input motion

$$f = \frac{\beta_s}{62.4 \cdot \sin\gamma}. \qquad (4.6)$$

For incident angle $\gamma = 60^0$, $f = 4.63\,Hz$ and for $\gamma = 30^0$ the frequency f is larger and is not in the considered frequency range.

Because of the presence of the foundation, which is stiffer than the soil, there is scattering of the incoming wave from the soil-foundation contact (more scattering for higher input frequencies). Also, because of the larger wave velocity in the foundation, the phase wavelength is longer than that computed in equation (4.5). Finally, the effect of the building as added mass increases the motion at the building-foundation contact. While for small input frequencies (smaller than the first natural frequency of the building) the effect of the building as an added mass is dominant compared with the effects of scattering from the foundation and the differential motion, in this frequency range $(2.5\,Hz \le f \le 5\,Hz)$, the effects of the scattering and of the differential motion are substantial in the response of the building-foundation contact due to higher input frequency and smaller phase wavelength λ_x relative to the length of the building L_b. For stiffer foundations (Figures 4.3 and 4.5), the effect of the scattering from the soil-foundation contact, which decreases the amplitudes of the motion at the building-foundation contact, is larger than the same effect for the softer foundation. Also, because of the larger velocity of propagation in the foundation, the effect of the differential motion at the building-foundation contact is smaller for a stiffer foundation. The outcome of these two facts is the absence of peak amplitude in Figures 4.3 and 4.5 in this frequency range.

For the softer foundation, the effect of the scattering from the soil-foundation contact is smaller due to smaller difference in impedances between the soil and the foundation. Also, the effect of the differential motion at the building-foundation contact is stronger due to smaller phase wavelength λ_x (smaller β_f). The sum of the effects of the building as an added mass and the differential motion on the building-foundation contact is stronger than the effect of the scattering at the end of the considered frequency range. The outcome is the appearance of peak amplitudes of the displacement at points O and B (larger than 1) for input frequencies close to the end of the considered frequency range (Figures 4.2 and 4.4). These peak amplitudes are larger for larger angles of incidence because of the stronger effect of the differential motion (Eq. 4.5 and 4.6).

The above trends can be seen in the plots of the motion of the model in Figures 4.8a,b,c,d for $\Omega = 3.5\,Hz$ (approximately where all curves meet) and at $\Omega = 5\,Hz$ (where the effect of the torsion is most pronounced in this frequency range). Reaching the second natural frequency, the displacement at the middle point of the building-foundation interface approaches zero, while the displacements of the end points are not zero (the right end has bigger amplitudes), which is the consequence of torsional excitation.

Finally, Table 1 provides the extreme values of the foundation motion, the relative response, and their frequencies for the middle point O on the contact between the building and the foundation.

TABLE 1. MAXIMA OF FOUNDATION DISPLACEMENT AND RELATIVE DISPLACEMENT

β_f (m/s)	γ (^{0})	$\Omega(\Delta_{max})$ (Hz)	Δ_{max}	$\Omega(w_{r\,max})$ (Hz)	$w_{r\,max}$ (m)
300	30	1.675	1.554	1.75	10.89
500	30	1.675	1.338	1.75	10.84
300	60	1.675	1.562	1.75	10.90
500	60	1.675	1.346	1.75	10.86

4.3 Conclusions

From the above analysis, it can be seen that most of the general trends for the rigid foundation also hold for the flexible foundation, except the one that the foundation motion does not depend upon the incident angle. The reason for this difference is the dependence of the response on the wave passage through the foundation and the generated differential motions in the foundation-building contact.

For a flexible foundation, the amplitudes Δ are larger except in the narrow frequency range immediately after the natural frequencies of the building on a fixed base. This increase is mostly due to the fact that the rigid foundation scatters more of the incident energy and so the radiation damping caused by scattering is larger. This means that the equivalent single-degree-

of-freedom oscillator (SDOF) has a larger damping ratio ζ for the system with a stiffer foundation.

To find the damping ratio of the SDOF, the system is loaded with a transient half-sine pulse as an input displacement function. The duration of the pulse is chosen so that the frequency of the input motion is close to the system frequency $\Omega_{sys} \approx 1.675\,Hz$, where the differences between the amplitudes for different combinations of foundation stiffness β_f and incident angles γ are the largest. The amplitude of the pulse is A = 0.5 m, and its dimensionless frequency is

$$\eta = \frac{2a}{\lambda} = \frac{a\omega}{\pi\beta_s}, \tag{4.7}$$

where a is the radius of the foundation, β_s is the shear wave velocity in the soil, and ω is the frequency of the ground motion. For $\omega = 1.6\,Hz \approx \Omega_{sys}$, from (4.7) $\eta = 0.1$. The procedure for numerical computation is explained in the next Chapter V. The time histories of the motion for points O and O' (see Fig. 4.1) are illustrated in Fig. 4.9 with solid and dashed lines, respectively, for the combinations of incident angles γ and foundation stiffnesses β_f corresponding to those presented in Figures 4.2 to 4.5.

The first peaks in the building that depend upon the scattering of the incident wave from the foundation, for different cases of foundation stiffness and angles of incidence, are as follows:

1. $\beta_f = 300\,m/s$, $\gamma = 30^0$ $\qquad u_{o'\max} = 1.8528\,m$

2. $\beta_f = 300\,m/s$, $\gamma = 60^0$ $\qquad u_{o'\max} = 1.8408\,m$

3. $\beta_f = 500\,m/s$, $\gamma = 30^0$ $\qquad u_{o'\max} = 1.8398\,m$

4. $\beta_f = 500\,m/s$, $\gamma = 60^0$ $\qquad u_{o'\max} = 1.8340\,m$.

The scattering from the foundation is larger for a stiffer foundation (smaller amplitudes in the building), but the variation is small for this example. Also, the scattering is slightly stronger for a larger incident angle. The ratios $\frac{u_{o'}^{i}}{u_{o'}^{i+1}}$ (the superscript denotes the ordered number of the positive amplitudes i=1,2,3,...) for the first case (in which the analysis lasted for 8 s) are:

$\frac{u_{o'}^{1}}{u_{o'}^{2}} = \frac{1.8528}{1.3851} = 1.338$ and further (for i=2,3,...10)

R= $\frac{u_{o'}^{i}}{u_{o'}^{i+1}}$ =1.377; 1.395; 1.411; 1.421; 1.415; 1.407; 1.405; 1.413; 1.408 .

It can be seen that for the first three periods the ratio changes due to reflection of the pulse from the building-foundation contact back into the building. After the fourth period, the ratio of the consecutive amplitudes becomes fairly constant. In Fig. 4.9, we illustrate eight positive peaks, so we can find seven amplitude ratios. The last three ratios (fifth, sixth, and seventh) and their average values for all of the cases above are:

1. $\beta_f = 300\,m/s$, $\gamma = 30^0$ $\qquad R_5 = 1.421$, $R_6 = 1.415$, $R_7 = 1.407$ $\qquad R^{(1)} = 1.414$

2. $\beta_f = 300\,m/s$, $\gamma = 60^0$ $\qquad R_5 = 1.412$, $R_6 = 1.423$, $R_7 = 1.414$ $\qquad R^{(2)} = 1.416$

3. $\beta_f = 500\,m/s$, $\gamma = 30^0$ $R_5 = 1.428$, $R_6 = 1.439$, $R_7 = 1.428$ $R^{(3)} = 1.432$

4. $\beta_f = 500\,m/s$, $\gamma = 60^0$ $R_5 = 1.429$, $R_6 = 1.439$, $R_7 = 1.423$ $R^{(4)} = 1.430$.

The corresponding damping ratios $\zeta = \frac{\delta}{2\pi}$ ($\delta = \ln R$ is a logarithmic decrement) of the equivalent single-degree-of-freedom oscillator are

$\zeta_1 = 0.055$; $\zeta_2 = 0.055$; $\zeta_3 = 0.057$; $\zeta_4 = 0.057$.

We can conclude that the stiffer foundation radiates the energy faster and that the radiation does not depend upon the incident angle. In Chapter III, from the diagram of the instantaneous energy in the building, we found that the damping ratio is roughly $\zeta_{HSB} = 0.059$. The ratio obtained here is more precise because the flat parts of the curve representing the instantaneous energy in the building in terms of time are not ideally flat.

As the foundation becomes more flexible, more of the incident energy is transmitted from the soil to the foundation, which causes larger amplitudes of displacement of the foundation. Also, the larger amplitudes in a flexible foundation are the consequence of the presence of the elastic forces generated in the flexible foundation and in the contact points by the wave passage, both of which do not contribute in a rigid foundation. At low frequencies, the elastic forces are negligible and the differences in the foundation motion for different angles of incidence and the same foundation stiffness are negligible. As the frequencies become higher, after the first natural fixed-base frequency, the dependence of the foundation motion on the incident angle is more pronounced.

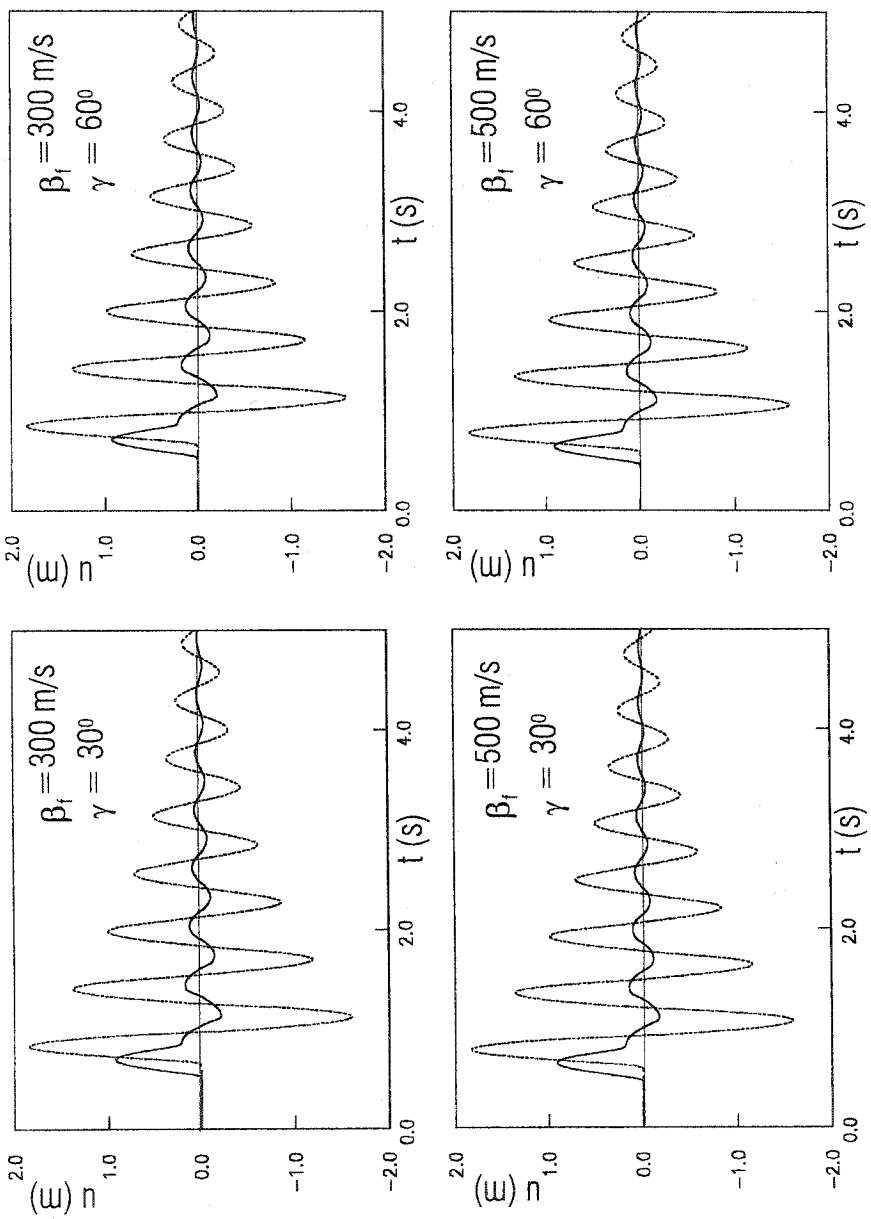

Fig. 4.9 TIME HISTORIES OF THE RESPONSE TO THE HALF-SINE PULSE AT O (SOLID LINE) AND AT O' (DASHED LINE)

The dependence of the foundation motion on the foundation stiffness is obvious at all frequencies. As the foundation becomes stiffer, the amplitudes of the center (O) and end contact points (A and B) become closer and converge to the amplitudes of the rigid foundation.

As given in Table 1, the maximum amplitudes occur at the same frequency for any stiffness and for any incident angle. The peak of the relative response of the building occurs at the system frequency $\Omega(w_{r\max}) \leq \omega_{n0}$ and is relatively independent of the incident angle and foundation stiffness.

CHAPTER V

SOIL-STRUCTURE INTERACTION WITH A FLEXIBLE FOUNDATION: TRANSIENT ANALYSIS

5.0 Introduction. 1-D Model

In the beginning of this chapter we give a brief review of the solution of the linear and nonlinear shear beam sitting on linear soil. This is the simplest model of soil-structure interaction, but it is useful to get some further insight into this phenomenon.

The 1-D model is shown in Figure 5.0a, together with the assumed displacement pulse in the soil. The densities of the soil and of the beam are the same: $\rho_b = \rho_s =$ 2700 kg/m^3. The velocity of propagation of the shear waves in the soil is $\beta_s = 300\, m/s$ and in the building $\beta_b = 100\, m/s$. As pointed out in Dablain (1986), a numerical scheme on the order of accuracy $O(\Delta t^2, \Delta x^2)$ has an exact solution for $\frac{\beta \Delta t}{\Delta x} = 1$, and with the ratio of the spatial interval $\frac{\Delta x_b}{\Delta x_s} = \frac{\beta_b}{\beta_s}$ we can meet this requirement. In the model in Fig. 5.0a, $\Delta x_b = 0.1\, m$ and $\Delta x_s = 0.3\, m$. The prescribed incoming displacement in the soil is in the form of a trapezoidal pulse with the properties given in Fig. 5.0a. The absorbing boundary is the one explained in Fujino and Hakuno (1978) (Fig.5.0b). In Fig. 5.0b, the horizontal axis is time and the vertical axis is space. The column consisting of points 1, 2, 3 represents a time step.

Fig. 5.0a 1-D TEST : MODEL AND LOAD

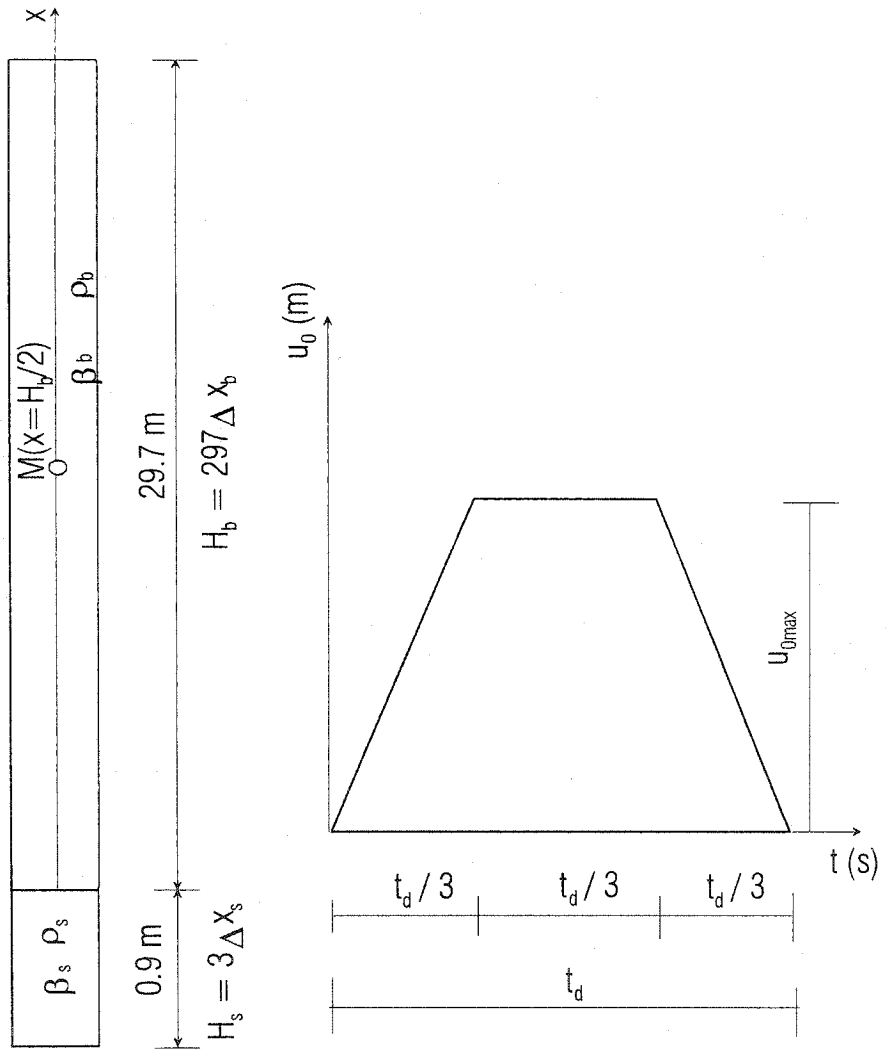

Fig. 5.0b AN ARTIFICIAL BOUNDARY FOR 1-D WAVE PROPAGATION

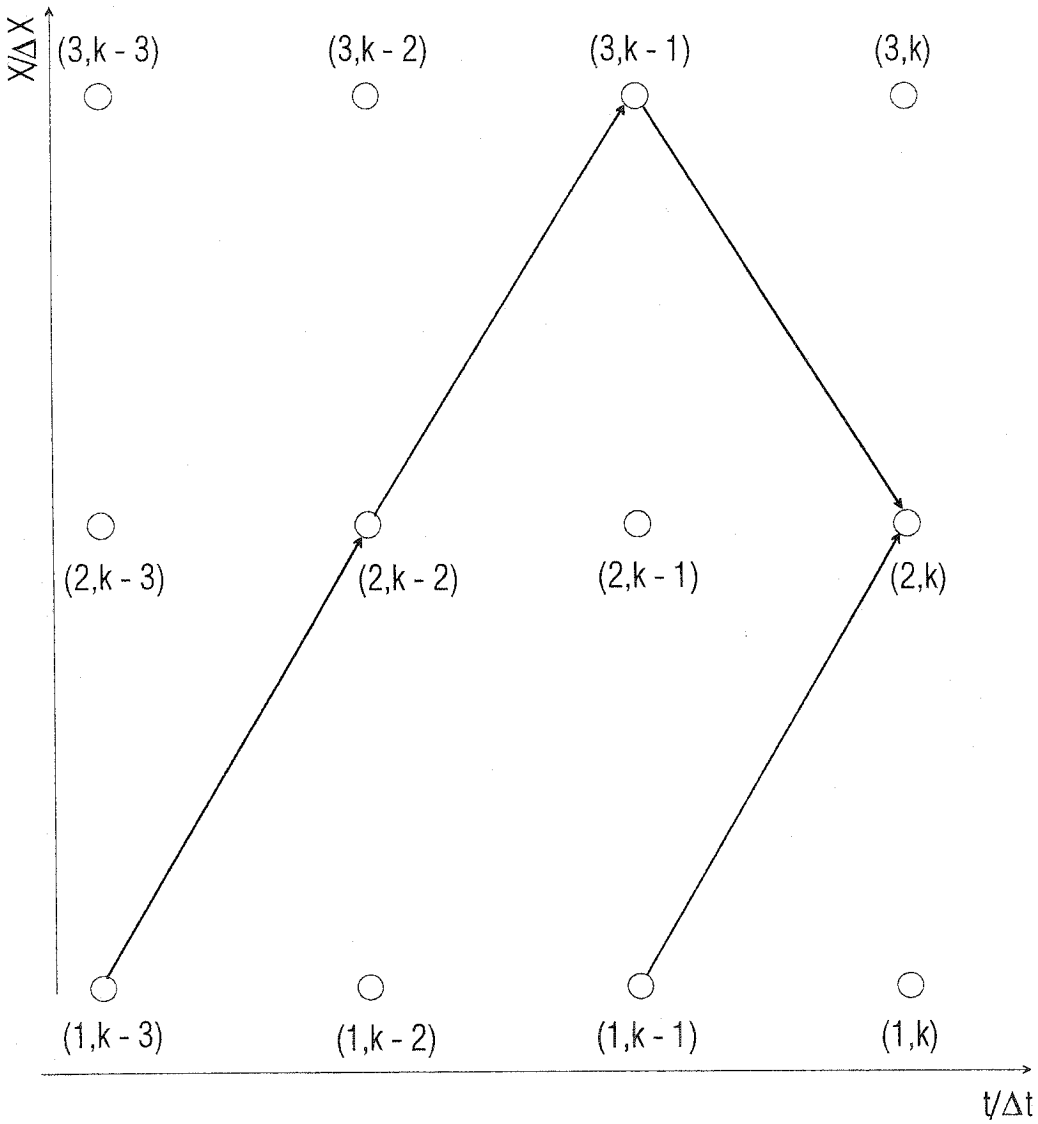

Point 1 is a dummy point where the assumed displacement is applied. We assume that this displacement travels upward in each time step. Point 2 is the boundary point of the model where the quantities of the motion are updated in each time step, as will be shown, and point 3 is the first spatial point where the motion is computed by finite differences.

The motion at each point results from two component motion - from the wave going upward, and the wave going downward. To update the quantity of motion at boundary point 2 in time step k, we proceed as follows. The total motion at 2 is

$$u(2,k) = \uparrow u(2,k) + \downarrow u(2,k), \tag{5.0a}$$

where the arrows denote the direction of the wave propagation ($\uparrow$ upward and $\downarrow$ downward). The motion at point 1 is assumed from the upgoing wave

$u(1, t/\Delta t) = \uparrow u(1, t/\Delta t) = u_0(t/\Delta t)$, then

$$\uparrow u(2,k) = u(1,k-1) = u_0(k-1). \tag{5.0b}$$

The component of motion from the wave traveling downward is

$$\downarrow u(2,k) = \downarrow u(3,k-1). \tag{5.0c}$$

From $u(3,k-1) = \uparrow u(3,k-1) + \downarrow u(3,k-1)$, it follows that

$$\downarrow u(3,k-1) = u(3,k-1) - \uparrow u(3,k-1). \tag{5.0d}$$

The motion at point 3 in time step (k - 1) from the wave traveling upward is the motion at 2 from the wave traveling upward in the previous time step (k - 2). From equation (5.0b), the motion at 2 from the wave traveling upward in time step (k - 2) is the assumed motion in time step (k - 3), so if $\uparrow u(3,k-1) = \uparrow u(2,k-2) = u_0(k-3)$ equation (5.0c) becomes

$$\downarrow u(2,k) = \downarrow u(3,k-1) = u(3,k-1) - u_0(k-3). \qquad (5.0e)$$

Inserting (5.0b) and (5.0e) into (5.0a), the motion at point 2 is

$$u(2,k) = u_0(k-1) + u(3,k-1) - u_0(k-3) \qquad \forall k\,. \qquad (5.0f)$$

Equation (5.0f) is the boundary condition at the artificial boundary point 2, where u stands for velocity, strain or stress in our formulation.

For the linear case, at the contact one part of the incoming wave is transmitted into the other medium and one part is reflected back in the same medium. The corresponding coefficients are obtained from the boundary conditions of continuity of the displacements and stresses at the contact. For a transmitted wave from medium B to medium A, and for a reflected wave from medium B back to medium B, the above coefficients are:

$$k_{trB\to A} = \frac{2}{1+\dfrac{\dfrac{\mu_a}{\beta_a}}{\dfrac{\mu_b}{\beta_b}}} = \frac{2}{1+\dfrac{\rho_a\beta_a}{\rho_b\beta_b}} \qquad (5.0.1)$$

and, similarly,

$$k_{refB\to B} = \frac{1-\dfrac{\rho_a\beta_a}{\rho_b\beta_b}}{1+\dfrac{\rho_a\beta_a}{\rho_b\beta_b}}. \qquad (5.0.2)$$

For the opposite direction of propagation, the numerator and the denominator in the fractions exchange places.

Fig. 5.0c PROPAGATION OF TRAPEZOIDAL PULSE THROUGH SHEAR BEAM

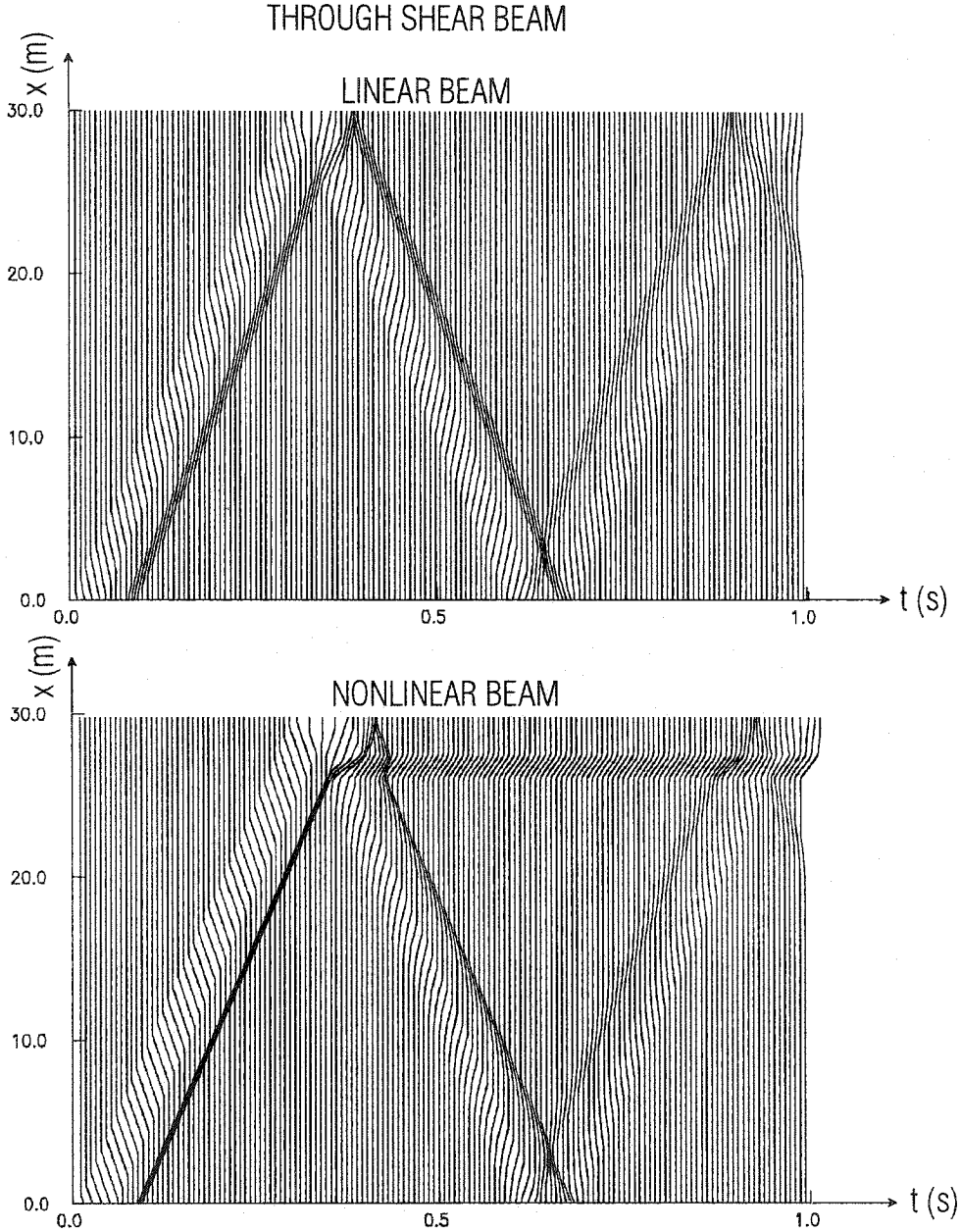

Fig. 5.0d RESPONSE IN THE MIDDLE OF THE 1-D MODEL

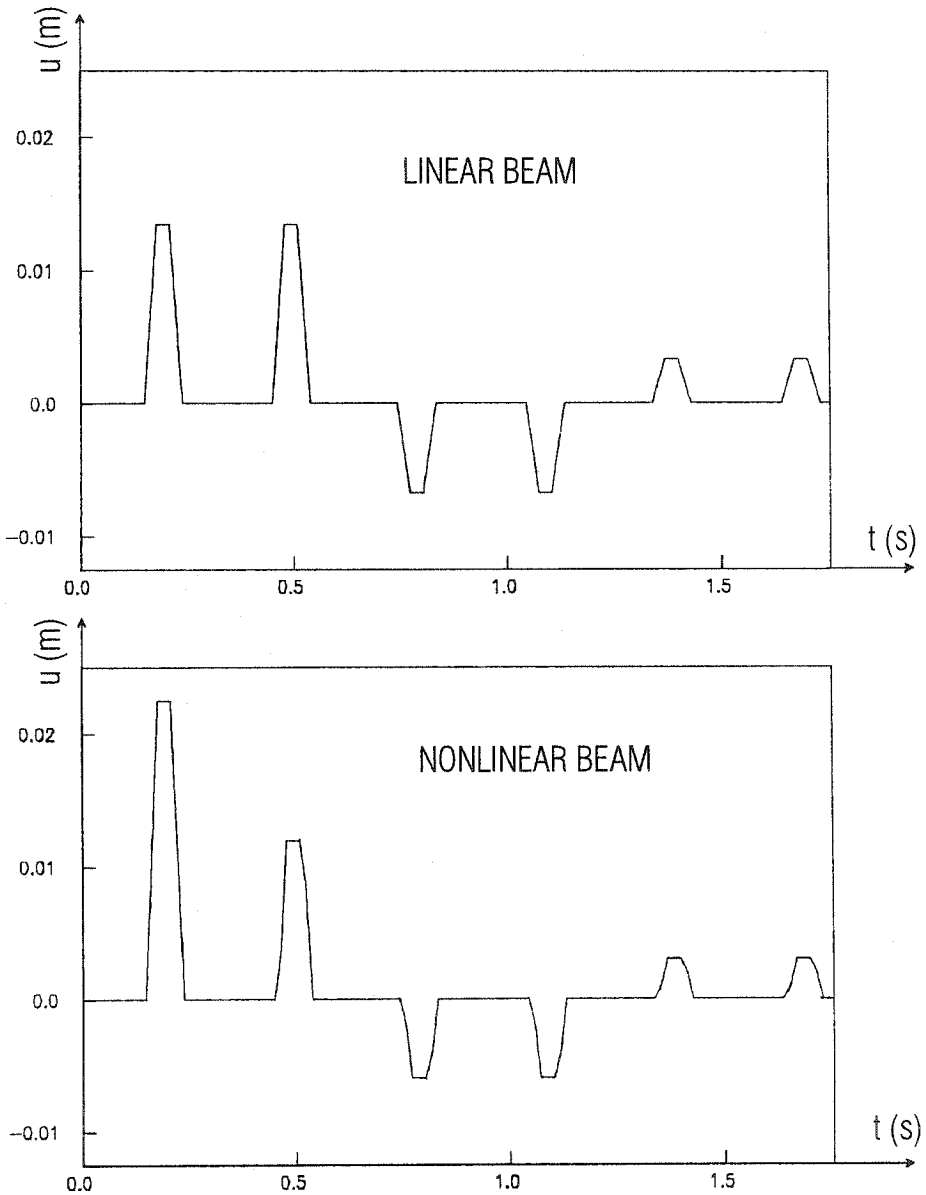

Once the wave enters the beam, there are multiple reflections from the top with no loss of energy in the linear case and multiple reflections and transmissions at the contact with soil with loss of energy (amplitude) computed from (5.0.1), where medium B is the beam and medium A is the soil. For the values given above, the coefficient of the reflected wave in the beam is $k_{refB\to B} = -0.5$, and the coefficient of the transmitted wave into the soil (the loss in the beam) is $k_{trB\to A} = 0.5$. This means that the wave in the beam after reflecting from the contact will have an amplitude equal to half of the wave amplitude before reflection. The wave that entered the beam (transmitted from the soil into the beam with coefficient of transmission $k_{trA\to B} = \frac{3}{2}$) will have amplitude

$$A = (-1)^n k_{trA\to B} u_{0\max} \cdot 2^{-n}. \qquad (5.0.3)$$

In Fig.5.0c the displacement in the beam is plotted for time intervals $\delta t = 0.007s$. The bottom line (x = 0) is the contact between the soil and the beam, while the top of the beam is at x = 29.7 m. The propagation of the pulse is shown in the top plot for a linear beam, and in the bottom plot for a nonlinear beam. It can be seen that the first nonlinear zone occurs close to the top, where the reflected wave from the top meets the incoming wave from bottom.

The solution at point $M(x = 15m)$ is given in Fig.5.0d. For the linear case, the displacement at M in time occurs in couples of equal responses. The first pulse corresponds with the wave propagating upward, and the second is the same wave reflected from the top and propagating downward. The next two pulses at M are with opposite amplitude and are twice as

small. This is because of the reflection from the soil-beam contact. Using equation (5.0.3), the response can be found at any time and at any point on the beam.

The 2-D models are more complicated, but in a general sense the 2-D soil-structure interaction (SSI) system works in a similar way.

5.1 Input and grid parameters for the 2-D model

The input is a plane SH wave with prescribed motion at Γ_1, as given in Fig. 5.1 (for clarity, only the inner region R_1 with the artificial boundary $\mathcal{B}$ of the model in Fig.2.2 is shown):

$$u(x_i, y_j, t) = A\begin{bmatrix} \sin\left(\frac{\pi}{t_d}(t-t_1)\right)\left(H(t-t_1)-H(t-t_1-t_d)\right)+ \\ \sin\left(\frac{\pi}{t_d}(t-t_2)\right)\left(H(t-t_2)-H(t-t_2-t_d)\right) \end{bmatrix} \qquad (5.1)$$

$$\forall(x_i, y_j) \in \Gamma_1,$$

where

$A = 0.5\,m$ is the amplitude of the half-sine pulse,

t_{d0} is the duration of the half-sine pulse,

t_d is the duration of the filtered pulse,

$t_1 = \frac{x_i \sin\gamma}{\beta} + \frac{y_j \cos\gamma}{\beta}$ is the arrival time of the wave going upward,

$t_2 = \frac{x_i \sin\gamma}{\beta} + \frac{(H_s + y_j)\cos\gamma}{\beta}$ is the arrival time of the wave going downward,

Fig. 5.1 MODEL WITH COMPONENTS OF THE MOTION IN THE SOIL

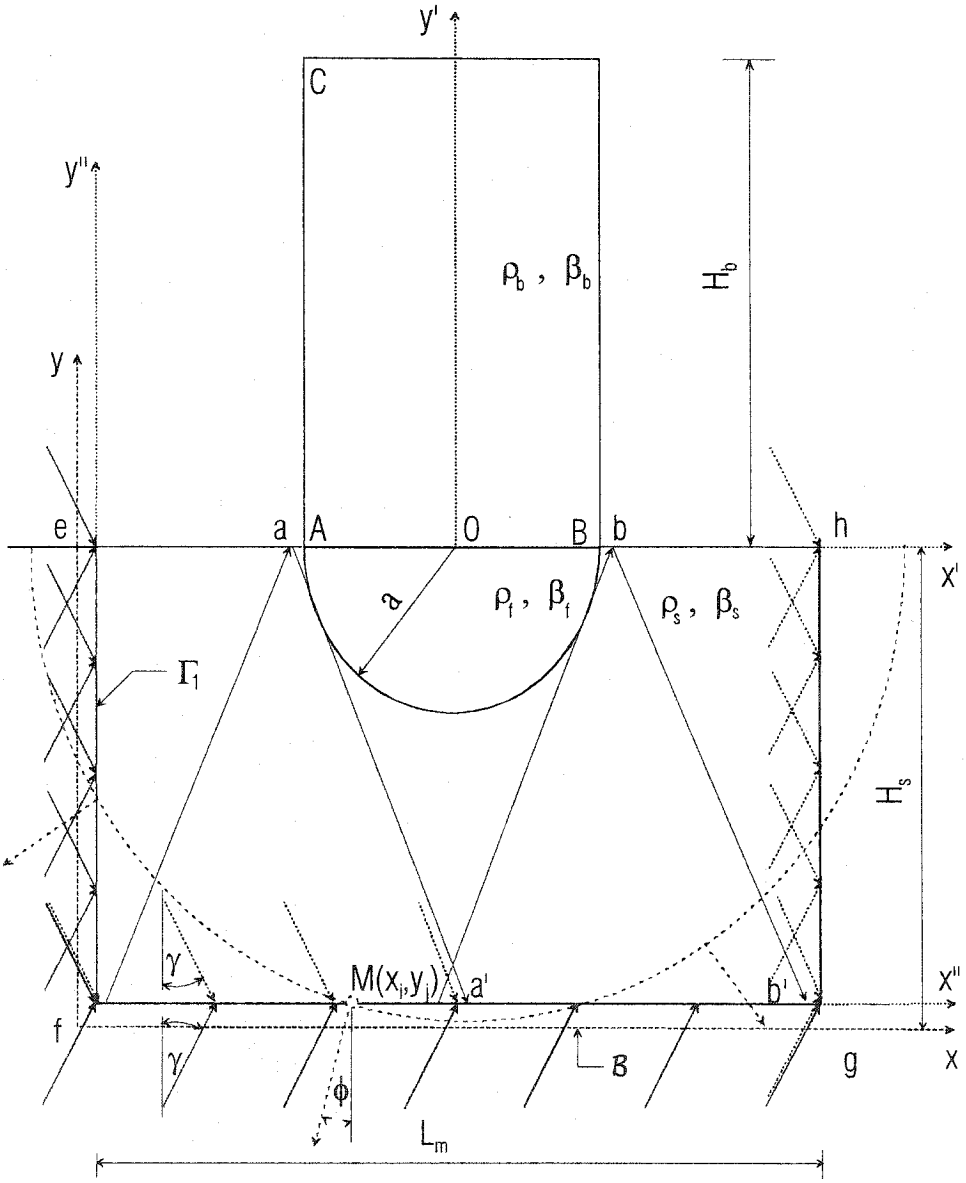

γ is the angle of incidence, and

H() is the Heaviside function.

Spatially, in the direction of propagation this plane SH wave has the form:

$$w(s) = A \sin \frac{\pi s}{\beta_s t_{d0}}, \qquad (5.2)$$

where s is the spatial coordinate in the direction of propagation, and β_s is the velocity of propagation in the soil. The length $L_w = \beta_s t_{d0}$ is discretized into 2^n intervals, $\Delta s = \frac{L_w}{2^n}$, and the spatial pulse (Eq. 5.2) is then Fourier transformed. To find the optimal sampling interval, we should minimize the error in the numerical group velocity $\frac{\partial \omega}{\partial k}$.

The propagation of the pulse consists of propagation of infinitely many modes. If the modes propagate with different velocities, dispersion of the solution will occur. The sampling interval can be found by trial and error to satisfy the numerical group velocity requirement $\frac{\Delta \omega}{\Delta k} = \frac{\frac{1}{2^n \Delta t}}{\frac{1}{2^n \Delta s}} = \frac{\Delta s}{\Delta t} = \beta$, but minimizing the error in the group velocity can increase the error in the phase velocity. Using the recommendation in Fig.5 of Holberg (1987), we proceed as follows.

The half-sine pulse is sampled by small enough sampling interval by taking $n = 10$, for example. Then the half-sine pulse is Fourier transformed. The biggest Fourier amplitude is at zero spatial frequency k_1 (Fig.5.4a), and as the frequency $\kappa_j = \frac{j-1}{2^n \Delta s}$ $j = 1,2,3,...,2^{n-1}$

Fig. 5.2 FILTERED HALF-SINE PULSE

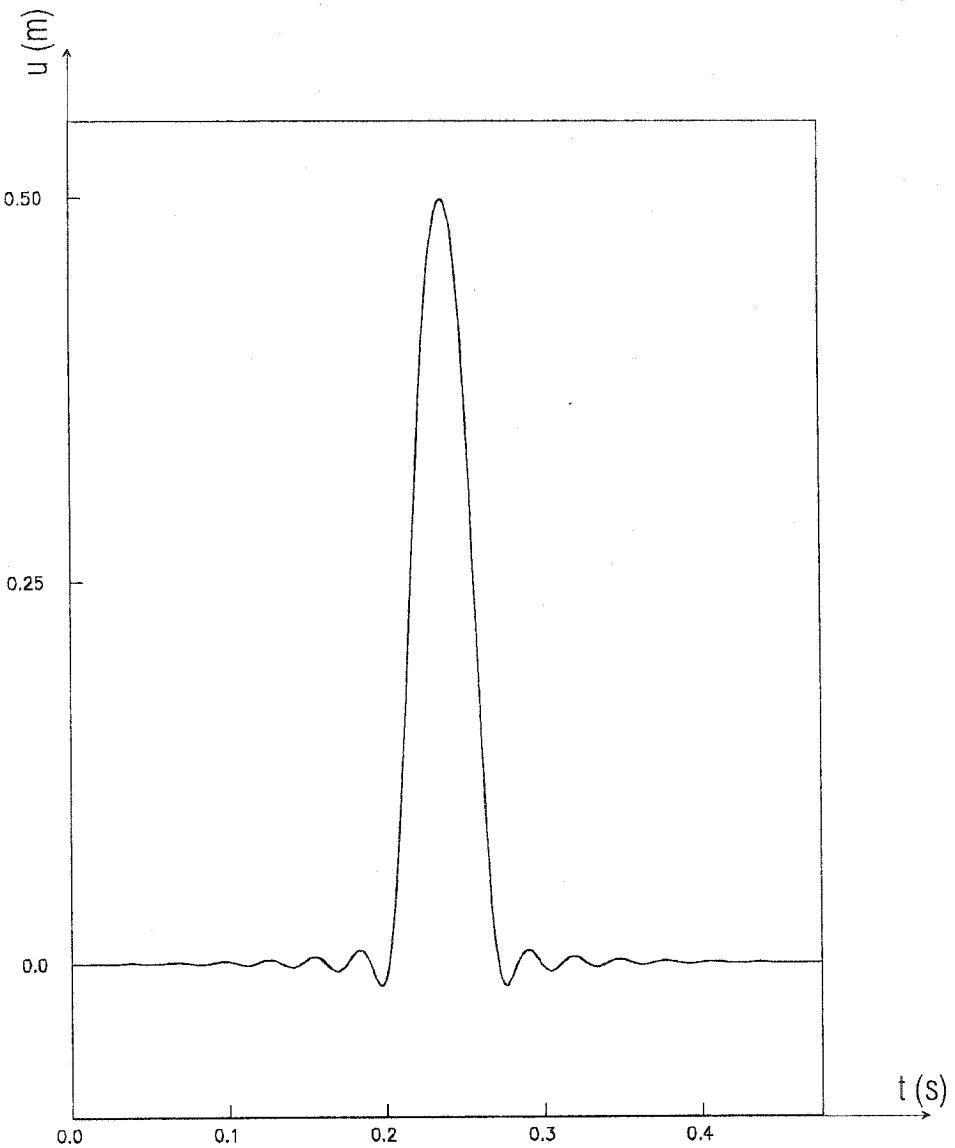

increases, the Fourier amplitudes decrease. For empirically adopted percentage p, we can find the highest mode $j_{\max}$ for which the Fourier amplitude satisfies

$$F(\kappa_{j\max}) \geq F(\kappa_1) \cdot p/100 . \tag{5.3}$$

The corresponding wave number for this mode is $k_{j\max} = 2\pi\kappa_{j\max}$, and the corresponding wavelength is $\lambda_{j\max} = \frac{1}{\kappa_{j\max}}$. Following the recommendations for the grid parameters given in Section 2.1, twelve points for this shortest wavelength are chosen in the grid. The highest angular frequency corresponding to the highest mode is $\omega_{\max} = \beta_s k_{j\max}$. We use this frequency as the cut-off frequency in low-pass filtering of the pulse. The time dependence of the motion,

$$w(t) = A \sin \frac{\pi t}{t_{d0}}, \tag{5.4}$$

is filtered using a low-pass Ormsby filter (Trifunac, 1971) with a cut-off frequency of $\omega_{\max}$. From numerical testing, it was realized that for very high cut-off frequencies ($\omega > 200\, rad/s$) the solution deteriorates. The maximum frequency allowed in the system will be $\omega = 200\, rad/s$, even though for short pulses higher frequencies $\omega_{\max}$ are obtained from the procedure explained above (Fig.5.4a). In Fig. 5.2, the filtered pulse with $t_{d0} = 0.0624\, s$ and a cut-off frequency $\omega = 200\, rad/s$ is shown. Again, point f(0,0) is taken as a point with prescribed displacement in the form of a filtered half-sine pulse, and the input at all points on Γ_1 is computed using (5.1).

5.2 Energy distribution in the system

In Chapter 3 we tested our model for a building when the input displacement was provided at the top. Now, the model is loaded from below, with input motion described with equation (5.1). In Appendix II we show that for the model studied here the energy that reaches the foundation does not depend upon the angle of incidence, so the results presented here are only for incident angle $\gamma = 30^0$. From the law of conservation of energy, the energy entering the system (solid arrows in Fig.5.1) should be equal to the energy going out of it. Using the energy formula for plane waves (Aki & Richards, 1980) the input energy is computed as

$$E_{inp} = \rho_s \beta_s \Delta x \sum_{i,j,t} \cos\phi_{i,j} v_{i,j}^2(t) \Delta t \,, \tag{5.5}$$

where $\phi_{i,j}$ is the angle between the normal erected at a point (x_i, y_j) on Γ_1, and the radial direction centered at O (see Fig. 5.1). The input energy enters the model along

a. The left boundary (x = 0), due to the incident wave going upward and the reflected wave from the half space going downward, and

b. The bottom boundary (y = 0), due to the incident wave going upward.

The outgoing energy from the model is:

1. E_1: Due to the reflected plane-wave field reflected from the half space, going downward toward the bottom and the right boundaries, and due to the incident plane-wave field going upward toward the right boundary (x = L_m), for all points on these two boundaries except the points in the shadow of the foundation (the points that belong

to the interval $\overline{a'b'}$ in Fig.5.1). The component of the energy E_1 is shown with dotted arrows in Fig.5.1 and is computed from equation (5.5) with velocities from the half-space solution.

2. E_2: Due to scattering from the foundation and the building, computed from (5.5) with velocities obtained as a difference between the total and the half-space solution.

3. E_3: Due to the energy radiated from the building through the foundation in the form of a cylindrical wave field (dashed circle with dashed arrows in Fig. 5.1) computed from (5.5) with velocities obtained as a difference between the total and the half-space solution.

The numerical tests are performed for models of the Hollywood Storage building (HSB) (Duke et al., 1970) and the Holiday Inn hotel (HIH) (Blume & Assoc.,1973), with geometry and material properties given in Section 3.3.

For different dimensionless frequencies $\eta = \frac{2a}{\lambda} = \frac{2a}{2\beta_s t_d} = 0.05; 0.5; 1; 2$ the error is computed from:

$$\varepsilon = \frac{E_{inp} - E_{out}}{E_{inp}} \cdot 100\,(\%). \qquad (5.6)$$

The results of the error calculations are illustrated in Table 2 together with the dimensionless depth of the soil island, H_s / a, as a parameter describing the size of the model (Fig.5.1). The length of the model is again $L_m = 2 \cdot H_s$. In E_{out}, besides the measured cumulative energy flowing through the curve Γ_1, the residual energy in the building is included,

which is of the order of several hundredths to several tenths of a percent of the cumulative outgoing energy at the end of the analysis. This energy is computed as an instantaneous quantity (3.3.7) rather than as cumulative one.

In the calculations, as the frequency η increases, the percentage p in (5.3) that determines the number of significant modes (for which the Fourier amplitudes are larger than $p/100$ of the largest Fourier amplitude) increases as well. This is done for practical reasons because at higher η, following the discretization procedure in 5.1, the grid spacing decreases tremendously due to the increase in the frequency, so that for the frequencies in the table $p = 0.5; 3; 3; 3$ percent, respectively.

TABLE 2. ERROR IN ENERGY CALCULATIONS FOR TWO DIFFERENT BUILDINGS

Hollywood Storage Building					Holyday Inn Hotel				
η	H_s/a	E_{inp}(KJ)	E_{out}(KJ)	ε(%)	η	H_s/a	E_{inp}(KJ)	E_{out}(KJ)	ε(%)
0.05	5.0	95750.7	95637.5	0.12	0.05	25.0	506697.4	502050.9	0.92
0.50	5.0	908950.8	909775.3	-0.09	0.50	6.0	1103821.0	1088928.0	1.35
1.00	5.0	1618250.0	1645651.1	-1.69	1.00	5.0	1758780.0	1766575.0	-0.44
2.00	4.7	1124830.0	1155606.0	-2.74	2.00	4.7	1623363.0	1729975.0	-6.57

As can be seen from Table 2, for the longest pulse under consideration, the HIH model requires a large soil island to achieve satisfactory accuracy, while the results for HSB are accurate with a relatively small soil island in the model $H_s = 5a$. Computing the energy with the soil island $H_s = 5a$, the above error in the HIH model is about 11%. It is obvious that for this building, with a relatively small soil island, the model is not accurate enough. The error comes from the assumption that the outgoing field has a cylindrical form propagating in a radial direction from point O in Fig.5.1 as a center and that it reaches Γ_1 at point $M(x_i,y_j)$ with angle

$$\phi = \tan^{-1}\left(\frac{\frac{L_m}{2} - x_i}{H_s}\right).$$

This assumption obviously does not hold for long pulses for HIH when the building is soft and the ratio of the masses $\frac{M_b}{M_s} \approx 1$. The spatial gradients of the motion quantities are small, and practically the model moves as a rigid body. In this case, the shear stress at the building-foundation contact in the vertical direction is small, and the variation of the shear stress in the horizontal direction is small, too. The building attracts a small amount of energy, and these conditions are close to the free surface condition. This causes the scattered field to be closer to that of the half-space solution - that is, a plane wave with an angle of propagation equal to the incident angle γ. The cylindrical pattern is not formed, and the error comes from the difference between the angles γ and ϕ.

A remedy for this case is to put the artificial boundary that is the main source of error as far away from the building as possible. In that way, the outgoing field decreases substantially, so that the error from the artificial boundary is not so pronounced.

On the other side, for the stiff building at the building-foundation contact the boundary conditions differ. The building attracts more energy and acts as a sink for a field reaching it. The scattered field is mostly due to the two corner points of building-foundation-soil contact and the other contact points along the building-foundation contact, which all transmit the incoming field in the building. This sudden change in the rigidity causes the two corner points to become sources of additional field that changes the pattern of the reflected field even, for long wavelengths, from plane to cylindrical waveforms.

For shorter pulses, which "feel" better the contrast between the soil and the foundation, the resulting outgoing field is always cylindrical. The assumption for computing the angles ϕ and the appropriate flow areas at the points on Γ_1, are satisfied and the errors in the Table 2 are negligible even for relatively small soil islands. The shorter pulses excite the building with a higher frequency, and the response of the building results from superposition of its higher modes. The results of the energy distribution in the whole model are shown on Figure 5.3a for HSB and in Figure 5.3b for HIH. The dashed line represents the input energy, the solid line indicates outgoing energy measured at Γ_1, and the dotted line represents the instantaneous energy in the building.

Trifunac (1972) showed that "light" and "soft" buildings on heavy soil (small $\frac{M_b}{M_s}$) respond as buildings on fixed bases. The radiation damping is small, and the energy is trapped in the building. The situation for a stiff building is opposite. The building releases the energy faster through the contact with the foundation, and after a few periods the amplitude at the top of the building decreases rapidly. The above observations are further illustrated in Fig.5.4, where the time histories of displacements at points A (x'= - a, y' = 0) and C (x'= - a, y' = H_b) are shown for different dimensionless frequencies. The motion at contact point A is shown with a solid line, and the motion at the top of the building C is indicated with a dotted line. It is obvious that the stiff HSB has greater radiation damping, and after approximately 5 s the motions in the foundation and the building practically cease. However, for the HIH building the situation is different. To compare the input dimensionless frequency $\eta = \frac{a\omega}{\pi\beta_s}$ with the fundamental frequency of the building ω_N, the latter is written as

$$\omega_N = \frac{\pi\beta_b}{2H_b} = \frac{\pi\beta_s}{a} \cdot \frac{\frac{\beta_b}{\beta_s}}{\frac{2H_b}{a}} = \eta_b \frac{\pi\beta_s}{a},$$

where $\eta_b = \frac{a\beta_b}{2H_b\beta_s}$ is the dimensionless fundamental frequency of the building. For the buildings under consideration, we have $\eta_{HSB} = 0.11544$ for the Hollywood Storage building and $\eta_{HIH} = 0.0955$ for the Holiday Inn hotel.

Fig. 5.3a BALANCE OF ENERGY FOR WHOLE MODEL
HOLLYWOOD STORAGE BUILDING

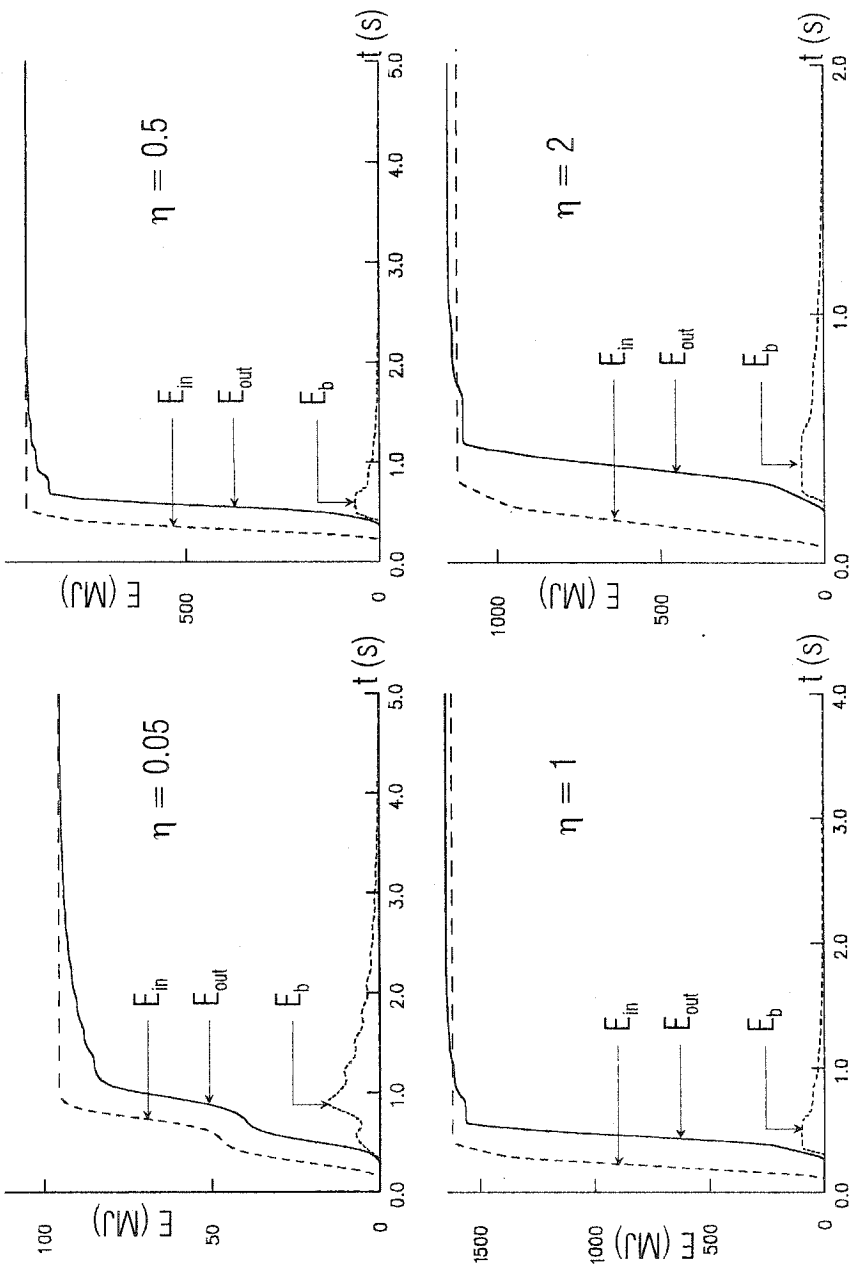

Fig. 5.3b BALANCE OF ENERGY FOR WHOLE MODEL OF HOLIDAY INN HOTEL

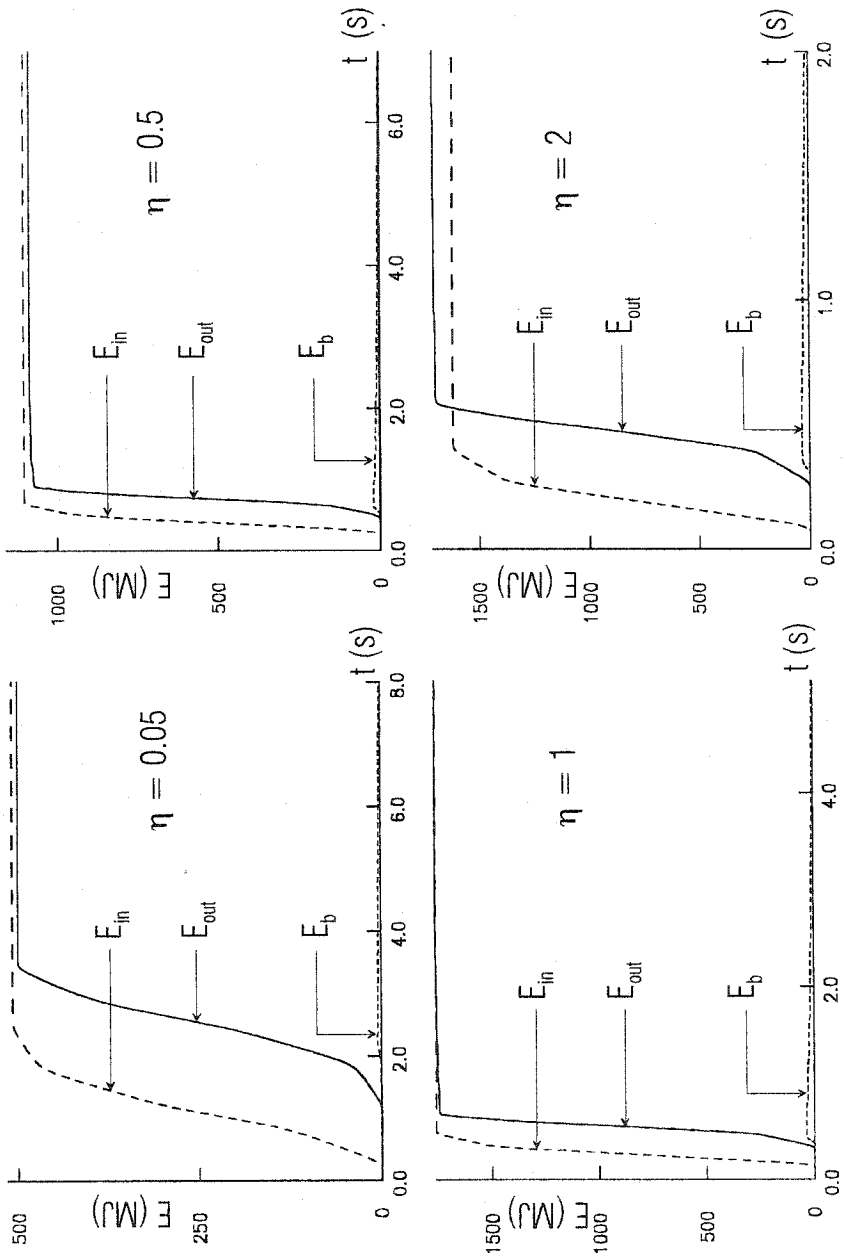

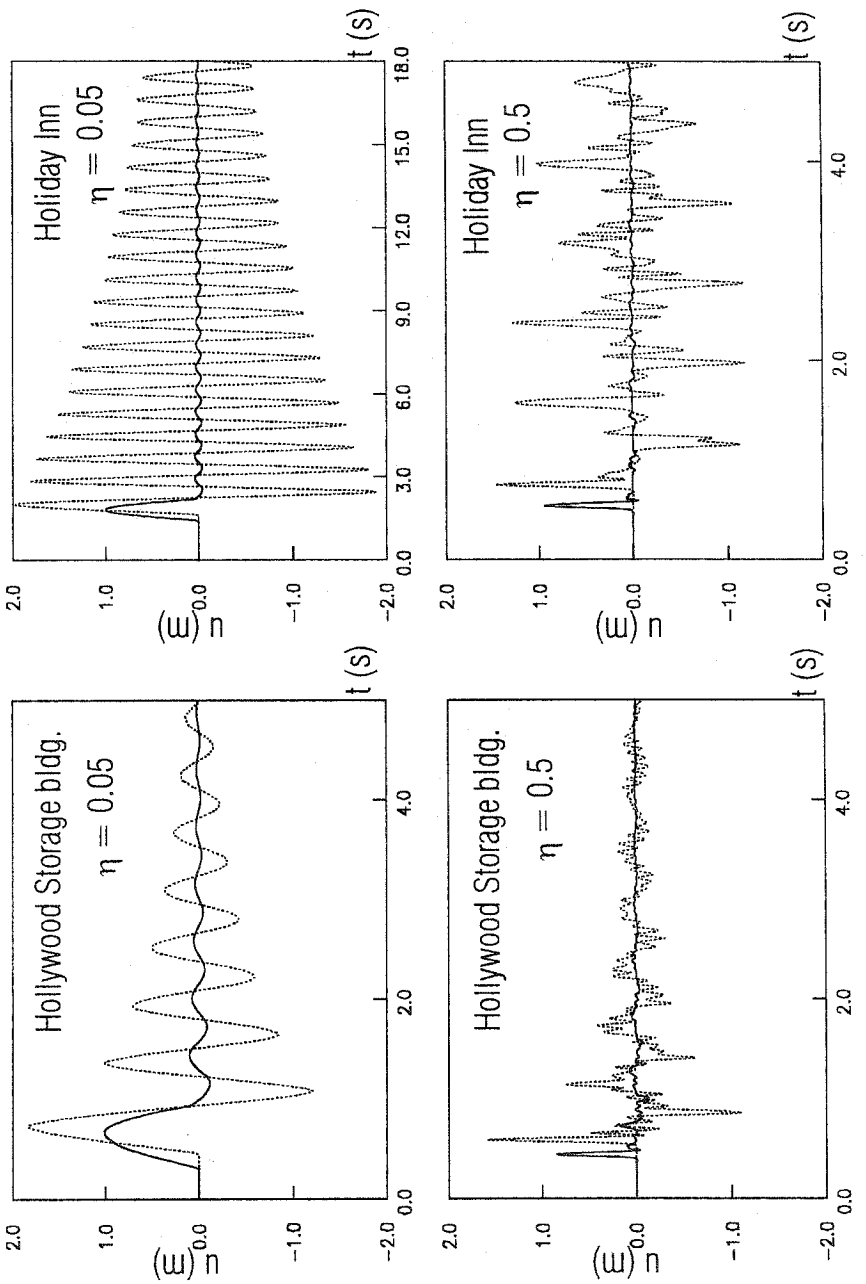

Fig. 5.4 TIME HISTORIES OF DISPLACEMENTS AT THE TOP AND BOTTOM OF THE BUILDING

In Fig. 5.4, it is obvious that for $\eta = 0.05 < \eta_{HIH} < \eta_{HSB}$ both buildings respond with their fundamental modes only, and this presents the idea that the response of a building can be replaced with a single-degree-of-freedom damped oscillator. For $\eta = 0.05$ at HIH, after $t_2 = 17.5$ s some small motion at A can still be seen, and at C the amplitude is still about 29% of the initial amplitude. The first amplitude of the displacement at the top occurs at $t_1 = 2.1$ sec, so in time $t = t_2 - t_1 = 15.4$ s the amplitude decreases to 0.29 of the initial amplitude. This result agrees fairly well with the result obtained in Eq. 3.3.12b, where we found that the required time for amplitude decrease from 1 m to 0.25 m is t = 14.75 sec.

In the plots for $\eta = 0.5$ it can be seen that the buildings respond with higher modes. In the plot for HIH, it is interesting to notice that after the input ground motion has passed the foundation the motion at point A is practically zero until the reflected pulse from the top of the building comes again to point A, with one part of it being reflected back to the building and one part being radiated, at which time the motion at A ceases again. From Table 2 it can also be seen that as the pulse becomes shorter the error increases which is mostly the consequence of the Saint-Venant principle at the points of application of the load - curve Γ_1. While the half-space solution for the velocity jumps from 0 to $\frac{\pi}{t_d} A$ (Eq. 5.1), the velocity of the field computed with finite differences changes gradually. When these two fields meet at Γ_1, the outgoing velocity computed as a difference between the total field and the analytical (half-space) field jumps, as well. This jump is greater for larger velocities (smaller t_d and bigger η), and that is the main reason the outgoing energy at larger η is always greater than the input one.

The other reason for the error is that while almost the whole temporal Fourier transform of the pulse for lower η is contained in frequencies smaller than $\omega = 200\, rad/s$, higher η values have a substantial amount of the response for $\omega > 200\, rad/s$ (Fig. 5.4a), and the big part of this frequency response is filtered out. This can cause errors in the transmitted and reflected field at the contacts (Holberg, 1987). One more reason for the error is the diffraction around the corners of the foundation. The diffraction violates the assumption in the half-space analytical solution (5.1) that the waves propagate in directions of straight rays normal to their fronts so that the outgoing diffracted waves impinge upon the boundary with angles different than expected.

To gain better insight about the energy distribution, only the rays (energy) reaching the foundation should be considered. This energy is extracted from the total energy in the model by subtracting the half-space outgoing energy on $\Gamma_1 \setminus [a', b']$ from the total input energy. In Fig.5.1, this corresponds to subtracting the "dotted-arrows" energy from the "solid-arrows" energy. In this way, the scattered + radiated energy (the second and the third parts of the outgoing energy) should balance the input energy on the interval $[a', b']$. Theoretically the difference between (1) the difference of the input (solid arrows) energy (Eq. 5.5) and the first part of the outgoing energy (dotted arrows); (see page 110), $E_I = E_{inp} - E_1$, and (2) the sum of the second and the third parts of the outgoing energy (page 111), $E_{II} = E_2 + E_3$, gives us the instantaneous energy in the soil:

$$E(t) = E_I - E_{II}. \qquad (5.7)$$

Fig. 5.4a FOURIER TRANSFORM OF HALF-SINE PULSE FOR DIFFERENT DURATIONS OF THE PULSE

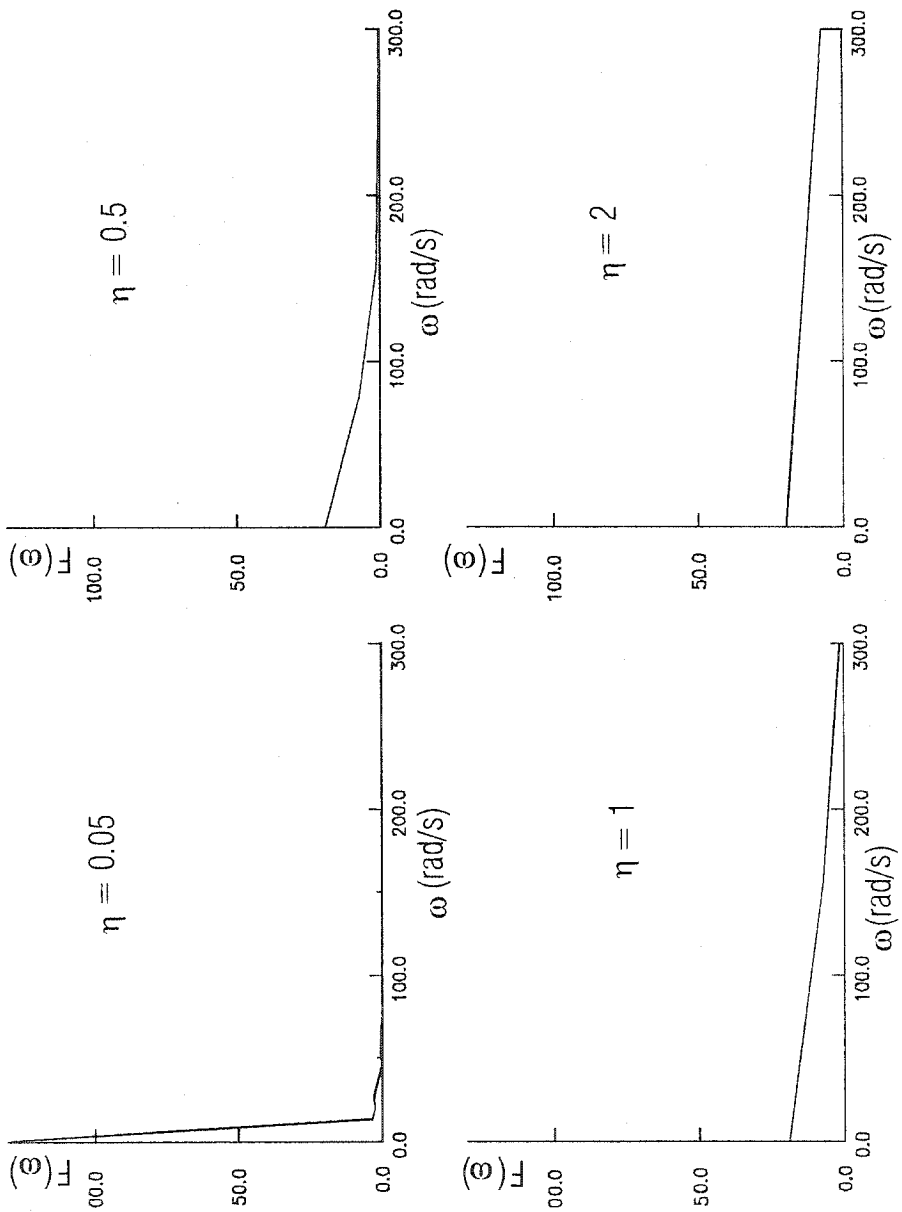

In Figures 5.5a and 5.5b the energies E_I and E_{II} are given together with the instantaneous energy in the building E_b for η= 0.05, 0.5, 1, and 2 for HSB and HIH, respectively. Also, the duration of the pulse t_{d0} and the error computed from (5.6) at the end of the analysis ε(%) are given when E_b is virtually zero. To provide a more detailed view (i.e., to avoid the peak of the energy E_I), only the energy E_I after the pulse has left the model is shown as a constant in time. These plots are given in Fig. 5.5c and Fig. 5.5d for HSB and HIH, respectively.

We should mention here that the results for high η depend upon the choice of grid parameters, especially on the parameter p in Eq. (5.3). For the shortest duration of the pulse, $\eta = 2$, and for the highest input frequency allowed in the model (from numerical tests $\omega_{\max} = 200\, rad/s$), from Fig. 5.4a we can see that a significant part of the frequency response is filtered. Because we allow temporal frequencies up to 200 rad/s in the model, we should choose higher p in sampling the grid (Eq. 5.3) to prevent the dispersion relation of the wave propagation in the soil. In Table 3, the error in energy calculation is presented for different choices of the cut-off frequency and the parameter p. Taking smaller p in (5.3) and cut-off frequency ω_c = 200 rad/s, we obtain a large velocity at Γ_1, and severe error in the balance of energy occurs in the computation, mostly due to the previously mentioned Saint-Venant principle. A remedy is to decrease the input velocity by specifying a lower cut- off frequency in the filter. A question arises as to how large the cut-off frequency should be in the low-pass

filtering of the pulse. One good indicator is given in the next chapter (Fig.6.1b for our example for HIH), where it will be seen that after some input η_g the response does not change with increasing η, indicating that the grid behaves as a low-pass filter, with the highest frequency being

$$\omega_g = \frac{\eta_g \pi \beta_s}{a}. \tag{5.8}$$

In our example one can estimate $\eta_g \approx 1.7$, and from (5.8) $\omega_g = 139.8\, rad/s$. The plots in Fig. 5.5 are obtained from models with the most accurate combination of grid parameters (p, ω_c) for each building. For smaller η, the grid parameters (p, ω_c) are kept the same as in Table 2.

The best insights about the energy distribution can be obtained for the cases in which the pulse is short enough to be completely contained in the building - e.g. when $t_{d0} \le \frac{2H_b}{\beta_b}$. In our examples, this is a case for η = 0.5, 1, and 2 for both buildings. The energy distribution is shown for these cases in Table 4.

From the plots, it can be seen that the HSB attracts more energy (the dotted lines) but radiates it faster for any input frequency. This behavior is mostly due to the coefficient of transmission between the building and the foundation, given by (5.0.1). The HSB has k_{tr} closer to 1 than HIH, which means that a larger amount of flow occurs in both directions at the building-foundation contact and also smaller reflection. For HIH, the situation is the opposite.

Fig. 5.5a THREE COMPONENTS OF THE ENERGY IN THE MODEL AS FUNCTIONS OF TIME: HOLLYWOOD STORAGE BUILDING

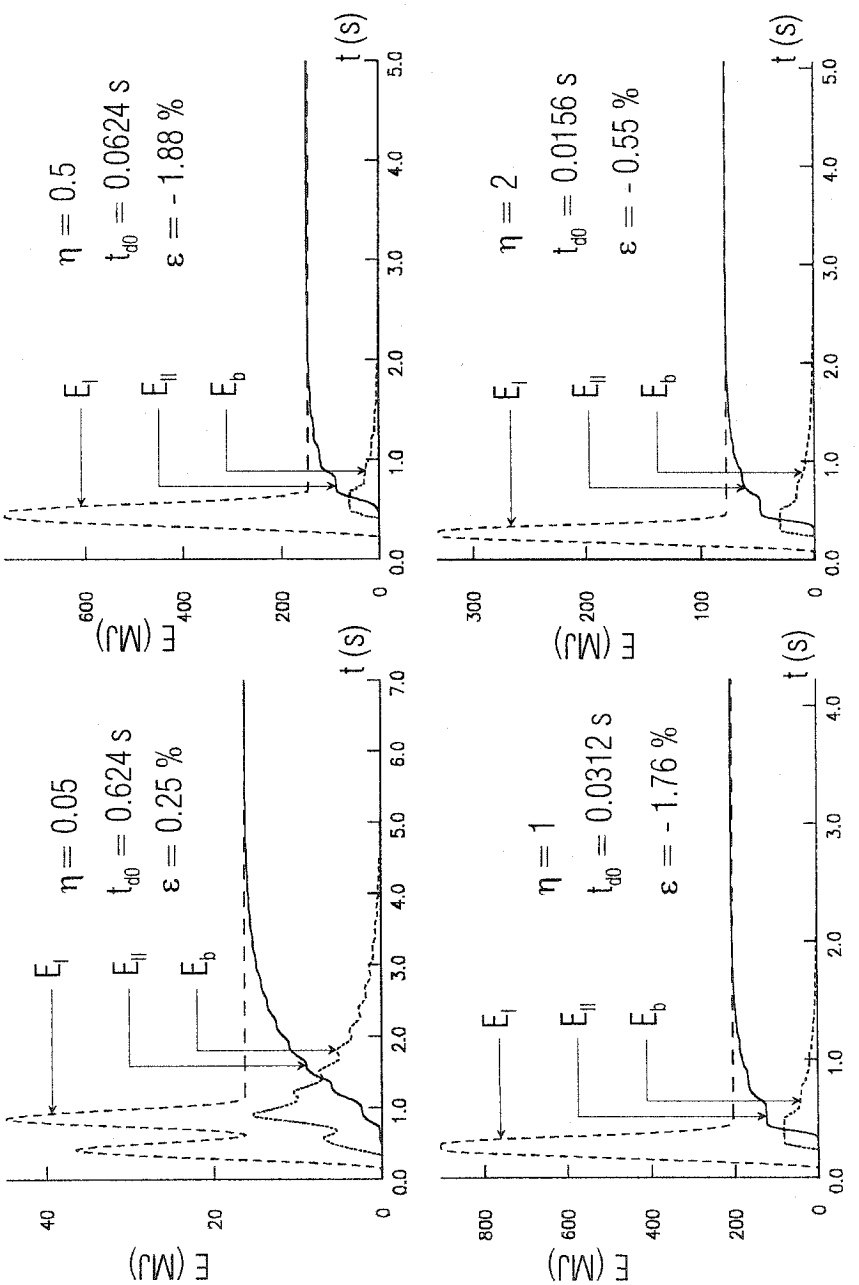

Fig. 5.5b THREE COMPONENTS OF THE ENERGY IN THE MODEL AS FUNCTIONS OF TIME: HOLIDAY INN HOTEL

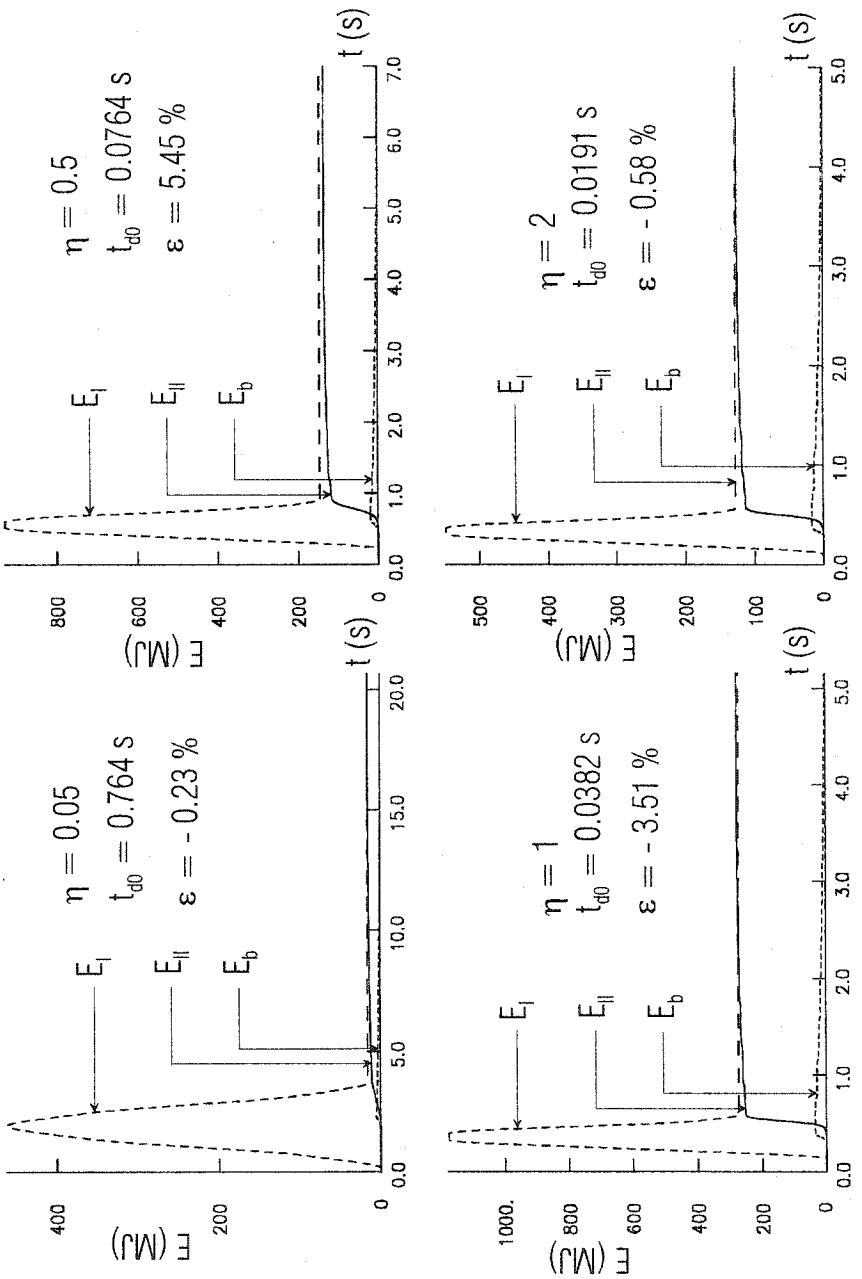

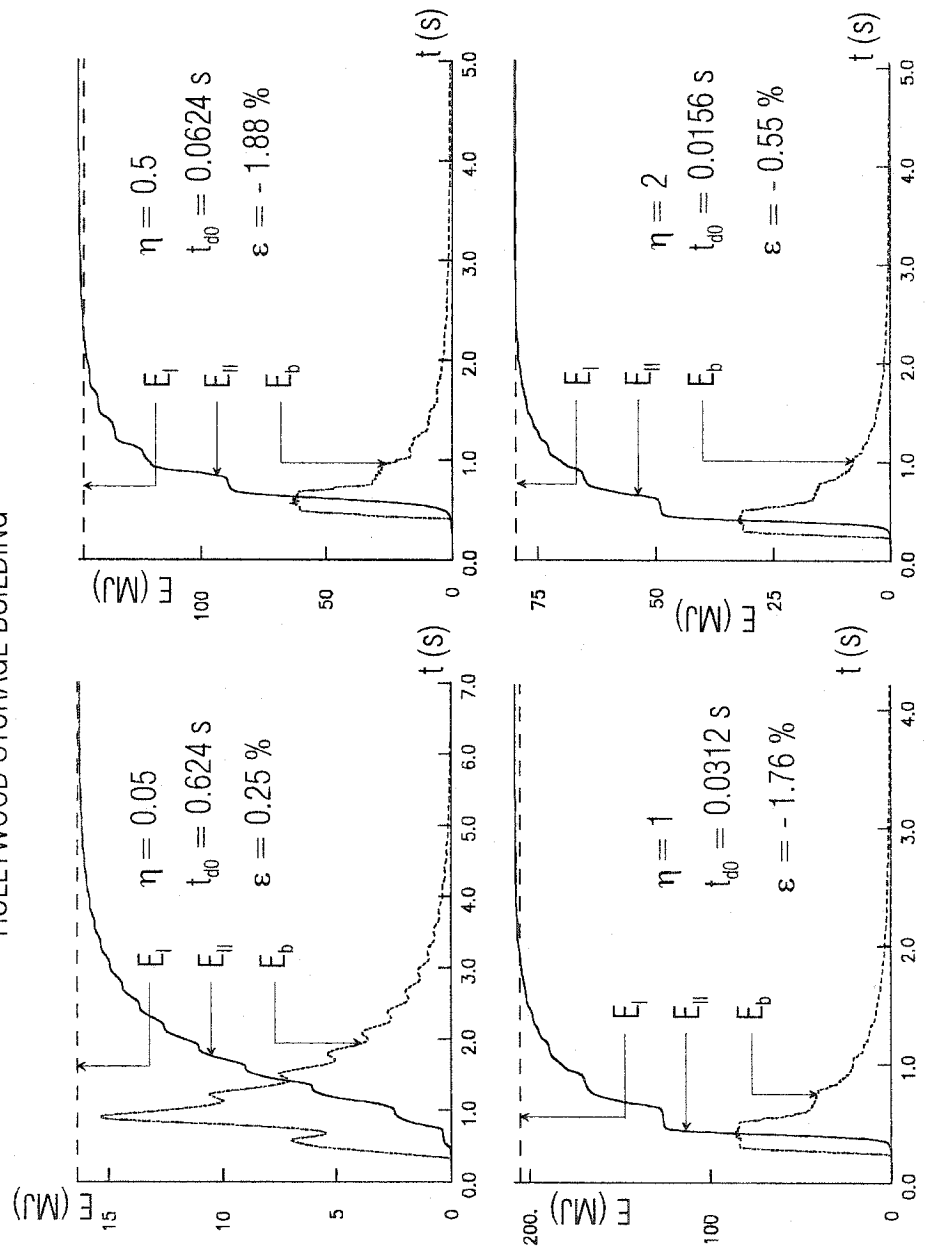

Fig. 5.5c DISTRIBUTION OF ENERGY REACHING THE FOUNDATION: HOLLYWOOD STORAGE BUILDING

Fig. 5.5d DISTRIBUTION OF ENERGY REACHING THE FOUNDATION:
HOLIDAY INN HOTEL

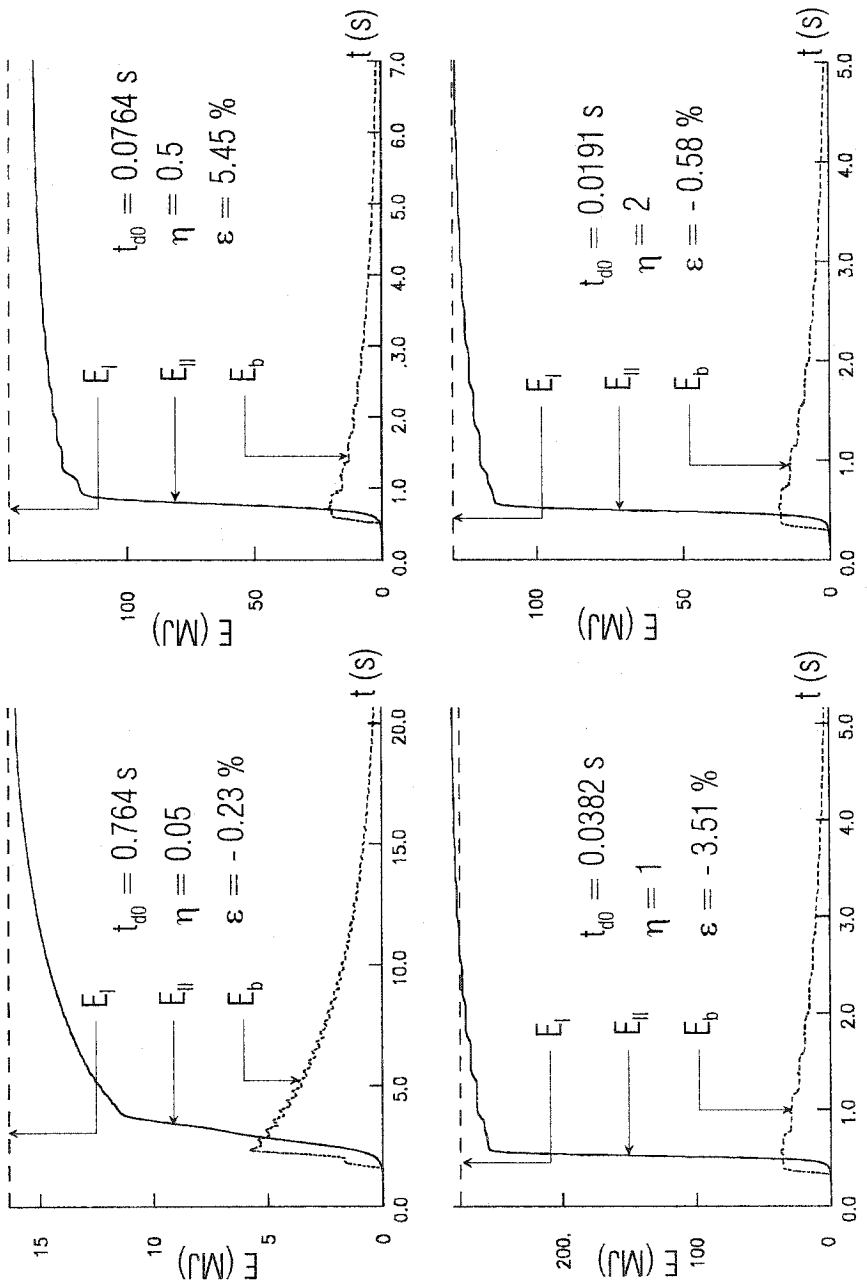

TABLE 3. DEPENDENCE OF THE ERROR FROM THE GRID PARAMETERS

Building	η	p (%)	$\omega_c\,(rad/s)$	E_I (MJ)	E_{II} (MJ)	ε (%)
HSB	1	4	200	245.41	272.46	-11.02
HSB	1	4	160	205.43	209.04	-1.76
HSB	2	5	200	181.18	230.17	-27.04
HSB	2	5	160	130.91	149.77	-14.4
HSB	2	8	140	77.84	78.27	-0.55
HIH	2	4	200	258.74	370.84	-43.33
HIH	2	4	160	189.32	224.76	-18.72
HIH	2	8	135	113.17	105.48	6.80
HIH	2	8	145	128.89	129.64	-0.58

TABLE 4. ENERGY DISTRIBUTION OF THE FIELD REACHING THE FOUNDATION

Building	η	E_I (MJ)	$E_{bmax}=E_3$ (MJ)	$\frac{E_{b\max}}{E_I}(\%)$	$\frac{E_2}{E_I}(\%)$
HSB	0.5	146.5	61.8	42.2	57.8
HSB	1.0	205.4	86.9	42.3	57.7
HSB	2.0	77.8	32.0	41.2	58.8
HIH	0.5	147.0	20.7	14.1	85.9
HIH	1.0	276.4	37.1	13.1	86.9
HIH	2.0	128.9	17.5	13.6	86.4

As the ratio of the mechanical impedances $\frac{\alpha_f}{\alpha_b} = \frac{\mu_f \beta_b}{\mu_b \beta_f}$ is closer to 1, and as the angle of incidence is closer to zero, the building attracts and radiates more energy. That the percentage of the energy distribution does not depend upon the input frequency can be seen from Table 4, where for any duration of the pulse HSB attracts (radiates) about 42% of the energy reaching the foundation and the rest (about 58%) is immediately scattered from the soil-foundation and building foundation contacts. The HIH building "sees" only about 13.5% of the input energy reaching the foundation, and the rest (about 86.5 %) is scattered from the contacts. The scattered energy, E_2, never enters the building and for design of earthquake resistant structures, it is important to learn how to increase the percentage of this part of the outgoing energy (last column of Table 4).

The scattered energy depends primarily upon the coefficients of reflection and transmission at the soil-foundation and building-foundation contacts (Eqs. 5.0.1 and 5.0.2 for 1-D problem), which depend upon the properties of the media meeting at the contacts. Assuming a 1-D propagation and particle velocity of the incident wave equal to 1, the energy reaching the building in unit time per unit area is

$$e_b = \rho_b \beta_b v_b^2 = \rho_b \beta_b \left(k_{tr}^{s-f} \cdot k_{tr}^{f-b} \right)^2, \tag{5.9}$$

where

$k_{tr}^{s-f} = \frac{2}{1 + \frac{\rho_f \beta_f}{\rho_s \beta_s}}$ is the coefficient of transmission from soil to foundation, and

$k_{tr}^{f-b} = \dfrac{2}{1+\dfrac{\rho_b\beta_b}{\rho_f\beta_f}}$ is the coefficient of transmission from foundation to building.

Using these coefficients in (5.9) and assuming that $\rho_f = \rho_s$, we have

$$e_b = \frac{16\rho_b\beta_b}{\left(1+\dfrac{\beta_f}{\beta_s}\right)^2 \cdot \left(1+\dfrac{\rho_b\beta_b}{\rho_f\beta_f}\right)^2} = \left(k_{tr}^{s-f}\right)^2 \cdot \frac{4\rho_b\beta_b}{\left(1+\dfrac{\rho_b\beta_b}{\rho_f\beta_f}\right)^2}. \qquad (5.10)$$

Substituting $\dfrac{\rho_f\beta_f}{\rho_b\beta_b} = r$, (5.10) becomes

$$e_b = \left(k_{tr}^{s-f}\right)^2 \cdot \frac{4\rho_b\beta_b \cdot r^2}{(1+r)^2}. \qquad (5.11)$$

From (5.11) we can analyze three limiting cases for (5.11):

1. $\rho_b\beta_b >> \rho_f\beta_f$, $\lim_{r\to 0} e_b = 0$. Because of the empty space between the elements of the structure, the structure is usually "softer" and "lighter" than the foundation, so this case is only of theoretical interest. It corresponds to a structure floating on fluid.

2. $\rho_b\beta_b \to \rho_f\beta_f$, $\lim_{r\to 1} e_b = \left(k_{tr}^{s-f}\right)^2 \cdot \rho_f\beta_f$. This is more realistic, but a rare case.

3. $\rho_b\beta_b << \rho_f\beta_f$, $\lim_{r\to\infty} e_b = \left(k_{tr}^{s-f}\right)^2 \cdot 4 \cdot \rho_b\beta_b$. This is the most realistic case.

As can be seen from the above limiting cases, the energy is completely scattered from the building-foundation contact for case 1, and the energy reaching the building is zero. This case cannot exist in the modeling of real structures because the density of the structures is smaller than the density of the foundation, and, as a consequence, the impedance of the

structure is smaller than the impedance of the foundation. When the impedances of the structure and the foundation are equal (case 2), the building-foundation contact does not exist, and the wave motion is not altered between the foundation and the structure. The energy passing through unit area in unit time in the structure is equal to that in the foundation, which means that 100% of the energy entering the foundation is transmitted into the building. Finally, which applies to most buildings, there is loss of energy due to scattering at the building-foundation contact, and the percentage of the energy in the foundation entering the building is smaller than that in case 2.

The influence of the soil-foundation contact on e_b is expressed by

$$\left(k_{tr}^{s-f}\right)^2 = D = \frac{4}{\left(1+\frac{\beta_f}{\beta_s}\right)^2} = \frac{4}{(1+p)^2}, \tag{5.12}$$

where $p = \frac{\beta_f}{\beta_s}$ is the ratio of the impedances of the foundation and the soil for the same densities for these two media.

We can distinguish three limiting cases for D in (5.12):

a. $\beta_s >> \beta_f, p \to 0$: $\lim_{p\to 0} D = 4$

b. $\beta_f \to \beta_s, p \to 1$: $\lim_{p\to 1} D = 1$

c. $\beta_s << \beta_f, p \to \infty$: $\lim_{p\to \infty} D = 0$.

With combination of the cases 2, 3, a, b, and c, the system soil-foundation-structure can be designed to minimize the energy e_b entering the structure (5.11). From the above limiting

cases, the best combination to minimize e_b (i.e., to maximize the energy scattered from the contacts) is combination 3c which means a "light" and "soft" structure on "heavy" and "stiff" foundation embedded in "soft" soil. In the real world, usually the properties of the structure and the soil are known in advance. There are two approaches to achieve the combination 3c:

- Design a stiff foundation, so that the limiting cases 3 and c are fullfiled.
- Design the weaker contacts between the building and the soil. For example, if the soil is stiff, a layer of soft material around the foundation can be inserted before the filling of the foundation, so that case c is simulated; if the building is stiff, soft material acting as a base isolator can be inserted above the foundation.

The scattered energy E_2 also depends upon the angle of incidence γ, as will be shown in Chapter VII. As γ becomes larger, the smaller is the amount of energy entering the building and the larger is the scattered energy from the soil-foundation and building-foundation contacts.

Finally, in Figures 5.6a and 5.6b the solution in the soil island for HSB and HIH, respectively, at the end of the analysis is shown normalized to 2A/50, or in scale 1:0.02, to visualize the radiation.

5.3 Conclusion

From the above analysis, it can be concluded that for the same amount of energy reaching the foundation (the input energy), when the material properties of the foundation are

close to the material properties of the soil, a building that has coefficient k_{tr} closer to 1 will attract more energy and radiate it out faster.

The error in the solution arises mostly because of the error in the scattered field, E_2, due to the consequence of the Saint-Venant principle. It states that if some distribution of forces acting on some region of the body is replaced by a different distribution of statically equivalent forces acting on the same region, then the effects of the two different distributions on the parts of the body sufficiently far away from the region of application of the forces are essentially the same. At the region of application of the forces, different distributions cause different effects. The error depends mainly upon the duration of the pulse and is more pronounced for shorter pulses (larger velocities). The overlapping of the scattered field and the half-space field at Γ_1 is inevitable for any size of the soil island, and it overestimates the outgoing energy, especially the energy E_2 for ground motion frequency $\Omega = \frac{\pi}{t_{do}} > 100\, rad/s$.

To keep the balance of energy, we need to filter out the higher frequencies. To use higher frequencies (velocities) of the input, we need either faster computers or higher-order accurate finite difference schemes, especially with respect to space coordinates. For example, for $\eta = 2$ and p = 3%, the algorithm generates a grid with 321*370 spatial points. The ordinary PC with a Pentium IV processor needs roughly about 40 hours (the speed depends upon the speed of the hard-disk controller and the available space on the hard disk) for simulation of $T_{end} = 2.5$ s. To take more modes into the analysis, for example for p = 2%, we

Fig. 5.6a DISPLACEMENT OF THE SOIL ISLAND AT THE END OF THE ANALYSIS: HOLLYWOOD STORAGE BUILDING

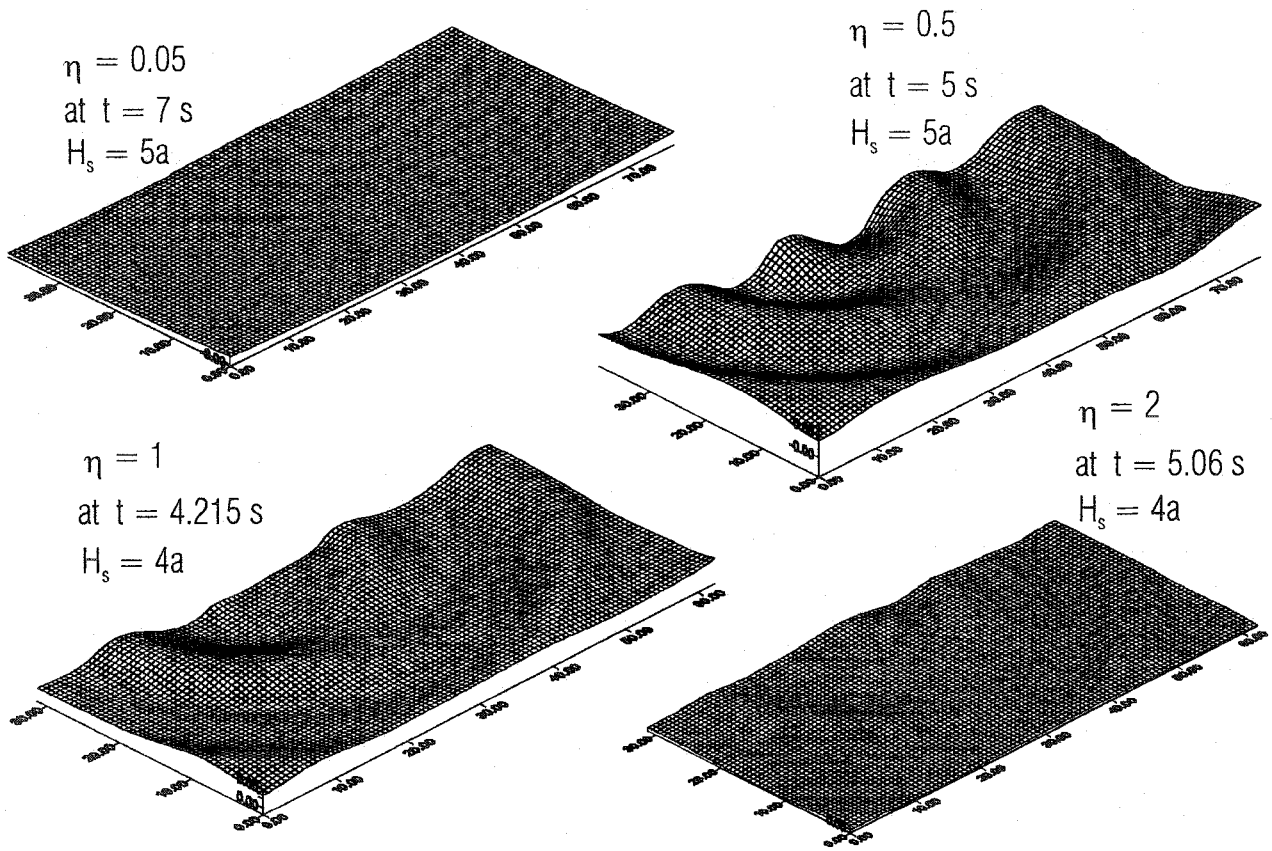

Fig. 5.6b DISPLACEMENT OF THE SOIL ISLAND AT THE END OF THE ANALYSIS: HOLIDAY INN HOTEL

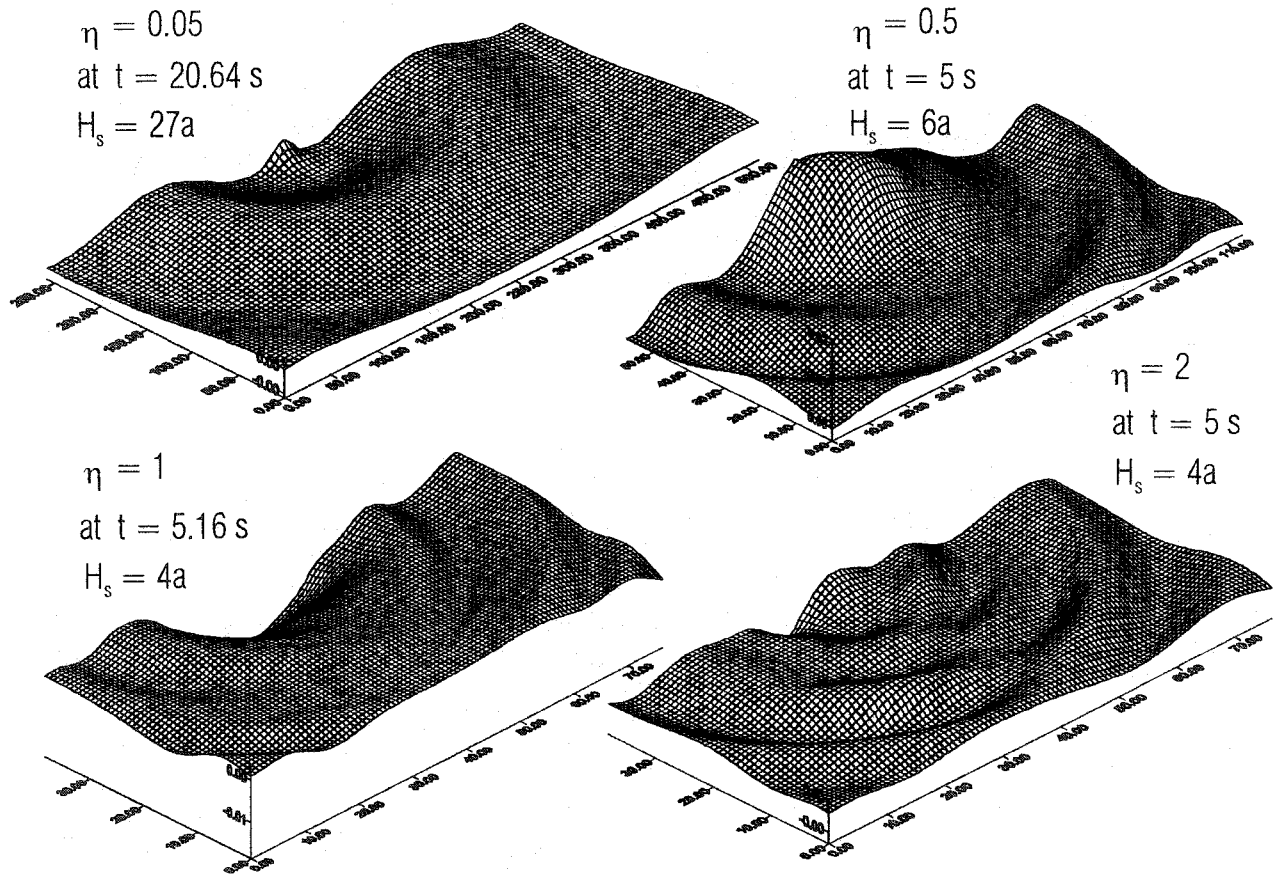

need spatial grid of 481 * 555 points which is $1.5^2 = 2.25$ more points than the grid for p = 3%. Also, to preserve the Courant condition (Eq. 2.1), Δt should be made 1.5 times smaller. Knowing that the order of complexity is O(N), where N is the total number of spatial points, the simulation for p = 2% should last about 3.375 times longer than for p = 3%. From tests, it was noticed that runs for bigger N values, lasted longer than expected. Probably this is because of the larger number of I-O operations and the fact that the controller needs more time to find a record in larger files.

As shown in Appendix II (II.9), the input energy brought to the foundation depends only upon the soil properties, the amplitude of the pulse, and η, and it is the same for two different buildings sitting on the same soil and having the same η. Indeed, in our examples this is the case when η is so small that all of the modes involved in the grid have temporal frequency $\omega_{\max} = \beta_s k_{\max} \leq 200 rad/s$. For example, for $\eta = 0.05$, HIH has $E_I = 16.400 MJ$ and HSB has $E_I = 16.385\ MJ$. For $\eta = 0.5$, when p = 3%, the highest mode for HSB has dual $(k_{\max}, \omega_{\max}) = (0.8055\, m^{-1}, 201.34\, rad/s)$. As was shown in Table 4, although $\omega_{\max}$ is slightly larger than the cut-off frequency $\omega_c = 200\ rad/s$ again the input energies are essentially equal. It is obvious that for $\eta > 0.5$ the input energies are not equal because of the filtering of the original pulse and the loss of the higher modes. The shorter pulse (HSB) at the same η loses more significant modes, and that is the reason $E_I^{HSB} < E_I^{HIH}$ at higher η.

CHAPTER VI

INPUT PARAMETERS FOR STRUCTURAL DESIGN

6.0 Introduction and Model

In engineering practice, the response spectrum method is a popular tool for structural design because it is simple and does not depend upon the details in the structure (Trifunac, 2003). The stiffness and the mass matrix can be diagonalized using eigenvectors of the system so that an uncoupled system of second-order ordinary differential equations can be obtained. When the excitation is the ground motion, the right-hand side of this system includes acceleration of ground motion.

It is obvious that these input parameters should be well defined to get an accurate prediction of the response of the system. The codes usually prescribe the spectral acceleration as a function of the period and of the soil properties at the site. Solving for the system response, first the vector of maximum modal displacements is obtained, from which, using the square root of the sum of squares technique (SRSS), the vector of maximum displacement shears and moments is obtained.

A different approach to the design problem is to evaluate maximum local drift in the structure in terms of the peak velocity of the velocity pulse entering the structure (Trifunac et al., 2001). The building starts to respond to the ground motion with its fundamental mode

Fig. 6.0 THE MODEL FOR TRANSIENT ANALYSIS

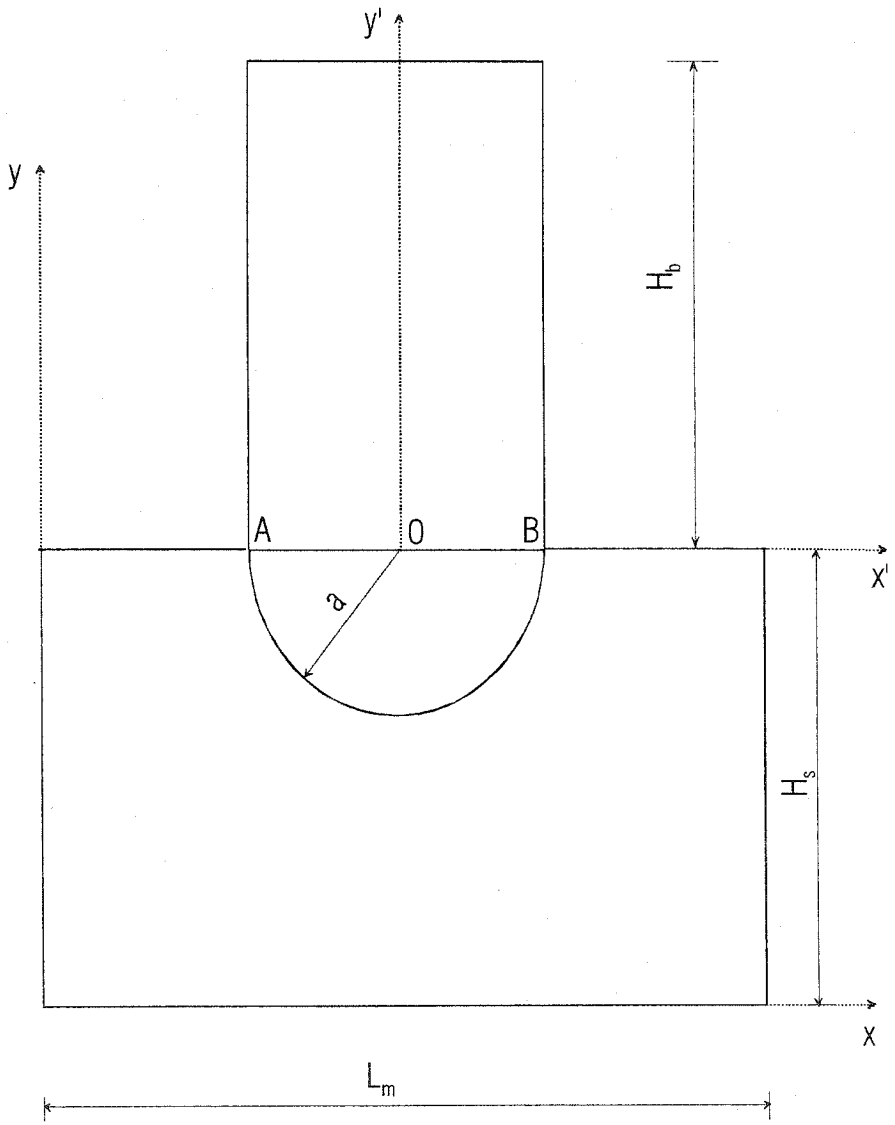

after time $t_1 = \frac{2H_b}{\beta_b}$ (H_b is the height of the building, and β_b is shear wave velocity in the building) has passed from the entrance of the pulse into the building. For early transient response in time t$(0 < t < t_1)$ when the pulse is still in the building, designing with the response spectrum method is inappropriate because the representation of the displacement field in the building requires representation in terms of many modes, and thus for studying the response in this time interval the wave propagation approach is natural and also the most efficient and direct.

As further discussed in Trifunac et al. (2001) the velocity amplitude of the pulse when it enters the building depends upon the soil, the foundation, and the building properties, and because of local dissipation of the energy due to soil-structure interaction (for the SH case this involves scattering from the soil-foundation and building-foundation contacts) the amplitude of the velocity pulse entering the building is reduced and is always smaller than the amplitude in the soil.

Our goal in this chapter is to find the amplitudes with which the pulse is entering the system building-foundation. For that purpose, the peak average displacements and the peak average velocities at the building-foundation and soil-foundation contacts are studied for a range of dimensionless frequencies $0.05 \leq \eta \leq 2$ when the incident wave excitation is a half-sine pulse. All of these quantities are normalized with respect to the peaks in half space so that the ratios give the effect of the soil-foundation-structure interaction and enable us to evaluate

the peak velocities entering the structure. The curves are constructed with 40 points $(\eta, F(\eta))$ with an increment $\Delta\eta = 0.05$.

The model (Fig.6.0) has the same soil properties as the model in Chapter 5. The example building has the properties of the Holiday Inn hotel, and the foundation has density equal to the soil density. The analysis is performed for three different velocities of propagation of the SH waves in the foundation: β_f = 250, 300, and 500 m/s. To avoid interference of the incoming pulse in the structure and the reflected pulse from the top of the structure, the height of the structure H_b is computed from the condition $\frac{2H_b}{\beta_b} \geq t_d + \frac{2a}{\beta_f}$. The size of the soil island is taken as $H_s = 4a$. The pulse is Fourier transformed in space, and only the frequencies that have response amplitudes larger than p(%) of the frequency response of the zero-th mode (k = 0) are used. The percent p varies depending upon the angle of incidence, and it is taken as p = 5, 6, 6, 7 for γ = 0°, 30°, 60°, and 90°, respectively. For proper modeling of the foundation, the minimum number of spatial intervals per length of the foundation is $m_f = 18/2a$, and the maximum number of intervals per length of the foundation is $m_f = 40/2a$ (Fig. 2.3). For the highest spatial frequency $k_{\max}$, the corresponding highest temporal frequency of the pulse is $\omega_{\max} = \beta_s k_{\max}$. This is the cut-off frequency for the Ormsby low-pass filter, so the higher frequencies are filtered out from the analysis. The analysis ends when the pulse has completely passed point B in Fig. 6.0.

6.1 Results

In figures 6.1a,b,c,d the normalized amplitudes of the average displacements at the soil-foundation (dashed lines) and building-foundation (solid lines) contacts are shown for three different foundation stiffness. The averaging is done in every time step k as:

$$u^k_{av.s-f} = \frac{1}{N}\sum_{i=1}^{N} w_i^k \tag{6.1}$$

$$u^k_{av.b-f} = \frac{1}{M}\sum_{j=1}^{M} w_j^k \,, \tag{6.2}$$

where:

N is the number of points on the soil-foundation contact,

M is the number of points on the building-foundation contact,

$k = \frac{t}{\Delta t}$ is the current time step,

w_i^k is the displacement of the i-th point on the soil-foundation contact at time step k, and

w_j^k is the displacement of the j-th point on the building-foundation contact at time step k.

The amplitudes of the quantities (6.1) and (6.2) for a certain η are

$$A_{av.s-f} = \max_{\forall k} \left| u^k_{av.s-f} \right| \tag{6.3}$$

$$A_{av.b-f} = \max_{\forall k} \left| u^k_{av.b-f} \right| . \tag{6.4}$$

The amplitude at the free surface of the half-space solution is

$$A_{hs} = 2 \cdot \max_{\forall k} \left| u_0^k \right|, \tag{6.5}$$

where u_0^k is the prescribed displacement in time step k at the point x = 0, y = 0, and the normalized amplitudes are

$$\alpha_{b-f} = \frac{A_{av.b-f}}{A_{hs}} \tag{6.6}$$

$$\alpha_{s-f} = \frac{A_{av.s-f}}{A_{hs}}. \tag{6.7}$$

For small η, the amplitudes do not depend upon the angle of incidence γ or upon the stiffness of the foundation and all curves approach 1 as η approaches 0. The pulse occupies all contact points, and in addition the displacement at all of the contact points is approximately equal because of the small spatial gradient $\varepsilon = \frac{\nu}{\beta}$ which is due to small ν. This is in agreement with the energy distribution for long pulses when there is virtually no scattering from the foundation and all of the energy reaching the foundation reaches the building-foundation contact. In Fig. 6.1a, when the incidence is vertical, as the pulse becomes shorter α_{s-f} decreases, which is a consequence of the fact that the pulse does not occupy all contact points simultaneously. When the displacement at the bottom points of the contact reach their peak amplitudes, the pulse has not yet reached the points close to the building-foundation contact, and later, when the other points reach their peak amplitudes, the pulse has passed the former points and their displacements are small. The coefficient α_{s-f} does not depend much

Fig. 6.1a AMPLITUDES OF THE NORMALIZED AVERAGE DISPLACEMENT AT THE CONTACTS

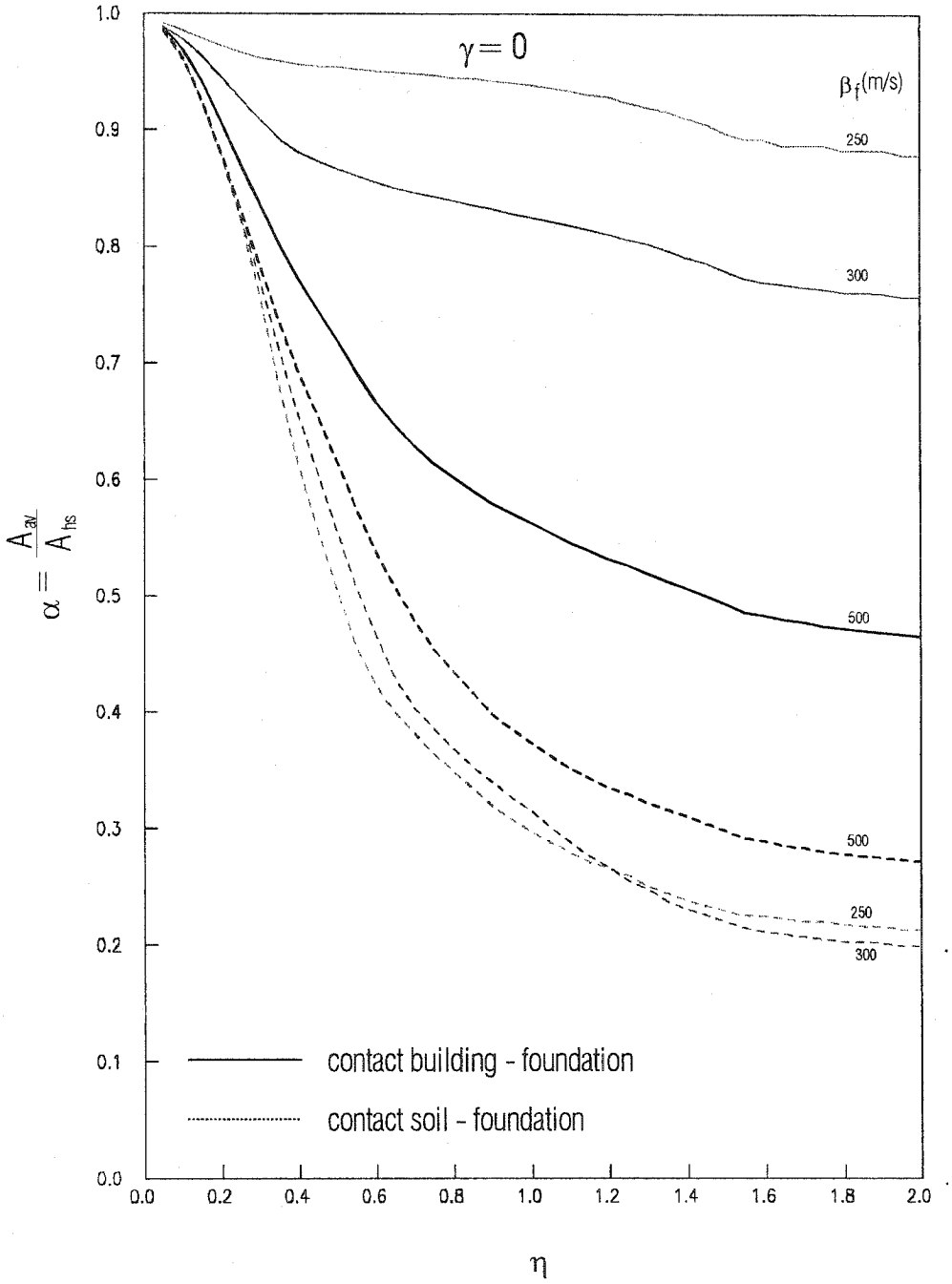

Fig. 6.1b AMPLITUDES OF THE NORMALIZED AVERAGE DISPLACEMENT AT THE CONTACTS

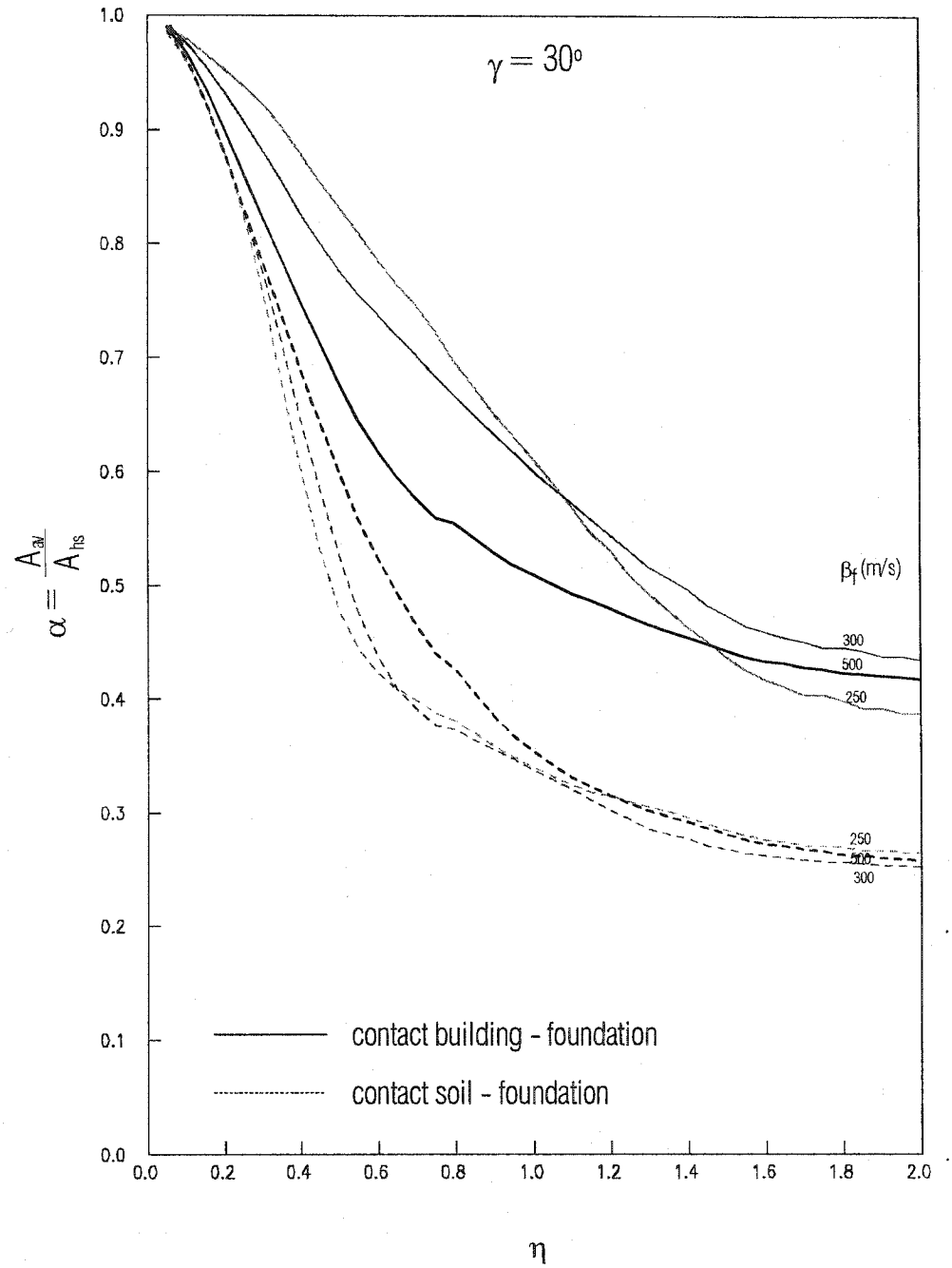

Fig. 6.1c AMPLITUDES OF THE NORMALIZED AVERAGE DISPLACEMENT AT THE CONTACTS

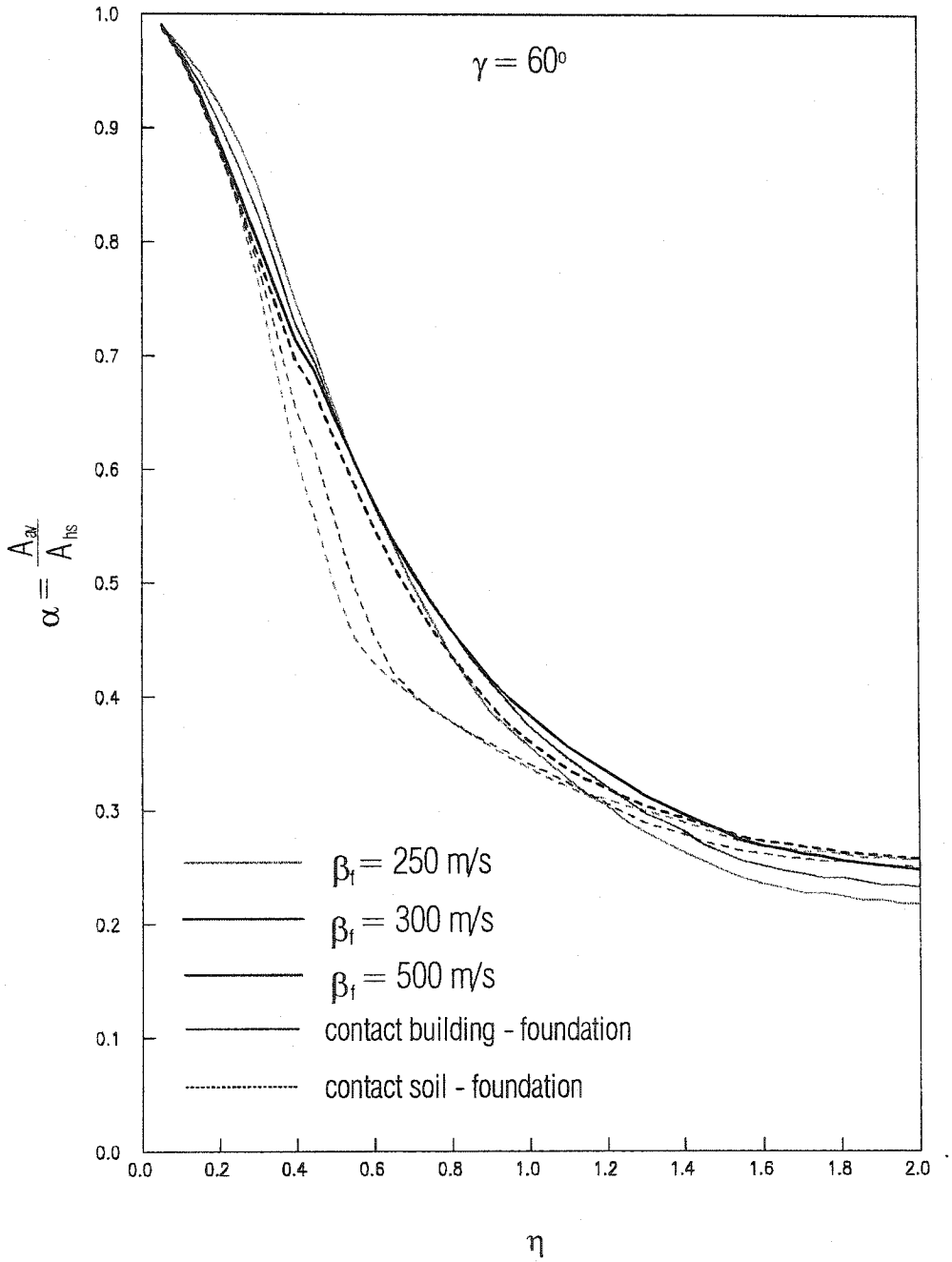

Fig. 6.1d AMPLITUDES OF THE NORMALIZED AVERAGE DISPLACEMENT AT THE CONTACTS

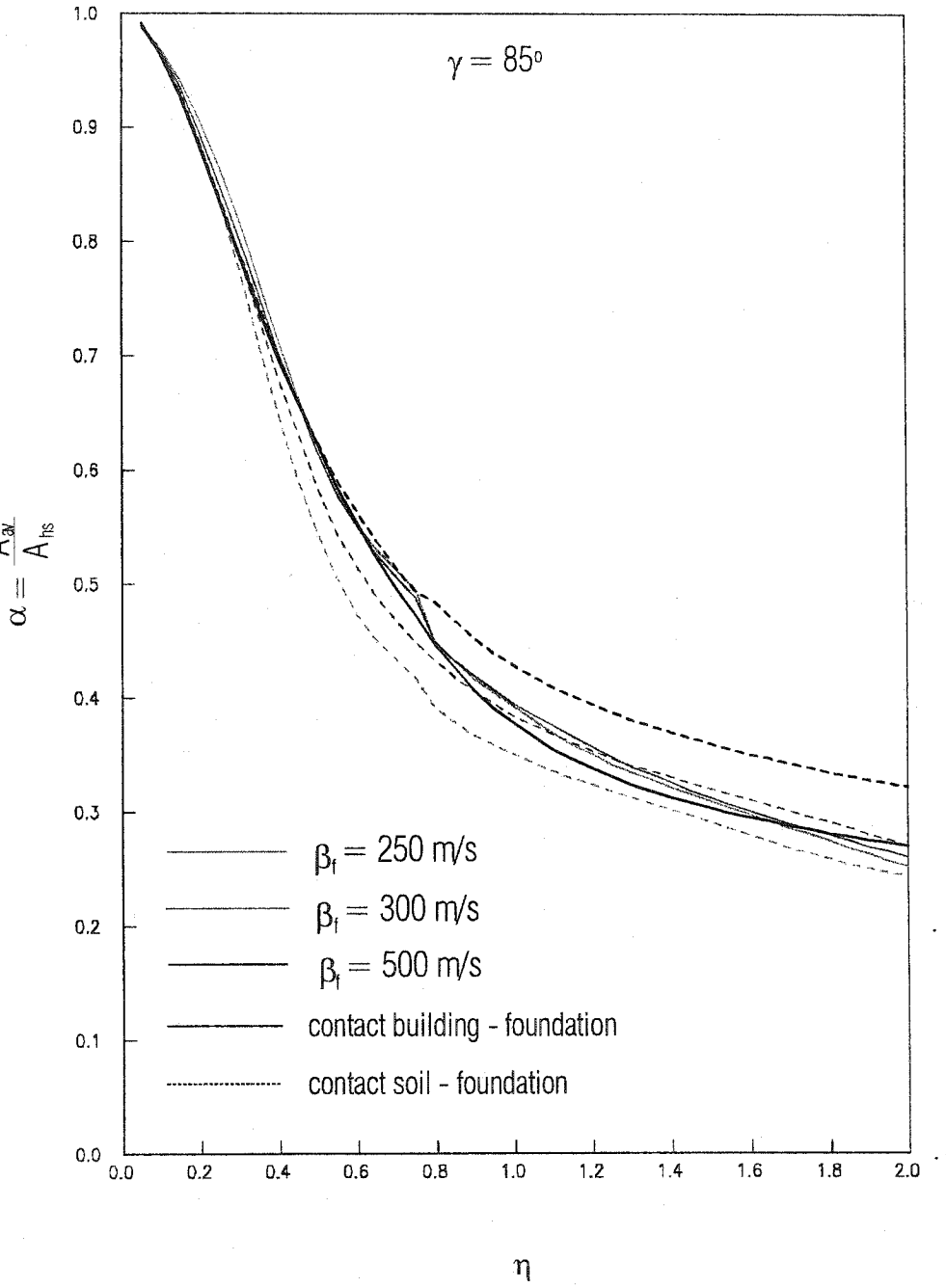

upon the foundation stiffness because there is a trade-off. Because of the larger velocity of propagation, as the foundation become stiffer, more points on the soil-foundation contact reach the zone of peak displacements simultaneously.

This is not so for the building-foundation contact because for vertical incidence, the pulse reaches the points simultaneously. For vertical incidence, the curves $\alpha_{b-f}(\eta)$ depend upon the stiffness of the foundation (parameter β_f). When the stiffness of the foundation is equal to the soil stiffness, there is no scattering from the foundation, and in the previous chapter it was shown that for a soft building the reflected field from the building-foundation contact is almost equal to the incident field. The system behavior is close to the half-space behavior, and α_{b-f} is close to one. For short pulses, there is some decrease of α_{b-f} due to scattering from the building-foundation contact, especially at the corner points, but the amplitudes are still about 90% of the half-space amplitudes.

As the foundation become stiffer, there is a decrease of α_{b-f} due to scattering from the foundation, and α_{b-f} is the smallest for the stiffest foundation. It can be seen that for very short pulses α_{b-f} becomes virtually constant and does not decrease with increasing η. As we concluded in the previous chapter, the foundation behaves like a low-pass filter. As the pulse reaches the cut-off frequency of this "filter", every further increase in the frequency (i.e., decrease in the pulse duration) is irrelevant, and beyond some η (in our example $\eta = 1.7$) the responses α_{b-f} and α_{s-f} are practically constant.

In Figure 6.1b, the same curves are given for incident angle $\gamma = 30^0$. The situation here is more complicated because the angle of incidence appears as an additional factor. Everything that was said for the soil-foundation (s-f) contact at vertical incidence is relevant here, with slightly larger amplitudes at higher frequencies. This can be explained by diffraction around the foundation, which causes the larger part of the incident field to reach the foundation at higher frequencies.

The pulse does not reach all of the points at the building-foundation contact (b-f) simultaneously. The average response is due to the scattering from the foundation, and the distribution of the pulse along the contact points (b-f). At smaller η, the pulse occupies all of the points at the contact b-f with small spatial variations of the displacements due to small v:

$$\varepsilon_x = \frac{v}{\beta_{fx}}. \tag{6.8}$$

At small η, the pulse starts to "feel" first the greater difference in the stiffness between the soil and the foundation. As η increases and the duration of the pulse decreases, due to the increase in the particle velocity at the contact b-f, ε_x increases too, so that the spatial variation of the displacement is larger. From (6.8), this is the most pronounced for the smallest stiffness of the foundation, where ε_x is largest, and it is less pronounced for the higher stiffnesses of the foundation, when ε_x is smaller. At higher η, again the foundation behaves as a low-pass filter, so that α_{b-f} has almost no dependence upon η. In figures 6.1c and 6.1d, the dimensionless amplitudes for angles of incidence $\gamma = 60^0$ and $\gamma = 85^0$ are shown, respectively.

For smaller η, we have the same trends as for $\gamma = 30^0$. The amplitudes at the contact b-f again are the largest for the softer foundation, but the difference is smaller than in the previous case. This is due to larger ε_x because of smaller $\beta_{fx} = \frac{\beta_f}{\sin\gamma}$. The change of the displacement is large along the contact, so that although the pulse occupies all of the contact points, when some of the contact points are in the zone of big displacements, the others are not. This is why the amplitudes of α_{b-f} for these two cases are smaller than for the case $\gamma = 30^0$. For the case $\gamma = 85^0$, it can be seen that there is a further decrease of α_{b-f} in the zone of high frequencies, which means that the foundation still feels the small decrease in t_d and that the foundation cut-off frequency has shifted to higher frequencies.

Everything that has been said about the average amplitudes α holds for the average velocities υ in Figures 6.2a,b,c,d, and only the plots are presented.

In Figures 6.3a,b,c,d the amplitudes at the left end (x' = - a, y' = 0) and at the right end (x' = a, y' = 0) of the b-f contact, normalized by the half-space amplitudes are shown as functions of η. The normalized amplitudes of the left end are shown with a solid line, those of the right end with a dotted line, and the average amplitude for all points of contact b-f with larger dashed lines.

For the softest foundation studied here ($\beta_f = \beta_s = 250m/s$) the amplitude at the left end practically speaking, does not depend upon the incident angle γ, and for larger η it essentially does not depend on η as well. Because there is no foundation, the scattering is due

to the difference between the soil and the building properties and to the existence of the building. The motion of the right end is different because there is attenuation due to scattering from the contact b-f while the pulse traverses the foundation. This loss is greater for larger incident angles when ε_x is larger.

When the properties of the foundation and the soil differ, the amplitudes at the left and right ends depend upon γ and η. In figure 6.3a, when the incidence is vertical, the pulse barely recognizes the foundation. The rays traveling close to the left from the left end and close to the right from the right end do not have contact with the foundation and do not experience loss from scattering. The "inner" rays that encounter the foundation undergo loss due to scattering from the foundation. This loss is greater for stiffer foundations.

As the incident angle increases, at smaller η the amplitude at the right end becomes larger than the amplitude at the left end. This is especially pronounced for stiffer foundations and larger angles of incidence. To explain this trend, we consider a simplified model of a stiff disk supported on elastic soil with the wave incidence from the left (Fig. 6.4). The stiffness of the disk is greater than the stiffness of the soil. If the disk had infinite stiffness, points A and B would have the same displacement.

In Figure 6.4b (view of the disk from above) after half of the pulse has entered into the disk there is maximum displacement at point A. As can be seen from this figure, the elastic forces in the disk resist the imposed motion. In the first quarter-cycle of the motion of point A, $\frac{\pi}{t_d} t_A \leq \frac{\pi}{4}$, the motion of the disk points is smaller than the ground motion at point A. The

Fig. 6.2a AMPLITUDES OF THE NORMALIZED AVERAGE VELOCITIES AT THE CONTACTS

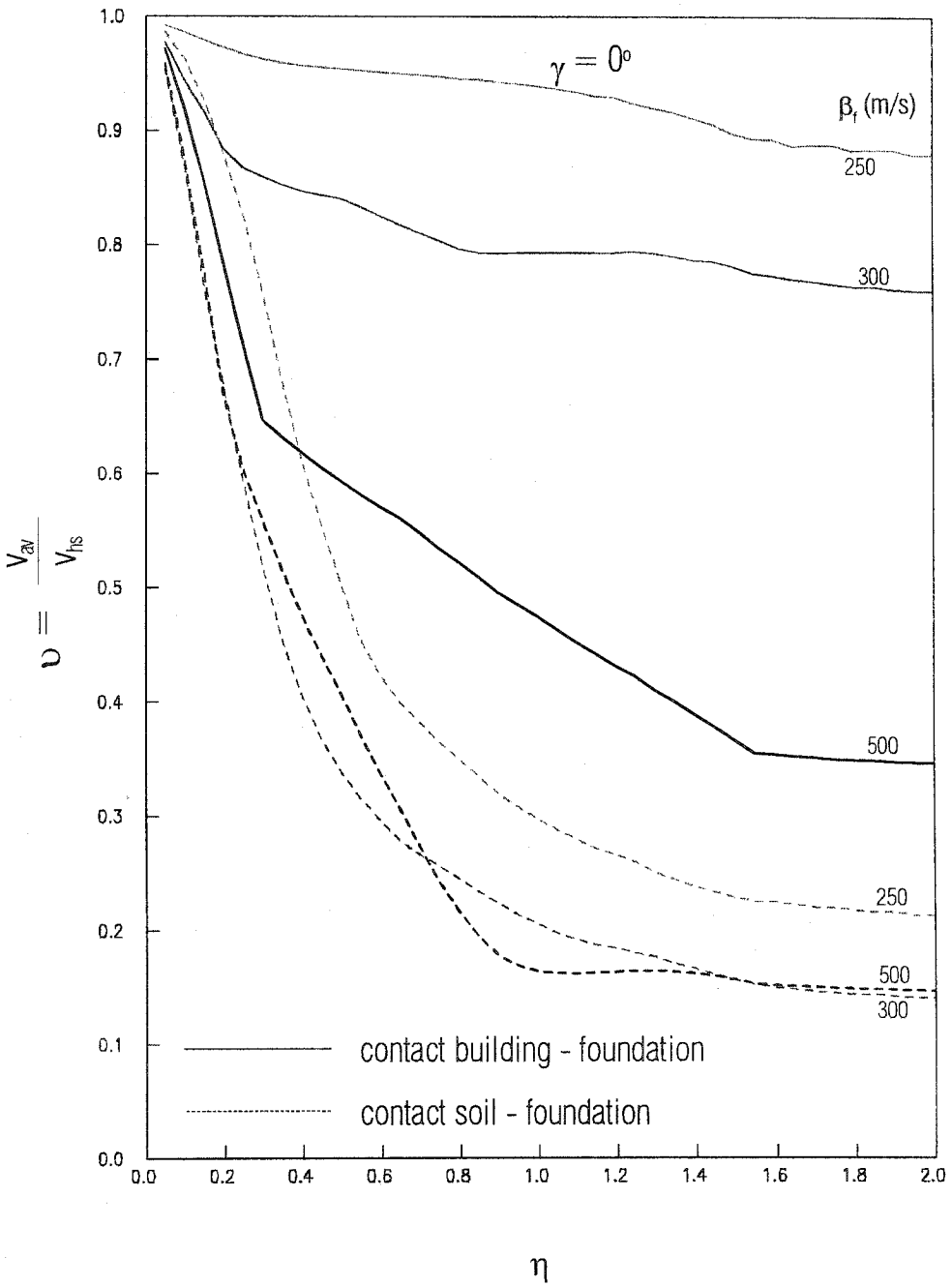

Fig. 6.2b AMPLITUDES OF THE NORMALIZED AVERAGE VELOCITIES AT THE CONTACTS

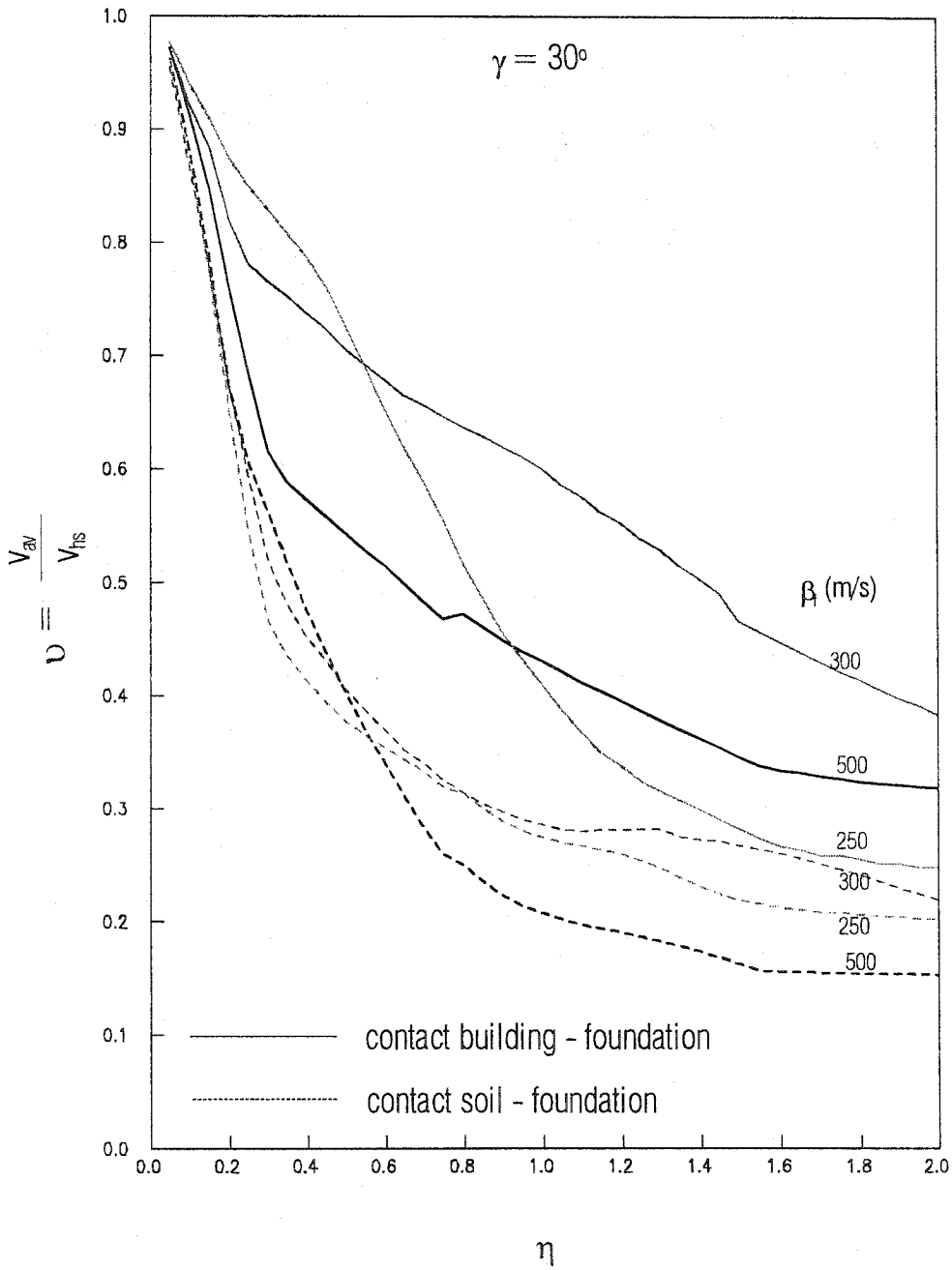

Fig. 6.2c AMPLITUDES OF THE NORMALIZED AVERAGE VELOCITIES AT THE CONTACTS

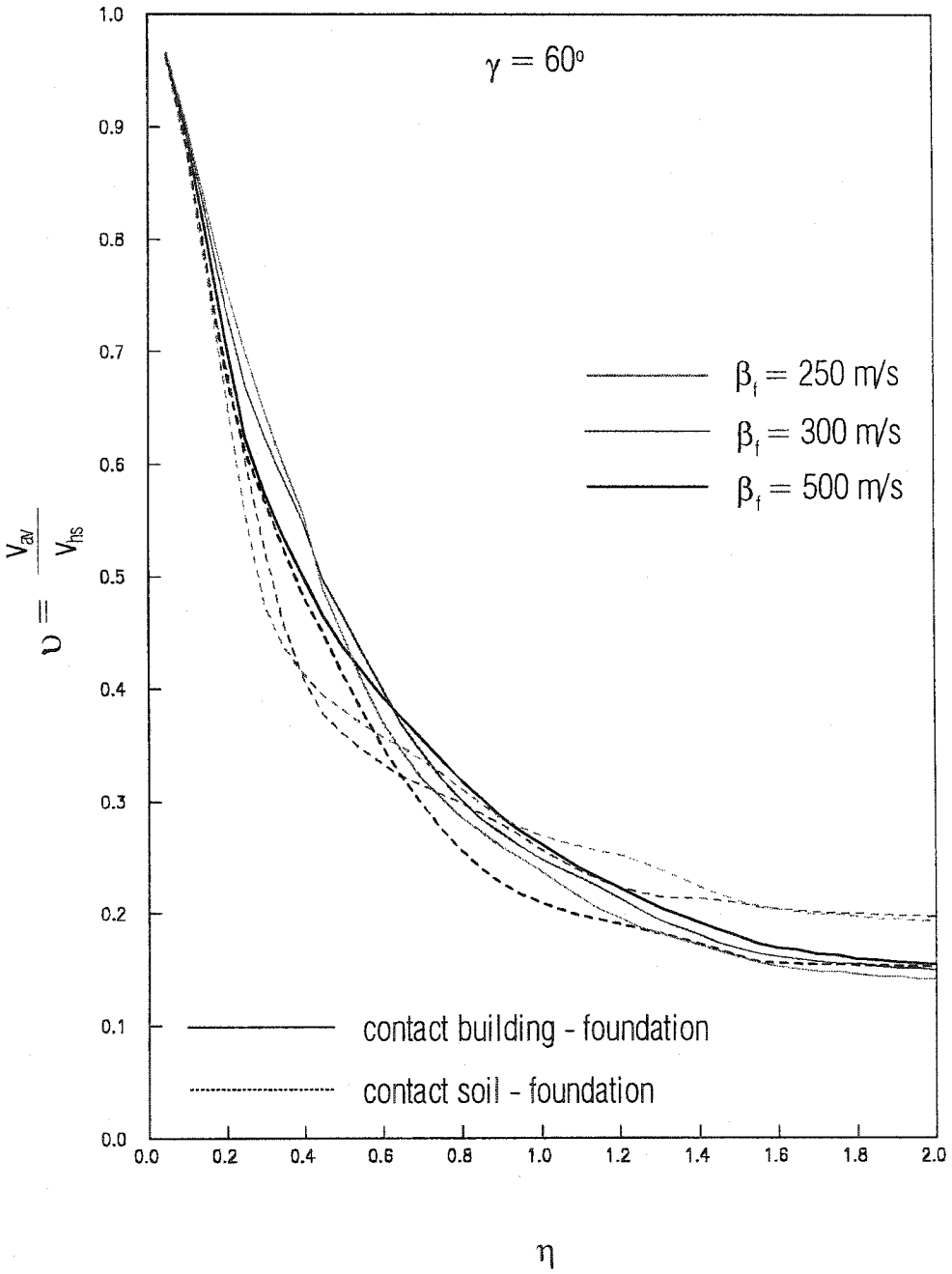

Fig. 6.2d AMPLITUDES OF THE NORMALIZED AVERAGE VELOCITIES AT THE CONTACTS

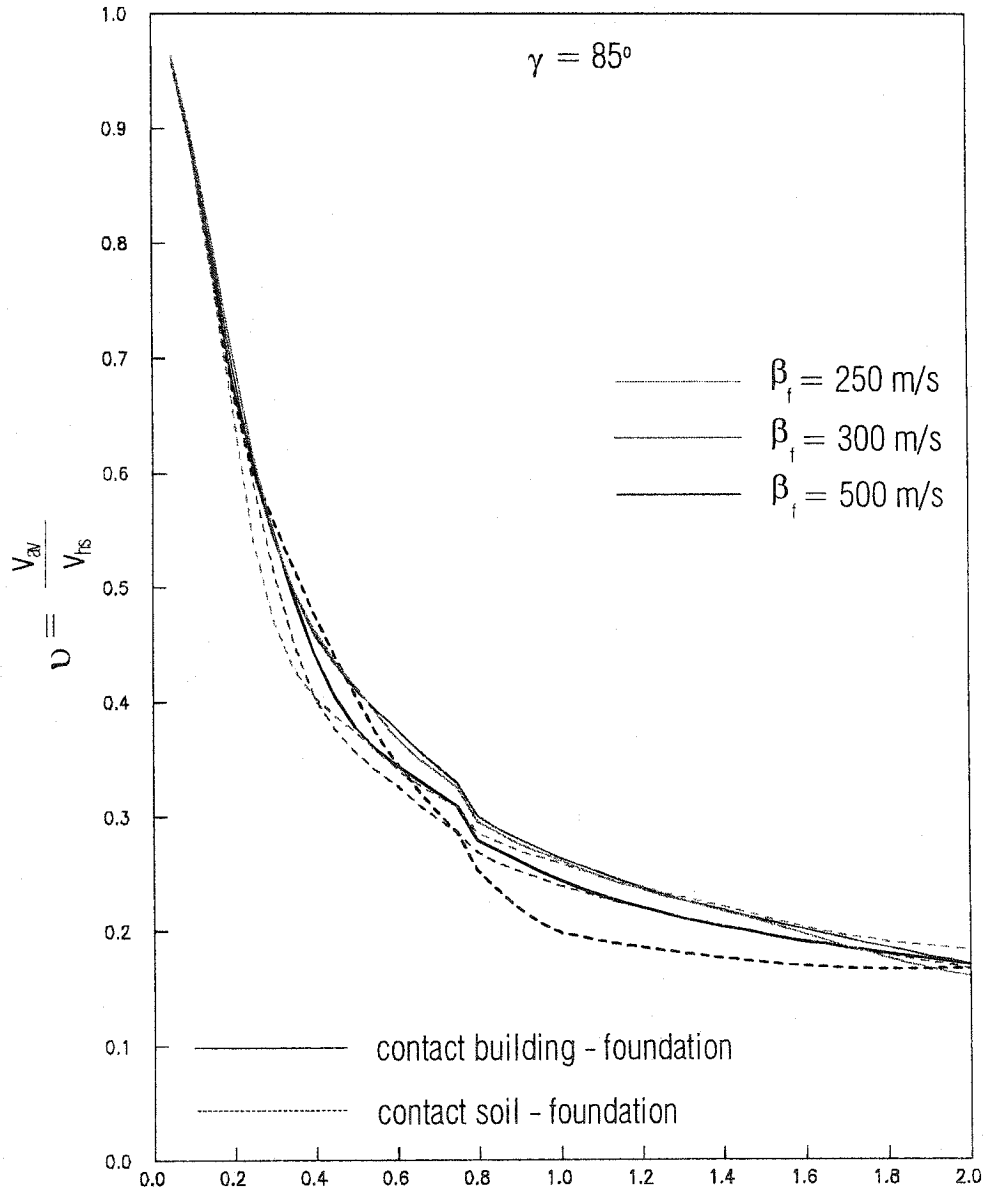

Fig. 6.3a NORMALIZED AMPLITUDES AT LEFT AND RIGHT ENDS OF THE BUILDING - FOUNDATION CONTACT

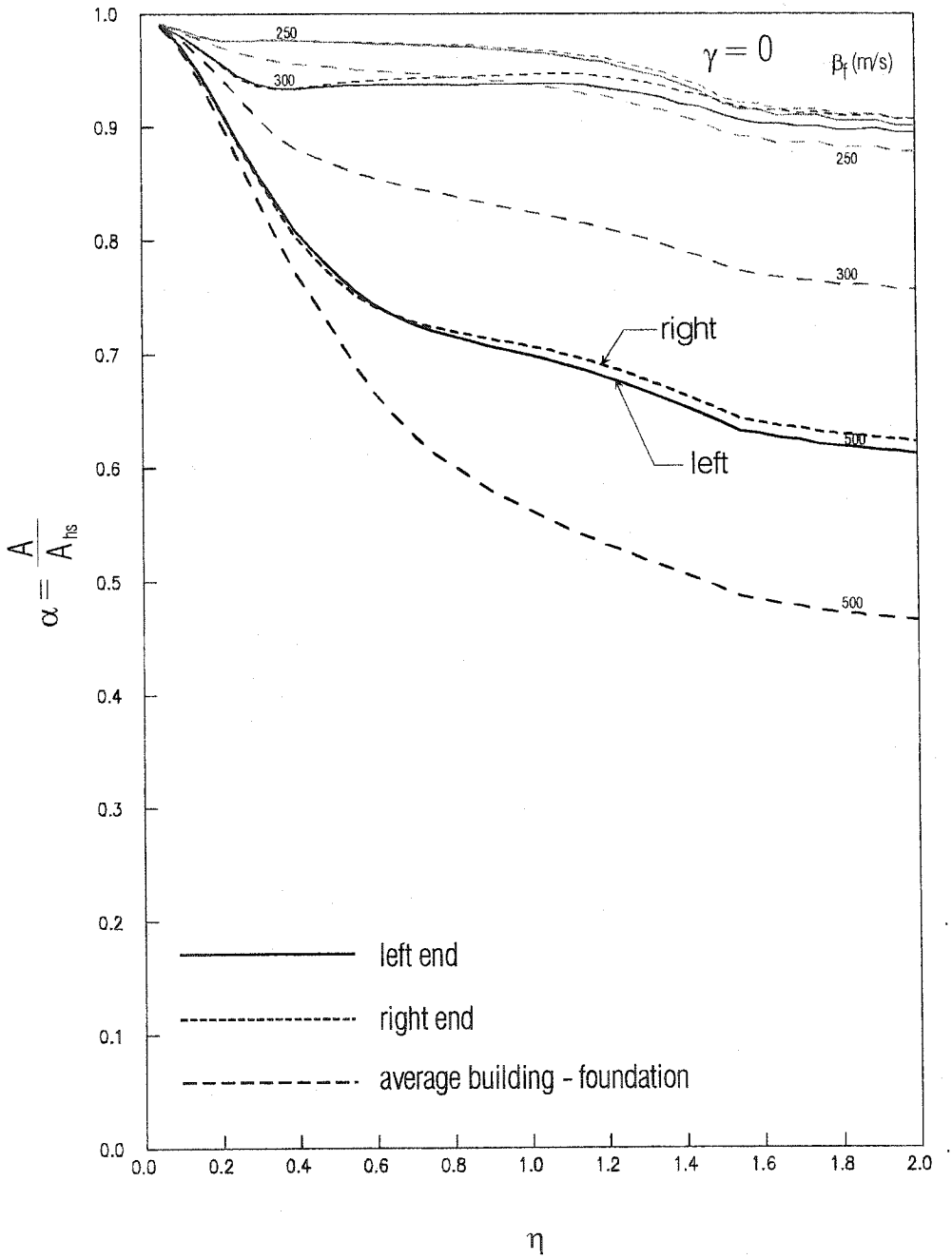

Fig. 6.3b NORMALIZED AMPLITUDES AT LEFT AND RIGHT ENDS OF THE BUILDING - FOUNDATION CONTACT $\gamma = 30^{o}$

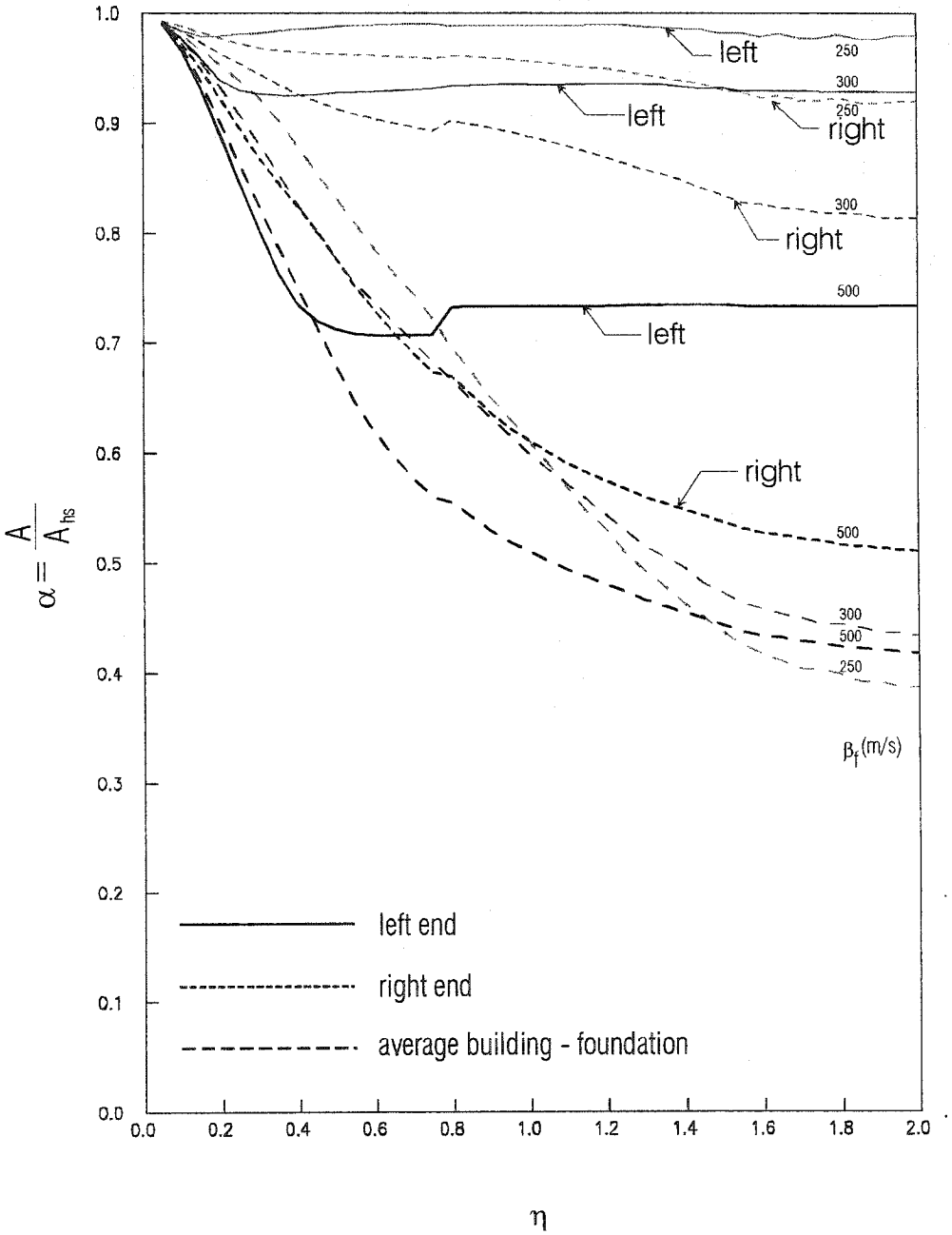

Fig. 6.3c NORMALIZED AMPLITUDES AT LEFT AND RIGHT ENDS OF THE BUILDING - FOUNDATION CONTACT $\gamma = 60^{o}$

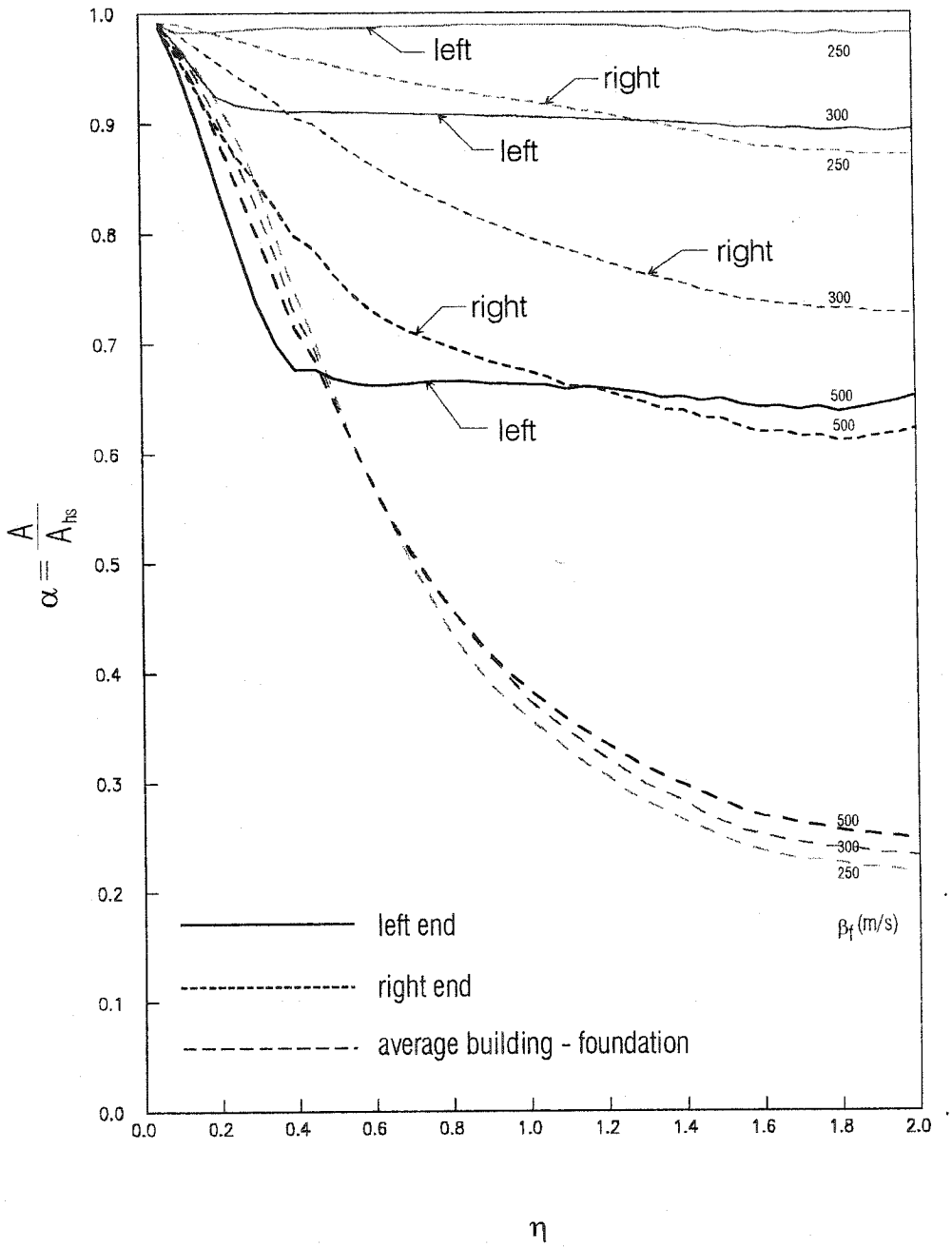

Fig. 6.3d NORMALIZED AMPLITUDES AT LEFT AND RIGHT ENDS OF THE BUILDING - FOUNDATION CONTACT $\gamma = 85^{o}$

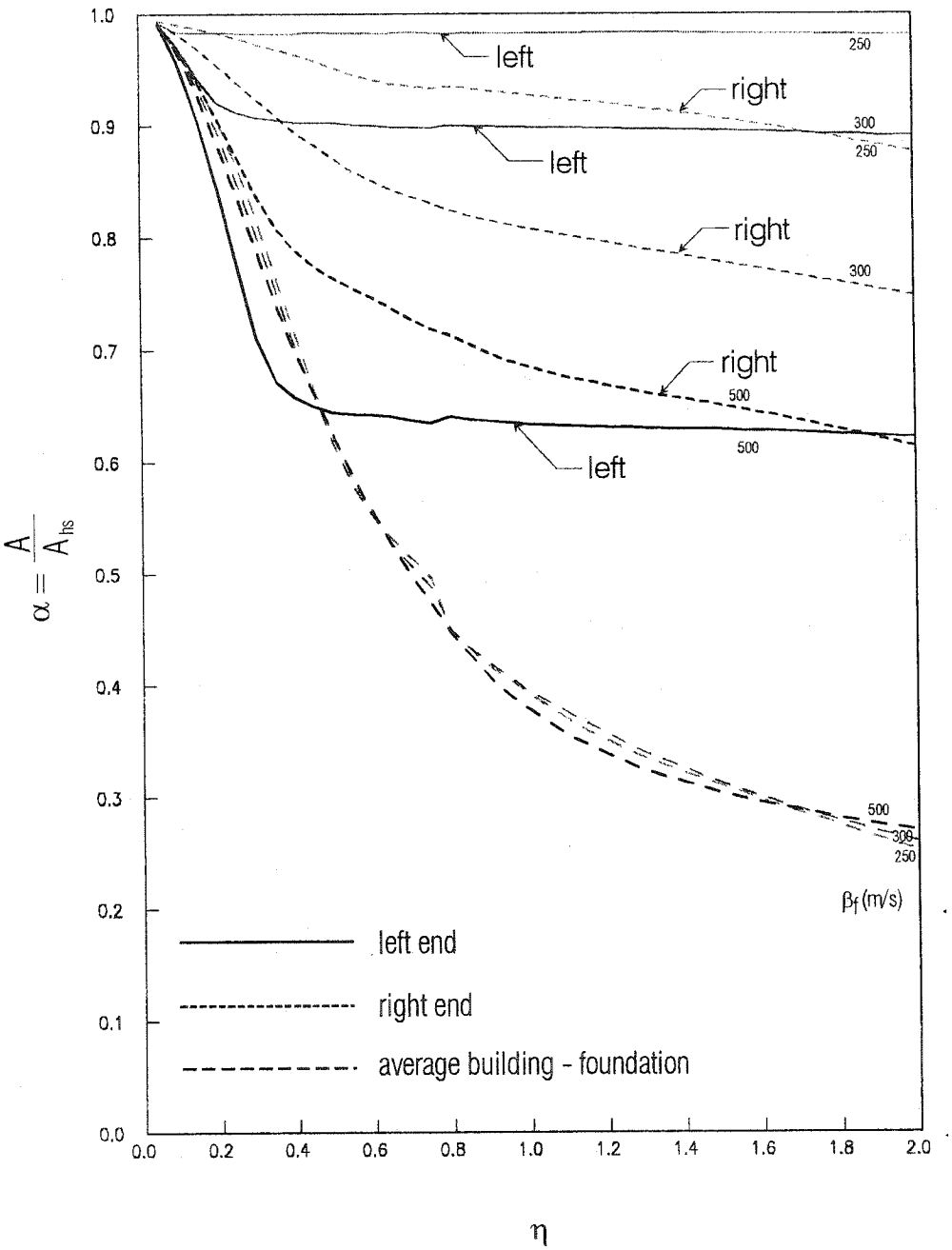

elastic forces in the disk diminish the amplitude at A. On the other side, in Figure 6.4c, as the wave progresses to right, the elastic forces act in the same direction as the soil motion, and this increases displacement at A. The elastic forces in this instant of convex deformation of the disk amplify the motion at B.

The behavior of our model is similar to the above simple example, because in the case of the soft building (e.g., Holiday Inn) it does not change the incoming half-space field significantly. This model can also explain why the motion at point B (at the right end) in the Figures 4.2 to 4.5 has the largest amplitudes in the steady-state response analysis of the Hollywood Storage building, for intermediate frequencies, in Chapter IV. As the pulse becomes short enough so that the motion at the left end reaches the peak amplitude before the right end starts to move, the amplitude at the left end can become larger because of additional losses of energy due to scattering from the building-foundation contact while the pulse travels from point A to point B. The above example and explanations are further supported by the results shown in Fig. 6.5. In this figure, the time histories of the displacements at point A (x' = - a, y' = 0) and point B (x' = a, y' = 0) are shown for $\gamma = 60^0$ and for two values of the dimensionless frequency, $\eta = 0.5$ and $\eta = 1.8$. For $\eta = 0.5$, the influence of the elastic forces in the building are so strong for the motion at point A that it cannot reach the zero displacement immediately after unloading (passage of the wave). It receives loads from the building near point B, and when the motion at B becomes equal to the motion at A both points pass the zero line almost simultaneously. For $\eta = 1.8$, the pulse has completely passed the left end (point A) before it reaches the right end. The pulses are separated, and the amplitude of the right end is

Fig. 6.4 MODEL : DISK SITTING ON HALF-SPACE

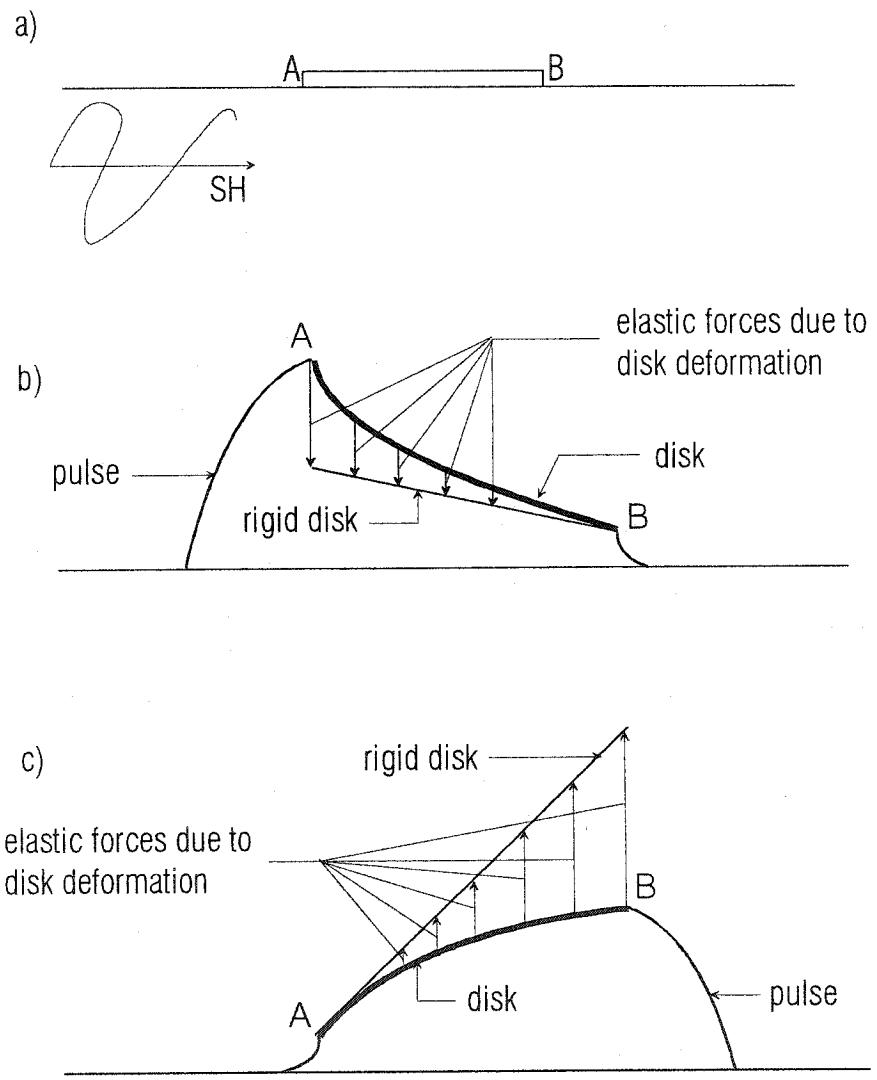

Fig. 6.5 TIME HISTORIES OF THE MOTION AT LEFT AND RIGHT ENDS OF THE BUILDING-FOUNDATION CONTACT $\beta_f = 500$ m/s

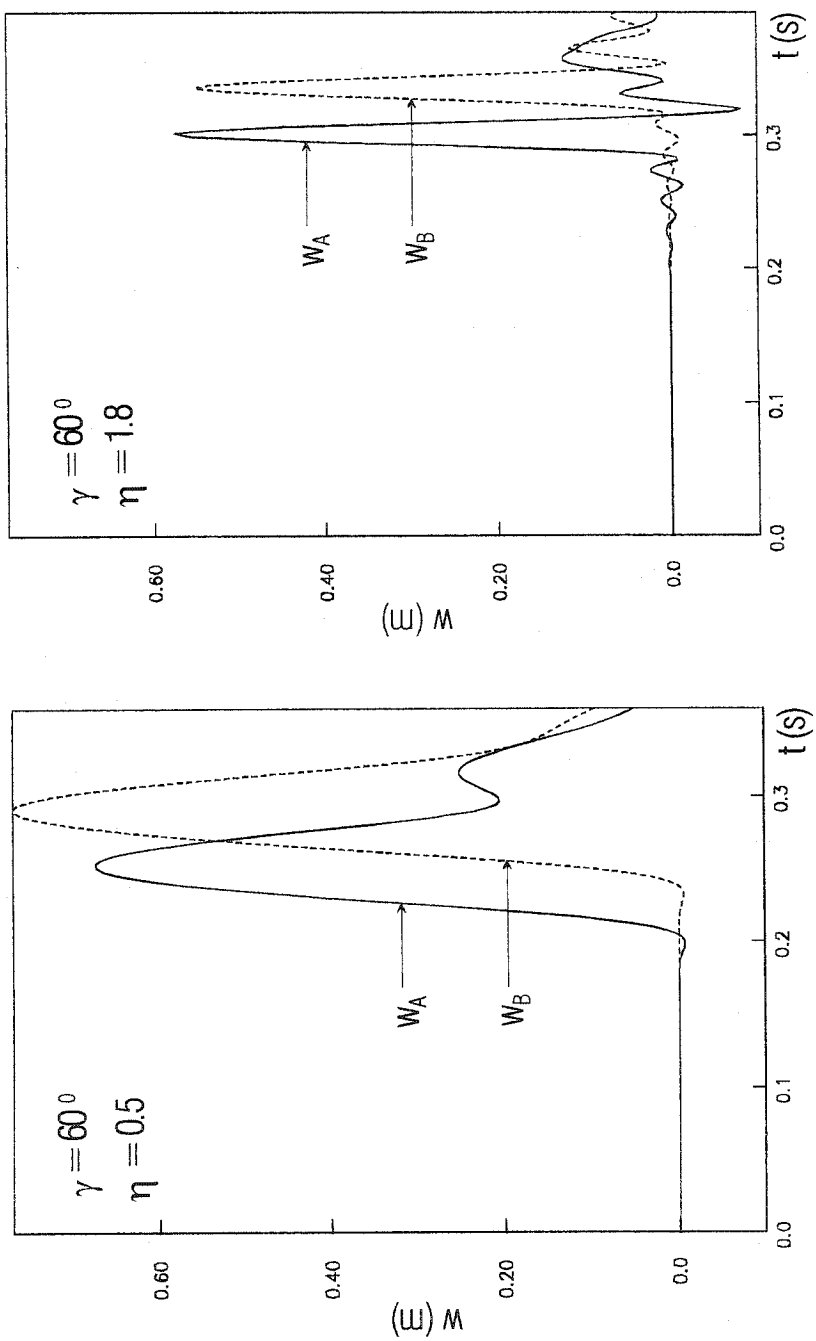

slightly smaller due to the local losses of energy through scattering on the way from point A to point B.

6.2 Conclusion

In this chapter, some examples were presented for excitation by strong ground motion pulses to help in the use of such pulses in the design of earthquake-resistant structures. A simple, single, half-sine pulse was considered. The strong ground motion in the free field can be seen as a train of such pulses, and the total foundation response then consists of superposition of the responses of each pulse in the train. With data on how such pulses are modified in different buildings, the least squares method can be used to construct an empirical formula that will describe the pulse amplitudes entering the buildings. The parameters in this formula should include the angle of incidence; the stiffness of the soil, the foundation, and the building; and the geometry of the foundation. Development of such an empirical equation is beyond the scope of this thesis.

CHAPTER VII

NONLINEAR ANALYSIS

7.0 Model

In the real world, parts of our model will undergo nonlinear deformations and permanent strains during the wave passage. For simplicity, we here consider nonlinear response in the soil only, while the foundation and the building will remain linear. The model is the one shown in Figure 7.1, in which points A and B in the soil, as well as the points 1, 2, 1', 2' and S are allowed to undergo permanent strain when the strain exceeds some prescribed maximum elastic strain ε_m. We assume that in one direction a point in the soil can yield and in the perpendicular direction it can remain linear. That is, the shear stress in the x direction depends only upon the shear strain in the same direction and is independent of the shear strain in the y direction (and vice versa for the y direction). The motivation for this assumption comes from our simplified representation of layered soil, which is created by deposition (floods and wind) into more or less horizontal layers. The soil is assumed to be ideally elastoplastic, and the constitutive $\sigma - \varepsilon$ diagram is shown on Fig. 7.1a. It is assumed that the contacts remain bonded during the analysis and that the contact cells C, D, E, F, G, and H in Figure 7.1 remain linear, as does the zone next to the artificial boundary (the bottom four rows and the left-most and right-most four columns), as was described in Section 3.2. A question arises how to choose the strain ε_m (Fig.7.1a).

Fig. 7.1 MODEL WITH NONLINEAR SOIL

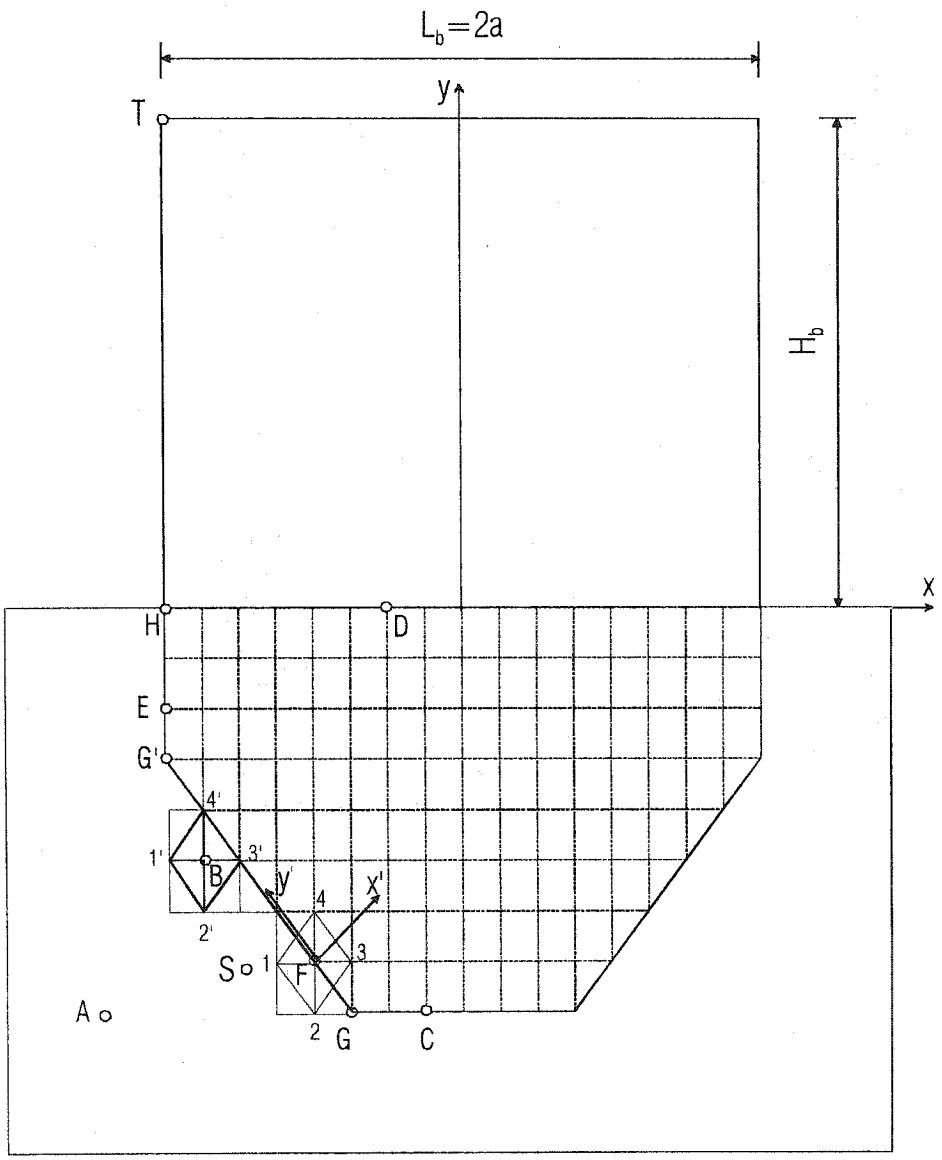

Fig. 7.1a CONSTITUTIVE LAW σ - ε
FOR NONLINEAR SOIL

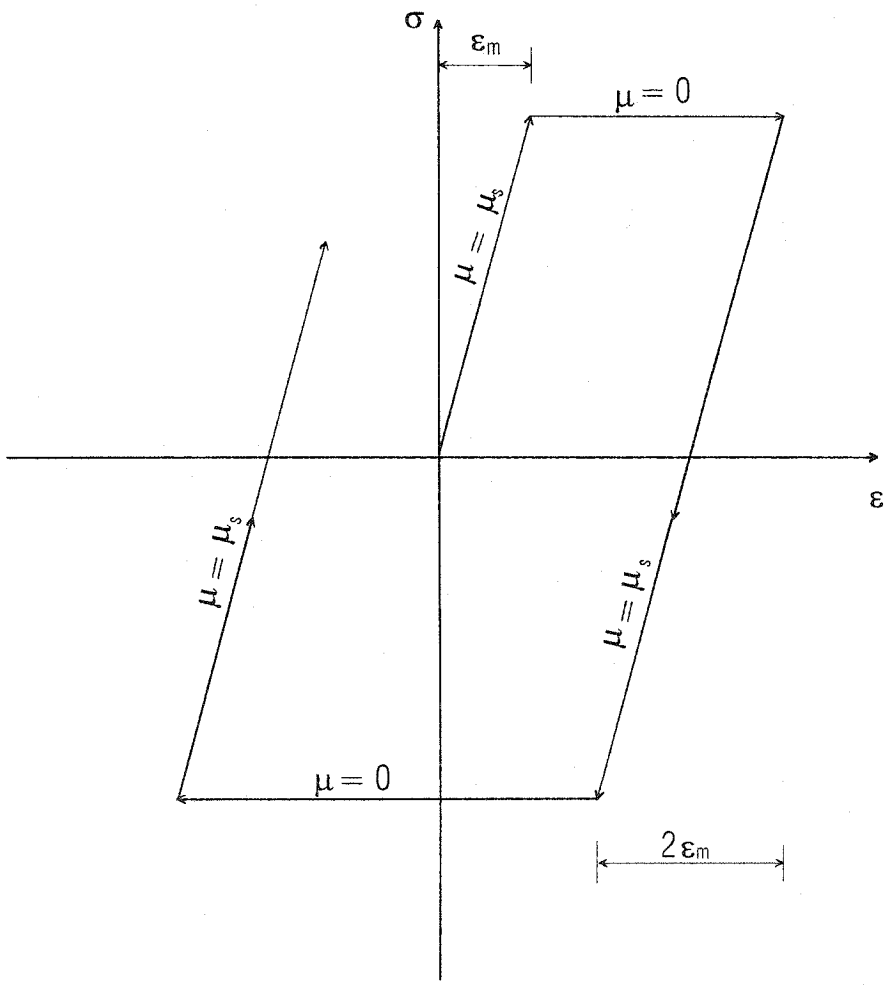

The velocity in the soil points due to passage of the plane wave (5.4) is

$$v = \dot{w} = \frac{\pi}{t_{d0}} A \cos \frac{\pi t}{t_{d0}}, \tag{7.1}$$

and the maximum strain in the direction of propagation of the plane wave is

$$|\varepsilon| = \frac{v_{\max}}{\beta_s} = \frac{\pi A}{\beta_s t_{d0}}. \tag{7.2}$$

If for a given input plane wave we choose the maximum strain ε_m, given by (7.2), the strains in both directions may remain linear before the wave reaches the free surface or the foundation. We will call this case "intermediate nonlinearity."

If we want to analyze only the nonlinearity due to scattering and radiating from the foundation, we should avoid the occurrence of the nonlinear strains due to the half-space boundary, including both the incoming and the reflected waves. Then we may choose

$\varepsilon_m = \max\left(\frac{2\pi A \sin\gamma}{\beta_s t_{d0}}; \frac{2\pi A \cos\gamma}{\beta_s t_{d0}}\right)$. We call this case "small nonlinearity."

If the soil is allowed to undergo permanent strains only due to wave passage of incident waves in the full space, then we may choose the maximum strain

$\varepsilon_m < \max\left(\frac{\pi A \sin\gamma}{\beta_s t_{d0}}; \frac{\pi A \cos\gamma}{\beta_s t_{d0}}\right)$. This condition guarantees that in either x or the y direction the soil will undergo permanent strains during the passage of the plane wave.

This yielding strain can be written as

$$\varepsilon_m = C \frac{v_{\max}}{\beta_s} = C \frac{\pi A}{\beta_s t_{d0}}, \tag{7.3}$$

where C is a constant that controls the yielding stress (strain) in the soil. We have the following cases of nonlinearity, depending upon C:

1. $C > 2$: **Small nonlinearity**. Permanent strain does not occur until the wave hits the foundation with any angle of incidence.
2. $1 \leq C \leq 2$: **Intermediate nonlinearity**. Permanent strain does not occur until the wave is reflected from the free surface or is scattered from the foundation, for any angle of incidence. Permanent strain will or will not occur after the reflection of the incident wave from the free surface depending, upon the angle of incidence.
3. $C < 1$: **Large nonlinearity**. Permanent strain occurs after reflection from the free surface. Permanent strain may or may not occur before the wave reflects from the free surface, depending upon the angle of incidence.

7.1 Distribution of the energy and the permanent strains

In Chapter V the distribution of the energy was illustrated for two different buildings, for SH waves with an angle of incidence $\gamma = 30^0$, and for four different dimensionless frequencies. Here we consider the same two buildings with the same dimensionless frequencies, for two different angles of incidence $\gamma = 30^0$ and $\gamma = 60^0$, and for intermediate nonlinearity in the soil (C = 1.5).

In Figures 7.2a,b, the energy distribution in the system is shown for HSB for angles of incidence of 30^0 and 60^0, respectively, and in 7.3a,b the energy distribution is shown for HIH for the same angles of incidence. In the linear case (Fig.5.3a,b), the energy components that balanced the total input energy entering the model were the total energy exiting the model and some small residual energy in the building at the end of the simulation. Here, we have additional component of the energy, which is lost to develop permanent strains at the points of the soil where this nonlinear strain occurs. This energy, called hysteretic energy, is computed from

$$E_{hys} = \sum_{i=1}^{N} \left(\sigma_{xi} \Delta\varepsilon_{xpi} + \sigma_{yi} \Delta\varepsilon_{ypi} \right), \tag{7.4}$$

where:

N is the total number of soil points,

σ_{xi}, σ_{yi} are the stresses at the point i in the x and y directions, respectively,

$\Delta\varepsilon_{xpi} = \varepsilon_{xpi}^{t+\Delta t} - \varepsilon_{xpi}^{t}$ is the increment of the permanent strain in the x direction at point i, and

$\Delta\varepsilon_{ypi} = \varepsilon_{ypi}^{t+\Delta t} - \varepsilon_{ypi}^{t}$ is the increment of the permanent strain in the y direction at point i.

The hysteretic energy balances the system energy. The numerical computation error can be expressed as

$$\varepsilon = \frac{E_{inp} - \left(E_{out} + E_{hys} \right)}{E_{inp}} \cdot 100 \ (\%) \tag{7.5}$$

with same definition for E_{inp} and E_{out} as in Chapter V.

Fig. 7.2a ENERGY DISTRIBUTION IN MODEL WITH NONLINEAR SOIL : HOLLYWOOD STORAGE BUILDING $\gamma = 30^0$

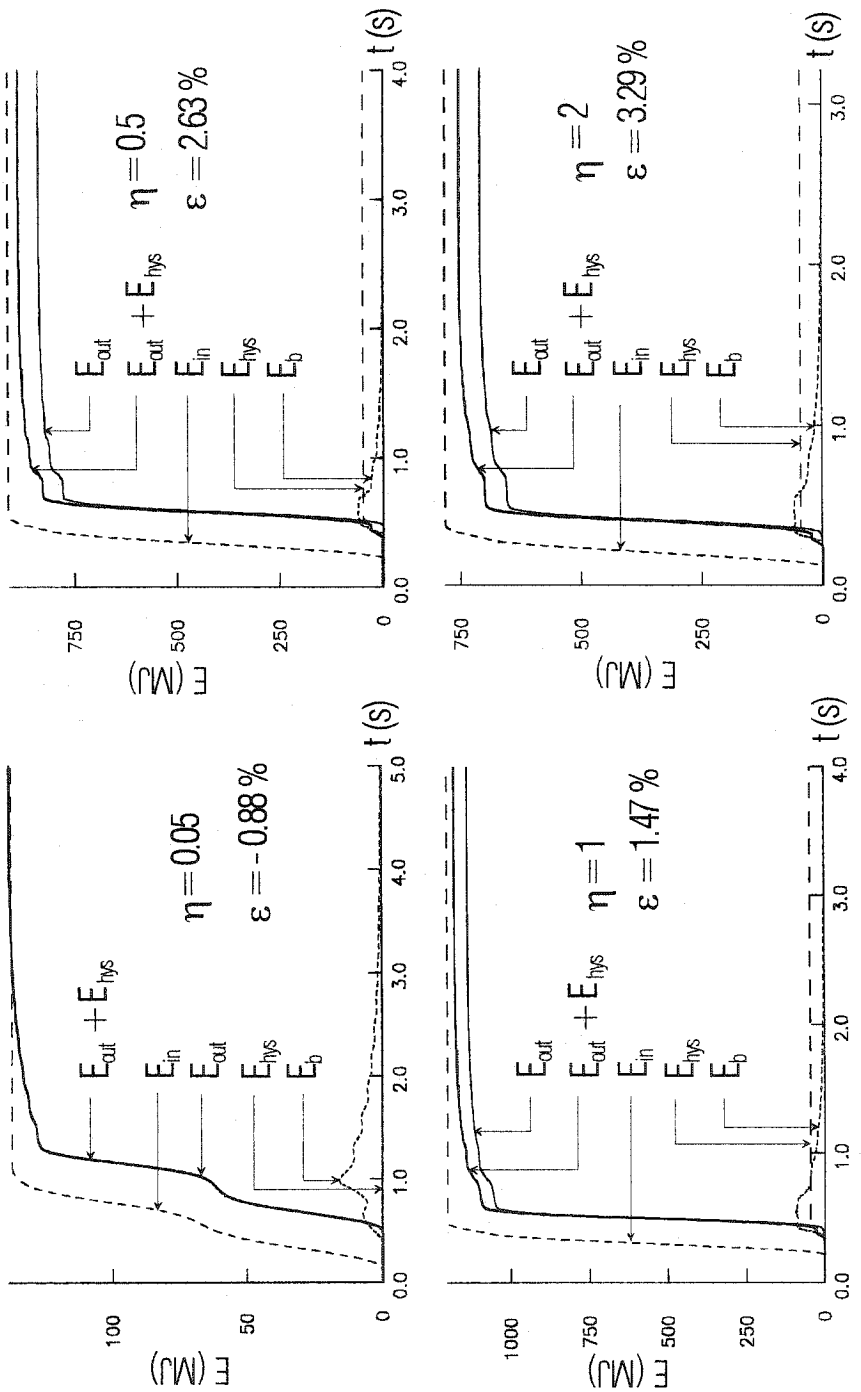

Fig. 7.2b ENERGY DISTRIBUTION IN MODEL WITH NONLINEAR SOIL :
HOLLYWOOD STORAGE BUILDING $\gamma = 60^0$

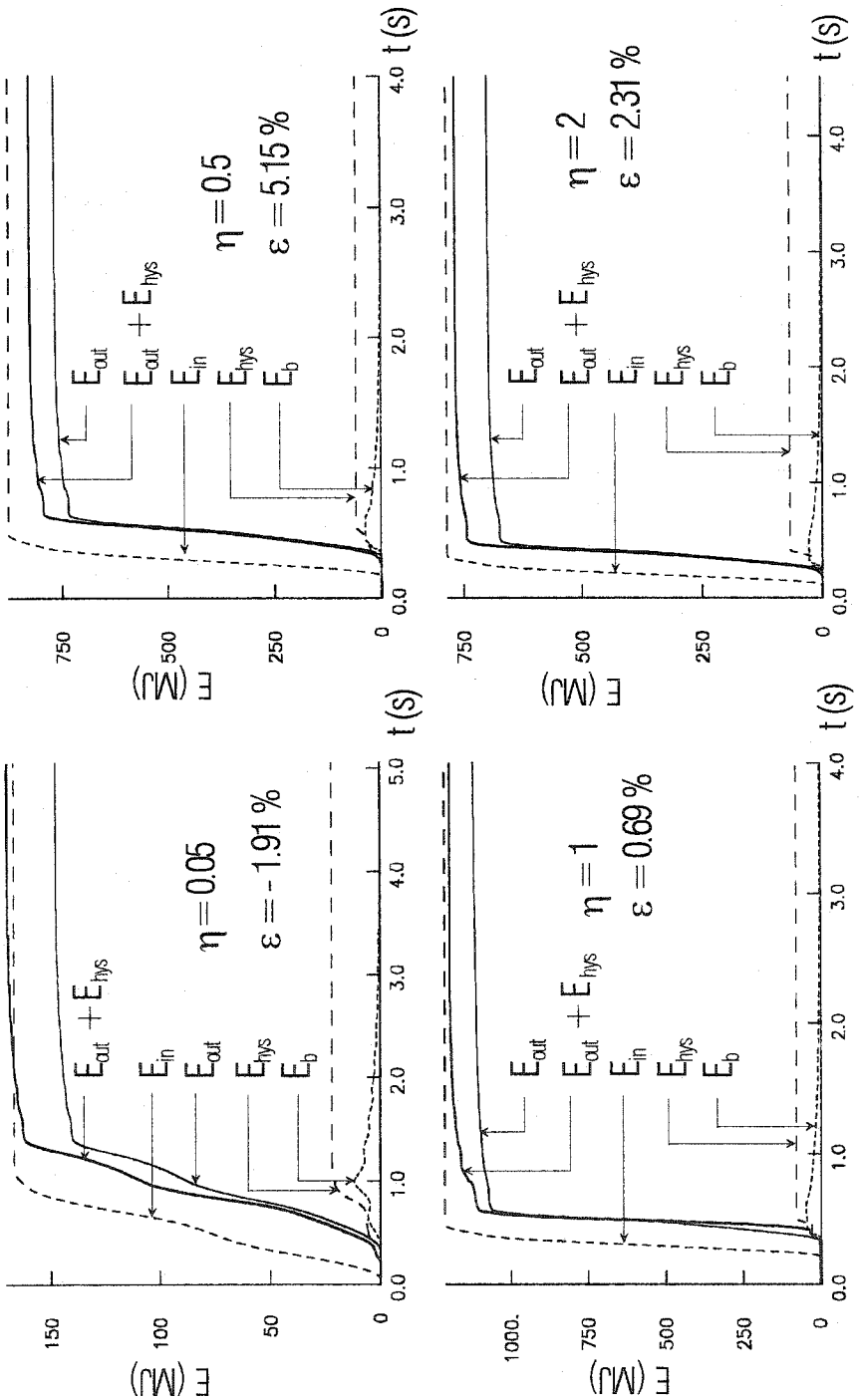

Fig. 7.3a ENERGY DISTRIBUTION IN MODEL WITH NONLINEAR SOIL :
HOLIDAY INN HOTEL $\gamma = 30^0$

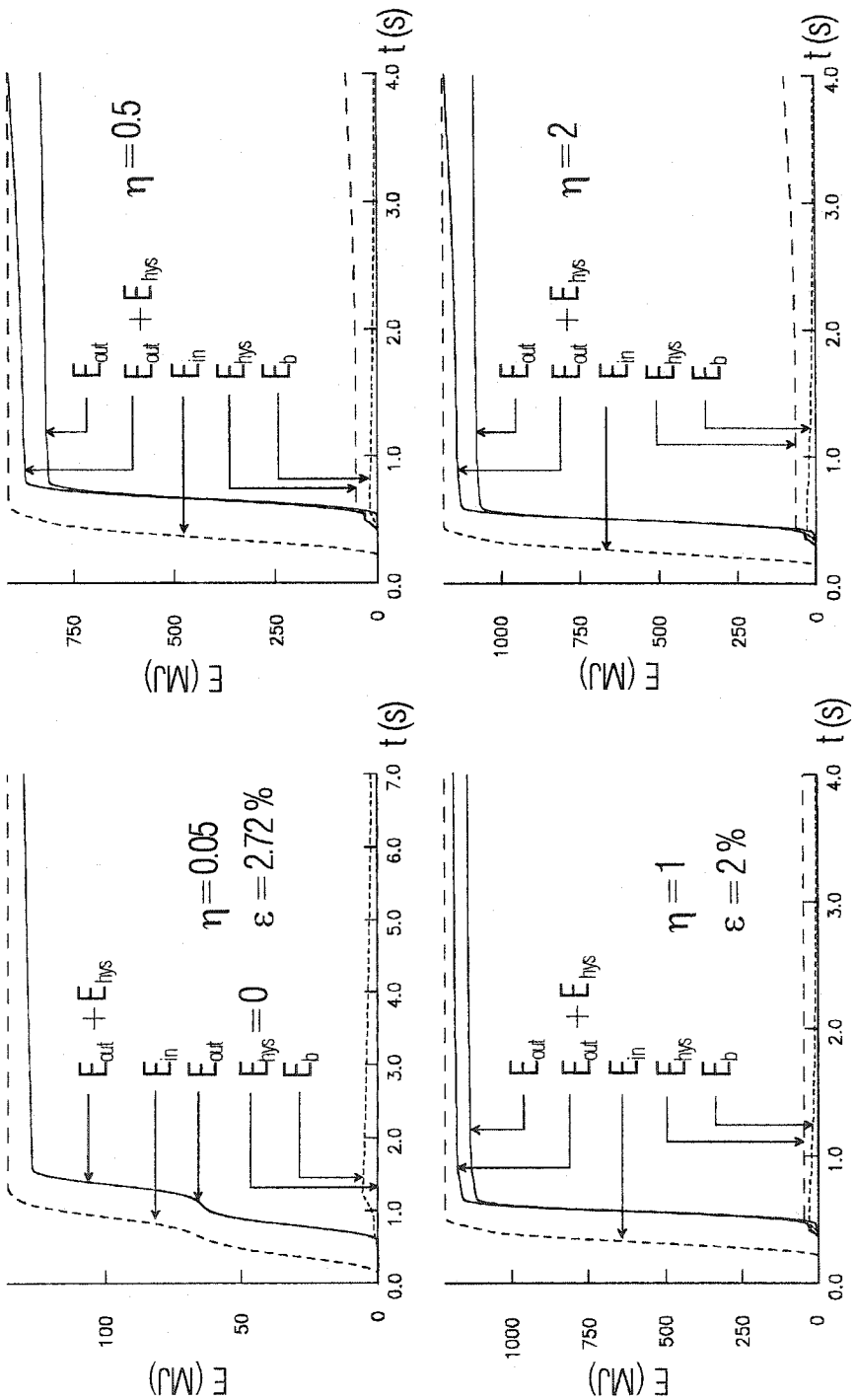

Fig. 7.3b ENERGY DISTRIBUTION IN MODEL WITH NONLINEAR SOIL:
HOLIDAY INN HOTEL $\gamma = 60^0$

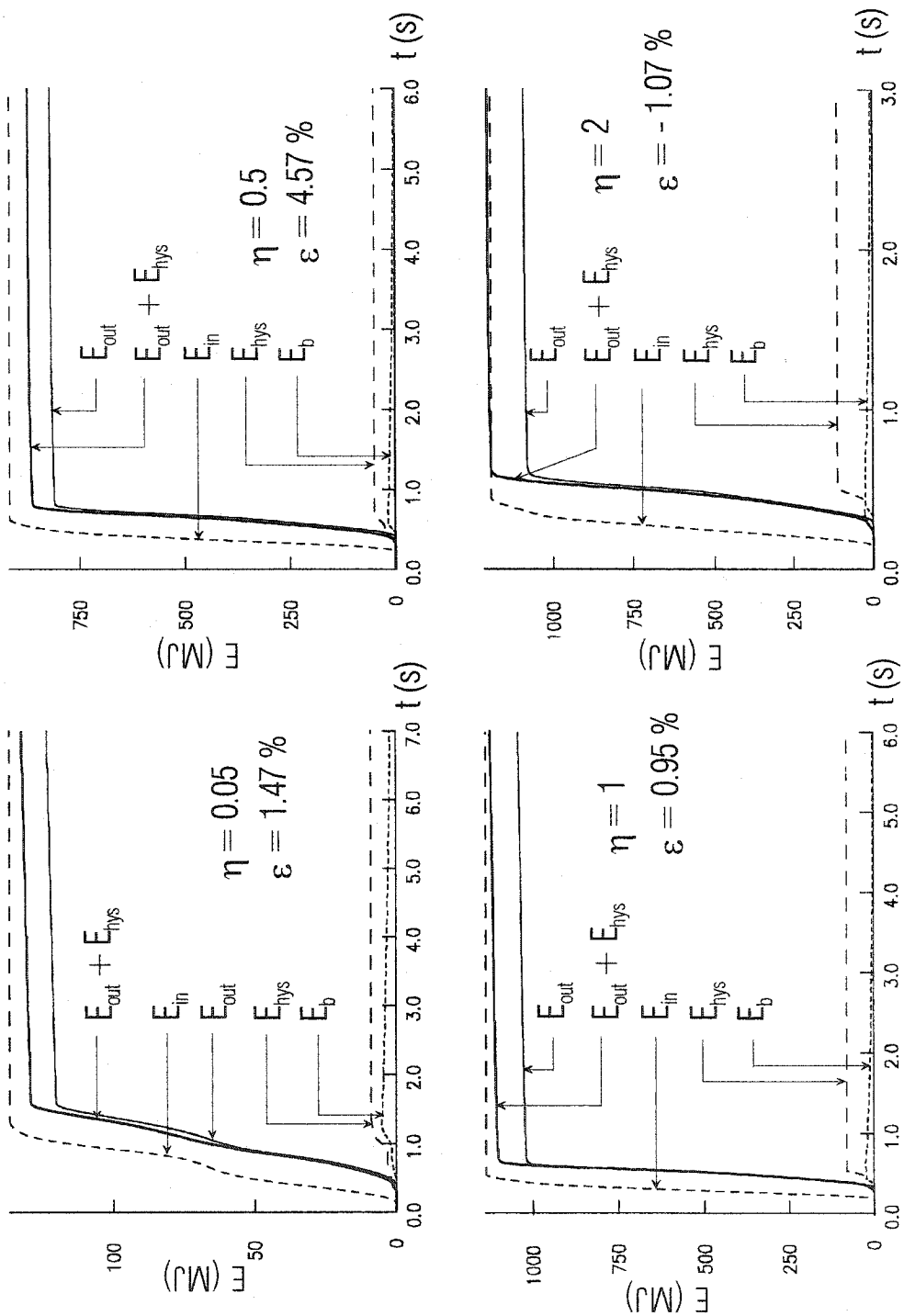

The energy distribution for HSB is shown in Figures 7.2a and 7.2b for the angles of incidence $\gamma = 30^0$ and $\gamma = 60^0$, respectively. The thick curve shows the sum $E_{out} + E_{hys}$ that balances the input energy. For $\gamma = 30^0$ and small η the hysteretic energy is practically zero. As the incident wave pulse becomes shorter, the hysteretic energy is developed and, for this case the hysteretic energy is between 4 and 6 percent of the input energy. For all η, the total hysteretic energy is smaller than the maximal instantaneous energy in the building. For $\gamma = 60^0$, the hysteretic energy is larger than for $\gamma = 30^0$, about 6 to 9 percent of the input energy and up to 15 percent of the input energy for the smallest considered η. In this case, in contrast to the case $\gamma = 30^0$, the hysteretic energy is larger than the maximal instantaneous energy in the building. The maximum E_b is smaller for $\gamma = 60^0$ than for $\gamma = 30^0$. As can be seen from the plots, once the hysteretic energy reaches its maximum it remains flat until the end of the analysis. This is because 100 percent of the permanent strain is developed due to the wave passage in the model, and the scattering from the foundation and the radiation from the building do not contribute to additional permanent strains.

The trends are similar for the HIH building (Fig. 7.3a,b) except that here after some time, for case $\gamma = 30^0$, the hysteretic energy starts to grow monotonically. An explanation of this phenomenon is shown in Figure 7.5a, where the time histories of the displacements in points H(- a,0) (solid line) and T(- a,H_b) (dotted line) are shown for HSB and HIH, for $\eta = 0.5$, and for $\gamma = 30^0$ and $\gamma = 60^0$. Unlike in Figure 5.4 for the linear case in which point H remains in the initial position after the motion has ceased, for the nonlinear case point H has

permanent displacement at the end of the analysis even though it is treated as a linear point. As point H develops permanent displacement, point T at the top of the building vibrates (dotted curve) around the new equilibrium, which follows the permanent motion of point H (the base). This is more pronounced for $\gamma = 30^0$ and for the Holiday Inn hotel, where the radiation damping is smaller. The reason for this behavior is that several points close to the soil-foundation contact (around point S in Fig.7.1) undergo permanent strains during the wave passage and are not completely unloaded when the radiation from the building takes place. The progress of the permanent strain at the point $S(x_s, y_s)$ with $x_s = \frac{x_{G'} + x_G}{2}$, $y_s = y_g + \Delta x$ is illustrated in Fig. 7.5b.

In Figures 7.4a and 7.4b, the permanent strains are shown for HSB and HIH. As can be seen from the figures, while the angle of incidence is small, the permanent strain in the x direction can be zero with only the permanent strain in the y direction occurring. The zone of the permanent strain is parallel with the free surface at some depth and has a width that is dependent upon the duration of the pulse. This appearance is mostly due to the 1-D effect of the wave propagation illustrated in Section 5.0. As the angle of incidence becomes larger, the strain in the y direction eventually vanishes, and the strain in the x direction appears. The largest zone of the permanent strain ε_{xp} is along the free surface, where it occurs to some depth. Mostly, this zone is a consequence of the reflection from the half space, where the maximum strain at the free surface is $\varepsilon_{x\max} = 2 \cdot \frac{v_{\max}}{\beta_s} \sin\gamma$. Because the foundation stiffness in this example

Fig. 7.4a PERMANENT STRAIN DISTRIBUTION IN THE SOIL ISLAND: HOLLYWOOD STORAGE BUILDING

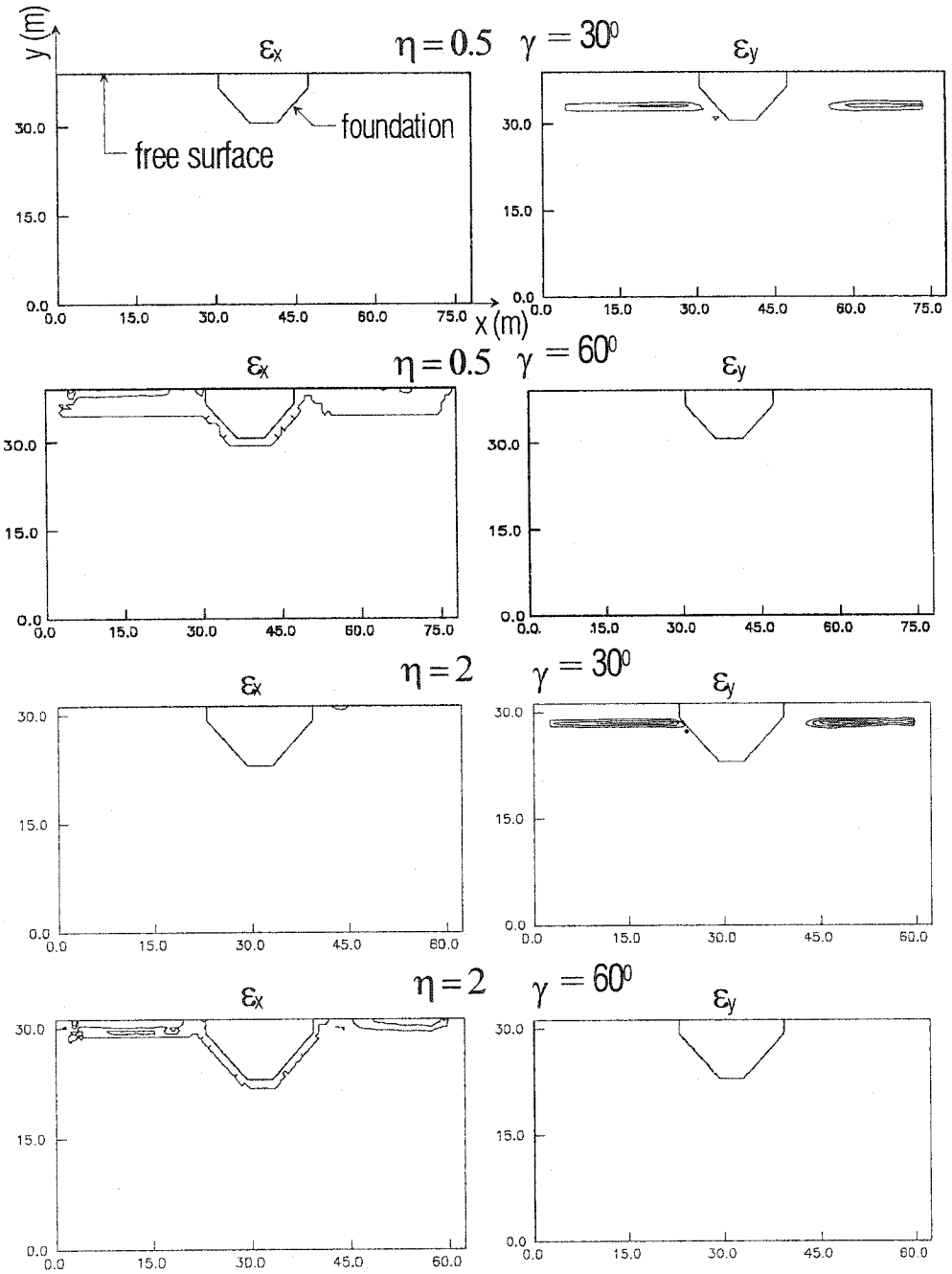

Fig. 7.4b PERMANENT STRAIN DISTRIBUTION IN THE SOIL ISLAND: HOLIDAY INN HOTEL

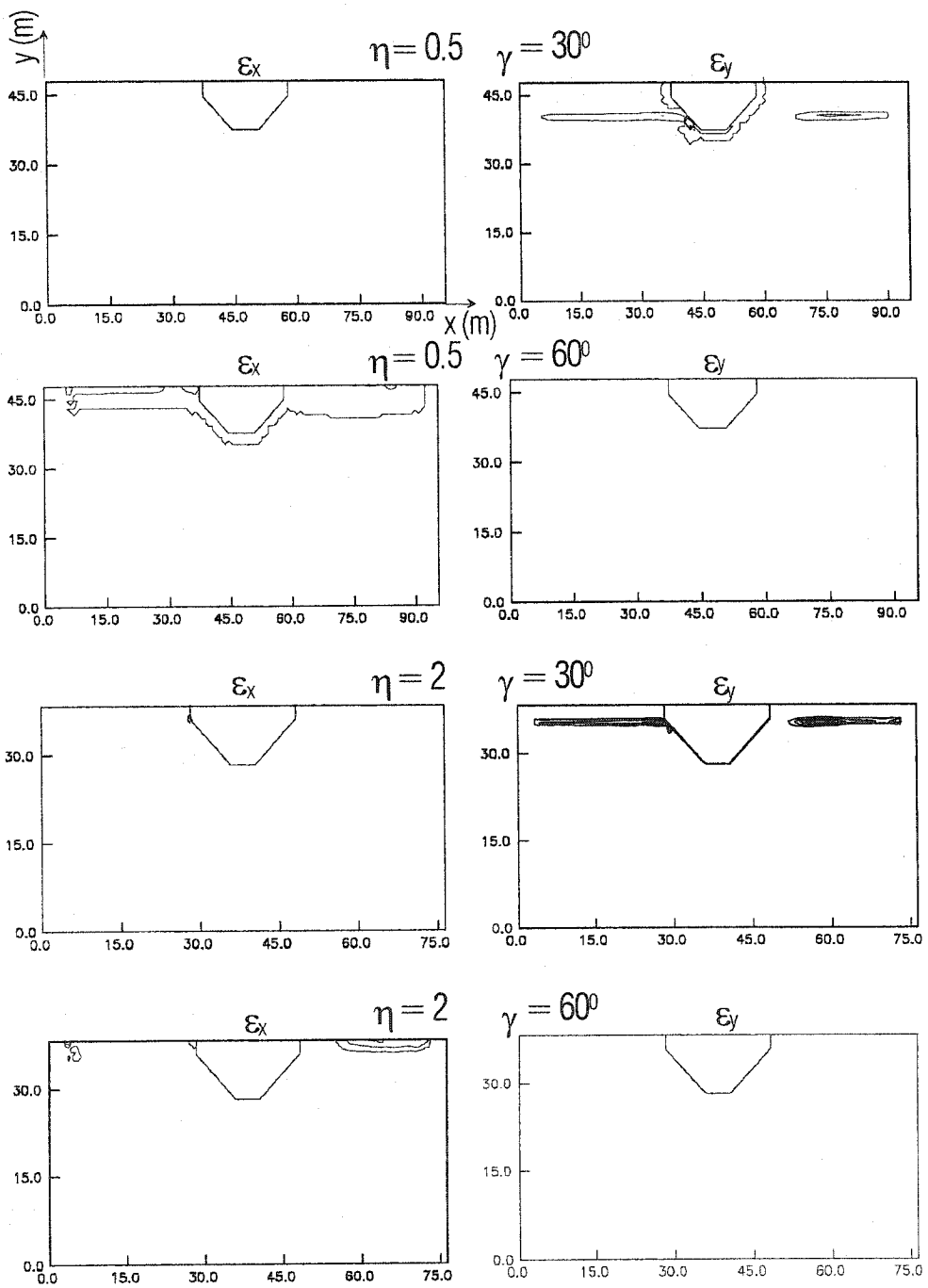

Fig. 7.5a TIME HISTORIES OF DISPLACEMENTS AT THE TOP AND THE BOTTOM OF THE BUILDING FOR NONLINEAR SOIL

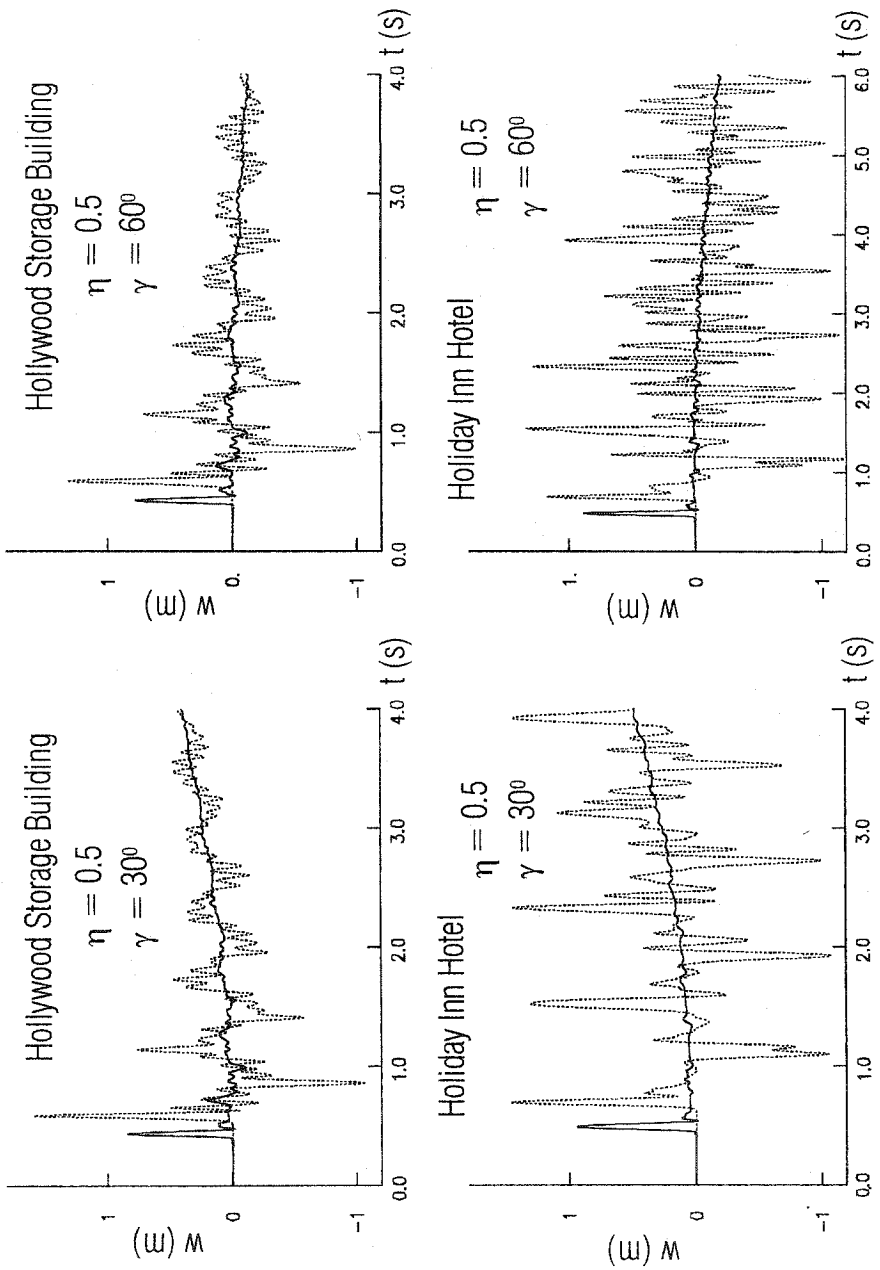

Fig. 7.5b DEVELOPMENT OF THE PERMANENT STRAIN ε_y IN TIME AT POINT S

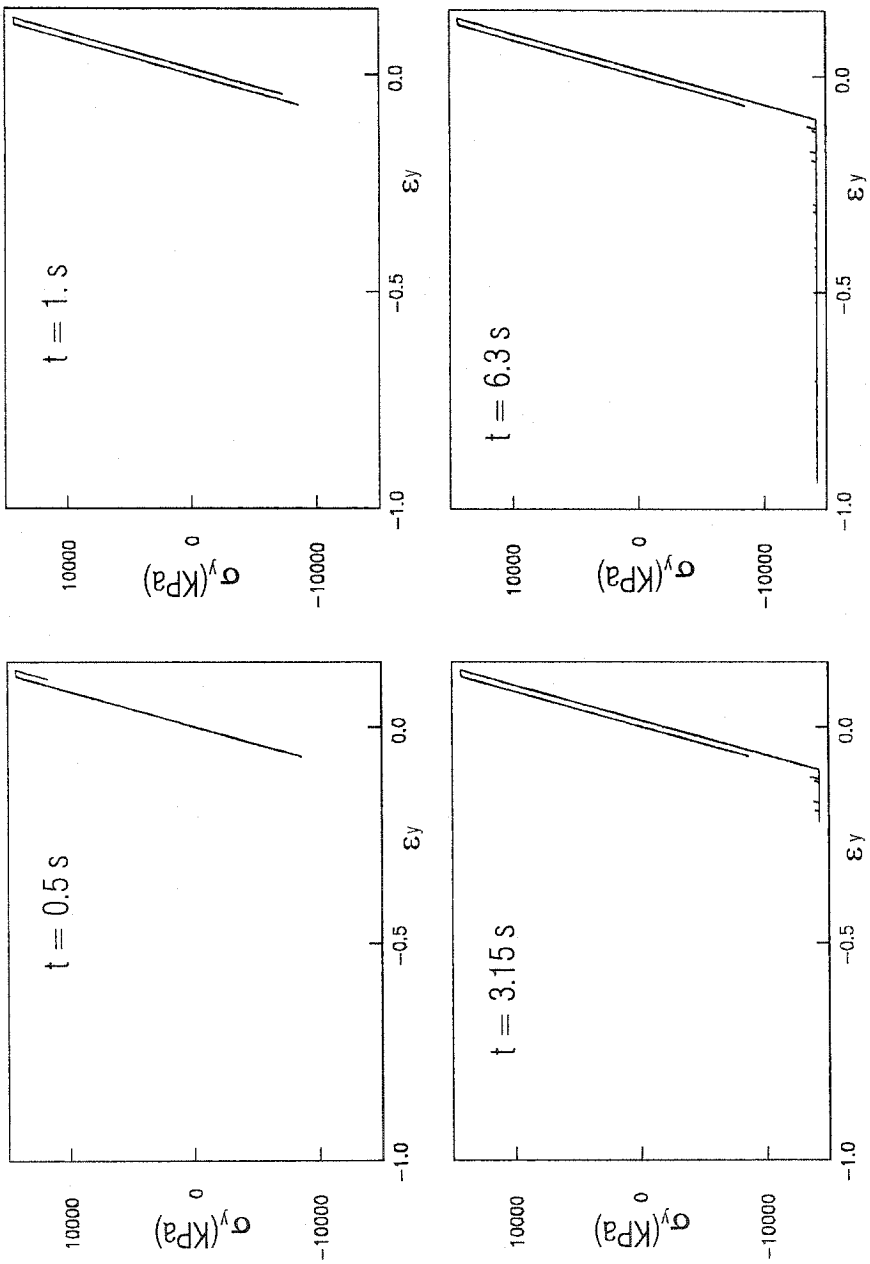

is close to the soil stiffness, there is no permanent strain around the foundation. Of course, this does not mean that this will be the case when there is a big difference between the soil and foundation properties.

7.2 Average displacements at the contacts and distribution of the permanent strains

In this section we analyze the model of the Holiday Inn hotel with the geometry and properties given in Section 3.3. In Chapter VI, this analysis was illustrated for the linear case. Here, we consider the case of intermediate nonlinearity with $C = 1$ and of large nonlinearity with $C = 0.7$. The case of small nonlinearity gives practically the same results for the average displacement as does the linear case. It is obvious that for every η, one would have to change ε_m in accordance with (7.3) to get the same level of nonlinearity.

Together with the curves for the nonlinear case, the results for the linear case (Fig.6.1) are shown for four different angles of incidence: $\gamma = 0^0, 30^0, 60^0$, and 85^0. The normalized average displacements α at the building-foundation contact for nonlinear case are shown with solid dark curves and for the linear case with solid light curves. At the soil-foundation contact, for the nonlinear case these amplitudes are shown with curves with longer dashes, and for linear case they are shown with curves with shorter dashes. In the same figures, the cases for three examples of foundation stiffness are shown:

Fig. 7.6a NORMALIZED AVERAGE AMPLITUDES AT THE CONTACTS OF THE MODEL WITH NONLINEAR SOIL $\gamma = 0$

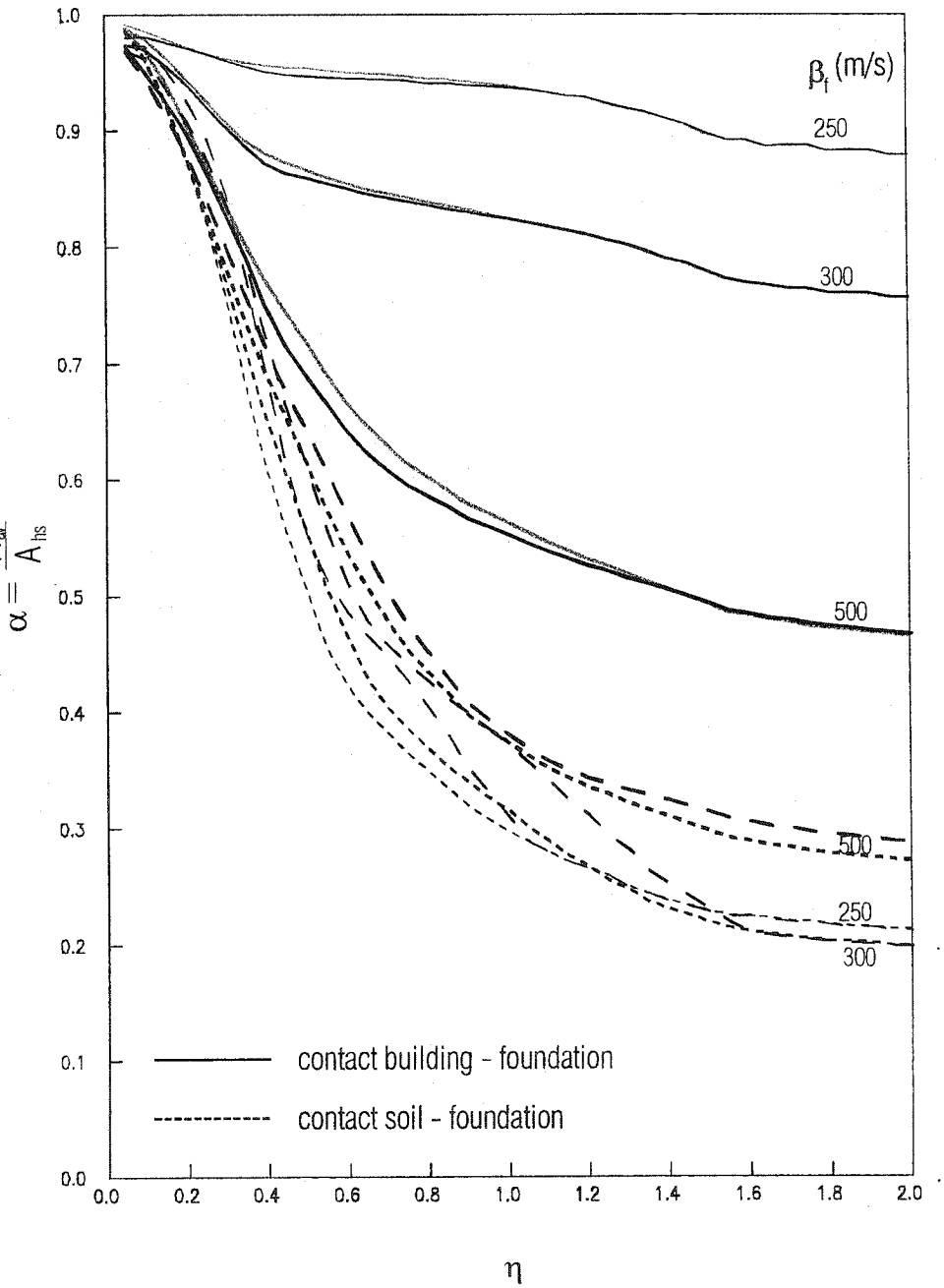

Fig. 7.6b NORMALIZED AVERAGE AMPLITUDES AT THE CONTACTS OF THE MODEL WITH NONLINEAR SOIL $\gamma = 30^{o}$

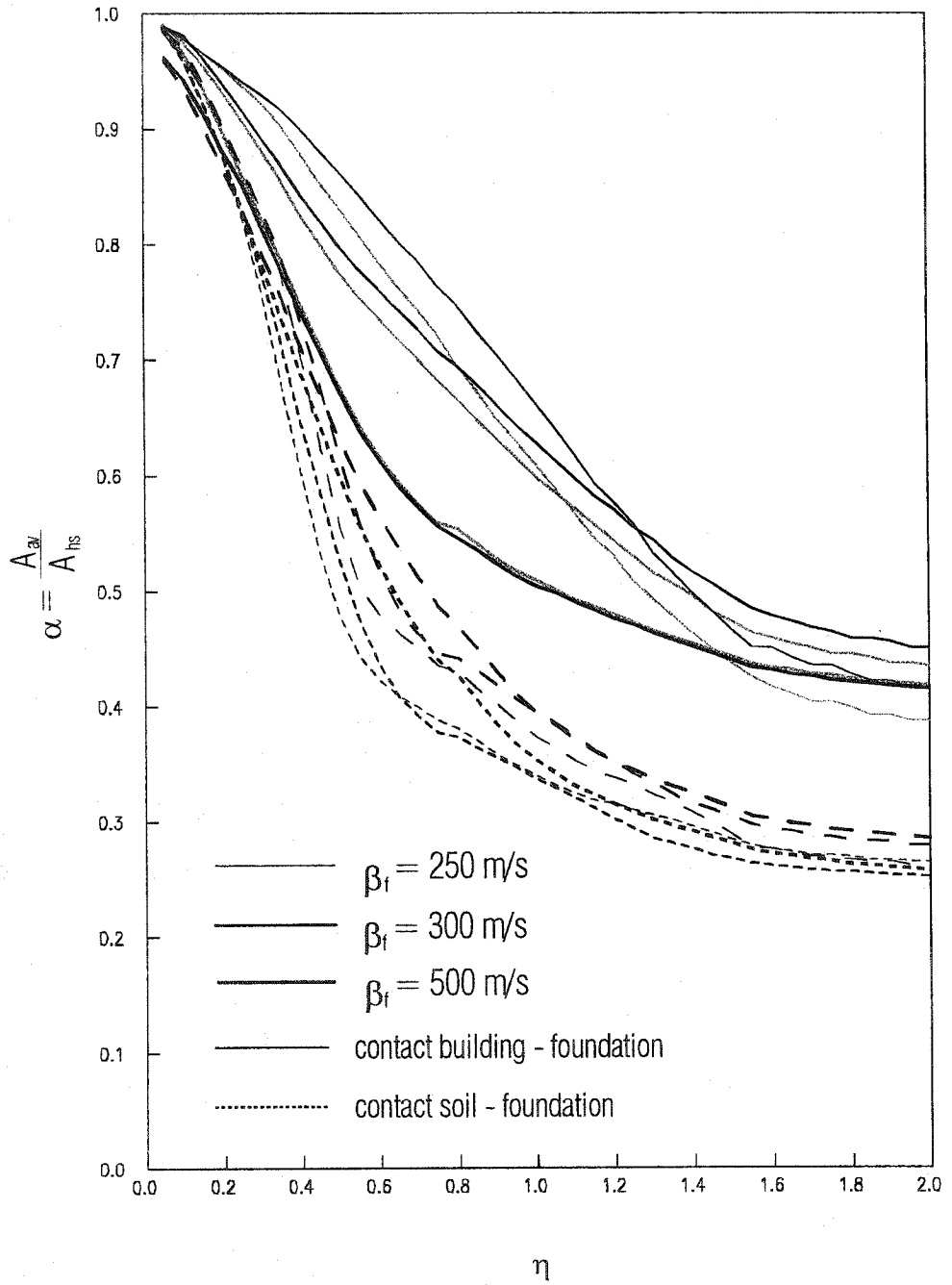

Fig. 7.6c NORMALIZED AVERAGE AMPLITUDES AT THE CONTACTS OF THE MODEL WITH NONLINEAR SOIL $\gamma = 60^{o}$

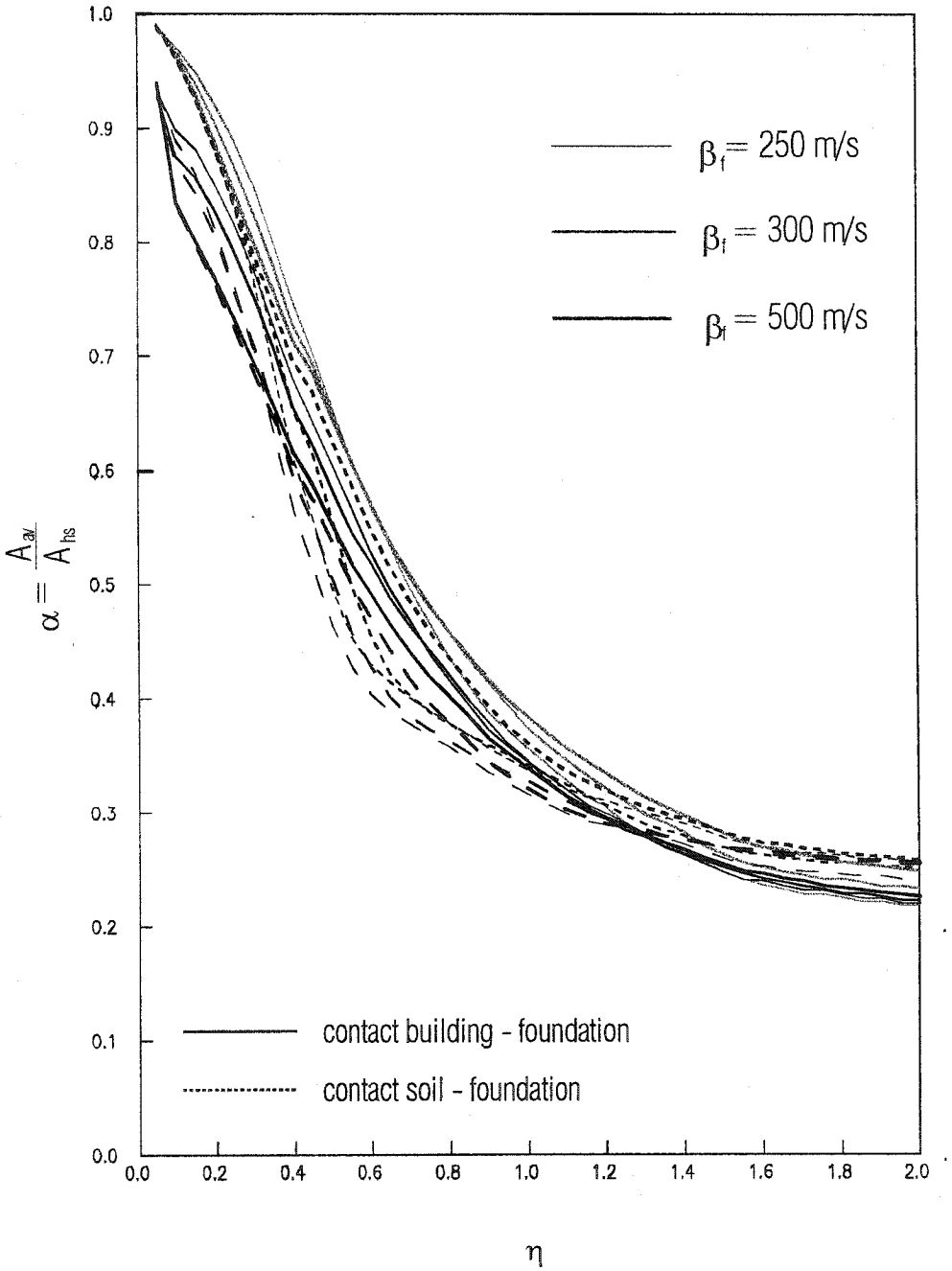

Fig. 7.6d NORMALIZED AVERAGE AMPLITUDES AT THE CONTACTS OF THE MODEL WITH NONLINEAR SOIL $\gamma = 85^{o}$

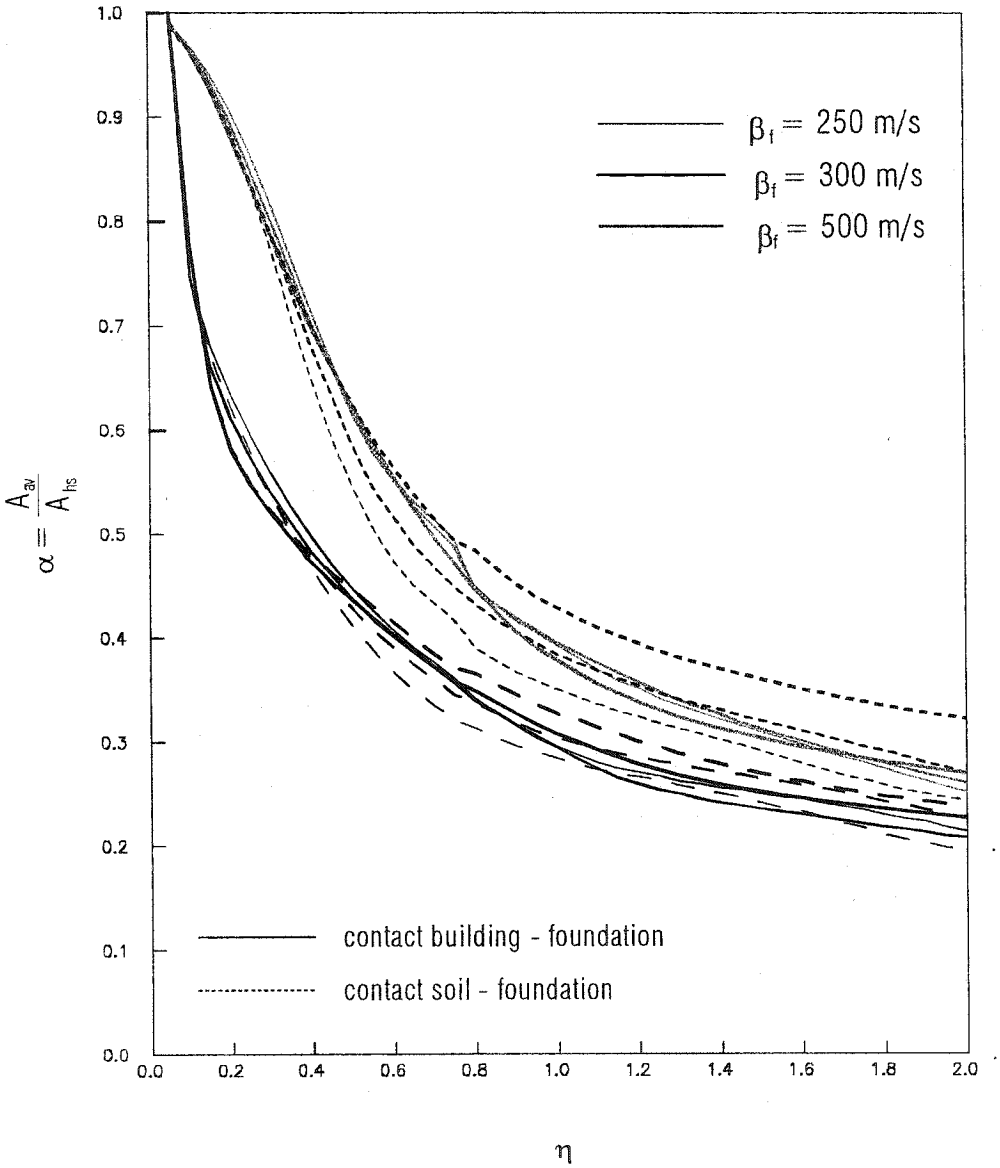

- $\beta_f = 250m/s$ with the thinnest curve,
- $\beta_f = 300m/s$ with the thicker curve,
- $\beta_f = 500m/s$ with the thickest curve.

For example the normalized average displacement at b-f for the nonlinear case with foundation stiffness $\beta_f = 300m/s$ is shown with a solid dark curve with intermediate thickness. Again, as explained in section 6.0, the interference of the incoming wave and the reflected wave from the top of the building is avoided by assuming a high enough building, and the analysis is stopped as the wave completely passes the right point of the triple soil-foundation-building contact.

The distribution of the components of the permanent strain $\varepsilon_{px}, \varepsilon_{py}$ for the case of intermediate nonlinearity C = 1 is shown in the figures 7.8a,b1,b2,c,d at the end of the analyses. The contours of equal strain are drawn with steps of 0.02 in all of the plots in Fig. 7.8.

In Figures 7.6a,b,c,d the results for the case C = 1 are shown. When the incidence is vertical (Fig.7.6a), the differences at the contact b-f between the linear and the nonlinear cases are small, and they are largest at small η. In this case, the permanent strains occur only in the y direction, mostly close to the free surface. This results from the interference of the incident and reflected fields from the free surface. The nature of this phenomenon was illustrated for the 1-D case in Section 5.0 (Fig.5.0b). This nonlinearity appears after the reflection of the wave from the free surface. For smaller η, nonlinearity appears close to the contact s-f and is due to scattering especially for a stiffer foundation (Fig.7.8a). For all cases of foundation stiffness, the

Fig. 7.7b NORMALIZED AVERAGE AMPLITUDES AT THE CONTACTS
CASE : BIG NONLINEARITY IN THE SOIL $\gamma = 30^o$

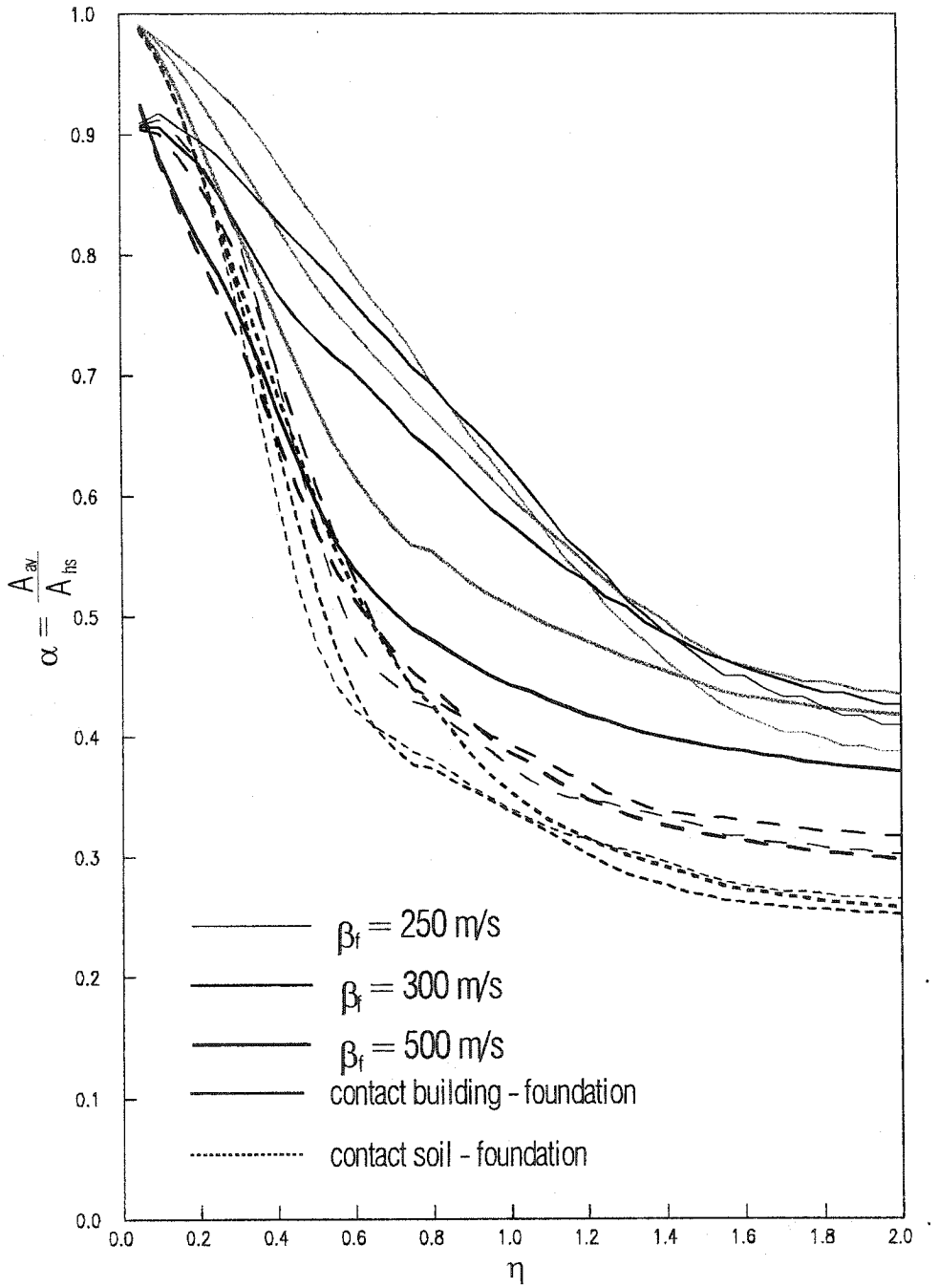

Fig. 7.7c NORMALIZED AVERAGE AMPLITUDES AT THE CONTACTS: CASE OF LARGE NONLINEARITY IN THE SOIL $\gamma = 60^{o}$

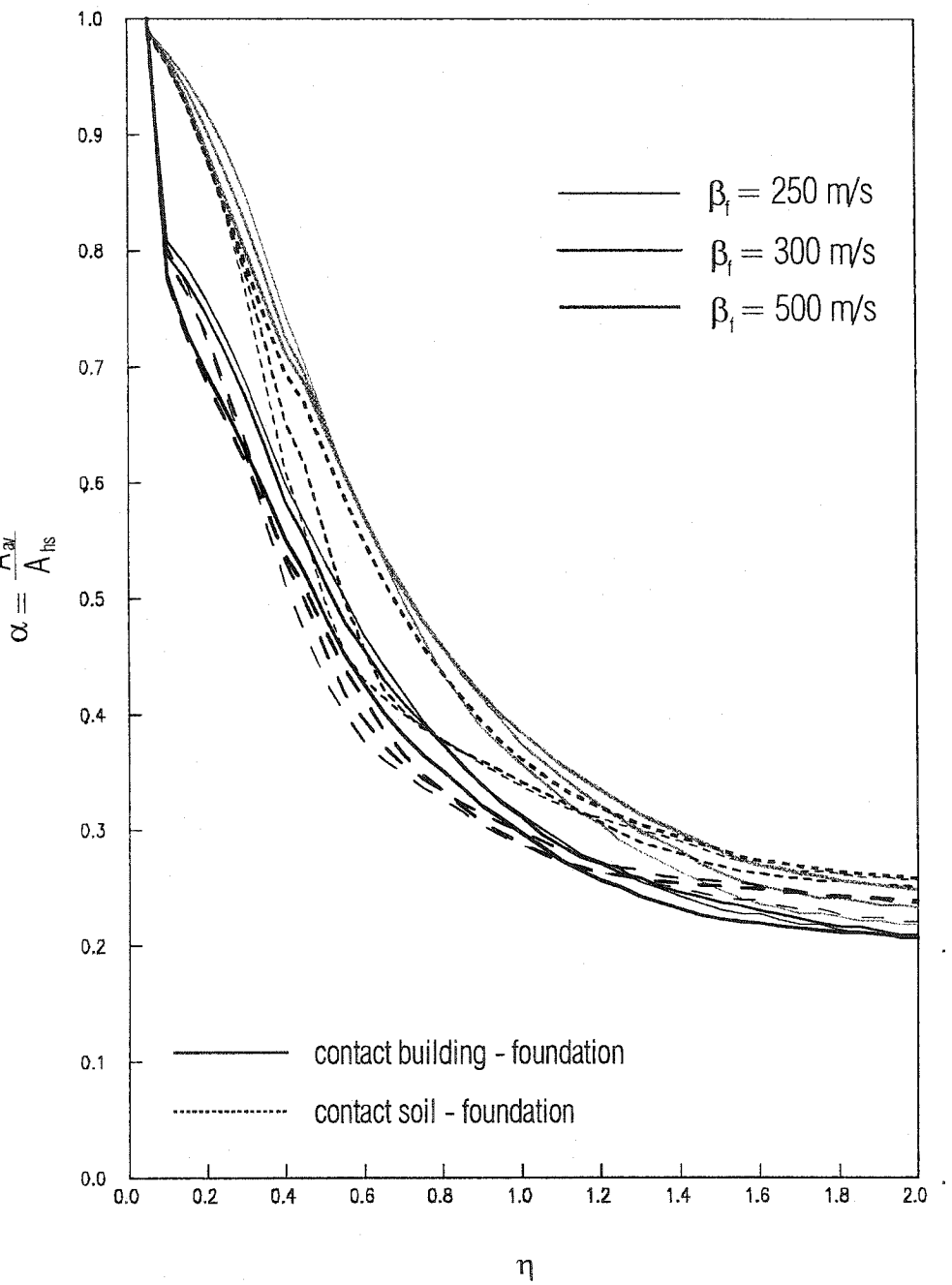

Fig. 7.7d NORMALIZED AVERAGE AMPLITUDES AT THE CONTACTS: CASE OF LARGE NONLINEARITY IN THE SOIL $\gamma = 85^0$

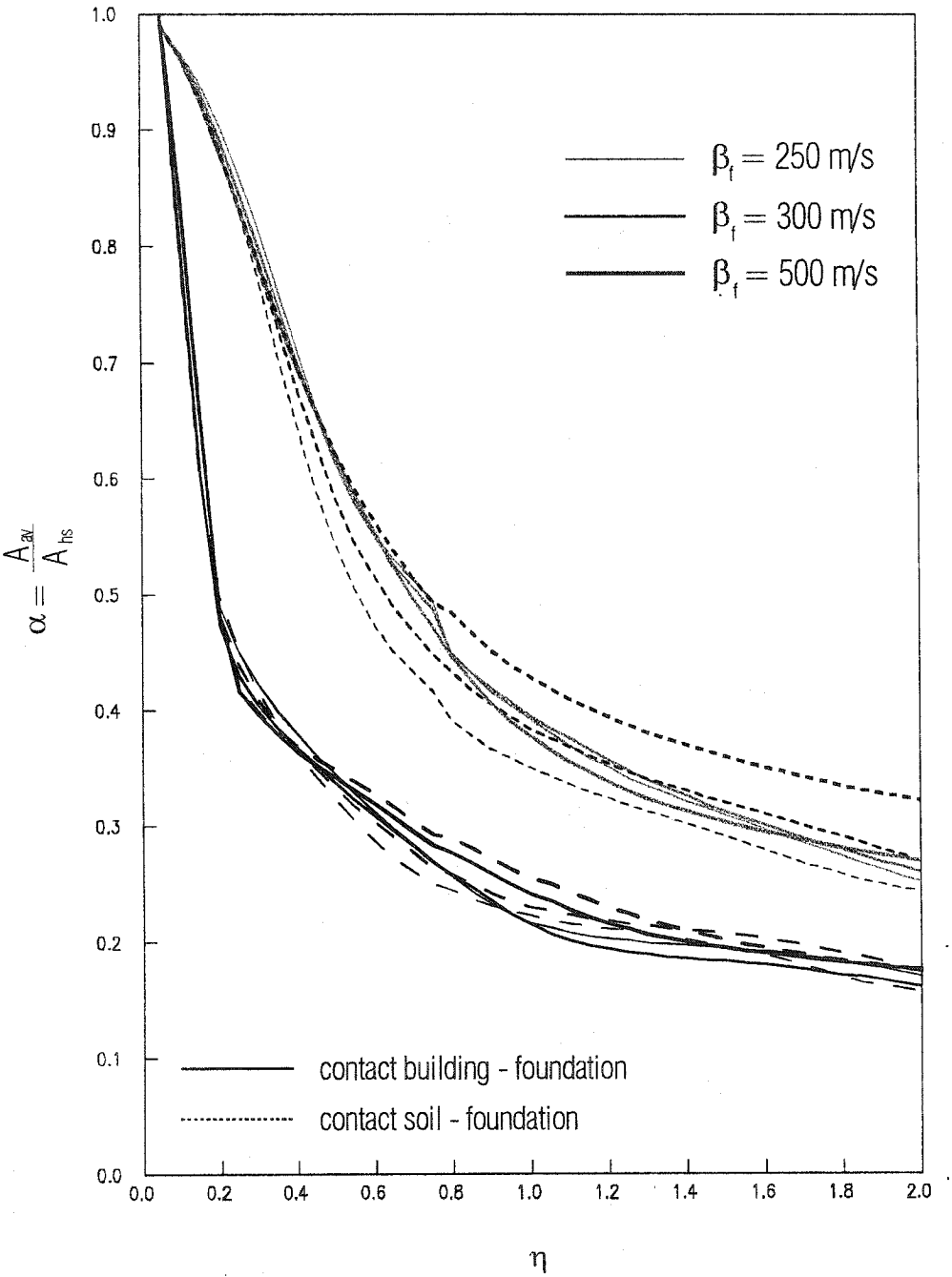

curves for nonlinear response although almost equal, are slightly smaller, because of the loss of energy due to nonlinear strains. The difference is largest at smaller η when the pulse is longer. At intermediate η, the difference is the greatest for the stiffest foundation because the nonlinear zone below the foundation is the largest, and it attenuates the incoming wave (Fig.7.8a). For high η, there is no nonlinear zone around the foundation, and for η larger than 1.5 the curves for the linear and nonlinear cases are identical. Close to the left and right boundaries in Fig.7.8a some zones of very small nonlinearities can be seen. For this case (C = 1), with vertical incidence we are at the limit between intermediate and large nonlinearities, and any small reflection from the artificial boundary brings the soil points into a nonlinear state even when the wave has not reached the foundation. Nevertheless these permanent strains are small, and they do not affect the overall accuracy in our models. The small nonlinear zone at the bottom of the model is real and, it occurs when the scattered pulse (mostly the extended part due to filtering) meets the incoming main part of the pulse and the resulting strain slightly exceeds ε_m.

For incident angle $\gamma = 30^0$ both components of the permanent strain exist. In figure 7.8b1, ε_{xp} and ε_{yp} are shown for η = 0.6, and in Figure 7.8b2 they are shown for η = 1.8. As can be seen in the plots for ε_{xp}, it is mostly distributed around the foundation. For the stiffest foundation (the lowest plot), because of the interference of the scattered and the half-space fields, there is a substantial amount of yielding behind the foundation, which decays with softening of the foundation (the second and first plots). As might be expected, this strain is larger for shorter pulses because of increased diffraction. Theoretically, at the free surface

Fig.7.8a DISTRIBUTION OF THE PERMANENT STRAIN JUST AFTER THE WAVE HAS PASSED THE FOUNDATION

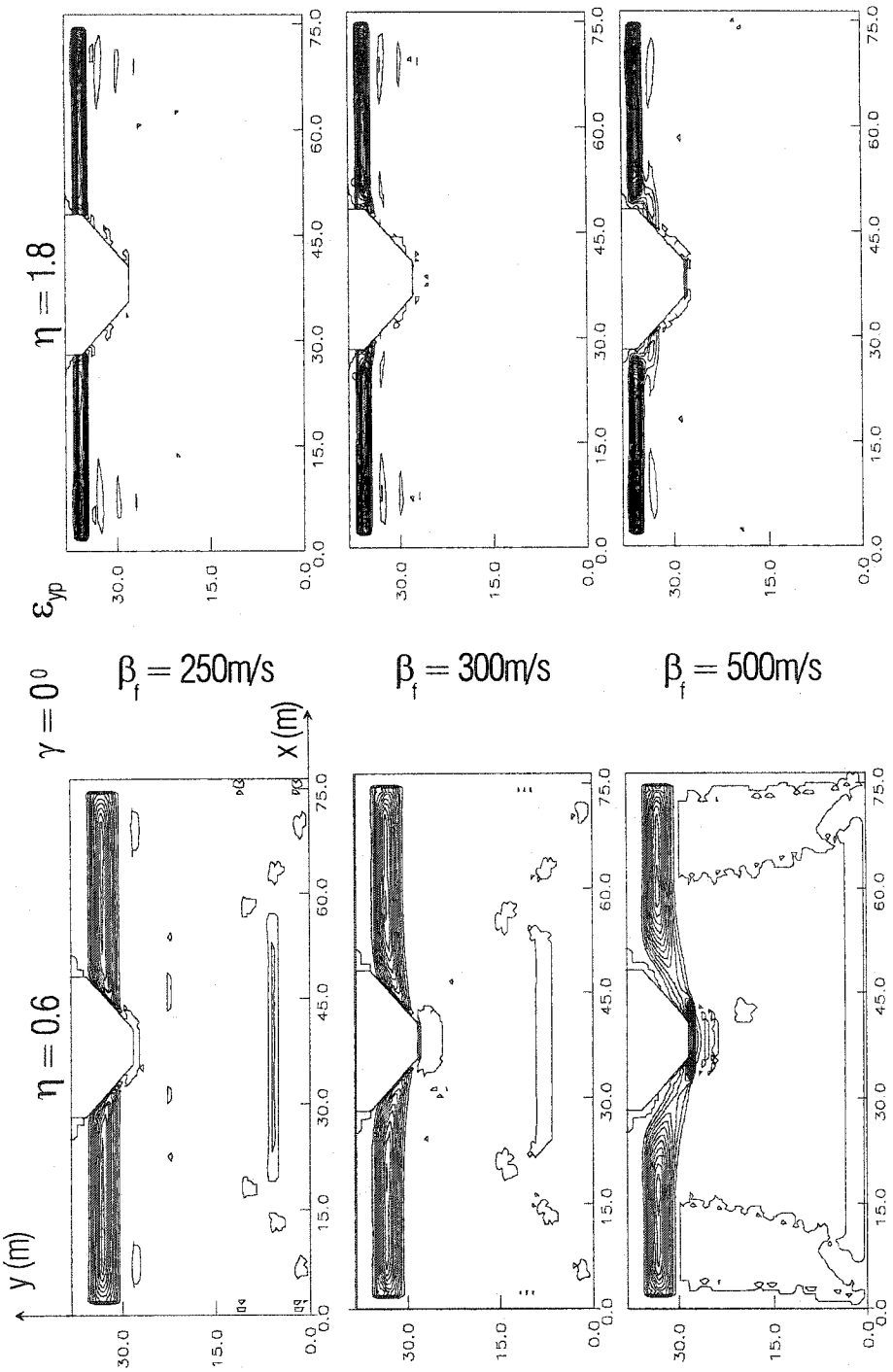

Fig.7.8b1 DISTRIBUTION OF THE PERMANENT STRAIN JUST AFTER THE WAVE HAS PASSED THE FOUNDATION

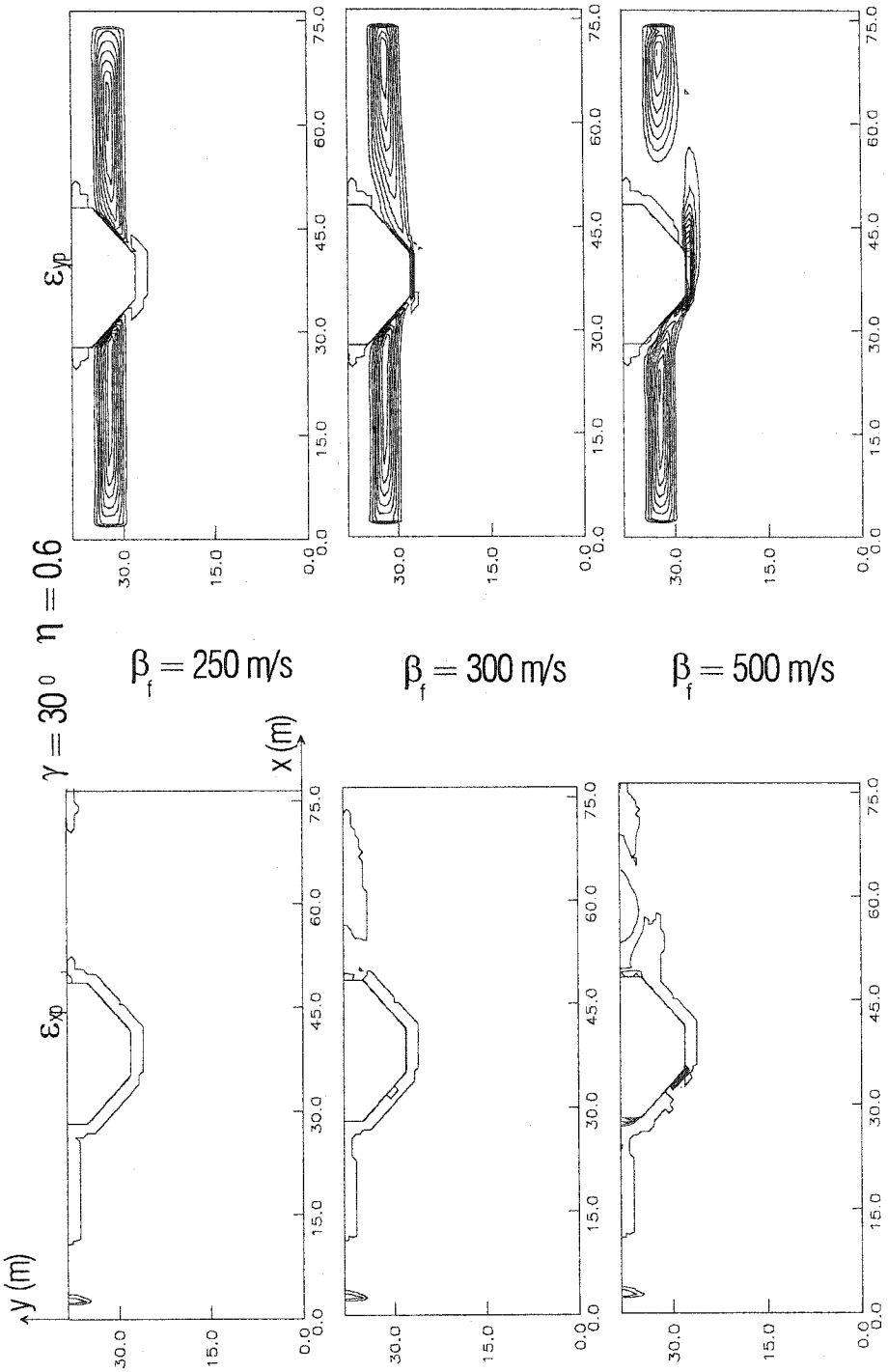

Fig.7.8b2 DISTRIBUTION OF THE PERMANENT STRAIN JUST AFTER THE WAVE HAS PASSED THE FOUNDATION

$\gamma = 30^0$ $\eta = 1.8$

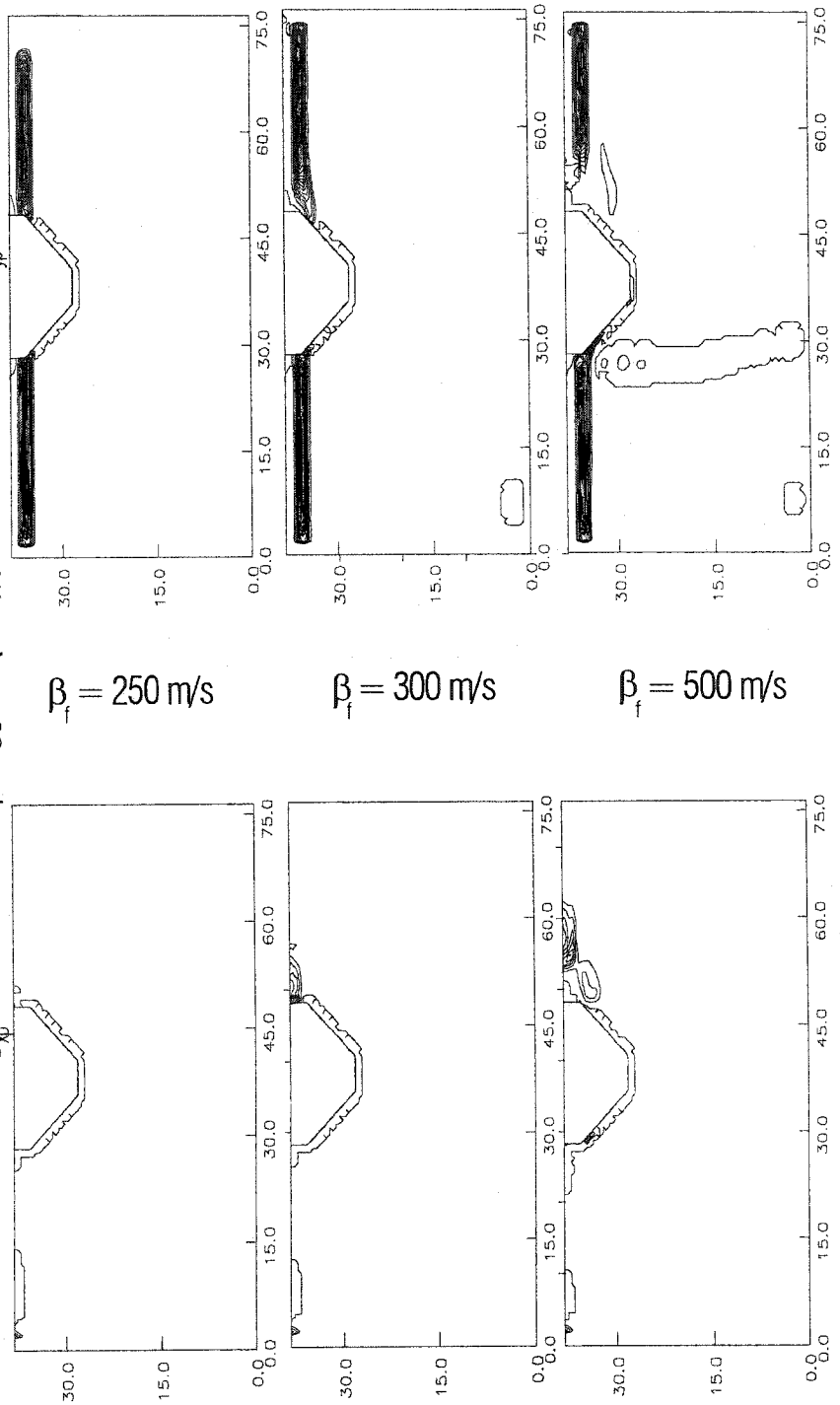

Fig.7.8c1 DISTRIBUTION OF THE PERMANENT STRAIN JUST AFTER THE WAVE HAS PASSED THE FOUNDATION

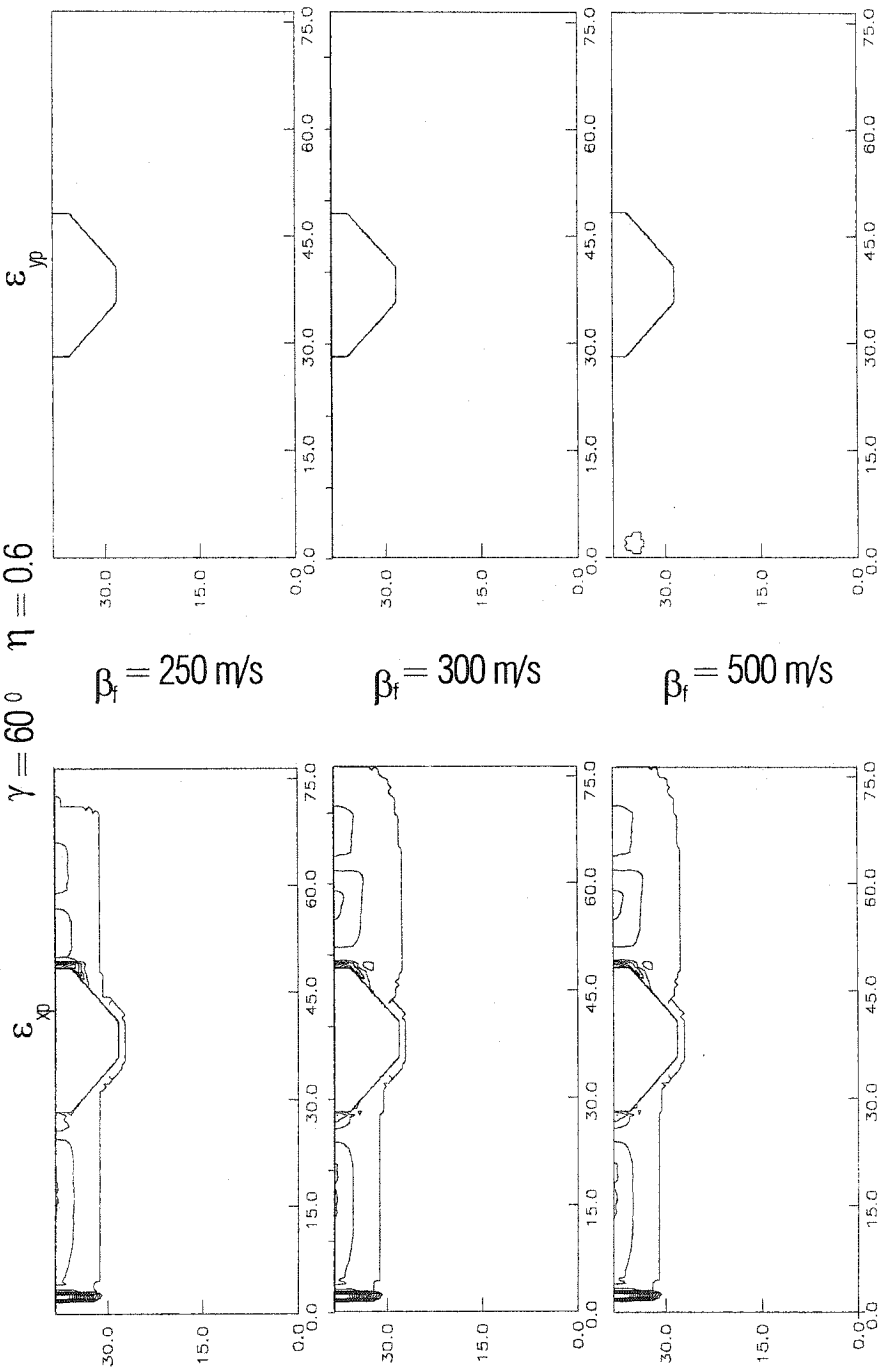

Fig.7.8c2 DISTRIBUTION OF THE PERMANENT STRAIN JUST AFTER THE WAVE HAS PASSED THE FOUNDATION

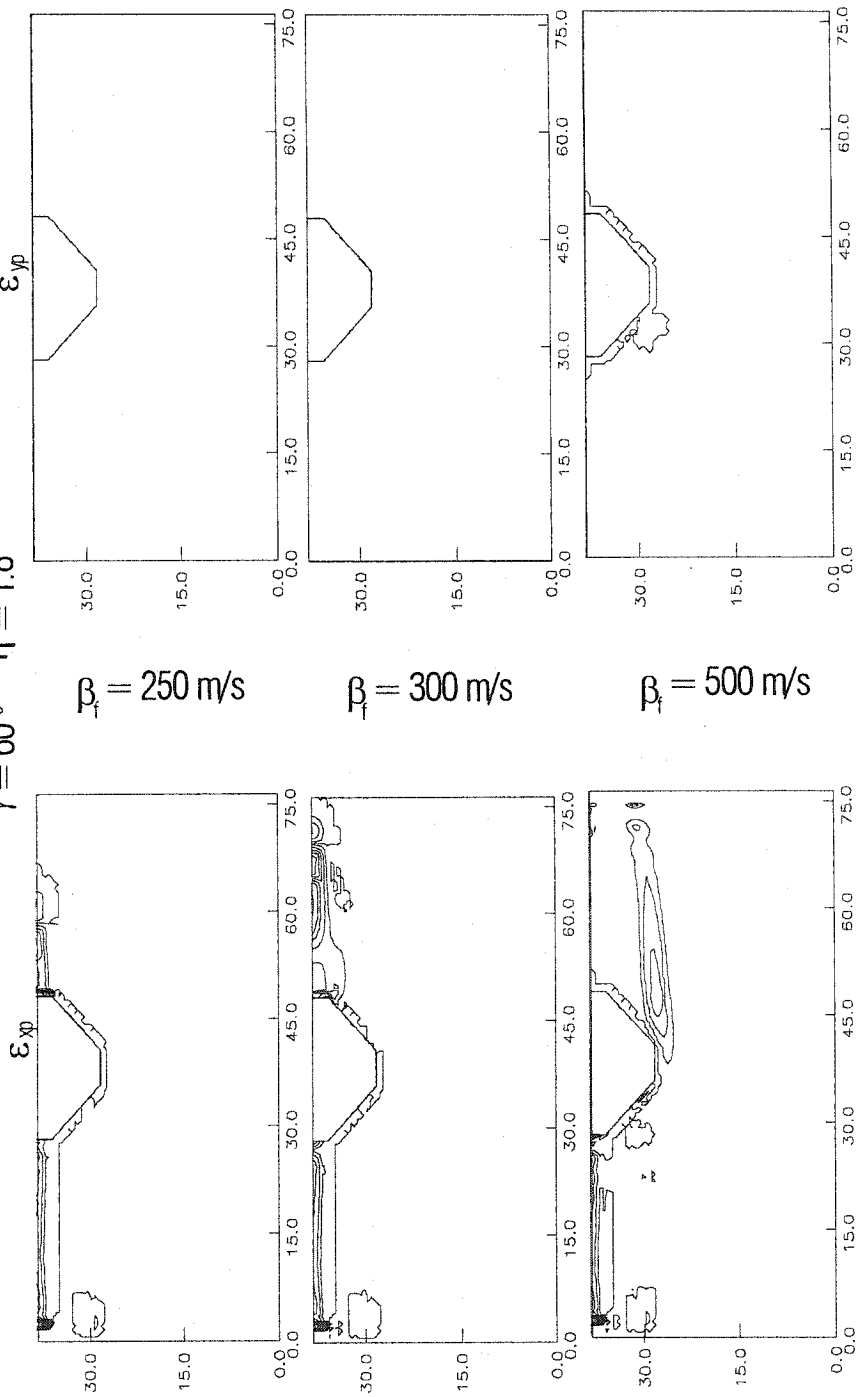

Fig.7.8d DISTRIBUTION OF THE PERMANENT STRAIN JUST AFTER THE WAVE HAS PASSED THE FOUNDATION

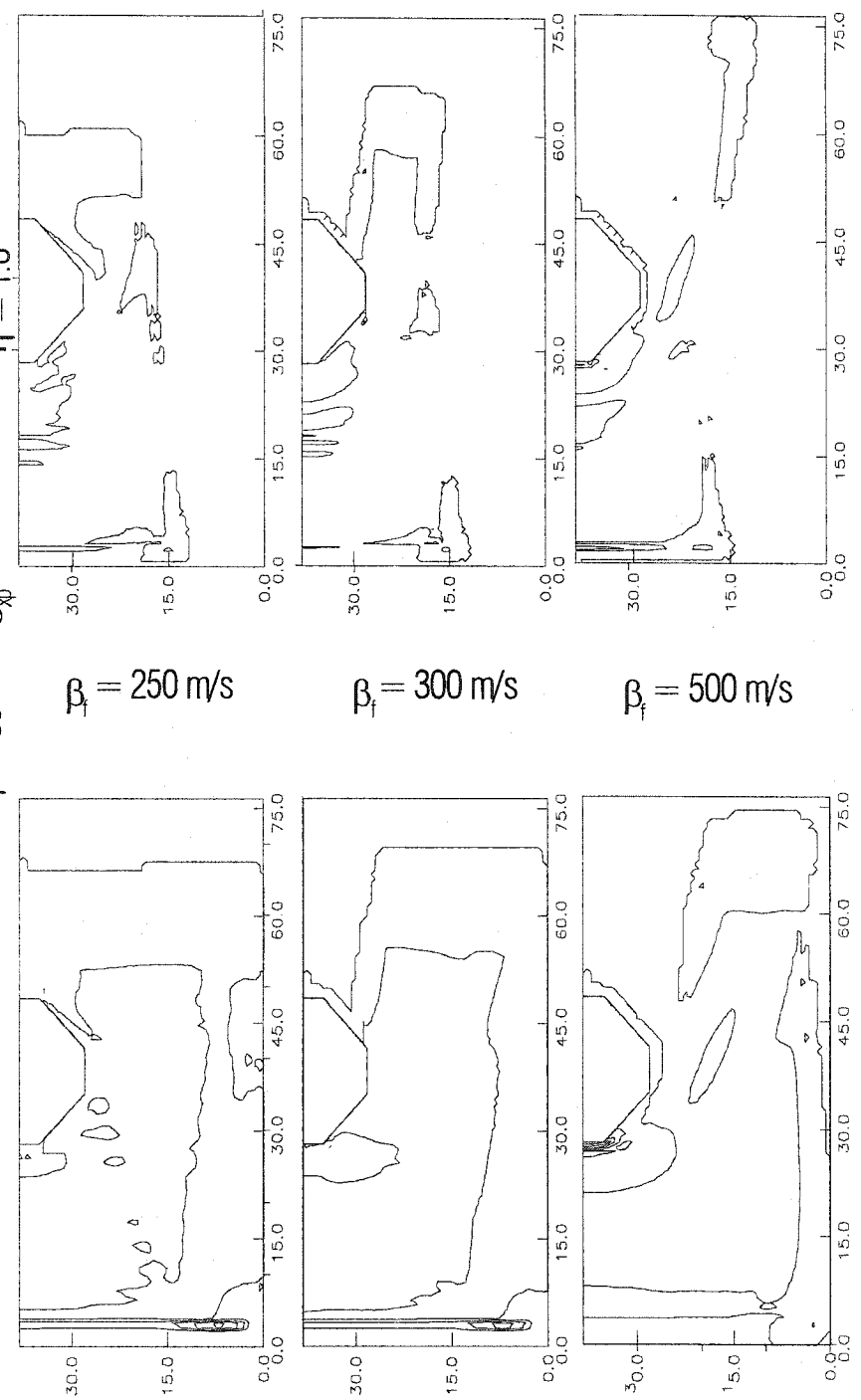

$\varepsilon_x = 2\frac{v_{\max}}{c_x} = 2\frac{v_{\max}\sin\gamma}{\beta_s}$, and for C = 1 and $\gamma = 30^0$ we are at the limit between the linear and nonlinear states. Because of the artificial change of the soil properties (the first four columns of points in the grid must be always linear for constructing the boundary) and the imperfect artificial boundary, some small permanent strain in the x direction occurs at the free surface. The biggest strain occurs close to the lowest left corner of the foundation.

While the strain ε_{xp} is generally distributed around the foundation, the strain ε_{yp} is mostly distributed close to the free surface, due to the 1D effect already mentioned for the case of vertical incidence. Although the incidence is not vertical, the vertical components of the motion are large enough to create a big nonlinear zone close to the free surface. As for vertical incidence, this zone is wider but has smaller intensity for a longer pulse (Fig. 7.8b1) and it is narrower and has greater intensity for a shorter pulse (Fig.7.8b2). The curves for the average displacement at the contacts are shown in Figure 7.6b. The displacement for the pulse $\eta = 0.6$ is shown in figure 7.9. Because of the nonlinear zones in the soil around the foundation, for nonlinear case the resistance of the soil to the foundation motion is weaker, and for all three cases the contact s-f has greater average displacement than for the linear case. On the other hand, while for the stiffest foundation there is no substantial difference at the contact b-f between the linear and nonlinear case, for a softer foundation the displacement for the nonlinear case is larger in the entire frequency range. From Fig.7.9 it can be seen that after the yielding of the soil around the foundation the stiffest foundation moves as a rigid body, while in the softer foundations the part of the pulse entering the foundation causes elastic deformations.

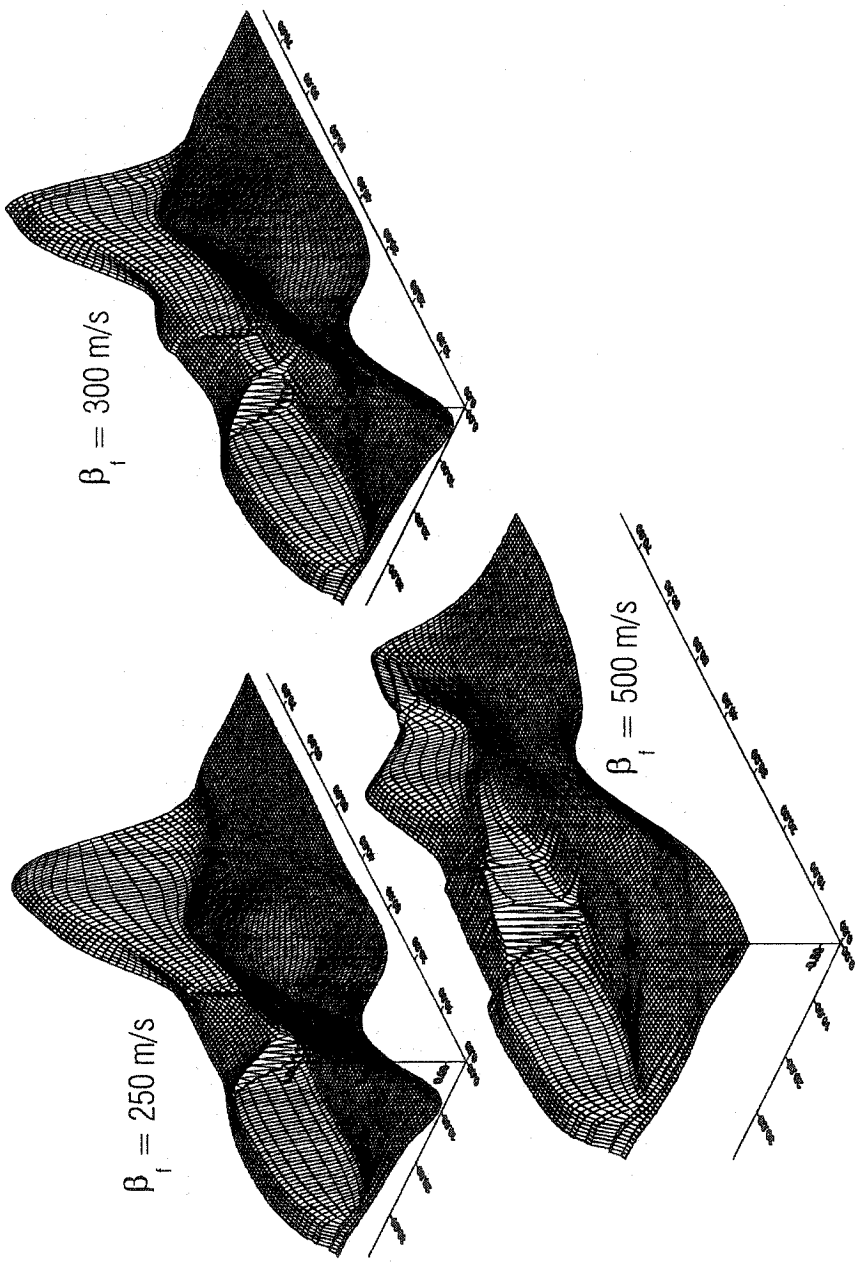

Fig. 7.9 DISPLACEMENT IN THE SOIL AFTER THE PULSE HAS PASSED THE FOUNDATION

In Figures 7.8c1 and 7.8c2, the permanent strain for incident angle $\gamma = 60^0$ is shown, where the component ε_{xp} is dominant. Some negligible permanent strain in the y direction can be seen close to the bottom left corner for short pulses and the stiffest foundation (Fig. 7.8c2). In front of the foundation, the nonlinear zone starts from some depth in the soil, depending upon the duration of the pulse, where the permanent strain is the smallest. Advancing to the free surface, the strain magnitude increases, and it is largest at the free surface. For longer pulses (Fig.7.8c1), the zone behind the foundation is nonlinear close to the free surface, with approximately the same thickness and magnitude of strain as in front of the foundation and being the largest close to the right top corners of the foundation. Again this strain concentration can be attributed to the effects of elastic forces, as was shown for the simple disk example in the previous chapter. As the duration of the pulse becomes shorter (Fig.7.8c2), for the softer foundations the zone behind the foundation has stronger nonlinearity than the zone in front of the foundation. Also, the softest foundation has the strongest nonlinearity behind the foundation for all three considered foundation stiffnesses. This results from the elastic forces at the right end of the contact b-f, which are greatest for the softest foundation and more pronounced for short pulses. What is interesting to note here is that, for the stiffest foundation, behind the foundation the soil remains linear close to the free surface, but a nonlinear zone occurs at some depth. This can be attributed to the diffracted field around the foundation. The stiffer the foundation, the longer is the diffracted field.

The average amplitudes at the contacts α (Fig.7.6c), for nonlinear case are smaller due to the immediate appearance of permanent strain and the loss of energy of the incoming waves close to the free surface.

As for the average amplitudes, what was stated for the case with $\gamma = 60^0$ can be said for $\gamma = 85^0$ (Fig.7.6d). The difference between the linear and nonlinear cases is greater for this incidence. In Figure 7.8d it can be seen that the nonlinear zone behind the foundation and close to the free surface appears only for the softest foundation, while for stiffer foundations it is shifted deeper.

In Figures 7.7b,c,d the plots of the average displacement at the contacts are shown for the case of large nonlinearity C = 0.7 and for $\gamma = 30^0, 60^0, 85^0$ together with the corresponding displacements for the linear case. Depending upon the angle of incidence, one or both components of the permanent strain appear until the pulse reaches the free surface or the foundation. Everything that was said for intermediate nonlinearity is applicable to this case, except that the differences between the nonlinear and linear cases are greater.

Finally, to illustrate attenuation of the pulse due to the energy dissipation from development of permanent strains, Figure 7.10 shows the displacement for $\beta_f = 300\,\mathrm{m/s}$ and $\eta = 1$ for different incident angles, at the instant when the pulse has completely passed the right corner of the building-foundation-soil contact. The plots are normalized with respect to the half-space amplitude of the pulse.

Fig. 7.10 DISPLACEMENT IN THE SOIL AFTER THE PULSE HAS PASSED THE FOUNDATION FOR DIFFERENT INCIDENT ANGLES AND $\eta = 1$

CHAPTER VIII

SUMMARY

The numerical simulation of wave propagation was used to explore the two-dimensional soil-foundation-structure interaction with a flexible foundation for incident SH-waves. The finite differences numerical method (Lax-Wendroff) was used to solve the wave equation.

First, for steady-state, monochromatic incident plane waves, the solution for the foundation motion and the relative displacement of the building in terms of the input frequency were studied for the Hollywood Storage building for two angles of incidence and two foundation stiffnesses. The results for the foundation motion were illustrated at three points (left, middle, and right) at the contact of the building and the foundation in order to study the torsional effects. It was shown that relative to the case in which the foundation is absolutely rigid the displacement amplitudes for the flexible foundation are generally larger, except for frequencies close to the natural frequencies of the building. The motion at the right end and at the middle are generally larger than the motion at the left, as was explained in the Chapter VI.

In Chapter V the distribution of the energy for the linear case was considered for two different buildings, the Hollywood Storage building (tall and "rigid") and the Holiday Inn hotel (intermediate height and "soft"). It was shown that the former building attracts more energy and radiates it faster. The plots of energy distribution were illustrated for four different dimensionless frequencies and for the angle of incidence $\gamma = 30^0$. It was shown that the input energy reaching the foundation does not depend very much upon the angle of incidence. In Table 4, the

percentage of the maximum energy in the building (radiated) energy and the scattered energy from the foundation were given for both buildings. It was shown that the energy distribution does not depend upon the frequency of the input motion, but rather on the building's properties.

In Chapter VI, average displacements and average velocities at the building-foundation and soil-foundation contacts as functions of the dimensionless frequency were presented. The displacements at the left and the right corners of the building-foundation contact as functions of the dimensionless frequency were also given. These results are important for the designing of earthquake-resistant structures based on the power of incident strong motion pulses.

Finally, in Chapter VII, the response of the model with nonlinear soil was studied by considering energy, permanent strain distribution, and the average displacements at the contacts. It was shown that normaly the total permanent strain is developed during the wave passage through the soil, although for some angles of incidence in a small zone close to the contact large permanent strains in the y direction can develop. The permanent strain in the x direction occurs for larger angles of incidence (closer to the horizontal incidence), and it appears in a zone close to the surface, including the free surface, while the permanent strain in the y direction occurs for smaller angles of incidence (closer to the vertical incidence), and it appears in a zone at some depth from the free surface. It was shown that the width of the zone and the intensity of the permanent strain are inversely proportional. For longer pulses, the zone is larger with smaller maximum permanent strains, and for shorter pulses the trend is the opposite.

The numerical simulation of the wave propagation is powerful tool for the study of all aspects of soil-structure interaction. Here, we assumed that at the contacts there is no sliding. The next step in this research can be to explore more realistic models where the points on the soil-foundation contact can slide and separate. Further, the nonlinear model can be extended by including nonlinearity in the building and in the foundation. In the future, the soil-structure interaction should be studied in 3D models allowing sliding and gaps at the contacts. Finally, by introducing more "structures" the response of the structure-soil-structure and of bridge structures can be investigated.

Here we studied the response for a simple elementary input. This model can be used to study the soil-structure interaction for arbitrary input $w = w(t)$, including real seismograms.

BIBLIOGRAPHY

1. Abdel-Ghaffar, A.M., & Trifunac M.D. (1977). Antiplane dynamic soil-bridge interaction for incident plane SH-waves, Proc. 6th World Conf. on Earthquake Eng., Vol.II, New Delhi, India.

2. Aki, K., & Richards, P. (1980). Quantitative seismology, theory and methods. (Publication): W.H. Freeman & Co.

3. Alford, R.M., Kelly, K.R., & Boore D.M. (1974). Accuracy of finite-difference modeling of the acoustic wave equation. Geophysics 39, 834 – 842.

4. Alterman, Z. & Caral, F.C. (1968). Propagation of elastic waves in layered media by finite difference methods. Bull. Seism. Soc. of Amer., 58 (1), 367 – 398.

5. Aviles, J., Suarez, M., & Sanchez-Sesma, F.J. (2002). Effects of wave passage on the relevant dynamic properties of structures with flexible foundation. Earthq. Eng. and Struct. Dynamics, 31, 139 – 159.

6. Bayliss, A., & Turkel, E. (1980). Radiation boundary conditions for wave-like equations, Comm. Pure and Appl. Math. 33, 707 – 725.

7. Blume and Assoc. (1973). Holiday Inn, in San Fernando, California, Earthquake of February 9, 1971 (L.M. Murphy, Ed.) U.S. Dept. of Commerce, National Oceanic and Atmospheric Administration, Washington, D.C. (pp.359-393).

8. Boore, D.M. (1972). Finite difference methods for seismic wave propagation in heterogeneous materials. Methods in Comp. Physics 11, Academic Press Inc., New York.

9. Clayton, R., & Engquist, B. (1977). Absorbing boundary conditions for acoustic and elastic wave equations. Bull. Seism. Soc. Am., 67 (6), 1529 – 1540.

10. Dablain, M.A. (1986). The application of high-order differencing to the scalar wave equation. Geophysics 51 (1), 54 – 66.

11. Duke, C.M., Luco, J.E., Carriveau, P.J., Hradolek, J., Lastrico, R, & Ostrom, D. (1970). Strong earthquake motion and site conditions: Hollywood, Bull. Seism. Soc. of America, Vol.60 (4), 1271-1289.

12. Engquist, B., & Majda, A. (1979). Radiation boundary conditions for acoustic and elastic wave calculations. Comm. Pure and Appl. Math. 32, 313 – 357.

13. Eilon, B., Gottlieb, D., & Zwas, G. (1972). Numerical stabilizers and computing time for second-order accurate schemes. Journal of Computational Physics, 9, 387 – 397.

14. Fah D.J. (1992). A hybrid technique for the estimation of strong ground motion in sedimentary basins. Dissertation, Swiss Federal Institute of Technology, Zurich, Switzerland.

15. Fujino, Y., & Hakuno, M. (1978). Characteristics of elasto-plastic ground motion during an earthquake. Bull. Earthquake Res. Institute 53, 359 – 378.

16. Gachter, G.K., & Grote, M.J. (2003). Dirichlet-to-Neumann map for three-dimensional elastic waves. Wave Motion 37 (3), 293 – 311.

17. Givoli, D., and Keller, J.B. (1990). Non-reflecting boundary conditions for elastic waves. Wave Motion 12, 261 – 279.

18. Givoli, D. (2001). High-order nonreflecting boundary conditions without high-order derivatives. Journal of Computational Physics, 170, 849 – 870.

19. Graves, R.W., (1996). Simulating seismic wave propagation in 3-D elastic media using staggered-grid finite differences. Bull. Seis. Soc. of Am., 86 (4), 1091 – 1106.

20. Grote, M.J., & Keller, J.B. (1996). Nonreflecting boundary conditions for time-dependent scattering. Journal of Computational Physics 127, 52 – 65.

21. Hagstrom T., Hariharan, S.I., & Thompson, D. (2003). High-order radiation boundary conditions for the convective wave equation in exterior domains. SIAM Journal Sci. Comput. 25 (3), 1088 – 1101.

22. Hayashi, K., Burns, D.R., & Toksoz, M.N. (2001). Discontinuous-grid finite-difference seismic modeling including surface topography. Bull. Seis. Soc.Am. 91, 1750 – 1764.

23. Hayir, A., Todorovska, M.I., & Trifunac, M.D. (2001). Antiplane response of a dike with flexible soil-structure interface to incident SH waves. Soil Dynam. and Earthq. Eng. 21, 603 – 613.

24. Higdon, R.L. (1986). Absorbing boundary conditions for difference approximations to the multi-dimensional wave equation. Math. Of Comp., 47 (176), 437 - 459.

25. Higdon, R.L. (1991). Absorbing boundary conditions for elastic waves. Geophysics, 56 (2), 231 – 241.

26. Holberg, O. (1987). Computational aspects of the choice of operator and sampling interval for numerical differentiation in large-scale simulation of wave phenomena. Geophys. Prosp. 35, 629 – 655.

27. Kallivokas, L.F., & Lee, S. (2004). Local absorbing boundaries of elliptical shape for scalar waves. Comp. Methods in Appl. Mech. and Eng., (in press).

28. Katsaounis, T. & Levy, D. (1999). A modified structured central scheme for 2-D hyperbolic conservation laws. Applied Math. Letters 12, 89 – 96.

29. Kausel, E., & Tassoulas, J.L. (1981). Transmitting boundaries: A close-form comparison. Bull. Seism Soc. Am., 71 (1), 143 – 159.

30. Kausel, E. (1988). Local transmitting boundaries. Journal of Engineering Mechanics, 114 (6),1011 – 1027.

31. Kindelan, M., Kamel, A, & Sguazzero, P. (1990). On the construction and efficiency of staggered numerical differentiators for the wave equation. Geophysics 55, 107 – 110.

32. Kummer, B., Behle. A., & Dorau, F. (1987). Hybrid modeling of elastic-wave propagation in two-dimensional laterally inhomogeneous media. Geophysics 52 (6), 765 – 771.

33. Lax, P.D. & Wendroff B. (1964). Difference schemes for hyperbolic equations with high order of accuracy. Comm. on Pure and Applied Mathematics, XVII, 381 – 398.

34. Lee, S., & Kallivokas, L.F. (2004). Local absorbing boundaries of elliptical shape for scalar wave propagation in a half-plane, Finite Elem. in Anal. and Design, (in press).

35. Lee, V.W. (1979). Investigation of three-dimensional soil-structure interaction, Report No. CE 79-11.

36. Levander, A.R. (1988). Fourth-order finite-difference P-SV seismograms. Geophysics 53 (11), 1425 – 1436.

37. Levy, D., Puppo, G., & Russo, G. (2000). A third-order central WENO scheme for 2-D conservation laws. Applied Numerical Math. 33, 415 – 421.

38. Liao, Z.P., & Wong, H.L. (1984). A transmitting boundary for the numerical simulation of elastic wave propagation. Soil Dynamics and Earthquake Engineering 3, 174 – 183.

39. Liao, Z.P., Yang, P.P., & Yuan, Y.F. (1978). Feedback effect of low-rise buildings on vertical earthquake ground motion and application of transmitting boundaries for transient wave analysis, Institute of Eng. Mechanics, Academia Sinica, Harbin, China.

40. Lin, X. (1996). Numerical Computation of Stress Waves in Solids, Berlin: Akademie Verlag GmbH.

41. Luco, J.E. & Wong, H.L. (1977). Dynamic response of rectangular foundations for Rayleigh wave excitation. Proc. 6th World Conf. on Earthq. Eng., Vol.II, New Delhi, India.

42. Lysmer, J., & Kuhlemeyer, R.L. (1969). Finite dynamic model for infinite media, J. Eng. Mech. Div., ASCE, 98(EM1), 85 -105.

43. Mitchell, A.R. (1969). Computational methods in partial differential equations. New York: John Willey & Sons.

44. Moczo, P. (1989). Finite-difference tecnique for SH-waves in 2-D media using irregular grids-application to the seismic response problem. Geophys. Jour. Int., 99, 321 – 329.

45. Ohminato, T., & Chouet, B.A. (1997). A free surface boundary condition for Including 3-D topography in the finite-difference method. Bull. Seis. Soc. of Am. 87, 494 – 515.

46. Premrov, M., & Spacapan, I. (2004). Solving exterior problems of wave propagation based on an iterative variation of local DtN operators. Appl. Math. Model. 28 (3), 291 – 304.

47. Reynolds, A.C. (1978). Boundary conditions for the numerical solution of wave propagation problems. Geophysics, 43 (6), 1099 - 1110.

48. Smith, G.D. (1985). Numerical Solution of Partial Differential Equations, Finite Difference Methods. Oxford :Clarendon Press.

49. Smith, W.D. (1974). A non-reflecting plane boundary for wave propagation problems. Journal of Computational Physics, 15, 492-503.

50. Sochacki, J., Kubichek, R., George, J., Fletcher, W.R. & Smithson S. (1987). Absorbing boundary conditions and surface waves. Geophysics 52, 60 – 71.

51. Sod, G. (1985). Numerical Methods in Fluid Dynamics,Cambridge. UK Univ. Press.

52. Todorovska, M.I., Hayir, A., & Trifunac, M.D. (2001). Antiplane response of a dike on flexible embedded foundation to incident SH-waves. Soil Dynam. and Earthq. Eng. 21, 593 – 601.

53. Trifunac, M.D. (1971). Zero baseline correction of strong-motion accelerograms. Bull. Seism. Soc. of America, 61 (5) 1201-1211.

54. Trifunac, M.D. (1972). Interaction of a shear wall with the soil for incident plane SH waves. Bull. Seism. Soc. of America, 62 (1), 63 - 83.

55. Trifunac, M.D. (2003). 70th Anniversary of Biot Spectrum, 23rd Annual Lecture, Indian Society of Earthquake Technology Journal, Paper 431, Vol. 40, No.1, 19-50.

56. Trifunac, M.D., & Todorovska, M.I. (1997). Response spectra and differential motion of columns. Earthquake Eng. and Structural Dyn., 26, (2), 251-268.

57. Trifunac, M.D., Hao, T.Y., & Todorovska, M.I. (2001). On energy flow in earthquaqe response. Dept. of Civil Eng., Rep. 01-03, Univ. of Southern California, Los Angeles, California.

58. Tsynkov, S.V. (1998). Numerical solution of problems on unbounded domains. A review. Applied Numerical Mathematics 27, 465 - 532.

59. Vidale, J.E.& Clayton, R.W. (1986). A stable free surface boundary condition for two-dimensional Elastic Finite Difference Wave Simulation, Geophysics 51, 2247-2249.

60. Virieux, J. (1984). SH-wave propagation in heterogeneous media: Velocity-stress finite difference method, Geophysics 51, 889 – 901.

61. Wang, Y., Xu, J., & Schuster, G.T. (2001). Viscoelastic wave simulation in basins by a variable-grid finite-difference method. Bull. Seism. Soc. of Am. 91, 1741 - 1749.

62. Westermo, B.D. & Wong, H.L. (1977). On the fundamental differences of three basic soil-structure interaction models, Proc. 6th World Conf. of Eart. Eng., Vol.II, New Delhi, India.

63. Wong, H.L. & Trifunac, M.D. (1974). Interaction of a shear wall with the soil for incident plane SH waves : Elliptical rigid foundation. Bull. Seism. Soc. of America, 64 (6), 1825 - 1884.

64. Wong, H.L. & Trifunac, M.D. (1975). Two-dimensional antiplane, building-soil-building interaction for two or more buildings and for incident plane SH waves. Bull. Seism. Soc. of America, 65 (6), 1863 – 1885.

65. Zahradnik, J. & Urban, L. (1984). Effect of a simple mountain range on underground seismic motion. Geophys. J.R.astr.Soc. 79, pp.167-183.

66. Zahradnik, J., Moczo, P. & Hron F. (1993). Testing four elastic finite-difference schemes for behavior at discontinuities, Bull. Seism. Soc. of America 83, 107-129.

APPENDIX I

FINITE DIFFERENCE FORMULAE FOR CHARACTERISTIC POINTS

Introduction

For A, A_1, A_2, B and B_1 (Fig.2.4) all members of the vector $\underline{U}$ are computed simultaneously. To provide continuity of stresses and strains at the contact, at points C to H the stresses and strains are updated from the displacements, after the velocities and the displacements in all of the grid points have been computed. The displacements in all grid points are computed from the velocities using the rectangular quadrature rule:

$$w_{i,j}^{k+1} = w_{i,j}^{k} + \Delta t \cdot v_{i,j}^{k+1}.$$

Points A, A_1, A_2

$$\begin{aligned} v_{i,j}^{k+1} &= v_{i,j}^{k} + \frac{\Delta t}{2\Delta x \rho_{i,j}}\left(\sigma_{xi+1,j}^{k} - \sigma_{xi-1,j}^{k}\right) + \frac{\Delta t}{2\Delta y \rho_{i,j}}\left(\sigma_{y_{i,j+1}}^{k} - \sigma_{y_{i,j-1}}^{k}\right) + \\ &+ \frac{\Delta t^2}{2\rho_{i,j}\Delta x^2}\cdot\left[\mu_{xi+1/2,j}^{k}\left(v_{i+1,j}^{k} - v_{i,j}^{k}\right) - \mu_{xi-1/2,j}^{k}\left(v_{i,j}^{k} - v_{i-1,j}^{k}\right)\right] + \\ &+ \frac{\Delta t^2}{2\rho_{i,j}\Delta y^2}\left[\mu_{yi,j+1/2}^{k}\left(v_{i,j+1}^{k} - v_{i,j}^{k}\right) - \mu_{yi-1/2,j}^{k}\left(v_{i,j}^{k} - v_{i,j-1}^{k}\right)\right] \end{aligned} \qquad \text{(I.1A)}$$

$$\begin{aligned} \varepsilon_{xi,j}^{k+1} &= \varepsilon_{xi,j}^{k} + \frac{\Delta t}{2\Delta x}\left(v_{i+1,j}^{k} - v_{i-1,j}^{k}\right) + \frac{\Delta t^2}{2\Delta x^2 \rho_{i,j}}\left(\sigma_{xi+1,j}^{k} - 2\sigma_{xi,j}^{k} + \sigma_{xi-1,j}^{k}\right) + \\ &\frac{\Delta t^2}{8\Delta x \Delta y \rho_{i,j}}\left(\sigma_{yi+1,j+1}^{k} - \sigma_{yi+1,j-1}^{k} - \sigma_{yi-1,j+1}^{k} + \sigma_{yi-1,j-1}^{k}\right) \end{aligned} \qquad \text{(I.2A)}$$

$$\varepsilon_{yi,j}^{k+1} = \varepsilon_{yi,j}^{k} + \frac{\Delta t}{2\Delta y}\left(v_{i,j+1}^{k} - v_{i,j-1}^{k}\right) + \frac{\Delta t^2}{2\Delta y^2 \rho_{i,j}}\left(\sigma_{yi,j+1}^{k} - 2\sigma_{yi,j}^{k} + \sigma_{yi-1,j}^{k}\right) + \frac{\Delta t^2}{8\Delta x \Delta y \rho_{i,j}}\left(\sigma_{xi+1,j+1}^{k} - \sigma_{xi+1,j-1}^{k} - \sigma_{xi-1,j+1}^{k} + \sigma_{xi-1,j-1}^{k}\right). \quad \text{(I.3A)}$$

Points B, B_1

A typical cell of point B (B_1) has 7/8 of its area with material properties of soil (foundation) and 1/8 with material properties of foundation (soil). To avoid this heterogeneity, the cell is modified as shown in Fig.2.4. In this way, a uniform, square cell is obtained with lengths $d_{ab} = d_{bc} = d_{cd} = d_{da} = 2\Delta x' = \sqrt{2}\Delta x \Rightarrow \Delta x' = \frac{\Delta x}{\sqrt{2}}$. The stability condition for this cell is

$$\frac{\beta_{\max}\Delta t}{\Delta x'} = \frac{\sqrt{2}\beta_{\max}\Delta t}{\Delta x} \le \frac{1}{\sqrt{2}} \Rightarrow \frac{\beta_{\max}\Delta t}{\Delta x} \le \frac{1}{2}, \quad \text{(I.1B)}$$

where $\beta_{\max} = \max\left(\beta_f, \beta_s\right)$.

The condition (I.1B) is usually critical for obtaining Δt when $\beta_{\max}$ and Δx are prescribed.

The points labeled with small letters in Fig.2.4 are existing grid points, while the quantities at the midpoints of the cell sides are computed as mean values from the surrounding grid points. For example, if we want to compute $\underline{U}$ at point B(x_i, y_j) in the soil, we can use

$R_{ab} = R_{i-1/2,j-1/2} = \dfrac{R_{ij} + R_{i-1,j} + R_{i,j-1} + R_{i-1,j-1}}{4}$, and similarly for R_{bc} and R_{ad}. At the contact midpoint $R_{cd} = R_{i+1/2,j+1/2} = \dfrac{R_{ij} + R_{i+1,j} + R_{i,j+1}}{3}$.

The quantities R are velocities, radial and circular stresses, and radial and circular strains. To obtain the radial and circular components of the stresses at existing points, the orthogonal transformation is used, as follows:

$$\begin{Bmatrix} \sigma_{x'} \\ \sigma_{y'} \end{Bmatrix}_{i,j} = \begin{bmatrix} \cos\theta & \sin\theta \\ -\sin\theta & \cos\theta \end{bmatrix} \begin{Bmatrix} \sigma_x \\ \sigma_y \end{Bmatrix}_{i,j}, \qquad \text{(I.2B)}$$

where the angle $\theta = \begin{cases} \pi/4 & \text{for x} < 0 \\ 3\pi/4 & \text{for x} > 0 \end{cases}$.

The formulae for computing the quantities in vector $\underline{U}$ are the same as for the usual uniform cell A, so the formulae (I.1A)-(I.3A) are used with the substitutions $\Delta x' = \dfrac{\Delta x}{\sqrt{2}}$ for Δx and Δy and of course, $\sigma_{x'}, \sigma_{y'}$ for σ_x, σ_y. In this way, the velocities and the strains in the radial and in circular directions are obtained. The final step is to get back to the strains in Cartesian coordinates:

$$\begin{Bmatrix} \varepsilon_x \\ \varepsilon_y \end{Bmatrix}_{i,j} = \begin{bmatrix} \cos\theta & -\sin\theta \\ \sin\theta & \cos\theta \end{bmatrix} \begin{Bmatrix} \varepsilon_{x'} \\ \varepsilon_{y'} \end{Bmatrix}_{i,j}.$$

Points C - horizontal contact soil-foundation:

$$v_{i,j}^{k+1} = v_{i,j}^{k} + \frac{\Delta t}{4\Delta x \rho_{i,j}}\left(\sigma_{xi+1,j+0}^{k} - \sigma_{xi-1,j+0}^{k} + \sigma_{xi+1,j-0}^{k} - \sigma_{xi-1,j-0}^{k}\right) + \frac{\Delta t}{2\Delta y \rho_{i,j}}$$

$$\left(\sigma_{y_{i,j+1}}^{k} - \sigma_{y_{i,j-1}}^{k}\right) + \frac{\Delta t^2}{4\rho_{i,j}\Delta x^2}\cdot\left[\mu_{xi+1/2,j+0}^{k}\left(v_{i+1,j}^{k} - v_{i,j}^{k}\right) - \mu_{xi-1/2,j+0}^{k}\left(v_{i,j}^{k} - v_{i-1,j}^{k}\right)\right] +$$

$$+ \frac{\Delta t^2}{4\rho_{i,j}\Delta x^2}\cdot\left[\mu_{xi+1/2,j-0}^{k}\left(v_{i+1,j}^{k} - v_{i,j}^{k}\right) - \mu_{xi-1/2,j-0}^{k}\left(v_{i,j}^{k} - v_{i-1,j}^{k}\right)\right] +$$

$$+ \frac{\Delta t^2}{2\rho_{i,j}\Delta y^2}\left[\mu_{yi,j+1/2}^{k}\left(v_{i,j+1}^{k} - v_{i,j}^{k}\right) - \mu_{yi-1/2,j}^{k}\left(v_{i,j}^{k} - v_{i,j-1}^{k}\right)\right].$$

(I.1C)

The strains are continuous in the x direction and the stresses in y direction are:

$$\varepsilon_{xi,j}^{k+1} = \frac{w_{i+1,j}^{k+1} - w_{i-1,j}^{k+1}}{2\Delta x} \qquad \sigma_{xi,j+0}^{k+1} = \mu_f \varepsilon_{xi,j}^{k+1} \qquad \sigma_{xi,j-0}^{k+1} = \mu_s \varepsilon_{xi,j}^{k+1}$$

$$\sigma_{yi,j}^{k+1} = \frac{\mu_s \mu_f}{\mu_s + \mu_f}\frac{w_{i,j+1}^{k+1} - w_{i,j-1}^{k+1}}{\Delta y}.$$

Points D - horizontal structure-foundation contact:

$$v_{i,j}^{k+1} = v_{i,j}^{k} + \frac{\Delta t}{2\Delta x \rho_{i,j}}\left[\frac{\Delta y_b\left(\sigma_{xi+1,j+0}^{k} - \sigma_{xi-1,j+0}^{k}\right) + \Delta y_s\left(\sigma_{xi+1,j-0}^{k} - \sigma_{xi-1,j-0}^{k}\right)}{\Delta y_b + \Delta y_s}\right] +$$

$$\frac{\Delta t}{(\Delta y_s + \Delta y_b)\rho_{i,j}}\left(\sigma_{y_{i,j+1}}^{k} - \sigma_{y_{i,j-1}}^{k}\right) +$$

$$\frac{\Delta t^2}{2\rho_{i,j}\Delta x^2}\cdot\frac{\Delta y_b}{\Delta y_b + \Delta y_s}\left[\mu_{xi+1/2,j+0}^{k}\left(v_{i+1,j}^{k} - v_{i,j}^{k}\right) - \mu_{xi-1/2,j+0}^{k}\left(v_{i,j}^{k} - v_{i-1,j}^{k}\right)\right] +$$

$$+\frac{\Delta t^2}{2\rho_{i,j}\Delta x^2}\cdot\frac{\Delta y_b}{\Delta y_b + \Delta y_s}\left[\mu_{xi+1/2,j-0}^{k}\left(v_{i+1,j}^{k} - v_{i,j}^{k}\right) - \mu_{xi-1/2,j-0}^{k}\left(v_{i,j}^{k} - v_{i-1,j}^{k}\right)\right] +$$

$$+\frac{\Delta t^2}{\rho_{i,j}(\Delta y_b + \Delta y_s)}\left[\mu_{yi,j+1/2}^{k}\left(v_{i,j+1}^{k} - v_{i,j}^{k}\right)/\Delta y_b - \mu_{yi-1/2,j}^{k}\left(v_{i,j}^{k} - v_{i,j-1}^{k}\right)/\Delta y_s\right].$$

(I.1D)

The strains are continuous in the x direction and the stresses in y direction:

$$\varepsilon_{xi,j}^{k+1} = \frac{w_{i+1,j}^{k+1} - w_{i-1,j}^{k+1}}{2\Delta x} \qquad \sigma_{xi,j+0}^{k+1} = \mu_f \varepsilon_{xi,j}^{k+1} \qquad \sigma_{xi,j-0}^{k+1} = \mu_s \varepsilon_{xi,j}^{k+1}$$

$$\sigma_{yi,j}^{k+1} = \frac{\mu_b \mu_f}{\mu_b \Delta y_s + \mu_f \Delta y_b}\left(w_{i,j+1}^{k} - w_{i,j-1}^{k}\right).$$

Points E - vertical soil-foundation contact

$$v_{i,j}^{k+1} = v_{i,j}^{k} + \frac{\Delta t}{4\Delta y \rho_{i,j}}\left(\sigma_{y_{i+0,j+1}}^{k} - \sigma_{y_{i+0,j-1}}^{k} + \sigma_{y_{i-0,j+1}}^{k} - \sigma_{y_{i-0,j-1}}^{k}\right) + \frac{\Delta t}{2\Delta x \rho_{i,j}}$$

$$\left(\sigma_{x_{i+1,j}}^{k} - \sigma_{x_{i-1,j}}^{k}\right) + \frac{\Delta t^2}{4\rho_{i,j}\Delta y^2} \cdot \left[\mu_{yi+0,j+1/2}^{k}\left(v_{i,j+1}^{k} - v_{i,j}^{k}\right) - \mu_{yi+0,j-1/2}^{k}\left(v_{i,j}^{k} - v_{i,j-1}^{k}\right)\right] +$$

$$+ \frac{\Delta t^2}{4\rho_{i,j}\Delta y^2} \cdot \left[\mu_{yi-0,j+1/2}^{k}\left(v_{i,j+1}^{k} - v_{i,j}^{k}\right) - \mu_{yi-0,j-1/2}^{k}\left(v_{i,j}^{k} - v_{i,j-1}^{k}\right)\right] +$$

$$+ \frac{\Delta t^2}{2\rho_{i,j}\Delta x^2}\left[\mu_{xi+1/2,j}^{k}\left(v_{i+1,j}^{k} - v_{i,j}^{k}\right) - \mu_{xi-1/2,j}^{k}\left(v_{i,j}^{k} - v_{i-1,j}^{k}\right)\right]$$

(I.1E)

The strains are continuous in the y direction and the stresses in x direction are:

$$\sigma_{xi,j}^{k+1} = \frac{\mu_s \mu_f}{\mu_s + \mu_f} \frac{w_{i+1,j}^{k+1} - w_{i-1,j}^{k+1}}{\Delta x}.$$

For example, if $x < 0$, then

$$\varepsilon_{yi,j}^{k+1} = \frac{w_{i,j+1}^{k+1} - w_{i,j-1}^{k+1}}{2\Delta x} \qquad \sigma_{yi+0,j}^{k+1} = \mu_f \varepsilon_{yi,j}^{k+1} \qquad \sigma_{yi-0,j}^{k+1} = \mu_s \varepsilon_{yi,j}^{k+1}.$$

Points F - slant soil-foundation contact:

As for point B, the cell is modified so that one half of the modified cell has properties of the soil and another one half has the properties of the foundation.

$$v_{i,j}^{k+1} = v_{i,j}^{k} + \frac{\Delta t}{2\sqrt{2}\Delta x \rho_{i,j}}\left(\sigma_{y'14+}^{k} - \sigma_{y'23+}^{k} + \sigma_{y'14-}^{k} - \sigma_{y'23-}^{k}\right) + \frac{\Delta t}{\sqrt{2}\Delta x \rho_{i,j}}$$
$$\left(\sigma_{x'34}^{k} - \sigma_{x'12}^{k}\right) + \frac{\Delta t^2}{2\rho_{i,j}\Delta x^2}\cdot\left[\mu_{y'F14+}^{k}\left(v_{14}^{k} - v_{i,j}^{k}\right) - \mu_{y'F23+}^{k}\left(v_{i,j}^{k} - v_{23}^{k}\right)\right] +$$
$$+ \frac{\Delta t^2}{2\rho_{i,j}\Delta x^2}\cdot\left[\mu_{y'F14-}^{k}\left(v_{14}^{k} - v_{i,j}^{k}\right) - \mu_{y'F23-}^{k}\left(v_{i,j}^{k} - v_{23}^{k}\right)\right] +$$
$$+ \frac{\Delta t^2}{\rho_{i,j}\Delta x^2}\left[\mu_{x'+0}^{k}\left(v_{34}^{k} - v_{i,j}^{k}\right) - \mu_{x'-0}^{k}\left(v_{i,j}^{k} - v_{12}^{k}\right)\right]$$

(I.1F)

The stresses and the strains are obtained directly in the xOy system. For $x_F < 0$,

$$\sigma_{xf} = \mu_f \frac{w_3 - w_{i,j}}{\Delta x} \qquad \sigma_{xs} = \mu_f \frac{w_{i,j} - w_1}{\Delta x} \qquad \sigma_{yf} = \mu_f \frac{w_4 - w_{i,j}}{\Delta x}$$

$$\sigma_{ys} = \mu_s \frac{w_{i,j} - w_2}{\Delta x}.$$

Points G, G_1 – corners of the hexagon:

For example, for point G, $x = -a$, as follows:

$$v_{i,j}^{k+1} = v_{i,j}^{k} + \frac{\Delta t}{4\Delta y \rho_{i,j}}\left(\sigma_{y_{i+0,j+1}}^{k} + \sigma_{y_{i-0,j+1}}^{k} + \sigma_{ypp}^{k} + \sigma_{ymp}^{k} - 2\sigma_{y_{i,j-1}}^{k} - \sigma_{ymm}^{k} - \sigma_{ypm}^{k}\right) +$$

$$\frac{\Delta t}{4\Delta x \rho_{i,j}} \cdot \left(2\sigma_{x_{i+1,j}}^{k} + \sigma_{xpp}^{k} + \sigma_{xpm}^{k} - 2\sigma_{x_{i-1,j}}^{k} - \sigma_{xmm}^{k} - \sigma_{xmp}^{k}\right) + \frac{\Delta t^2}{4\rho_{i,j}\Delta y^2} \cdot$$

$$\left[\mu_{yi+0,j+1/2}^{k}\left(v_{i,j+1}^{k} - v_{i,j}^{k}\right) - \mu_{yi+0,j-1/2}^{k}\left(v_{i,j}^{k} - v_{i,j-1}^{k}\right)\right] + \frac{\Delta t^2}{4\rho_{i,j}\Delta y^2} \cdot$$

$$\left[\mu_{yi-0,j+1/2}^{k}\left(v_{i,j+1}^{k} - v_{i,j}^{k}\right) - \mu_{yi-0,j-1/2}^{k}\left(v_{i,j}^{k} - v_{i,j-1}^{k}\right)\right] + \frac{\Delta t^2}{2\rho_{i,j}\Delta x^2}$$

$$\left[\mu_{xi+1/2,j}^{k}\left(v_{i+1,j}^{k} - v_{i,j}^{k}\right) - \mu_{xi-1/2,j}^{k}\left(v_{i,j}^{k} - v_{i-1,j}^{k}\right)\right] \qquad \text{(I.1G)}$$

where:

$$\sigma_{ypp} = \frac{1}{2}\mu_f\left(\frac{w_{i,j+1} - w_{i,j}}{\Delta y_s} + \frac{w_{i+1,j} - w_{i+1,j-1}}{\Delta y_s}\right)$$

$$\sigma_{ypm} = \frac{1}{2}\left[\sigma_{ypp} + \mu_s\frac{w_{i,j+1} - w_{i,j-1}}{2\Delta y_s}\right]$$

$$\sigma_{ymp} = \sigma_{ymm} = \mu_s\frac{w_{i,j+1} - w_{i,j-1}}{2\Delta y_s}$$

$$\sigma_{xpp} = \frac{1}{2}\mu_f\left(\frac{w_{i+1,j+1} + w_{i+1,j} - w_{i,j+1} - w_{i,j}}{2\Delta x} + \frac{w_{i+1,j} - w_{i,j}}{\Delta x}\right) \qquad \text{(I.2G)}$$

$$\sigma_{xpm} = \frac{1}{2}\left[\sigma_{xpp} + \mu_s\frac{w_{i+1,j-1} - w_{i,j-1}}{\Delta x_s}\right]$$

$$\sigma_{xmp} = \sigma_{xmm} = \mu_s \frac{w_{i,j} - w_{i-1,j}}{\Delta x}.$$

After obtaining velocities and displacements at all grid points, the stresses are obtained from the formulae (I.2G). The procedure is similar for the points G' at the bottom $(y = -a)$.

Points H – corners on the soil-foundation-structure boundary:

There are two points of this kind in the model $(x = \pm a, y = 0)$. We consider the left point (- a, 0). The boundary conditions for the cell are

$$\sigma_{yi-1,j} = \sigma_{yi-0,j} = 0 \qquad \sigma_{xi,j+1} = \sigma_{xi,j+0} = 0 \qquad \text{(I.1H)}$$

To customize the cell for the numerical scheme, and having the boundary conditions (I.1H) with linear extrapolation in the fictitious points, we have:

Point (i-1,j+1): $\sigma_{xi-1,j+1} = -\sigma_{xi+1,j+1} \qquad \sigma_{yi-1,j+1} = -\frac{\Delta y_b}{\Delta y_s}\sigma_{yi-1,j-1}.$ (I.1Ha)

Point (i-1,j+0): $\sigma_{xi-1,j+0} = -\sigma_{xi+1,j+0}.$ (I.1Hb)

Point (i-0,j+1): $\sigma_{yi-0,j+1} = -\frac{\Delta y_b}{\Delta y_s}\sigma_{yi-0,j-1}.$ (I.1Hc)

$$v_{i,j}^{k+1} = v_{i,j}^{k} + \frac{\Delta t}{2(\Delta y_b + \Delta y_s)\rho_{i,j}} \left[\begin{array}{l} \left(\sigma_{y_{i+0,j+1}}^{k} + \sigma_{y_{i-0,j+1}}^{k} + \sigma_{ypp}^{k} + \sigma_{ymp}^{k} \right) - \\ - \left(\sigma_{y_{i+0,j-1}}^{k} + \sigma_{yi-0,j-1}^{k} + \sigma_{ymm}^{k} + \sigma_{ypm}^{k} \right) \end{array} \right]$$

$$+ \frac{\Delta t}{2\Delta x \rho_{i,j}} \left[\left(\sigma_{xp1}^{k} + \sigma_{xp0}^{k} - \sigma_{xm1}^{k} - \sigma_{xm0}^{k} \right) \right] + \frac{\Delta t^2}{4\rho_{i,j}\Delta y^2} \cdot$$

$$\left[\mu_{yi+0,j+1/2}^{k} \left(v_{i,j+1}^{k} - v_{i,j}^{k} \right) - \mu_{yi+0,j-1/2}^{k} \left(v_{i,j}^{k} - v_{i,j-1}^{k} \right) \right] + \frac{\Delta t^2}{4\rho_{i,j}\Delta y^2} \cdot \qquad \text{(I.2H)}$$

$$\left[\mu_{yi-0,j+1/2}^{k} \left(v_{i,j+1}^{k} - v_{i,j}^{k} \right) - \mu_{yi-0,j-1/2}^{k} \left(v_{i,j}^{k} - v_{i,j-1}^{k} \right) \right] + \frac{\Delta t^2}{2\rho_{i,j}\Delta x^2}$$

$$\left[\mu_{xi+1/2,j}^{k} \left(v_{i+1,j}^{k} - v_{i,j}^{k} \right) - \mu_{xi-1/2,j}^{k} \left(v_{i,j}^{k} - v_{i-1,j}^{k} \right) \right]$$

with:

$\sigma_{ypp}^{k} = \sigma_{ypm}^{k} = \dfrac{\mu_f \mu_b}{\mu_f \Delta y_b + \mu_b \Delta y_s} \left(w_{i,j+1}^{k} - w_{i,j-1}^{k} \right)$ from the continuity of the stresses in the y direction

$\sigma_{ymp}^{k} = \sigma_{ymm}^{k} = 0$ from (I.1H),

$\sigma_{xp1} = \dfrac{1}{\Delta y_s + \Delta y_b} \left(\Delta y_s \sigma_{xi+1,j-0} + \Delta y_b \sigma_{xi+1,j+0} \right)$, where

$\sigma_{xi+1,j+0} = \dfrac{\mu_b}{\mu_f} \sigma_{xi+1,j-0}$ from the continuity of the strains in the structure-foundation contact,

$\sigma_{xp0} = \dfrac{1}{\Delta y_s + \Delta y_b} \left(\Delta y_s \sigma_{xi+0,j-0} + \Delta y_b \sigma_{xi+0,j+0} \right) = \sigma_{xm0}$, where

$\sigma_{xi+0,j+0} = 0$ from (I.1H)

$\sigma_{xm1} = \dfrac{1}{\Delta y_s + \Delta y_b} \left(\Delta y_s \sigma_{xi-1,j-0} + \Delta y_b \sigma_{xi-1,j+0} \right)$, where

$$\sigma_{xi-1,j+0} = -\sigma_{xi+1,j+0}\,. \tag{I.1Hb}$$

And from the continuity of stresses in the soil-foundation contact we have:

$$\sigma_{xm0} = \sigma_{xp0} = \frac{\mu_f \mu_s}{\Delta x\left(\mu_f + \mu_s\right)}\left(w_{i+1,j-0} - w_{i-1,j-0}\right).$$

APPENDIX II

INPUT ENERGY FOR THE STRUCTURE

From the ray theory, and according to Fig.II, two types of rays reach the foundation and are relevant in the energy distribution:

- rays i reach the foundation directly without reflection from the free surface
- rays r reach the foundation after reflecting from the free surface

The energy brought to the foundation by rays i is

$$E_i = \rho_s \beta_s \int_A dA_i \int_t v^2 dt \,, \qquad \text{(II.1)}$$

where:

ρ_s is the soil density,

β_s is the velocity of propagation of the SH wave in the soil,

v is the particle velocity of the incoming plane wave, and

dA_i is the projection of the differential area of the semicircular foundation in the direction of propagation of the ray i: $dA_i = a \cdot d\theta \cdot \cos\alpha$.

Substituting dA_i in (II.1), we have

$$E_i = a\rho_s \beta_s \int_0^{\theta_i} \cos\alpha \cdot d\theta_i \int_0^T v^2 dt \,, \qquad \text{(II.2)}$$

where T is the time at the end of the analysis.

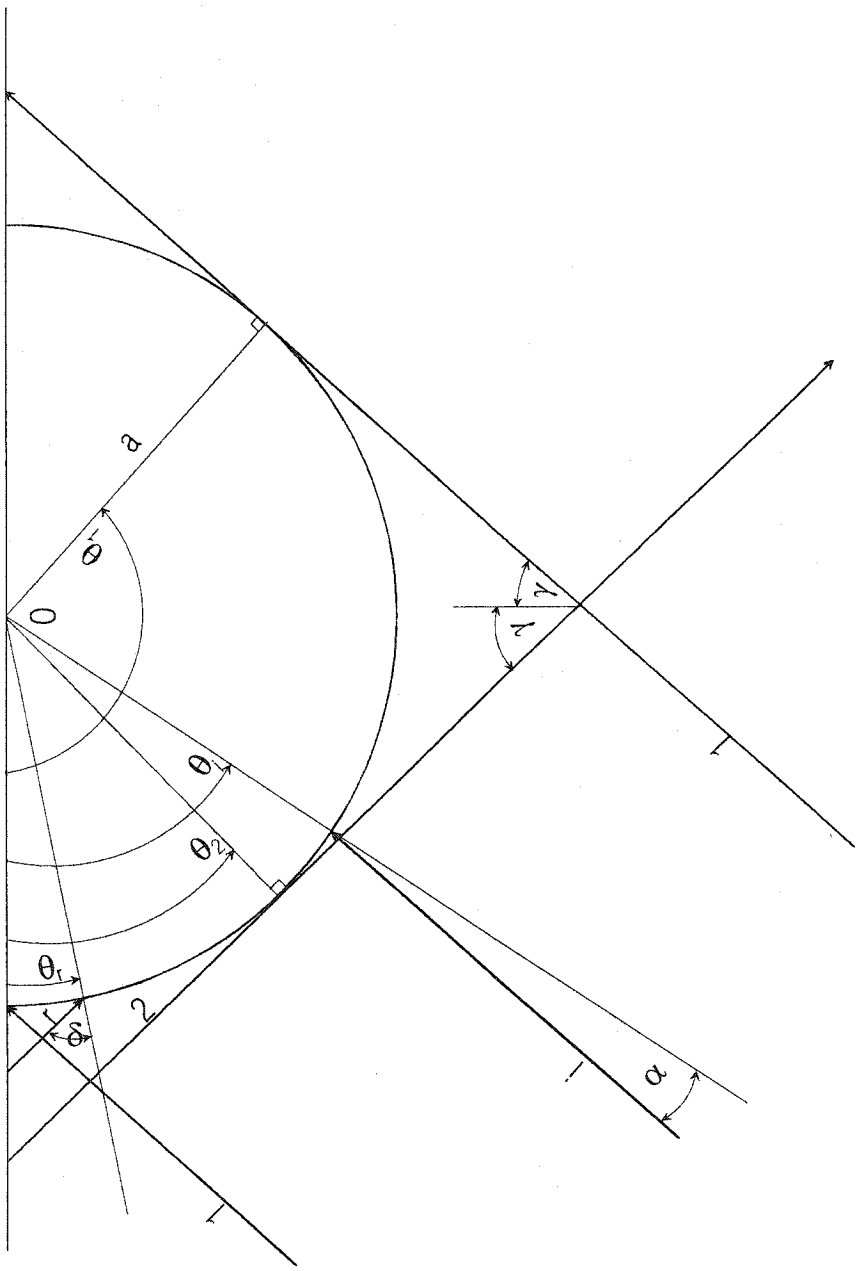

Fig. II INPUT ENERGY REACHING THE FOUNDATION

From geometry it can be readily seen that $\alpha = \left|\frac{\pi}{2} - \gamma - \theta_i\right|$, and because the cosine is an even function, we can omit the absolute sign. Also $\theta_1 = \pi - \gamma$ and (II.2) becomes

$$E_i = a\rho_s\beta_s \int_0^{\pi-\gamma} \cos\left[\frac{\pi}{2} - (\gamma + \theta_i)\right] d\theta_i \int_0^T v^2 dt = a\rho_s\beta_s \int_0^{\pi-\gamma} \sin(\gamma + \theta_i) d\theta_i \int_0^T v^2 dt, \quad \text{(II.3)}$$

with the solution:

$$E_i = a\rho_s\beta_s \cdot (1 + \cos\gamma) \int_0^T v^2 dt. \quad \text{(II.4)}$$

In a similar way, for the energy brought to the foundation by rays r having

$\delta = \frac{\pi}{2} - \gamma + \theta$ and $\theta_2 = \gamma$ and T is big enough so that the reflected pulse pass the foundation, the integrals in time are equal:

$$E_r = a\rho_s\beta_s (1 - \cos\gamma) \int_0^T v^2 dt. \quad \text{(II.5)}$$

Adding (II.5) to (II.4), the total energy brought to the structure is

$$E_{tot} = 2a\rho_s\beta_s \int_0^T v^2 dt. \quad \text{(II.6)}$$

It can be seen from (II.6) that the energy reaching the semi circular foundation does not depend upon the incident angle. Also, it is linearly proportional to the diameter of the foundation, the density, and the shear wave velocity of the soil.

We note finally that for both buildings studied in this thesis, the energy brought to the foundation for the same η is the same. This conclusion is straightforward from the definition of η:

$$\eta = \frac{2a}{\lambda} = \frac{a}{\beta_s t_{d0}}. \qquad \text{(II.7)}$$

The particle velocity from the definition of the half-sine pulse (5.4) is:

$$v = \frac{\pi A}{t_{d0}} \cos \frac{\pi t}{t_{do}}. \qquad \text{(II.8)}$$

Substituting (II.8) in (II.6) and performing the integration, we have

$E_{tot} = 2a\rho_s \beta_s \cdot \frac{\pi^2 A^2}{2t_{d0}}$. Multiplying the numerator and the denominator with β_s keeping in mind (II.7), the total input energy for the foundation is

$$E_{tot} = \pi^2 A^2 \beta_s^2 \rho_s \eta. \qquad \text{(II.9)}$$

It may seem that this equation has the dimension of force, but we should keep in mind that the third dimension (length) of the model is taken equal to unity and is therefore omitted in (II.9).